INFLUENCE OF INTERCRITICAL ANNEALING ON THE MECHANICAL PROPERTIES OF PLAIN-CARBON DUAL-PHASE STEELS

A THESIS

Submitted in fulfilment of the requirements
for the award of the degree
of
DOCTOR OF PHILOSOPHY
in
METALLURGICAL ENGINEERING

By

SUMEER KUMAR NATH

DEPARTMENT OF METALLURGICAL ENGINEERING
UNIVERSITY OF ROORKEE
ROORKEE-247667 (INDIA)

NOVEMBER, 1989

CANDIDATE'S DECLARATION

I hereby certify that the work which is being presented in the thesis entitled "Influence of Intercritical Annealing on the Mechanical Properties of Plain-Carbon Dual-Phase Steels" in fulfilment of the requirement for the award of the Degree of Doctor of Philosophy submitted in the Department of Metallurgical Engineering of the University is an authentic record of my own work carried during a period from 29.7.1983 to 31.3.1989 under the supervision of Dr.S.Ray, Reader; Dr.V.N.S.Mathur, Professor and Dr.M.L.Kapoor, Professor; in Metallurgical Engineering Department, University of Roorkee, Roorkee.

The matter embodied in this thesis has not been submitted by me for the award of any other Degree.

Candidate's Signature

S.K.Nath

(Sumeer Kumar Nath)

This is to certify that the above statement made by the candidate is correct to the best of my knowledge.

Signature of Supervisor(s)

Ray

(S. RAY)

Mathur 15.11.89

(V.N.S.MATHUR)

Kapoor

(M.L.KAPOOR)

Date : Nov 15, 1989.

The candidate has passed the Viva-Voce examination on at . The thesis is recommended for award of the Ph.D. Degree.

Signature of Guide(s)

Signature of External Examiner(s)

CONTENTS

ABSTRACT

Dual-phase steels consisting of martensite phase embedded in the ferrite matrix are becoming important engineering materials due to a unique combination of properties viz., (i) continuous yielding behaviour or the absence of yield point phenomenon, (ii) low 0.2 pct. off-set proof strength, (iii) high work hardening rate, (iv) high tensile strength & (iv) high ductility measured as uniform and total elongations. Consequently, although the dual-phase steels have strengths comparable to those of high strengths low alloy (HSLA) steels, yet their ductility and formability are comparable to those of the mild steels. These high strength steels are, therefore, increasingly used as thin-sheets in the automobile industry for fabrication of light vehicle bodies to achieve appreciable fuel-economy.

A critical review of the available literature reveals that most of the studies conducted so far on these steels have either been restricted to low alloy high strength (HSLA) steels or carried out at fixed intercritical annealing times at which the volume fraction of austenite reaches almost the equilibrium value. Little attempt has been made to study plain-carbon dual-phase steels, specially to elucidate the role of their carbon content in a wider range of composition. Further, the formation of austenite takes place through a series of steps and the composition

and volume fraction of the austenite and the matrix keeps on changing before attaining equilibrium. Therefore, a study of the effect of time of intercritical annealing on mechanical properties of dual-phase steels is imperative to get an optimum combination of strength, ductility and formability. In other words, a need for correlation of mechanism of formation of dual-phase microstructure with mechanical properties of such dual-phase steels exists. It is also necessary to reveal the role of variation of carbon content of these steels from very low to high values to analyse its effect on the different stages of formation of austenite and hence martensite on quenching, and therefore, on the overall mechanical properties of plain-carbon dual-phase steels. For theoretical prediction of strength of dual-phase steels and the impact of various microstructural parameters on it, these have been treated as composites and the law of mixtures has been applied by earlier workers. But no attempt has been made to incorporate the effect of shape of second phase particles embedded in the matrix in such composite materials, and also the effect of strain-hardening.

The present investigation has, therefore, been undertaken to, study plain-carbon dual-phase steels in order to gain an insight into the above mentioned areas.

The entire work has been presented in Seven Chapters in the thesis.

In Chapter-1, general introduction of dual-phase steels is presented with respect to their historical development and paramount importance.

Chapter-2 deals with a critical review of the available literature on dual-phase steels. After very briefly reviewing the production techniques of dual-phase steels, the different stages of austenite formation along with its kinetics when conducted non-isothermally have been focussed. The mechanical properties in respect of work-hardening, yielding behaviour, strength, ductility and formability have also been critically examined in the light of current understanding. The review of literature has culminated in identification of specific gaps where this investigation is directed.

Chapter-3 deals with theoretical analysis of the strength of dual-phase steels. Contribution of different strengthening mechanisms for example, strain-hardening and superior load bearing capacity of martensite islands have been investigated within the framework of shear-lag model of spherical and cylindrical with hemi-spherical ends of martensite islands. An effort has been made for the first time to take into account the entire range of shapes of second phase martensite particle in terms of the ratio of radius to length, (r/ℓ), varying from 0.4 to 0.6 within the framework of single-particle model. The following expression has been arrived at for the

theoretical tensile strength, of the dual-phase steels.

$$\sigma_{u,c} = \sigma_{u,f}\left[1-\left(\frac{r}{\ell}\right)\right]V_f + \sigma_{u,m}\left[1+\left\{\frac{2}{3}\left(\frac{r}{\ell}\right)-1\right\}V_f\right]+KG\sqrt{\frac{\bar{b}V_f\epsilon}{0.41\bar{D}_i}} \quad \ldots (1a)$$

which on substitution of relevant empirical parameters reduces to the following form,

$$\sigma_{u,c} = 2000\left[1-\left(\frac{r}{\ell}\right)\right]V_f+415\left[1+\left\{\frac{2}{3}\left(\frac{r}{\ell}\right)-1\right\}V_f\right]+0.67\sqrt{\frac{V_f}{\bar{D}_i}} \quad \ldots (1b)$$

Where $\sigma_{u,f}$ is the UTS of martensite, $\sigma_{u,m}$ is the UTS of the ferrite matrix, V_f is the volume fraction of martensite, the (r/ℓ) ratio represents a dimensionless parameter indicating deviation from the ideal spherical shape, $\bar{D}_i$ is the average size of the martensite islands on a planar section, K is a constant of the order of 1, G is the shear modulus of the matrix, $\bar{b}$ is the Burger's vector of the matrix dislocation, and ϵ is the true Strain.

Chapter-4 deals with the details of experimental set-up used and methods of preparation of specimen, heat-treatment and measurement of the different mechanical properties and study of corresponding microstructures. Specimens for tensile test along with extended end for metallographic examination, have been cut using a die specially fabricated for this purpose from plain-carbon

steel sheets of three compositions viz., 0.08 wt.pct., 0.115 wt.pct. and 0.4 wt.pct. carbon content along the direction of rolling. However, the specimens prepared for measurement of $\bar{R}$-values, have been cut in three directions viz., in a direction perpendicular, at an angle of 45°, and parallel to the direction of rolling. To develop dual-phase microstructures with varying martensite volume fraction (MVF), specimens are first normalised and then intercritically annealed at three selected temperatures viz., 740°C, 760°C and 780°C for different duration ranging from 1 minute to 3 hours and finally quenched in either water or oil depending on their carbon content. The extended ends of the tensile specimens have been cut for metallographic examination and the remaining portion is used for tensile test, which has been carried out on Monsanto tensometer for all specimens. From these tests values of 0.2 pct. off-set proof strength or the yield strength (YS), ultimate tensile strength (UTS), ductility and formability measured in terms of $\bar{R}$-value i.e., mean plastic strain ratio have been calculated. Martensite volume fraction (MVF) in each specimens of dual-phase steels has been measured using point counting technique and dimensions of martensite islands have been determined by linear-intercept method. On some selected specimens, microhardness of ferrite and martensite phases has also been determined. Typical fractured tensile specimens have been examined under Scanning Electron

Microscope (SEM). Transmission Electron Microscopic (TEM) study has also been conducted on one dual-phase steel specimen to depict the dislocation substructure in the ferrite phase. Kinetics of non-isothermal austenitisation has been studied using a Differential Scanning Calorimeter (DSC) at three different heating rates.

Chapter-5 presents analysis of the influence of temperature and time of intercritical annealing on the mechanical properties, viz., yield strength, ultimate tensile strength, ductility and formability or $\bar{R}$-values of different dual-phase steels under investigation. Strength of dual-phase steels has been found to increase initially with an increase in intercritical annealing time at any specific intercritical annealing temperature, then remains constant for some time and finally decreases. However, the maximum strength attained increases with the carbon content of the dual-phase steels as well as the intercritical annealing temperature. Ductility of dual-phase steels initially decreases with intercritical annealing time and then attains a minimum constant value. However, the minimum ductility value decreases with the increase in intercritical annealing temperature and also with an increase in carbon content of dual-phase steels. The formability measured in terms of $\bar{R}$-values of dual-phase steels containing 0.08 wt.pct and 0.115 wt.pct. carbon show a trend similar

to that of ductility of these steels. The $\bar{R}$-value for dual-phase steel containing 0.4 wt.pct. carbon could not be measured due to their very low ductility. The tensile fractured specimens of dual-phase steels containing 0.08 and 0.115 wt.pct. carbon show ductile fracture at all intercritical annealing temperatures and times used in the present investigation. However, fractured specimens of 0.4 wt.pct. carbon dual-phase steel show ductile fracture only when intercritically annealed for less than 5 minutes at 740°C and 760°C temperatures and for intercritical annealing times greater than 5 minutes at these temperatures mixed mode of fracture i.e., ductile plus brittle fracture is observed. Similarly, at 780°C intercritical annealing temperature, mixed mode of fracture is observed in 0.4 wt.pct. carbon dual-phase steel for all intercritical annealing times used in the present work.

Chapter-6 deals with non-isothermal kinetics of austenitisation of three plain-carbon steels studied by Differential Scanning Calorimeter (DSC). Kinetic parameters like activation energy and order of reaction or Avrami exponent have been calculated using Kissinger analysis. Using these parameters in Johnson-Mehl-Avrami equation, times for attaining equilibrium austenite volume fractions at different intercritical annealing temperatures have been determined. As this time is very important for a

given dual-phase steel during intercritical annealing for obtaining optimum mechanical properties.

Lastly, following conclusions based on the present investigation, have been presented in Chapter-7. The present study has revealed that intercritical annealing heat treatment for the development of dual-phase microstructure should not be carried out beyond the time required for the transformation to equilibrium volume fraction of austenite (martensite on quenching) at a given temperature as it causes strength to fall and ductility to saturate at its minimum. In order to obtain optimum mechanical properties for a given application, intercritical annealing time should be confined to the period when transformation to austenite is taking place. The decrease in strength and ductility is attributed to the grain growth of ferrite phase and redistribution of carbon content between ferrite and austenite phases during the final stage of intercritical austenitisation of steel.

The model for strengths of dual-phase steels reveals, the importance of shape of martensite island embedded in the matrix of ferrite and its variation with the process parameters of intercritical annealing has been studied.

Time to attain equilibrium austenite volume fraction at different intercritical annealing temperatures is thus

of paramount importance and it has been calculated with the help of kinetic parameters obtained from non-isothermal kinetics of austenitisation studied by Differential Scanning Calorimeter (DSC).

ACKNOWLEDGEMENTS

The author wishes to record his deep sense of gratitude and indebtedness to Dr.S.Ray, Reader, Dr.V.N.S.Mathur, Professor and Dr.M.L.Kapoor, Professor and Head, Department of Metallurgical Engineering, University of Roorkee, Roorkee, for their guidance, constructive criticism thought -provoking discussions and suggestions that they have very kindly made available to him during all phases of the investigation and preparation of this thesis. Without their timely and untiring help, it could not have been possible to present the work contained in this thesis in its present form.

The author is highly obliged and wishes to express his sincere thanks to the staff of various laboratories of Metallurgical Engg. Department, especially to Mr. Ajmer Singh, Mr. S.P.Kush, Mr. S.C.Kaushik, Mr. Balesh Sharma, Mr. Vidya Prakash, Mr. Karan Singh and Mr. Madhu Kumar who have helped him in all possible ways during the experimental work. The assistance rendered by the staff of the University Service and Instrumentation Centre, University of Roorkee, Roorkee, during thin film studies by Transmission Electron Microscopy, Fractographic studies by Scanning Electron Microscopy and Kinetic Studies by Differential Scanning Calorimetry is also gratefully acknowledged.

Thanks are also due to Tata Steel, Jamshedpur and Roadmaster Steel Strips Ltd., Rishikesh for providing steels and also B.H.E.L., Hardwar for carrying out Chemical analysis.

Special thanks are due to Mr.S.K.Seth, for preparing high quality micrographs, to Mr.S.C.Sharma for neat tracing and drawing work, and to Mr.R.P.Singh for flawless typing of the thesis.

The author also acknowledges his deep sense of appreciation for all the help rendered by his colleagues Dr.(Mrs.) Vijaya Agarwal, Prof.D.B.Goel and Prof.A.K.Patwardhan at the different stages of preparation of this thesis.

The author wishes to express his sincere gratitude to all his family members especially his mother, brothers and sisters who have shown keen interest in his work and contributed directly or indirectly towards his achievements.

The author expresses his sincere thanks to all his friends for the assistance and active cooperation rendered by them.

My wife Mala deserves special acknowledgement for her continuous encouragement, specially at difficult times and the perseverance shown by her to bear the extra responsibilities of the family due to gross negligence on my part. My son Vishnu had also to face similar neglect during

my involvement in this work. Most affectionate gratitude and appreciation are due to all of them.

Last but not the least, the author would also express his gratitude to some friends in India and abroad, who made available reprints of a few important references used in this work that were not available locally.

S.K. Nath

(SUMEER KUMAR NATH)

Roorkee , 1989.

LIST OF FIGURES

LIST OF TABLES

NOMENCLATURE

A	constant
a^P	edge length of pearlite colony with a truncated octahedron
b	Burgers vector
C_1, C_2	constants of non-isothermal transformation kinetic equation
C_m	carbon content of martensite phase in dual-phase steel
C_o	total carbon content of dual-phase steel
d	diameter of measuring circle/average particle diameter
D_i	sectional diameter of particle on selected plane
D_v	diameter of a spherical particle
E	activation energy of phase transformation
E_a	apparent activation energy of phase transformation
E_e	elastic strain
E_p	plastic strain
$e^o_{t,\alpha}$	total engg. strain of 100% ferrite in dual-phase steel
e_u	engg. strain for composite
$e^o_{u,\alpha}$	engg. uniform strain for 100% ferrite in dual-phase steel

f	volume fraction of second phase particle in composite
f_m	volume fraction of martensite in dual-phase steel
G	shear modulus of the matrix of composite
$\dot{G}$	growth rate
G_m	shear modulus of the matrix
G_p	shear modulus of the particle
$h(x)$	a polynomial functin of x
K	rate constant for phase transformation
K_o	preexponential factor of JMA Kinetic equation
K_1	rate constant of isothermal phase transformation
l	half length of the cylindrical second phase-particle of the composite having hemi-spherical ends
l_c	critical length of the second phase particle of the composite
L_f	final gauge length of tensile test specimen
L_i	initial gauge length of tensile test specimens
M	magnification term used for analytical quantitative metallography
n	order of reaction or the Avrami exponent Strain-hardening exponent

$\dot{N}$ nucleation rate

n_C strain-hardening index of composite

n_F strain-hardening index of ferrite of dual-phase steel

n_m strain-hardening index of martensite of dual-phase steel

N_L number of intersections of particle colony boundaries with a measuring circle of diameter .

$p(x)$ integral function of non-isothermal Kinetic equation

$P_2(\cos\theta)$ legendre. polynomial

r radius of cylindrical second phase particle of the composite having hemi-spherical ends

R universal gas constant/plastic strain ratio

$\bar{R}$ mean plastic strain ratio

R_o plastic strain ration in the direction of rolling

$R_{90°}$ plastic strain ratio in the direction perpendicular to rolling direction

$R_{45°}$ plastic strain ratio in the direction of 45° to the rolling direction

S determinant

$S_V^{p/\gamma}$ specific interface of pearlite/austenite colonies

S_1	determinant
T	temperature of transformation
t	time of phase transformation
T_{AC_1}	lower critical temperature
T_f	final thickness of tensile test specimen
T_i	initial thickness of tensile test specimen
T_m	temperature corresponding to a peak in the DSC response curve
V_m	volume fraction of matrix of the composite
V_p	volume fraction of martensite in dual-phase steel
W_f	final width of tensile test specimen
W_i	initial width of tensile test specimen
$\bar{Z}$	average of $1/D_i$ values
α	transformed volume fraction of JMA Kinetic equation ferrite phase of steel
α_m	austenite volume transformed at the maximum reaction rate (peak of DSC curve)
β	heating rate/constant of Melieko expression
ΔT	excess temperature over lower critical temperature (723°C)

ϵ	true strain
ϵ_C	true uniform strain of the composite
ϵ_F	true uniform strain of the ferrite in dual-phase steel
ϵ_m	true uniform strain of the martensite in dual-phase steel
θ	half of the cone angle subtended by the selected section
σ	true stress
$\bar{\sigma}_f$	average stress in the entire second phase particle
σ_m	stress in the matrix of composite
σ_p	stress in particle
$\sigma_{T,\alpha}$	tensile strength of 100% ferrite of dual-phase steel
$\sigma_{T,m}$	tensile strength of 100% martensite of dual-phase steel
$\sigma_{u,c}$	tensile strength of composite
$\sigma_{u,m}$	tensile strength of matrix of the composite
σ_y	yield strength of ferrite-martensite dual-phase steel
$\sigma_{y,\alpha}$	yield strength of 100% ferrite of dual-phase steel

$\sigma_{y,m}$ yield strength of 100% martensite of dual-phase steel

σ_o average true inter-lammellar spacing of pearlite / constant of the work-hardening expression

$\sigma_1, \sigma_2, \sigma_3$ average stress in the second phase particle of the composite upto a distance of r, from r to ℓ_c and ℓ_c to ℓ respectively

T_θ shear stress around a particle

CHAPTER - 1

INTRODUCTION

Innovations in materials have always been important to mankind right from the time immemorial, as evidenced by different stages viz. 'Stone Age', 'Bronze Age' and 'Iron Age' etc. of the development of human civilisation. Development of newer metals and materials have advanced human capabilities in different fields of activity for their very survival by making possible new implements and equipment for his housing, agriculture, industry and various other daily needs and even in the war-fare.

Materials as the primary building blocks for engineering developments have dictated nearly every design and every useful application that the engineer could devise. Even with the present sophistication of engineering science, it is no longer simply a question of being satisfied to design with existing materials, instead one requires new materials with new properties to fit new designs for specific applications. This is true in all fields of engineering and technology be it, a mechanical engineer trying to design high-strength light weight components for vehicles rolling on land, sea or air and even spacecrafts, or an electrical or electronic engineer trying to design solid state electronic devices operating at either low or elevated temperatures or the nuclear

engineer concerned with the materials needed to contain, control and utilise nuclear reactions.

Steels have by far proved to be the most important construction materials, as reflected by a large variety of products employed in different sizes and shapes in large tonnages for various engineering, technological and scientific applications.

The crisis in liquid fuel in the early seventies led to intensive efforts for energy saving. A demand for light weight designs for automobiles resulted in a search for cheap alloys with high strength/weight ratio, so that thin sheets could be used for the body of the vehicle. In the meantime the development of high strength polymers posed a serious challenge to the use of metals and alloys for this application. Although HSLA steels have been already developed to replace plain carbon steels, their poor formability has precluded their application in the body of a vehicle. Dual-phase steels overcome the poor formability of HSLA steels and therefore have emerged as the most successful material for light weight cars. Dual phase steels are a new class of high-strength steels having a very low carbon ($\simeq$0.1 per cent) with or without micro/low alloy additions. These steels are characterised by a microstructure consisting of a dispersion of about 20 per cent of hard martensite particles in a ductile ferrite matrix. The term, "dual-phase" essentially

refers to the presence of two phases, 'ferrite' and 'martensite' in the microstructure although small amounts of retained austenite, bainite and/or pearlite may also be present. Unique dual-phase properties possessed by these steels include (i) continuous yielding behaviour i.e. absence of yield point phenomenon, (ii) a low viz. 0.2 per cent offset yield strength (~340 MPa), (iii) a high tensile strength (~690 MPa), (iv) a high work-hardening rate, and, (v) high uniform and total elongations.

This high work-hardening rate results in a yield strength of 550 MPa after only 3 to 5 per cent deformation. As a result, in 'formed-parts', dual-phase steels have a yield strength comparable to that of other 550 MPa HSLA steels. Interestingly, the high work-hardening rate coupled with high uniform elongation of these steels, gives them a formability comparable to plain carbon steels as reflected by their stress-strain plots. Therefore, these steels are attractive substitute materials for weight-saving applications in automobiles.

Two methods have been used mainly for producing dual-phase structures. The first method involves either batch or continuous-intercritical annealing i.e., annealing at a temperature between A_1 and A_3 temperatures to produce a microstructure of polygonal ferrite and austenite. The steel is then cooled at a rate sufficient to cause the austenite to transform and produce the required martensite content. The required cooling rate depends on the 'alloy-content'

of the steel. While it is possible to add sufficient alloying elements to ensure the formation of martensite even during the batch annealing of large coils, the high alloy contents are expensive and may have severe disadvantages if the steels have to undergo subsequent welding operations during component assembly. The second method of producing the dual-phase structure involves direct hot-rolling. In this case, the alloy content and the rolling and coiling temperatures on the hot mill are so adjusted as to enable sufficient polygonal ferrite to form, but to inhibit formation of pearlite and thus producing a ferrite-martensite dual-phase structure.

The study of Grange [1] which is more than two decade old shows that creation of martensite in a ferrite matrix after quenching from an intercritical annealing temperature, results in material with reduced YS/UTS ratio but considerably improved tensile elongation. However, intense interest in these steels is of recent origin, beginning with the work of Hayami & Furukawa [2] in 1975 and of Rashid [3] in 1976. Hayami and Furukawa supported the results of Grange and have further showed that continuous annealing of cold-rolled Si-Mn sheet steels in the intercritical temperature range produced steels with a ferrite-martensite microstructure which have ductility superior to that of normal precipitation-hardened or solid-solution hardened HSLA sheet steels. Rashid subsequently observed that intercritical heat-treatment of V-N HSLA steel to produce ferrite-martensite microstructure,

has also resulted in a large increase in ductility without any change in tensile strength. Rashid has also mentioned that this ductility increase is accompanied by an increased formability, which in turn, yielded the potential utility of these dual-phase steels in the manufacture of several automotive parts. Mechanical behaviour of these dual-phase steels is mainly a function of the volume fraction of martensite phase and its carbon content. The tensile strength of dual-phase steel has been shown to vary linearly with martensite volume fraction consistent with prediction of deformation theory of two ductile phases. Both the total elongation and strain-hardening parameter have also been found to depend upon martensite volume fraction. Uniform elongation, total elongation and reduction of area - all decrease with increase in martensite volume fraction. It has also been observed that for a constant martensite volume fraction, both the YS and the UTS increase with an increase in the carbon content of the martensite but the increase of UTS is much more pronounced than the former.

These interesting results have fascinated material scientists and several studies have been reported in literature on these steels in the recent past. Typical results of studies covering production techniques, mechanism of austenite formation and transformation, and structure-property correlations, available to the author, are therefore briefly reviewed in the next chapter.

CHAPTER - 2

LITERATURE REVIEW

2.1 Production Techniques of Dual-Phase Steels

2.1.1 Intercritical annealing

Dual-phase sheet steels can be produced by intercritical heat treatment with either continuous annealing [4-9] or Box-annealing techniques [9,10]. Most of the present production have concentrated on using continuous annealing techniques because of higher production rates, better uniformity of properties, and the possibility of the use either low carbon steel strips or lower-alloy steels. However, box-annealing has also been considered where continuous-annealing facilities are not available.

In the continuous annealing technique, the steel strip is heated for a short time (~2 minutes) in the intercritical temperature range as shown in Figure 2.1, to form ferrite-austenite mixtures, followed by accelerated cooling to transform for austenite phase into martensite. The actual cooling rate is dependent on sheet thickness and the quenching conditions on a given annealing line. As a result, steel compositions must be adjusted to obtain the hardenability needed for the cooling rate (strip thickness). Typical chemical compositions are given in Table 2.1 [11].

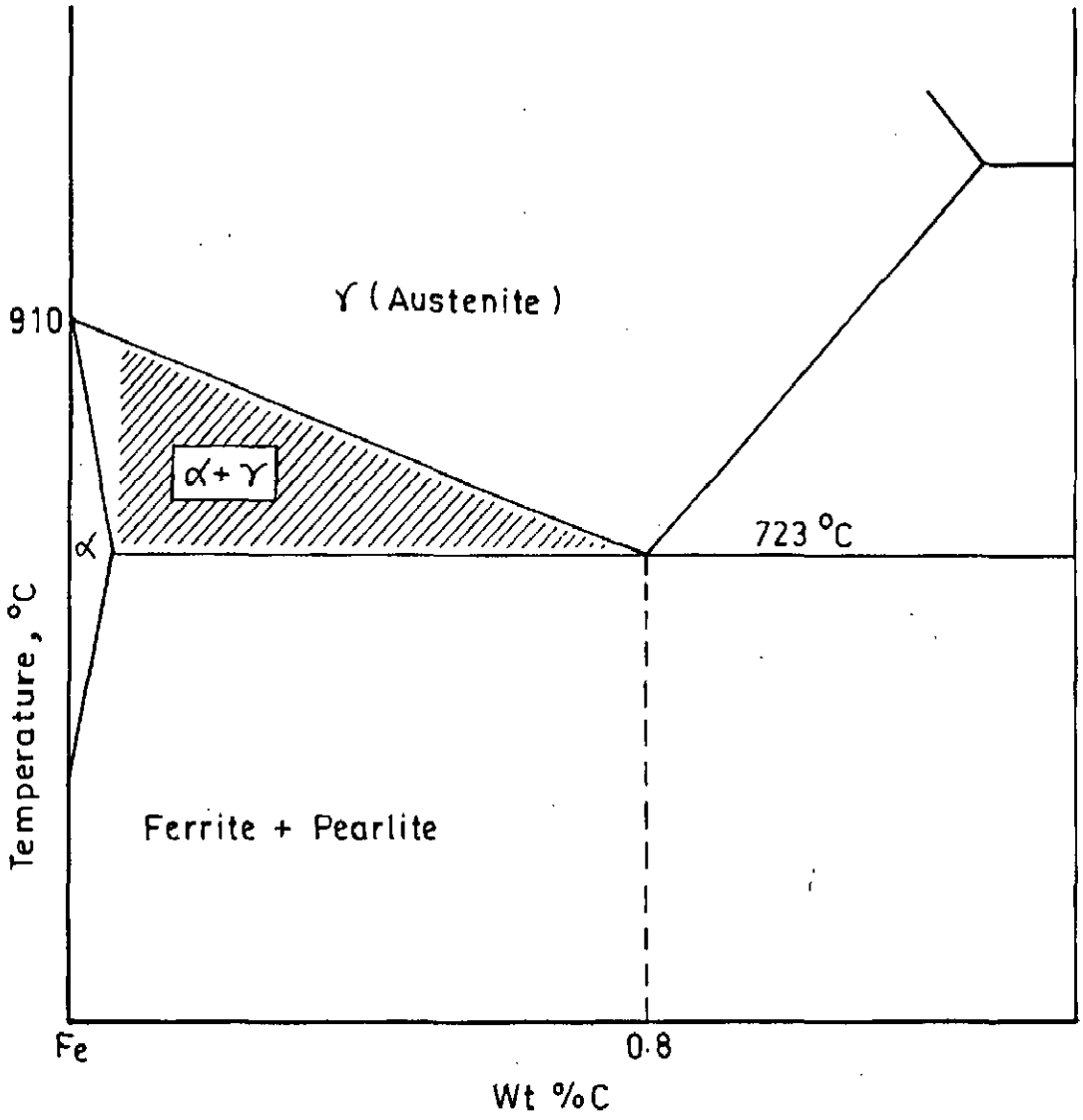

Fig. 2.1 _Schematic diagram of Fe-rich portion of Fe-C phase diagram; the shaded area indicates the region in which the hypoeutectoid steels are heated for intercritical annealing.

Talble 2.1

Typical Dual-Phase Steel Composition, wt. per cent [11]

Production Technique	C	Mn	Si	Cr	Mo	V	Al	N	S	P	Others
A. Plain carbon dual-phase steels											
Continuous annealing followed by water quenching	0.05	0.33	0.021	-	-	-	0.052	0.006	0.017	0.012	-
-do-	0.10	0.41	0.11	-	-	-	0.051	0.0063	0.007	0.011	-
-do	0.03	0.28	0.49	-	-	-	0.049	0.0058	0.006	0.017	-
-do-	0.04	0.39	-	-	-	-	-	0.0031	0.008	0.118	-
B. Low alloy dual-phase steels											
Continuous Annealing	0.12	1.55	0.61	-	-	0.06	0.05	0.007	0.006	0.015	Rare Earth
Hot-Rolled gages	0.11	1.43	0.58	0.12	0.08	-	0.04	0.007	0.012	0.015	-
Continuous Annealing Cold rolled gages	0.11	1.20	0.40	-	-	-	0.04	-	0.005	0.015	-
Box Annealing	0.13	2.20	1.50	1.0	-	-	0.08	-	0.020	0.02	Rare Earth
As-Rolled	0.06	0.90	1.35	0.50	0.35	-	0.03	0.007	0.010	0.010	Rare Earth

In the box-annealing technique, a similar heat treatment is performed but the durations of annealing times are much longer (~3 hours) and the cooling rates are slower (~20°C/hr). Because of the slow cooling rate, much higher alloy steels are required to achieve the desired hardenability. For this annealing technique, 2.5 Mn [9,10] steels containing appreciable amounts of Si and Cr, have been proposed.

2.1.2 Direct hot rolling technique

In addition to the use of intercritical heat treatment, dual-phase steels have also been produced by direct hot rolling method or in the as-rolled condition by carefully controlling the continuous-cooling transformation characteristics of the steel [12-14]. This generally requires the addition of substantial amounts of Si, Cr and Mo in addition to about 1.0 Mn, Table 2.1. In this method, on a hot strip mill after the last roll pass, the strip is allowed to cool rapidly on the run out table for about 10 seconds. At this stage a large amount of polygonal ferrite, about 80 per cent forms but the formation of pearlite is suppressed and the remaining islands of carbon-enriched austenite transform to martensite during the slow cooling in the coil. A desired type of continuous-cooling transformation diagram is shown in Figure 2.2 [15].

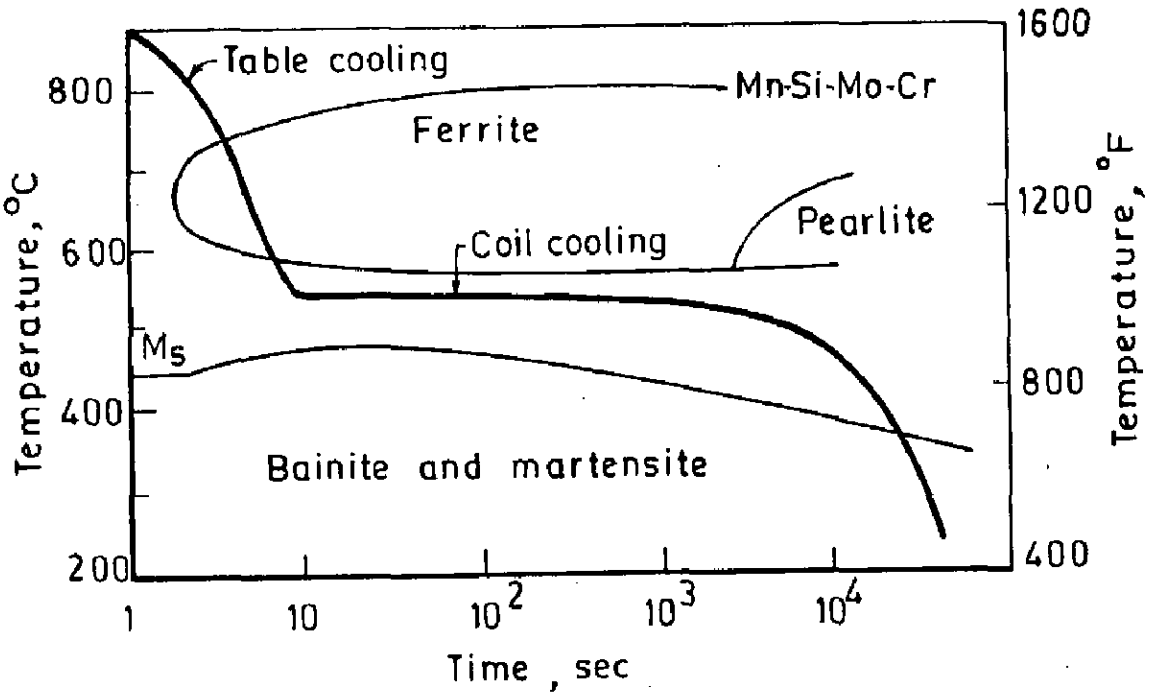

Fig.2.2_Continuous-cooling transformation behavior in Mn-Si-Mo-Cr steel resulting in dual-phase microstructure in as-rolled product [15]

Production of dual-phase steels by direct hot rolling has with the obvious advantage of saving energy costs by eliminating a heat treatment step. Also dual-phase steels can be produced when continuous annealing facilities are not available. However, balanced against these advantages are the disadvantages of a higher alloy cost and more variability in properties.

2.2 Mechanism of Austenite Formation and Its Kinetics

2.2.1 Mechanism of austenite formation during intercritical annealing

Several investigators such as Speich et al [16], Garcia et al [17], Yang et al [18], and Jeong et al [19], have reported that on heating plain-carbon or low-alloy steels above AC_1 temperature, transformation in following stages occur in sequence leading to the formation of equilibrium austenite:

Stage I

The changes in this initial stage include simultaneous dissolution of pearlite and formation of a high-carbon austenite phase.

The austenite phase nucleates preferentially at pearlite colony boundaries, ferrite-pearlite interface, at the junction between a cementite particle and two ferrite grains and

in case of pure iron, at the ferrite boundary shown in Figs. 2.3A (a) and (c). Austenite nucleation has also been found to occur preferentially in the banded region where there is a very fine interlamellar spacing of pearlite. Austenite nucleation not only occurs at ferrite grain boundaries but also within ferrite grains as austenite forms first on the boundaries between deformed and unrecrystallised ferrite grains and then on spheroidised cementite particles in recrystallised ferrite grains as shown in Figure 2.3B (b)&(c) [18]. This results partially into formation of austenite and ferrite in the remaining region of dissolved pearlite. Carbon atoms from the dissolving pearlitic cementite move simultaneously into growing austenite, adjacent to the pearlite ferrite and proeutectoid ferrite surrounding pearlite. The growth rate of austenite in this stage is controlled primarily by the rate of carbon diffusion in austenite.

Stage II

Here austenite grows into the supersaturated ferrite of originally the pearlite region. However, at the end of this stage, all the pearlitic region is nearly displaced by austenite and the amount of resulting austenite is approximately equal to that of the pearlite in the original microstructure. Further, the high carbon austenite so generated at the end of this stage is not in equilibrium with the proeutectoid ferrite.

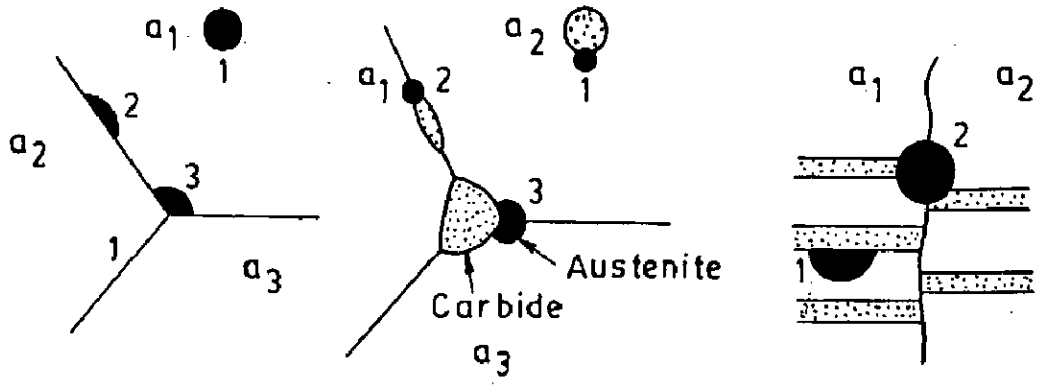

(a) Ferrite (b) Spheroidite (c) Pearlite

Fig.2.3 A _ Nucleation sites for austenite in ferrite and ferrite carbide aggregates (a) pure iron (b) spheroidite, and (c) pearlite

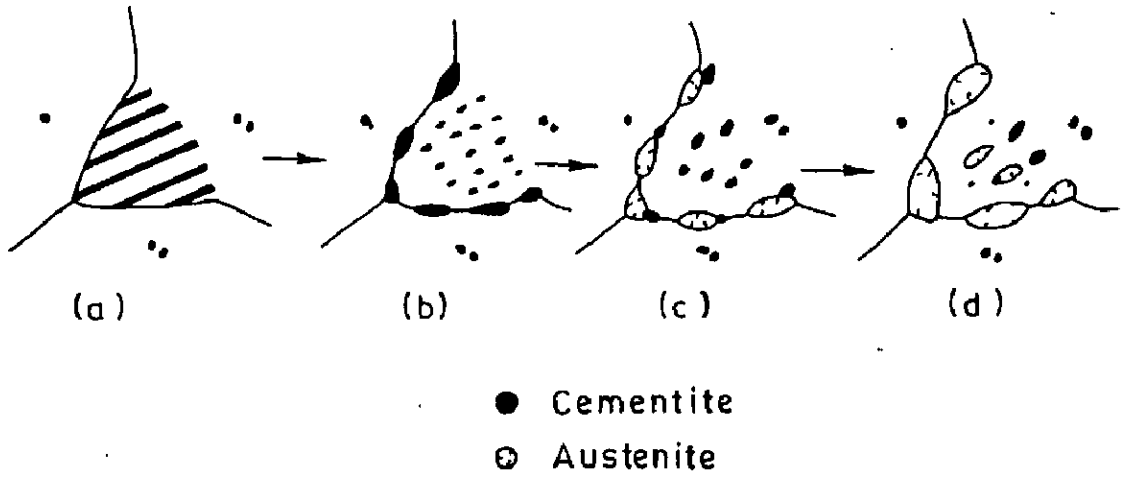

Fig.2.3B _ Schematic illustration of nucleation and formation of austenite in ferrite - pearlite microstructure steps (a) & (b) high light spheroidisalion and coarsening of cementite particles steps (c) and (d) are similar to Fig. 2.3 A(b) [18]

Stage III

In this stage, the austenite grows into the proeutectoid ferrite region of original microstructure. During this stage, the growth of austenite is controlled by carbon diffusion from austenite to ferrite. However, Speich et al [16] have pointed out that the dissolution of ferrite in austenite duirng austenite growth is not only controlled by carbon diffusion but also by Mn diffusion, which can occur along ferrite grain boundaries and accelerate the austenite transformation.

Stage IV

This stage is characterised by a constant volume per cent austenite and only redistribution and equilibration of carbon and alloying elements between the ferrite and austenite phase take place. Growth of austenite in this stage is negligible and not related to carbon diffusion but related to very slow diffusion of substitutional alloying elements such as Mn, Si etc. in austenite as also reported previously [16,20]. A very slow final equilibration of ferrite and austenite takes place due to this slow diffusion of substitutional alloying elements.

Gilmour et al [21] have reported that addition of Mn to plain carbon steels expands the austenite field and

depresses the AC_3 and AC_1 lines thereby reducing the size of intercritical region. Therefore, steels with higher Mn content are expected to form more austenite than plain carbon steels of the same carbon content after intercritical annealing at the same temperature. As indicated by Fe-C phase diagram, Fig.2.3c for any given carbon content, the amount of austenite increases with increasing intercritical annealing temperature, becoming equal to 100 per cent at the AC_3 temperature. Similarly, for any given intercritical temperature the amount of austenite increases with increasing carbon content, becoming equal to 100 per cent at a carbon content corresponding to the $\gamma/\alpha+\gamma$ boundary. Below AC_1, no austenite forms.

Dual-phase steels may also contain alloying elements such as vanadium, niobium, silicon, chromium, phosphorus, or molybdenum, in addition to manganese. These alloying elements will lead to more complex effects on austenite formation than indicated above. For example, vanadium and niobium interact strongly with carbon and nitrogen to form a fine dispersion of VCN or NbCN. Upon intercritical annealing, this dispersion may be dissolved in austenite as this phase grows into ferrite [22]. Similarly, silicon widens the $(\alpha+\gamma)$ phase field and permits a wider range of intercritical temperature to be used [23].

However, Speich et al [16], Garcia et al [17] and Souza et al [20] have proposed only a three stage mechanism by

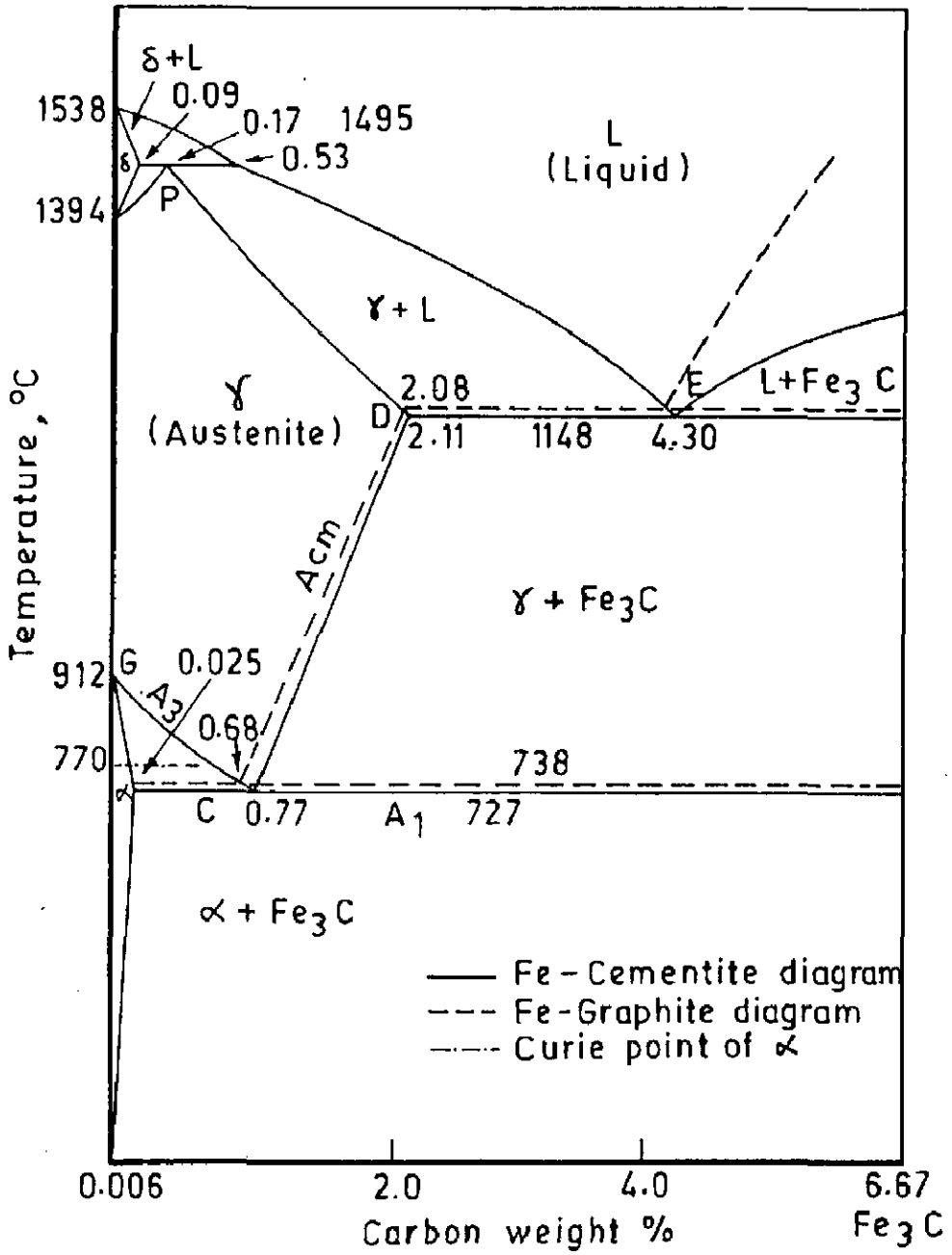

Fig.2.3c _ Iron - Carbon phase diagram (up to 6.67 % carbon)

combining the first two stages of mechanism of austenite formation, proposed by Jeong et al [19] into stage one.

2.2.2 Kinetics of isothermal austenite formation

The kinetics of inhomogeneous solid state isothermal transformation, including nucleation and growth, can be described, in general, making use of the Johnson-Mehl-Avrami (JMA) Kinetic equation,

$$\alpha = 1 - \exp\,[-(Kt)^n] \qquad \ldots (2.1)$$

where, α, represents the transformed volume fraction, K is a temperature dependent rate constant, t is the time and, n is a constant characterising the kinetics and the dimensionality of the transformation. Numerical values of parameters K and n, characterising the transformation process can be obtained by regression analysis of empirical data on volume fraction, α, transformed at different time interval, t, using the following alternate form of Eq. (2.1),

$$\ln\,[\ln\{\frac{1}{1-\alpha}\}] = n\ln K + n\ln t \qquad \ldots (2.2)$$

obtained by rearranging the terms in Eq.(2.1) and taking logarithm twice.

The plot of $\ln[\ln\{\frac{1}{1-\alpha}\}]$ VS t gives a straight line whose

slope is n, the Avrami [24] exponent.

In order to calculate the activation energy, E, (nK values are further plotted against 1/T i.e., the reciprocal of intercritical annealing temperatures in degree Kelvin. This gives again a straight line whose slope is equal to the activation energy.

The study of Roosz et al [25] on isothermal austenitisation in an eutectoid carbon steel at four different temperatures with four initial pearlite structures varying from coarse to fine pearlite, gives the values of n equal to 4, meaning thereby that nucleation rate ($\dot{N}$) and growth rate (G) are constant in time [26].

This gives a transformed volume fraction of

$$\alpha = 1 - \exp\left[-(Kt)^4\right] \qquad \ldots (2.3)$$

where $K = \frac{\pi}{3} \dot{N} G^3$ ... (2.4)

For n=4 the specific pearlite/austenite interface ($S_V^{P/\gamma}$) can be written as follows [27]

$$S_V^{P/\gamma} = (1-\alpha) K_1 t^3 \qquad \ldots (2.5)$$

where $S_V^{P/\gamma}$, the specific interface of the pearlite colonies is

$$S_V^{P/\gamma} = \frac{2 N_L M}{d \pi} \ (mm^2/mm^3) \qquad \ldots (2.6)$$

where M is the magnification and N_L is the number of intersections of pearlite colony boundaries with a measuring circle of diameter d and

$$K_1 = \frac{4\pi}{3}\dot{N}G^2 \qquad \ldots (2.7)$$

Taking (n of Eq. (2.5),

$$(n\, S_V^{P/\gamma} = (nK_1 + (n(1-\alpha)t^3 \qquad \ldots (2.8)$$

further a plot of $(n\, S_V^{P/\gamma}$ VS $(n(1-\alpha)t^3$ gives a straight line whose intercept at the y-axis gives the value of K_1.

$\dot{N}$ and G can be calculated from the knowledge of K and K_1

$$\dot{N} = \frac{3K_1^3}{64\pi K^2} \qquad \ldots (2.9)$$

$$G = \frac{4K}{K_1} \qquad \ldots (2.10)$$

The values of $\dot{N}$ and G can be calculated also from a knowledge of α and $S_V^{P/\gamma}$ for specimens heat treated for any period t, using Eqs. (2.3) and (2.5),

$$\dot{N} = \frac{3(S_v^{P/\gamma})^3}{64\pi(1-\alpha)^3 t[(n\frac{1}{1-\alpha}]^2} \qquad \ldots (2.11)$$

$$G = \frac{4(1-\alpha)\{n[\frac{1}{1-\alpha}]}{t\ S_V^{P/\gamma}} \qquad \ldots (2.12)$$

Roosz et al have further shown that nucleation rate of austenite is highly temperature dependent. The higher is the temperature of austenitisation, the higher is the nucleation rate and vice-versa. This is shown in Fig. 2.4a [25].

Roosz et al have derived the following relationship to show the temperature and structure dependence of the nucleation rate, $\dot{N}$, measured as number of nuclei per unit volume per second during isothermal transformation of austenite in eutectoid plain carbon steel,

$$\dot{N} = \frac{1.378.10^{-12}}{[(a^P)^2\sigma_o]^2} \exp(\frac{-25.38}{\Delta T}) \qquad \ldots (2.13)$$

where, a^P is the edge length of pearlite colony with a truncated octahedron, σ_o is the average true interlammellar spacing of pearlite and ΔT is the over heating ($\Delta T=T-T_{AC_1}$). T is actual temperature of heating and T_{AC_1} is the lower critical temperature. The variation of $\dot{N}[(a^P)^2\sigma_o]^2$ VS $1/\Delta T$ is shown in Fig.2.4b [25].

The dependence of growth rate of austenitisation (G) on the temperature of austenitisation expressed by the reciprocal value of over heating of ($\Delta T=T-T_{AC_1}$), as observed

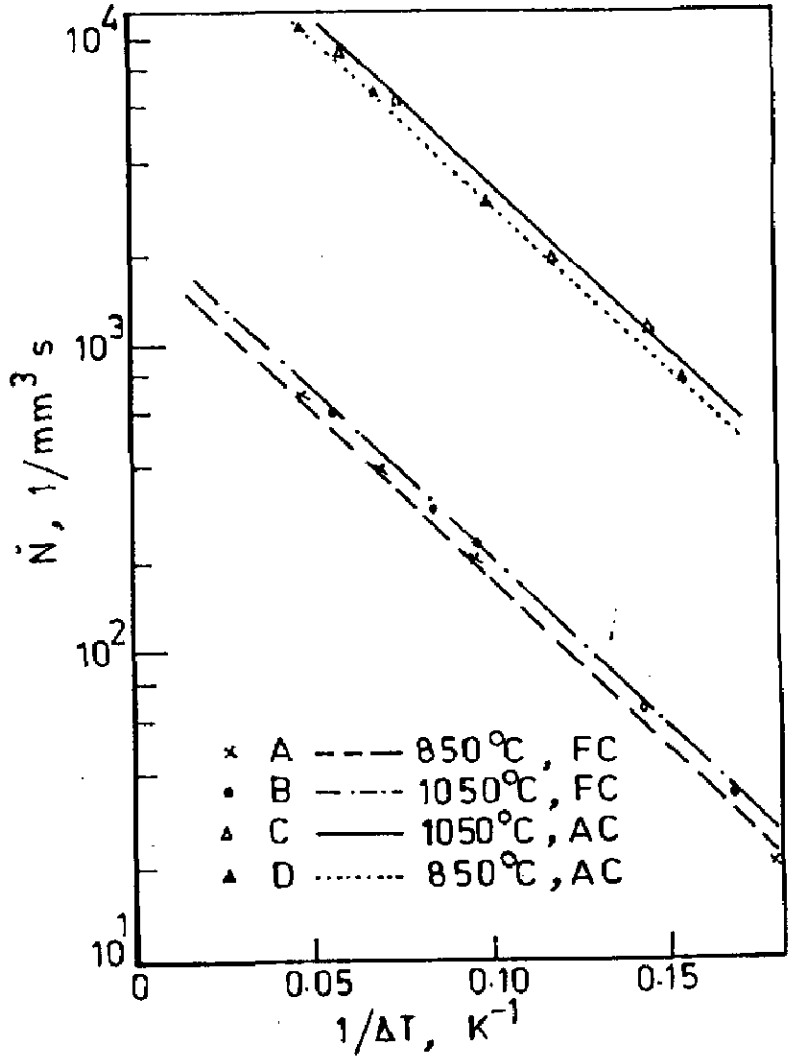

Fig. 2.4 a – The measured nucleation rates vs the reciprocal of overheating[25]

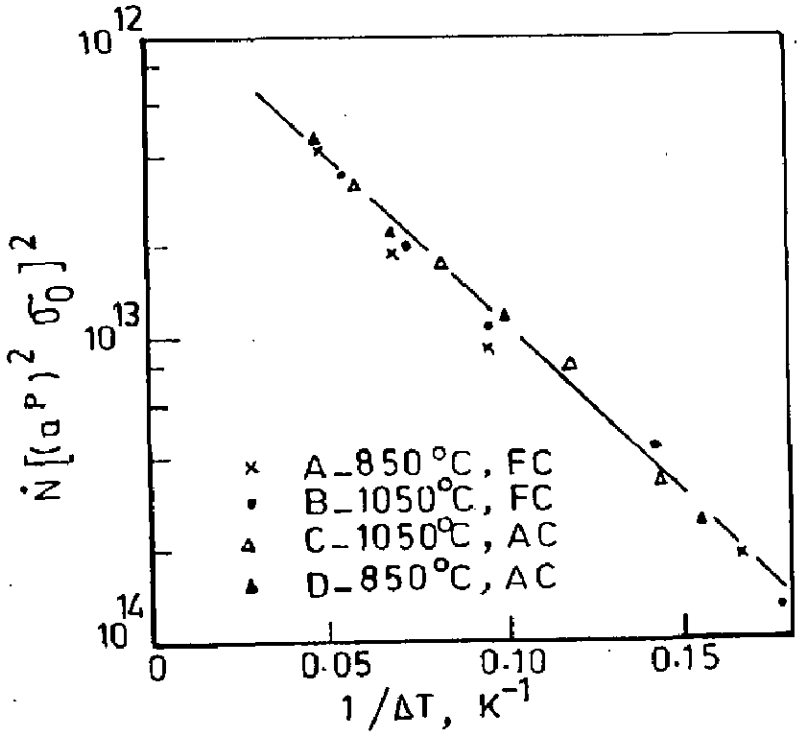

Fig. 2.4 b – The temperature dependence of the nucleation rate-structure dependent [25]

by Roosz et al [25] is shown in Fig. 2.4c. The following relationship as derived by Roosz et al [25], shows the dependence of G on initial structure.

$$G = \frac{7.10^{-11}}{\sigma_o^2} \exp.\left(\frac{-29.7}{\Delta T}\right) \qquad \ldots (2.14)$$

G is expressed in mm per second.

where σ_o is the average true interlammellar spacing of pearlite, ΔT is the over heating.

The above equation states that the finer the interlamellar, spacing (σ_o), the higher the growth rate, G, and vice-versa. This is shown in Fig. 2.4d by plotting $\ln(G\,\sigma_o^2)$ VS $\frac{1}{\Delta T}$.

2.2.3 Austenitisation diagram

Speich et al [16] have first constructed an austenite formation diagram for the 0.12C-1.5 Mn steel. By referring to this diagram it is easy not only to establish the time for formation of various amounts of austenite but also to quickly recognise the controlling kinetic processes at each stage of austenite formation.However, Roosz et al [25] have constructed an austenite formation diagram for an eutectoid steel.which takes into account a structural factor $F = a^P \sigma_o^2$ where a^P is the edge length of a truncated octahedron of pearlite colony and σ_o is the average true interlamellar

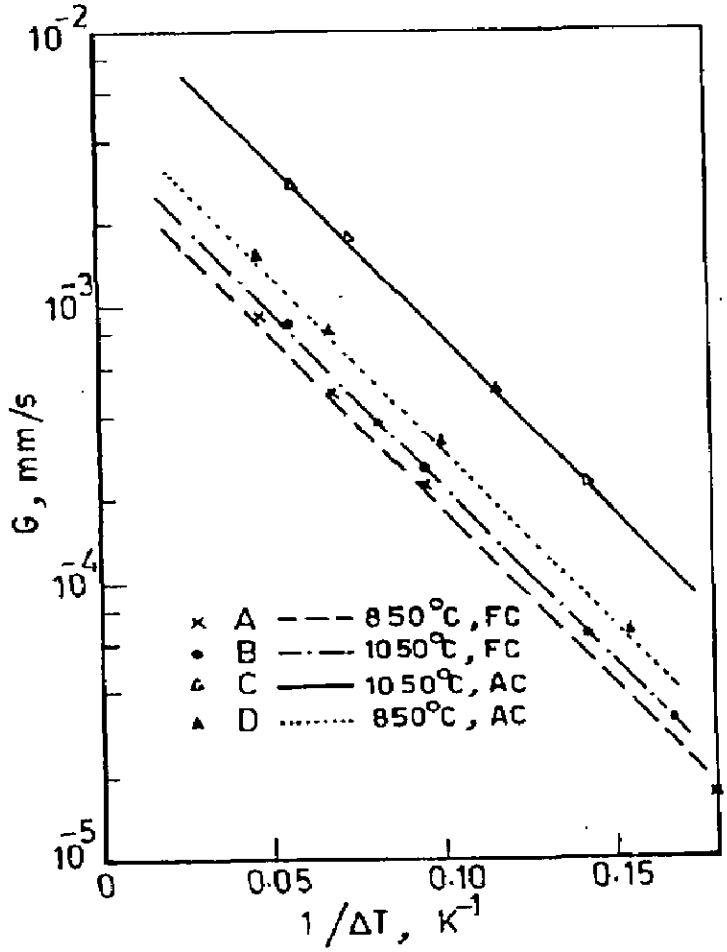

Fig. 2.4 c_ The measured austenite growth rates vs the reciprocal of overheating [25]

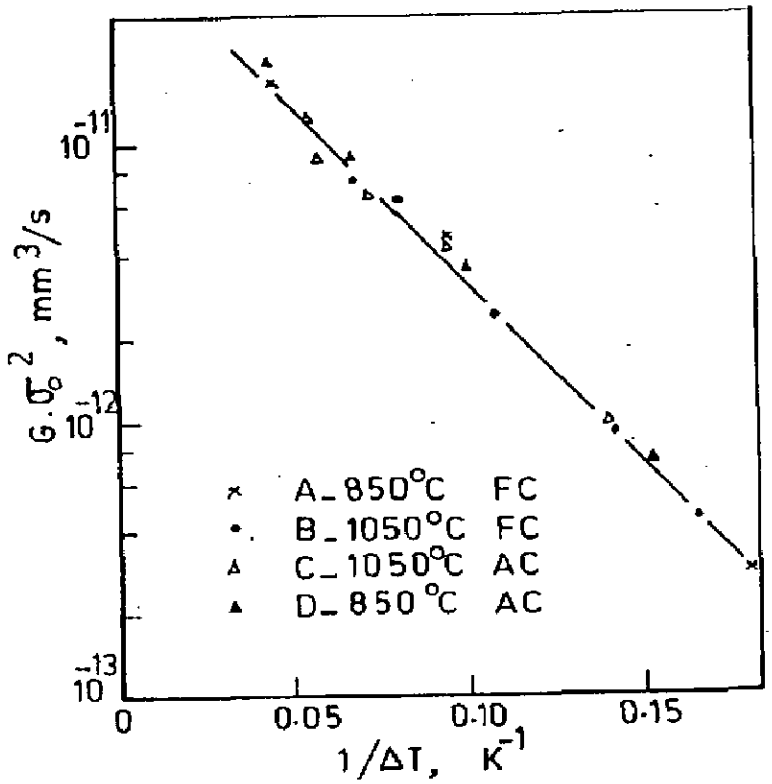

Fig. 2.4 d _ The temperature dependence of austenite growth rate-structure dependent [25]

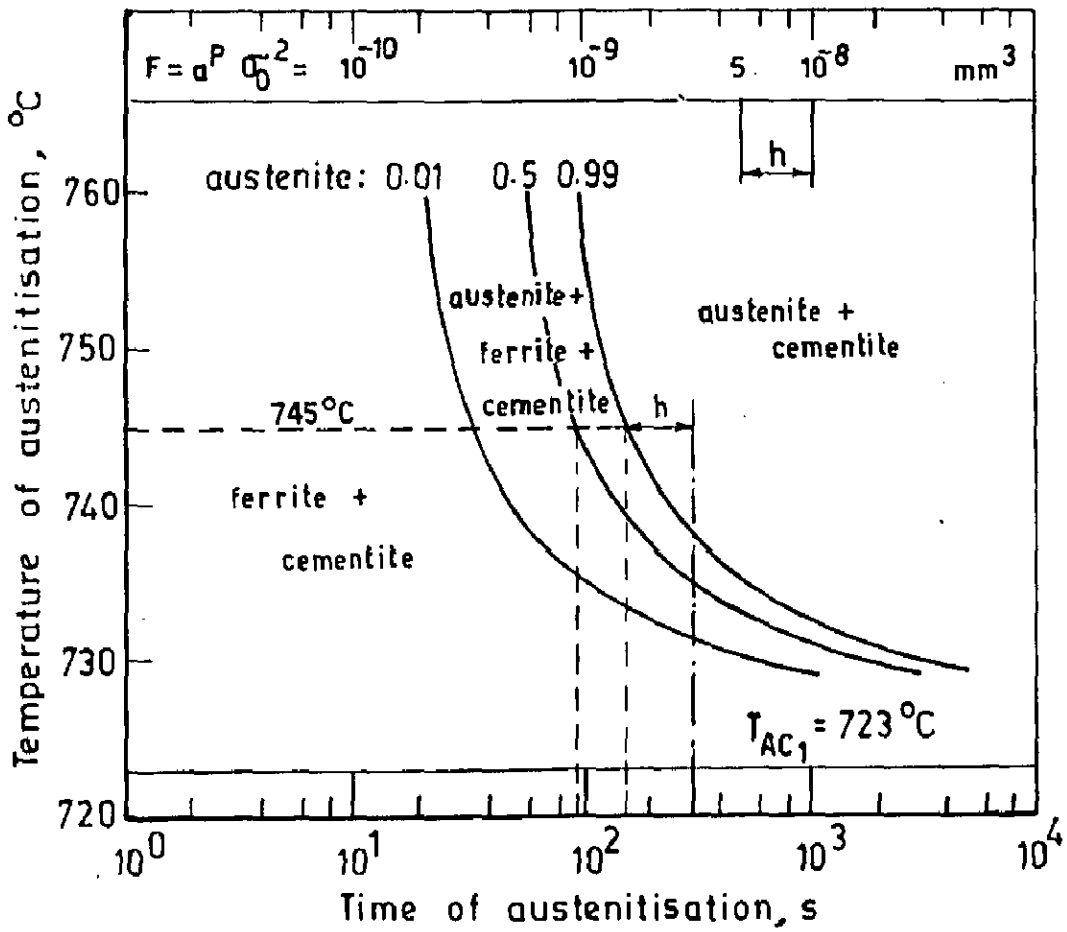

Fig. 2.5 – The new type of isothermic austenitising diagram [25]

spacing of pearlite, as shown in Fig.2.5. Accordingly to this diagram for a structural factor $F=5.10^{-9}$ mm^3, at 745°C, e.g. 95 seconds are required to transform half of the pearlite to austenite ($\alpha=0.5$) and 155 seconds are required for full transformation. Values of the structural factor F lower or higher than 5.10^{-9} can be taken into account by using the auxiliary bar shown on top of the diagram of Fig.2.5. For example $F=10^{-8}$ the distance h between $F=5.10^{-9}$ and $F=10^{-8}$ is measured on the auxiliary bar and applied to the isotherm for 745°C starting from 155 seconds for full transformation. In this case full transformation requires 320 seconds.

2.2.4 Application of non-isothermal method to determine kinetics of austenitisation

For a study of the mechanism and rate of austenite formation during heating of steels and subsequently controlling its amount and morphology, it is of vital importance to study the kinetics of austenitisation during heat treatment of steels.

Kinetics of austenitisation has been studied using non-isothermal technique. The quantitative metallography used to determine isothermal kinetics of austenitisation, has already been described in Section 2.2.2. The non-isothermal technique which involves Differential Scanning Calorimetry (DSC) employing Kissinger's analysis [28] is discussed here.

Kissinger [28] originally had proposed his method of kinetic analysis for homogeneous reactions but its applicability to inhomogeneous reactions such as nucleation and growth phenomenon has been questioned earlier [29,30]. Meisel and Cote [31] have provided the theoretical basis that justify the use of the Kissinger method for determining the activation energy of reactions obeying Johnson-Mehl Avrami (JMA) kinetic law by assuming E/RT larger than 25. Further, Meisel and Cote's analysis in the spirit of Kissinger's work does not allow to determine the actual value of the exponent 'n' of the JMA kinetic law. However, the kinetic equation derived by Criado and Ortega [32] in the light of Kissinger's work allows to determine activation energy, E, and Avrami exponent, n, of the JMA kinetic law from a set of non-isothermal experiments using DSC.

$$\alpha = 1 - e^{-(Kt)^n} \qquad \ldots (2.15)$$

where, α is the volume fraction transformed in time 't' at a particular temperature. K is a thermally activated rate constant, and, n is the Avrami exponent which depends on the mechanism of nucleation and the number of growth dimensions. Rearranging terms in Eq. (2.15) and differentiating both sides w.r.t. 't', one gets,

$$\frac{d\alpha}{dt} = K\, n(1-\alpha)[-(n(1-\alpha)]^{n-1/n} \qquad \ldots (2.16)$$

writing the value of K, in terms of Arrhenius equation as,

$$K = K_o e^{-E/RT} \qquad \ldots (2.17)$$

where, $K_o = A$, is a constant, E is the activation energy, T is the temperature (°K) of the transformation and R is the universal gas constant.

Substituting Eq. (2.17) in Eq. (2.16)

$$\frac{d\alpha}{dt} = An(1-\alpha)[-(n(1-\alpha)]^{n-1/n}\ e^{-E/RT} \qquad \ldots (2.18)$$

If it is assumed that the reaction is conducted under a constant heating rate, β, Eq. (2.18) can be integrated and one gets

$$[-(n(1-\alpha)]^{1/n} = \frac{AE}{\beta R}p(x) \qquad \ldots (2.19)$$

where, the function, p(x), isthe temperature integral defined as,

$$p(x) = \int_x^\infty \frac{e^{-x}}{x^2}dx \simeq \frac{e^{-x}}{x}\ h(x) \qquad \ldots (2.20)$$

where,

$$h(x) = \frac{x^3 + 18x^2 + 88x + 96}{x^4 + 20x^3 + 120x^2 + 240x + 120} \qquad \ldots (2.21)$$

An approximation to the integral of the Arrhenius equation (2.20)

after Doyle [33] is,

$$\ln p(x) = -5.33 - 1.05E/RT \qquad \ldots (2.22)$$

In order to determine the temperature, T_m, at which the maximum reaction rate is reached, one differentiates Eq.(2.18) to get,

$$\frac{d^2\alpha}{dt^2} = \left[\frac{E\beta}{RT^2} + \frac{n(n(1-\alpha)+n-1}{[-(n(1-\alpha)]^{1/n}} \cdot Ae^{-E/RT}\right]\frac{d\alpha}{dt} \qquad \ldots (2.23)$$

The value of T_m, is defined by equating Eq. (2.23) to zero. Therefore,

$$\frac{E\beta}{RT_m^2} = \frac{-n(n(1-\alpha m)+n-1}{[-(n(1-\alpha m)]^{1/n}} Ae^{-E/RT_m} \qquad \ldots (2.24)$$

α_m, being the reacted fraction at the maximum reaction rate. In the logarithmic form one can write this expression as,

$$\ln \beta/T_m^2 = \frac{-E}{RT_m} + \ln\frac{AR}{E} + \ln\left[\frac{-n(n(1-\alpha m)+n-1}{[-(n(1-\alpha m)]^{1/n}}\right] \qquad \ldots (2.25)$$

Horowitz and Metzger [34] based on a series of constant heating rate concluded that at the heating rates generally used in non-isothermal analysis, the influence of β on T_m does not lead to any significant change in the value of E/RT_m. Criado et al [32] further assumed that the following relationship is accomplished in a narrow range of E/RT around

any particular value of E/RT_m,

$$\ln\left[\frac{-n\{n(1-\alpha_m)+n-1\}}{\{-(n(1-\alpha_m)\}^{1/n}}\right] = C_1\frac{E}{RT_m} + \ln C_2 \qquad \ldots (2.26)$$

where, C_1 and C_2 are constants.

If this relationship is fulfilled, one obtains from Eqs. (2.25) and (2.26), the following expression,

$$\ln\beta/T_m^2 = \frac{-(1-C_1)E}{RT_m} + \ln\frac{C_2AR}{E} \qquad \ldots (2.27)$$

Criado et al [32], therefore, concluded from Eq.(2.27), that the slope of the linear plot of function $\ln\beta/T_m^2$ VS $1/T_m$ yields an apparent activation energy, E_a, as,

$$E_a = E(1-C_1) \qquad \ldots (2.28)$$

where, E is the actual activation energy.

To calculate the value of constant C_1, a knowledge of the order of reaction, n, is needed. To calculate, n, Eq. (2.19) can be rewritten in the following alternative form,

$$\frac{1}{n}\ln\left[\ln\left[\frac{1}{(1-\alpha)}\right]\right] = \ln\frac{AE}{\beta R} + \ln p(x) \qquad \ldots (2.29)$$

Substituting the Doyle's approximation [33] Eq. (2.22) in the above expression, one gets,

$$\ln\left[\ln\left[\frac{1}{(1-\alpha)}\right]\right] = n\ln\frac{AE}{\beta R} - 5.33n - \frac{1.05nE}{RT} \qquad \ldots (2.30)$$

Accordingly, straight line plot of function $\ln \ln \frac{1}{(1-\alpha)}$ against the reciprocal of the temperature, 1/T, gives the value of nE, from which using the value of E obtained earlier, the value of the coefficient, n, can be calculated.

To obtain, the value of constant C_1, Table 2.2 after Criado et al [32] for different values of n and E/RT ranges can be used. Firstly, the value of E_a/RT is calculated. Here, E_a is the apparent activation energy, T_m, is the maximum temperature in degree Kelvin and R is the universal gas constant. From the value of E_a/RT and n, the value of C_1 is worked out using Table 2.2, from which value, actual activation energy, E, is calculated using Eq.(2.26).

2.3 Mechanism of Transformation of Austenite After Intercritical Annealing

Although the transformation of austenite after intercritical annealing is similar to the transformation of austenite after normal austenitising, two features make this transformation unique. Firstly, because the carbon content of the austenite is fixed by intercritical annealing temperature and can be calculated by Lever's rule and hence the hardenability of austenite-phase varies with intercritical temperature. Thus, at low temperatures where the carbon content of the austenite is high, the hardenability of the austenite is high, at high temperature, it is low. Secondly, because ferrite phase already exists, transformation of the austenite

Table 2.2

Values of C_1, C_2 and of the percentage of error in the activation energy (E) calculated by the least squares method according to equation (2.26)

Kinetics		E/RT 2	5	10	30	60
	C_1	-0.307	0.239	-0.053	-0.007	-0.0020
n=0.5	C_2	18.160	10.311	2.976	1.472	1.313
	C_3	30.7	23.9	5.3	0.7	0.2
	C_1	0.132	0.028	0.008	0.001	0.0003
n=1.5	C_2	0.542	0.723	0.838	0.935	0.966
	C_3	13.2	2.8	0.8	0.1	0.03
	C_1	0.178	0.041	0.012	0.002	0.0004
n=2.0	C_2	0.423	0.634	0.769	0.905	0.948
	C_3	17.8	4.1	1.2	0.2	0.04
	C_1	0.169	0.037	0.011	0.001	0.0004
n=2.5	C_2	0.449	0.662	0.787	0.915	0.953
	C_3	16.9	3.7	1.1	0.1	0.04
	C_1	0.187	0.043	0.013	0.002	0.0005
n=3.0	C_2	0.406	0.617	0.754	0.898	0.944
	C_3	18.7	4.3	1.3	0.2	0.05
	C_1	0.196	1.047	0.018	0.003	0.0005
n=4.0	C_2	0.379	0.604	0.743	0.893	0.940
	C_3	19.6	4.7	1.8	0.3	0.05

can proceed by epitaxial growth of this 'old' or existing ferrite into austenite with no nucleation step required [35,36]. Due to the formation of epitaxial ferrite, the carbon concentration in still untransformed austenite further increases. This new ferrite called epitaxial ferrite, can be distinguished by its different response to certain etching reagents [36].

The transformation products produced on further cooling the remaining austenite depend, of course, on its carbon and alloy-contents, and the rate at which it is cooled. However, if the austenite contains only carbon and is water quenched, it transforms into dislocated (lath) martensite or into twinned accicular martensite depending on whether the carbon concentration is below or above 0.4%. Actually, the transition in microstructures on increasing the carbon concentration is more subtle than this bald statement implies. It has been described in detail by Krauss and Marder [37]. The carbon content at which the change from dislocated to twinned martensite occurs is greatly influenced by the presence of other alloying elements. Both types of martensite are found in dual-phase steels. Even at the fastest quenching rates available, some tempering occurs during quenching (autotempering) of the low-carbon austenites, which are those with the highest M_S temperatures. With slower cooling rates and leaner alloying, more extensively tempered marten-

site, pearlite, upper or lower bainite, or mixtures of all the four can occur.

The transformation of austenite-to-martensite is accompanied by volume expansion (~2 to 4 per cent) [38,39]. As a result, both a high dislocation density and residual stresses are generated in the ferrite phase immediately surrounding the martensite island. The residual stress patterns are on too small a scale to be directly measured but a theoretical analysis indicates that their maximum value would be of the order of the yield strength of the ferrite (at the M_S temperature) and decay exponentially away from the martensite-ferrite interface [40].

As the transformation of the austenite to martensite is not complete, retained austenite is also generally present in dual-phase steels in amounts varying from 2 to 9 per cent [15,41]. The retained austenite is generally believed to be contained within the martensite particles presumably as interlath austenite films, as reported for freshly quenched low-and medium-carbon content steels with internally twinned microstructure; the situation is less clear. A number of researchers, viz. Rigsbee and Vander Arend [41] and Nakaoka et al [6], have presented convincing evidence for the existence of isolated austenite particles in this case.

The amount of retained austenite appears to be sensitive to a number of variables, particularly cooling rate. Evidently thermal stabilization of the austenite phase will occur at slower cooling rates, typical of effects observed in normal quenched-and-tempered steels [42,43]. Thus, water quenched steels have less retained austenite than air-cooled steels. Although the retained austenite is generally stable with respect to subzero cooling, it transforms readily after straining a few per cent. Retained-austenite contents increase slightly with increasing inter-critical temperature and with increasing carbon content [41].

2.4 Mechanism of Change in Ferrite Phase During and After Intercritical Annealing

In cold rolled steels, recrystallisation of ferrite occurs rapidly and is generally complete before the steel reached intercritical annealing temperature, even during the rapid heating encountered on most continuous annealing lines [17]. Grain growth in the ferrite phase after re-crystallisation is generally restricted because of the pinning action of the second phase particles.

Changes in carbon content of the ferrite phase may occur during intercritical annealing and many investigators [7,23,44,45] believe that this has a pronounced effect on

the ductility of dual-phase steel. These changes may occur because of several reasons. First, the solubility of carbon in the ferrite phase may be lower at the intercritical temperature than that originally present in the ferrite phase of the 'as-received' material. In general, the solubility of carbon in the ferrite phase decreases with increasing intercritical temperature. However, it may also be markedly decreased by increasing the total alloy content of the steel.

Variations in the cooling rate from intercritical temperature can also affect the carbon content of the ferrite phase. As cooling rate is lowered, cementite may precipitate in the ferrite matrix resulting in a lower carbon content in it. Some investigators [35] have also suggested that the epitaxial ferrite formed at slower cooling rates will maintain equilibrium with the austenite phase into which it is growing, resulting into a lower carbon content. However, for a given steel, water-quenching results in a higher carbon content in the ferrite phase than that obtained after air-cooling. The changes in the carbon content of the ferrite in 'high alloy' steels for different quenching rates, however, appear to be very small, only in a few ppm range. Tempering after water-quenching also lowers the carbon content of the ferrite phase due to 'Carbide-precipitation'.

2.5 Microstructure and Mechanical Properties of Dual-Phase Steels

The structure of dual-phase steels essentially consists of ferrite matrix in which martensite islands are distributed along grain boundaries and grain corners of ferrite phase. Small amounts of pearlite and retained austenite have also been found to occur along with martensite phase.

2.5.1 Continuous yielding and work-hardening of Dual-Phase Steels

Ferrite-martensite dual-phase steels, in general, do not show a yield-point phenomenon [39,41,46]. This is reflected in Fig. 2.6 after Rashid [3] for a typical dual-phase steel. This is because of the combination of high residual stresses and a high mobile disclocation density generated in the ferrite phase immediately surrounding the martensite island as a result of transformation of the austenite phase into martensite, which is accompanied by a volume expansion between 2-4 per cent. Ferrite phase, therefore, plastically deforms to accomodate this volume expansion. Further, plastic flow begins simultaneously at many sites throughout the specimens, thereby suppressing the discontinous yielding or the yield-point phenomenon. Also, lack of the yield-point phenomenon in these steels eliminates Luder band formation and assures a good surface finish after drawing.

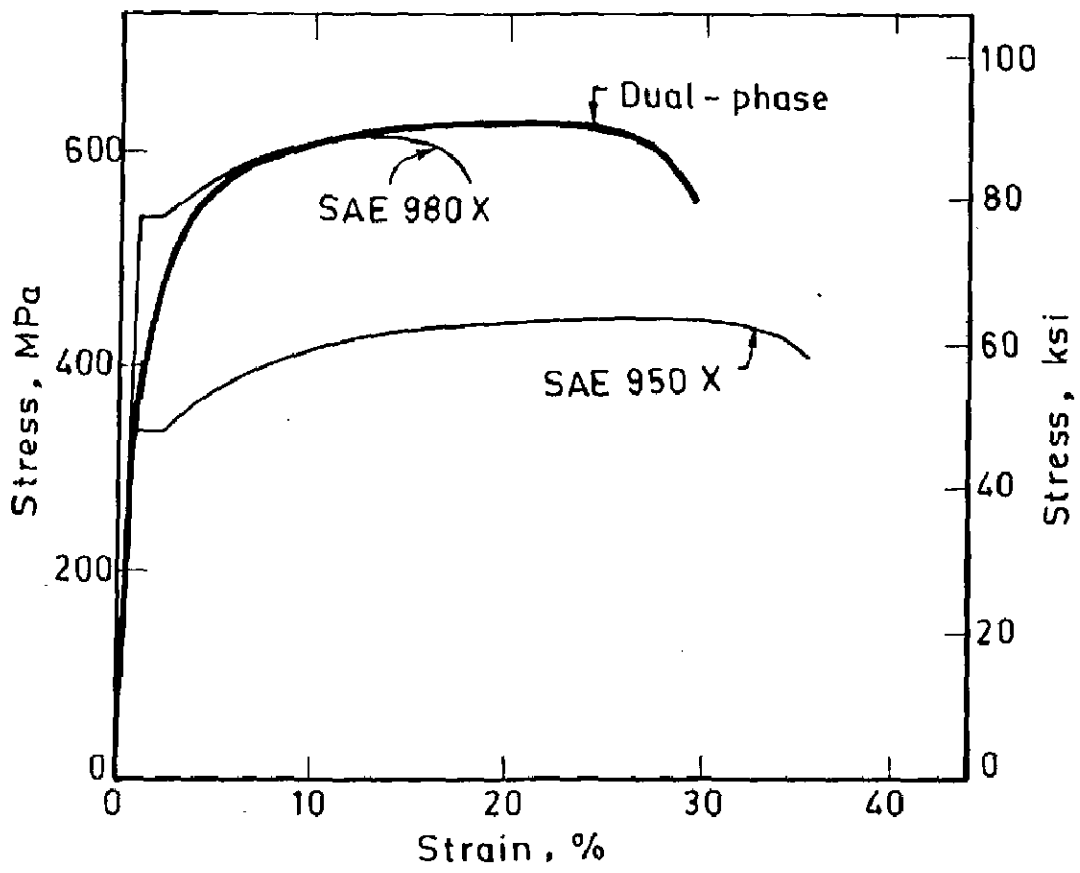

Fig. 2.6 _ Stress-strain curves for HSLA and dual-phase steels [3]

The enhanced work-hardening rates of dual-phase steels have been attributed to decomposition of retained austenite or the nature of the ferrite or both [47]. However, Balliger and Gladman [48] have indicated that the work-hardening rates are directly associated with the amount of martensite and the size of the martensite particles or islands. TEM examination of deformed dual-phase structures [48] has indicated that the martensite remains undeformed, even at relatively high strains, and that the polygonal ferrite flows extensively around the martensite.

The absence of deformation in the dispersed martensite has been analysed [48] in relation to Ashby's theory of work-hardening [49], where secondary dislocation loops in an expanding plastic shell around rigid non-deforming particles interact with the primary slip system. The principal predication of the theroy [49] is the relationship between true stress, σ, and, the true strain, ε, expressed as,

$$\sigma = \sigma_o + KG\sqrt{\frac{\bar{b}\,f\,\varepsilon}{0.4\,l\,\bar{d}}} \qquad \ldots\ldots\ldots(2.31)$$

where, σ_o is a constant, related to the initial flow strees, G is the shear modulus of the matrix, $\bar{b}$ is the Burgers vector of the matrix dislocations, f is the volume fraction of the second phase particle, d is the average particle diameter, and, K is a constant of the order of 1.

The work-hardening rate, $\frac{d\sigma}{dt}$, may be obtained by differentiating Eq.(2.31) w.r.t. strain as,

$$\frac{d\sigma}{d\epsilon} = 0.78\ KG\ \frac{b^{\frac{1}{2}}}{\epsilon^{\frac{1}{2}}}\ \sqrt{\frac{f}{d}} \qquad \ldots (2.31a)$$

This expression indicates that at a given strain, the work-hardening rate is directly proportional to the square root of the volume fraction of hard particles and inversly proportional to the square root of the mean particle diameter. A plot between the experimentally observed work-hardening rates and those calculated based on the Ashby theory is shown in Fig. 2.7. An excellent qualitative agreement between the experiment and theory is indicated by this plot although the gradient of the relationship shown in Fig.2.7 is slightly at variance with the predicted value. This plot therefore confirms that the work-hardening rate increases with increasing volume fraction of martensite and with decreasng martensite particle size. However, the volume fraction of martensite is important in controlling the strength level, but the refinement of martensite particle-size is important in enhancing the work-hardening rate, and therefore the uniform elongation, at a given strength level.

2.5.2 Yield strength and tensile strength

According to simple composite strengthening theory, it is expected that the strength of dual-phase steels should increase when either the volume fraction or the strength of the martensite phase is increased [16,44,50,

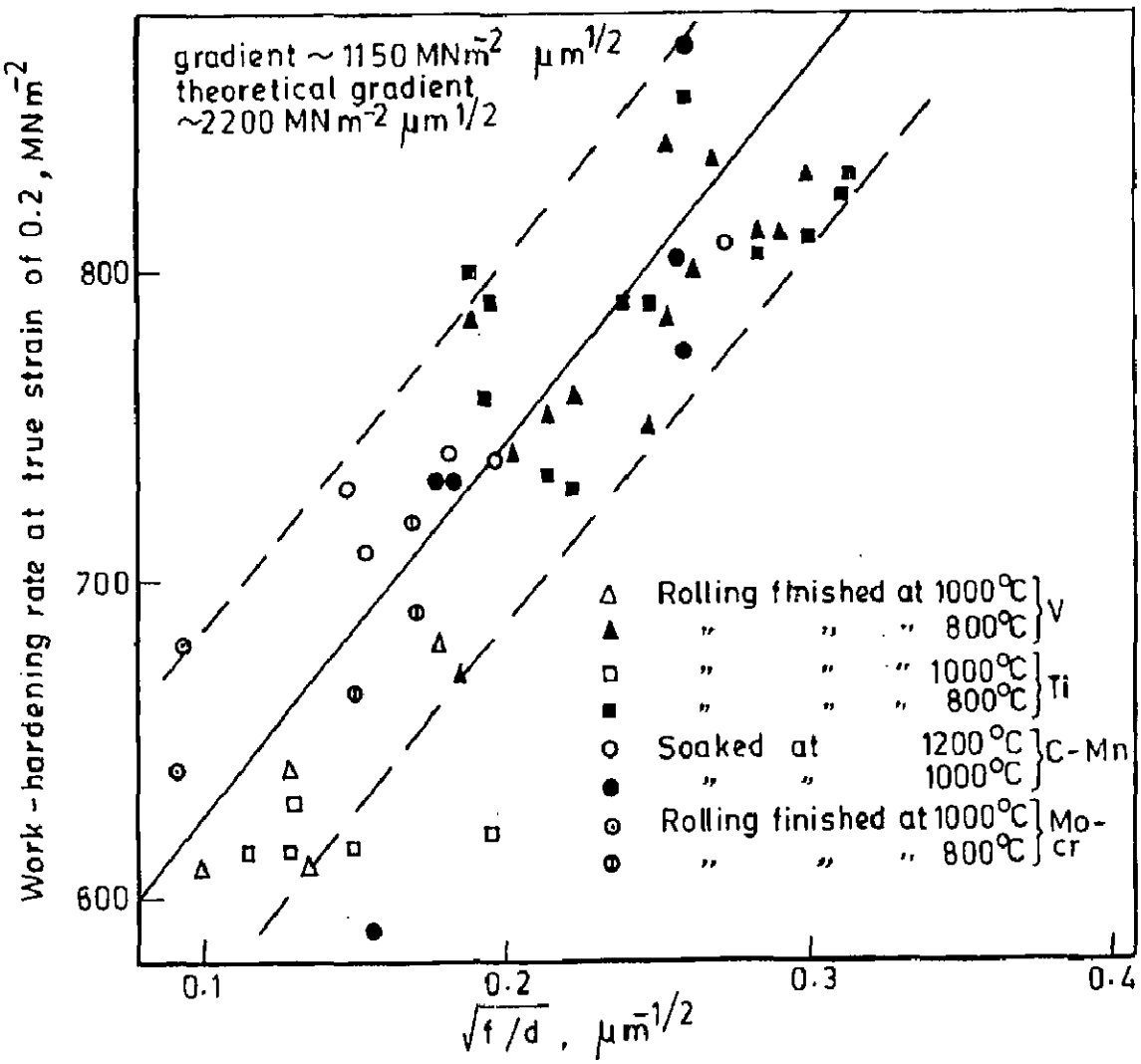

Fig. 2.7 _ Dependence of work-hardening rate, measured at true strain value of 0.2 on parameter $\sqrt{f/d}$ [48]

51,52]. If equal strains are assumed in both phases (which is far from reality in actual practice, being concentrated in the softer ferrite phase), the variation of yield strength σ_y and tensile strength, σ_T, of ferrite-martensite mixtures with volume fraction of martensite, f_m, can be deduced based on "Law of mixtures", as,

$$\sigma_y = \sigma_{y,\alpha} (1 - f_m) + \sigma_{y,m} f_m \quad \ldots (2.32)$$

and,

$$\sigma_T = \sigma_{T,\alpha} (1-f_m) + \sigma_{T,m} f_m \quad \ldots (2.33)$$

Where, $\sigma_{y,\alpha}$ and $\sigma_{y,m}$ are respectively the yield strengths, and, $\sigma_{T,\alpha}$ and $\sigma_{T,m}$, respectively the tensile strengths of 100 per cent ferrite and martensite pahses, α_m, and $(1-\alpha_m)$ are respectively the volume fractions of martensite and ferrite phase. Results of study by Davies [53] on tensile strength of ferrite-martensite dual-phase steels having 1.5 Mn, shown in Fig.2.8, reveal that Eqs.(2.32 and 2.33) are obyed over the entire range of volume fraction. Surprisingly, Davies [53] has observed that even though the carbon content of martensite phase is changed by varying the intercritical temperature, results also in an increase in $\sigma_{T,m}$, no effect on σ_T is detected. However, later studies by Speich and Miller [50] on dependence of both the yield and tensile strengths of ferrite-martensite mixtures in 1.5 Mn steels, quenched from different intercritical temperatures to vary both the volume fracton and carbon content of the martensite phase (0.3 per cent and

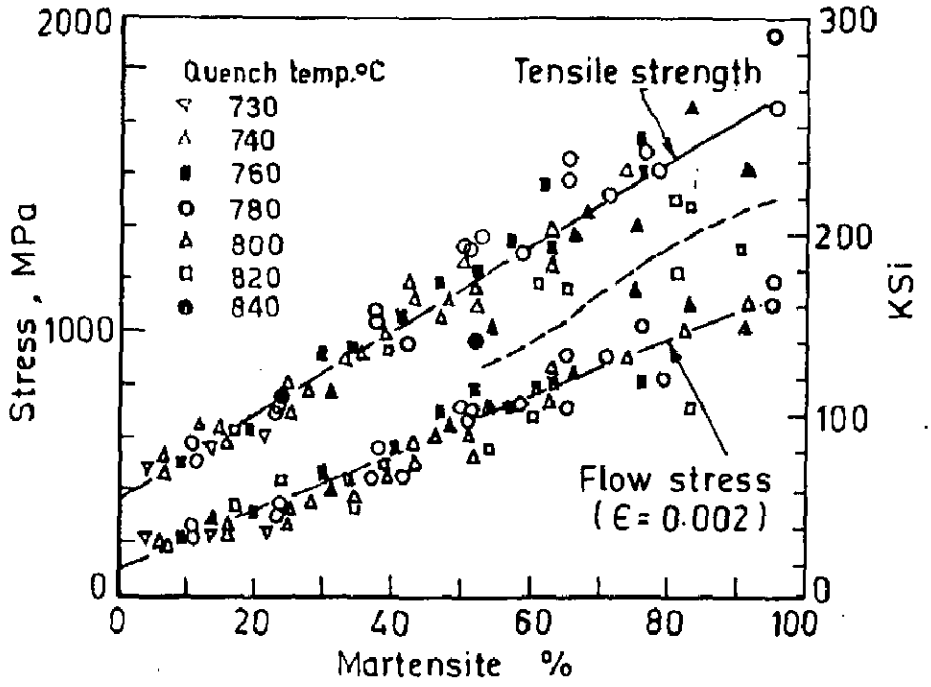

Fig. 2.8 The 0.2 pct flow stress and the tensile strength as a function of percent martensite for the Fe-Mn-C alloys [53]

0.5 per cent) as also done in the work of Davies [53], reveal a linear relationship between strength and volume fraction of martensite only over a limited range of martensite volume fraction (50 per cent) as shown in Fig. 2.9. Beyond this value the variation is non-linear. This is explained on the basis that the law of mixture is applicable only over a limited range of martensite volume fraction. To obtain a linear variation between yield strength or tensile strength and martensite volume fraction (> 50 per cent), a "modified law of mixtures" assuming a much lower value of effective stress in martensite phase is to be used.

Leslie and Sober [51] have shown that yield strength of the martensite phase, $\sigma_{y.m}$, is related to its carbon content, C_m, as weight per cent by the expression,

$$\sigma_{y,m}(\text{MPa}) = 620 + 2585\ C_m \qquad \ldots (2.34)$$

In simple ferrite-martensite mixtures, the value of C_m is given approximately by the expression,

$$C_m = 100\left(\frac{C_o}{f_m}\right) \qquad \ldots (2.35)$$

where, C_o is the carbon content of the steel, and it is assumed that the densities of the ferrite and martensite phases are equal and also that the carbon content of ferrite phase is negligible.

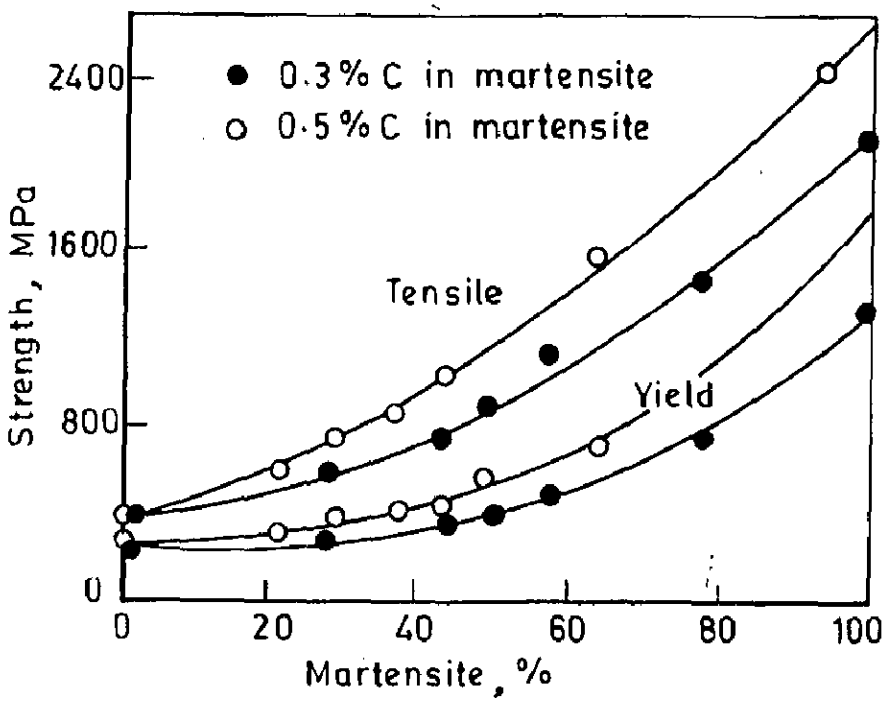

Fig.2.9 _ Yield and tensile strength of ferrite-martensite mixtures in 1.5 Mn steels [50]

It has also been found by Speich and Miller [50] that the martensite has smaller effect on yield strength than on tensile strength as a result of the initial yielding behaviour being related to elimination of residual stresses about the martensite particles. Thus, at low plastic strains, characteristic of the yield strength, the stress within the martensite phase only reaches about 1/3rd the yield strength of this phase. For higher plastic strains corresponding to the tensile strength, residual stresses have been eliminated and the stresses within the martensite phase increase, so its contribution to the overall strength increases. The marked increase in the strength above 50 per cent martensite for either the yield or tensile strength appears to result from the martensite phase becoming the matrix phase so that it can begin to support a major fraction of the load with little or no deformation occurring in the occluded ferrite phase. In support of the work of Speich and Miller [50], several other investigators [46,52] have found the effect of the strength or the carbon content of the martensite phase on the tensile strength of ferrite-martensite dual-phase steels. However, in support of the work of Davies [53], a number of other investigators [54,55] have reported no effect of the strength or the carbon content of the martensite phase on the tensile strength of the dual-phase steel. The reasons for these differences appear to be associated with a very large scatter band in the data

of Davies [53] and latter workers, so that the effects of carbon content of the martensite phase may be masked.

Prasad [56] has developed a theoretical model for tensile strength, based on shear-lag analysis, for Al-Cu cast composites having ductile second phase spherical particles embedded in brittle eutectic matrix. When such a composite is deformed, as with discontinuous fibre composites, the force is not directly applied to the particles but is transferred through the matrix. The case of load transfer in a single particle model is first discussed and then an expression is arrived at for theoretical calculation and prediction of the tensile strength of composite making use of law of mixtures. Basic assumptions of this model are,

(i) the matrix is continuous and contains randomly distributed discrete particles.

(ii) both the matrix and the particles are only elastically deformed.

(iii) particle-matrix interface is strong enough to affect load transfer.

(iv) Poisson's effect is negligible.

(v) both the matrix and the particle have equal shear moduli.

Since the expression arrived at by Prasad [56] will be used for the theoretical analysis in the present work, in the following the basic treatment by Prasad [56] is presented in slight detail.

Figure 2.10a shows a single spherical particle of diameter D_v embedded in the elastic matrix subjected to a tensile stress σ_m. If a random plane intersects the particle perpendicular to the direction of the applied stress, the sectional diameter of particle on the plane is denoted by D_i such that,

$$D_i = D_v \sin\theta \qquad \ldots (2.36)$$

where, θ is half of the cone angle subtended by the section, as shown in above referred figure. The forces acting on an element of the particle have been shown in Fig. 2.10b. If τ_θ is the shear stress at the particle-matrix interface, the elemental force balance in the direction of the applied stress yields the expression,

$$\tau_\theta . \pi , D_1 . \frac{D_v}{2} \, d\theta . \sin\theta = d\sigma \, . \frac{\pi}{4} . D_i^{\,2} \qquad \ldots (2.37)$$

which on simplification yields,

$$\frac{d\sigma}{d\theta} = 2\tau_\theta \qquad \ldots (2.38)$$

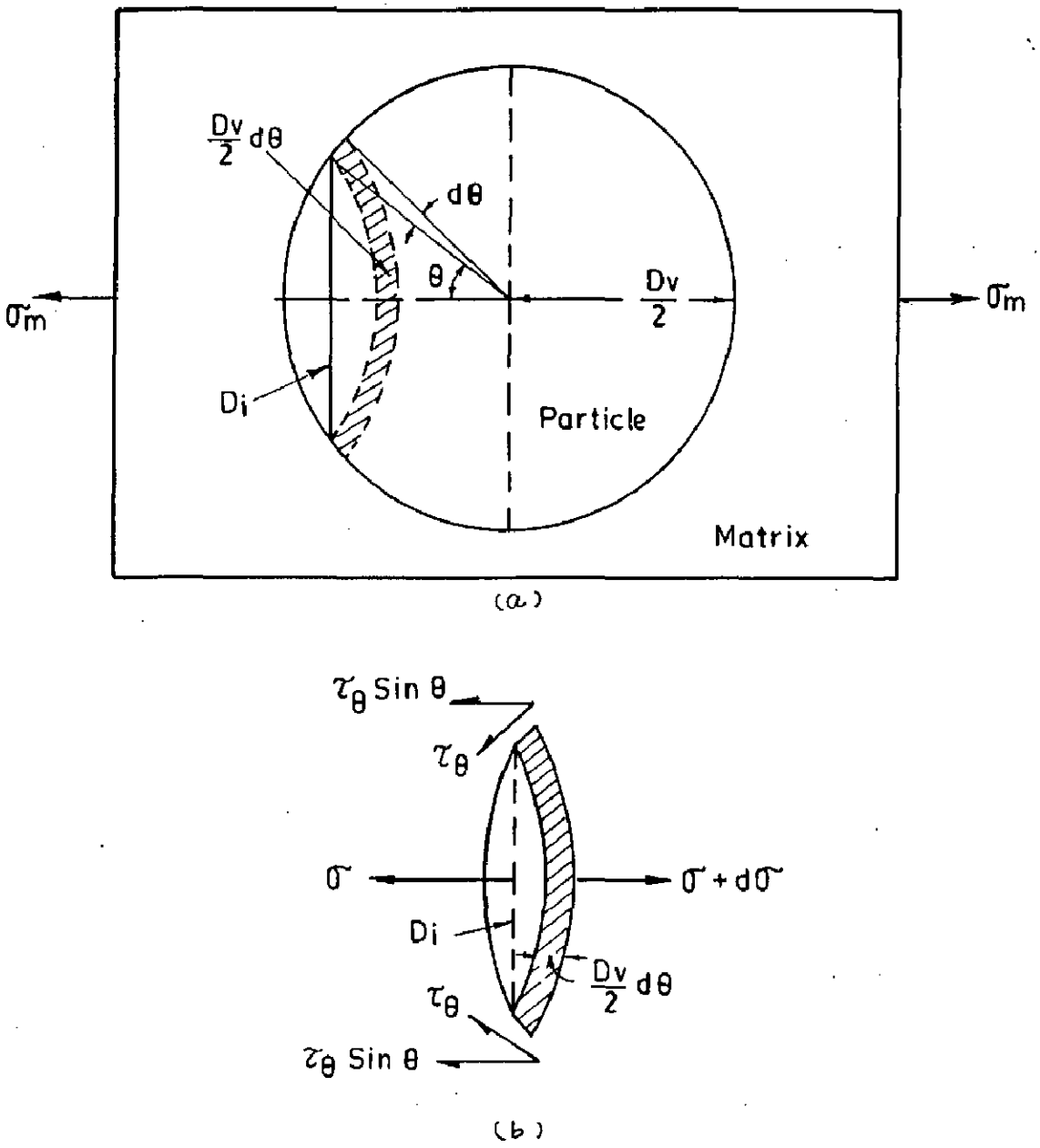

Fig. 2.10 - (a) Schematic representation of a single particle composite model (b) Elemental force balance at a section of the particle

Further, using Eq. (2.36), one can write,

$$\frac{dD_i}{d\theta} = D_v \cos\theta = [D_v^2 - D_i^2]^{\frac{1}{2}} \qquad \ldots (2.39)$$

$$\text{As,} \quad \frac{d\sigma}{dD_i} = \frac{d\sigma}{d\theta} \cdot \frac{d\theta}{dD_i} \qquad \ldots (2.40)$$

Combining Eqs. (2.38), (2.39) and (2.40),

$$d\sigma = 2T_\theta [D_v^2 - D_i^2]^{-\frac{1}{2}} \, dD_i \qquad \ldots (2.41)$$

The case of stress distribution around a spherical elastic particle embedded in an elastic matrix has been treated by Theocaris and Paipetis [57]. Following the work of Sezawa and Miyazaki [58], it can be shown that, the shear stress distribution, τ_θ, in the particle at the particle-matrix interface is given by the expression,

$$\tau_\theta = \sigma [2G_p \frac{S_1}{S} \frac{dP_2(\cos\theta)}{d\theta}] \qquad \ldots (2.42)$$

For the case when the matrix and the particle shear moduli are equal, i.e. if $G_m = G_p$, it has been shown [57] that,

$$S = 6G_p S_1 \qquad \ldots (2.43)$$

Substituting the value of S from Eq. (2.43) in Eq. (2.42),

$$\theta = \frac{\sigma}{3} \cdot \frac{dP_2(\cos\theta)}{d\theta} \qquad \ldots (2.44)$$

The Legendre polynomial $P_2(\cos\theta)$ is expressed as,

$$P_2(\cos\theta) = \tfrac{1}{2}[3\cos^2\theta \quad 1] \qquad \ldots (2.45)$$

Differentiating Eq. (2.45), one gets,

$$\frac{dP_2(\cos\theta)}{d\theta} = -3\sin\theta.\cos\theta \qquad \ldots (2.46)$$

From Eqs. (2.36) and (2.46), one can write,

$$\frac{dP_2(\cos\theta)}{d\theta} = -\frac{3D_i}{D_v^2}[D_v^2 - D_i^2]^{\frac{1}{2}} \qquad \ldots (2.47)$$

This expression, making use of Eq. (2.42), yields,

$$\tau_\theta = -\sigma.\ \frac{D_i}{D_v^2}\ [D_v^2 - D_i^2]^{\frac{1}{2}} \qquad \ldots (2.48)$$

Assuming $\sigma = \sigma_m$ and substituting magnitude of τ_θ from Eq. (2.48) in Eq. (2.41), and rearranging, the terms, one gets,

$$d\sigma = 2\sigma_m \frac{D_i}{D_v^2}\ d\ D_i \qquad \ldots (2.49)$$

This expression on integration within the limits $\sigma = 0$ at $D_i = 0$ and $\sigma = \overline{\sigma D_i}$ at $D_i = D_i$, yields,

$$\overline{\sigma D_i} = \sigma_m\left(\frac{D_i}{D_v}\right)^2 \qquad \ldots (2.50)$$

The above expression yields the value of the stress in the particle on a planar section D_i as a function of the matrix stress and the ratio of section diameter to true diameter of the particle. If the composite contains randomly distributed particles and if on the planar section the average

size of particles be D_i, the average stress carried by the particles may be written from Eq. (2.50) as,

$$\sigma_{D_i} = \sigma_m \left(\frac{\bar{D}_i}{D_v} \right)^2 \qquad \ldots (2.51)$$

The true size of particles, D_v, may be determined from the measurements made on the planar section. It has been shown [59] that,

$$D_v = \frac{\pi}{2\bar{Z}} \qquad \ldots (2.52)$$

where, the parameter Z is the reciprocal of the planar section size D_i. Therefore,

$$\bar{Z} = \frac{1}{N_o} \sum_{i=1}^{N_o} \frac{1}{D_i} \qquad \ldots (2.53)$$

where, N_o is the number of section sizes measured.

Now combining Eqs. (2.51) and (2.52), one gets,

$$\bar{\sigma}_{D_i} = \sigma_m \frac{4}{\pi^2} (\bar{D}_i \ \bar{Z})^2 \qquad \ldots (2.54)$$

Eq. (2.54) yields the average stress carried by the particles of average size $\bar{D}_i$ on a planar section. Using symbol σ_p for the stress in the single particle, one gets,

$$\sigma_P = \sigma_m \frac{4}{\pi^2} (\bar{D}_i \ \bar{Z})^2 \qquad \ldots (2.55)$$

On application of the rule of mixture, the composite stress σ_C for the material may be written as,

$$\sigma_C = \sigma_m V_m + \sigma_p V_p \qquad \ldots (2.56)$$

where, V_m and V_p are respectively the volume fractions of the matrix and the embedded particles in the composite material. Substituting Eq. (2.55) in Eq. (2.56), one gets,

$$\sigma_C = \sigma_m [V_m + \frac{4V_p}{\pi^2} (\bar{D}_i \bar{Z})^2] \qquad \ldots (2.57)$$

This expression yields the stress in the composite in terms of matrix stress and particle parameters. If σ_m reaches the ultimate tensile stress of the matrix, $\sigma_{u,m}$, and this condition leads to the ultimate tensile strength, $\sigma_{u,c}$, of the composite, one can write the following final expressions for $\sigma_{u,c}$, arrived at by Prasad [56].

$$\sigma_{u,c} = \sigma_{u,m} [V_m + \frac{4V_p}{\pi^2} (\bar{D}_i \bar{Z})^2] \qquad \ldots (2.58)$$

While testing the predictive value of this expression, Prasad [56] has observed that good agreement between the calculated and experimental values of the tensile strength of three rheocast Al-Cu alloys with 4.5, 6 and 10 weight per cent copper could be found only after incorporating corrections for porosity in the castings and use of Eq. (2.58) alone leads to scatter in the calculated values as compared to experimental values.

2.5.3 Ductility

The effect of dual-phase microstructure on uniform and total elongations is considered difficult to interpret because of a variety of factors influencing these, viz., volume fraction of martensite, carbon content of martensite, plasticity of martensite, distribution of martensite, alloy content of ferrite, carbon content of ferrite, amount of epitaxial ferrite, retained austenite etc.

Davies [53] has first studied systematically the effect of volume fraction of martensite on uniform elongation and interpreted his results based on Mileiko's theory [60] of ductility of composite materials. From, the considere' conditions [61],

$$\frac{d\sigma}{d\epsilon} = \sigma \qquad \ldots (2.59)$$

and assuming that a power stress-strain equation of the type,

$$\sigma = K\epsilon^n \qquad \ldots (2.60)$$

is obeyed, Dieter [62] has shown that

$$n = \epsilon_u \qquad \ldots (2.61)$$

where, σ and ϵ are respectively the true stress and true strain, n is the exponent of the power law, k, is a constant, and, ϵ_u, is the true uniform elongation. Assuming (i) a

power stress-strain law for the mixture of ferrite and martensite phases in the dual-phase structure, and, in addition, (ii) the strains to be equal in each phase. Mileiko [60] has shown that the uniform strain, ε_u of the composite can be calculated from the values of K and n for each of the phases. Davies [53] has used this theory to interpret his observations on 1.5 Mn steels and for V-N HSLA Steels, and his results are shown in Fig. 2.11. Good agreement is indicated between the value calculated based on Mileiko's theory and experimental data. However, later works by a number of investigators [50,63] have shown that Eq. (2.60) is not followed for dual-phase steels because the strain in the two phases i.e., ferrite martensite is widely different.

Experimental results obtained by Davies [53] and Araki et al [64] also indicate that the uniform elongation decreases in a non-linear manner with increasing per cent martensite. Speich and Miller [50] have also reported similar results, but in addition have found that the uniform elongation increased slightly on decreasing the carbon content of martensite phase. An empirical equation that fits in the data for several intercritical temperatures after Speich and Miller [50] is,

$$\frac{e_{u,c}}{e^{o}_{u,\alpha}} = 1 - 2.2\, C_m \left(\frac{f_m}{100}\right)^{\frac{1}{2}} \qquad \ldots (2.62)$$

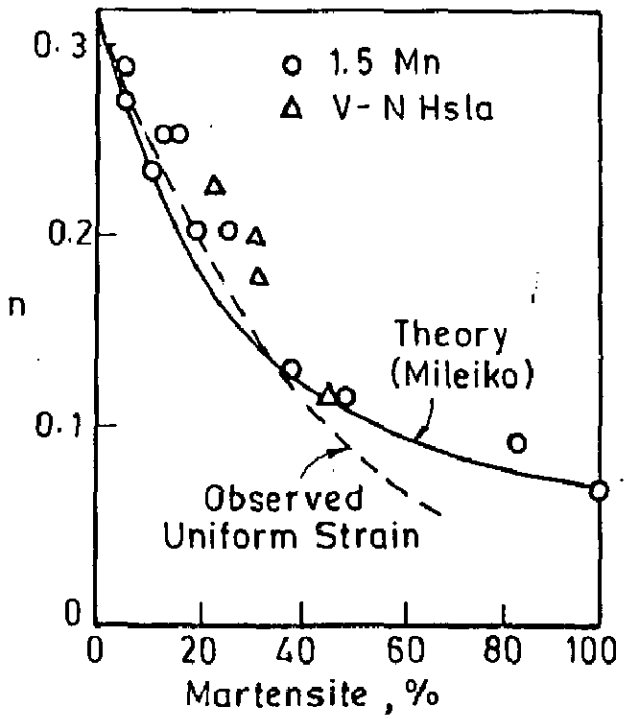

Fig. 2.11 _ A comparison of the calculated and observed n values from theory of Mileiko [53]

where, $e_{u,c}$ and $e^{o}_{u,\alpha}$ are the uniform elongations (in per cent engineering strain) respectively for the composite and for 100 per cent ferrite. A plot of experimental results after Speich and Miller [50] according to Eq.(2.62) is shown in Fig.2.12.

Total elongation of ferrite-martensite steels also decreases with increasing per cent martensite. Tamura et al. [65] have reported an exponential decrease in elongation and a higher total elongation for any given per cent martensite when the value of the ratio of the yield strength of martensite to that of ferrite increased. Speich and Miller [50] have found a relationship similar to Eq.(2.62) for total elongation,

$$\frac{e_{t,c}}{e^{o}_{t,\alpha}} = 1 - 2.5\, C_m (f_m/100)^{\frac{1}{2}} \qquad \ldots (2.62a)$$

where, $e_{t,c}$ and $e^{o}_{t,\alpha}$ are the total elongations (in per cent engg. strain) of the composite and 100 per cent ferrite respectively. Again, total elongation has been found to depend not only on the volume fraction martensite but also on the carbon content of the martensite phase, decreasing as the carbon content/strength) of the martensite phase increased. A plot of the total elongation data of Speich and Miller [50] according to Eq.(2.62a) is shown in Fig.2.12. Uniform and total elongations with increasing amount and carbon content of the martensite phase i.e., increasing tensile strength is shown in Fig.2.13, presenting data after Speich et al [50].

Speich and Miller [50] have argued that the lower carbon content of the martensite increased ductility because

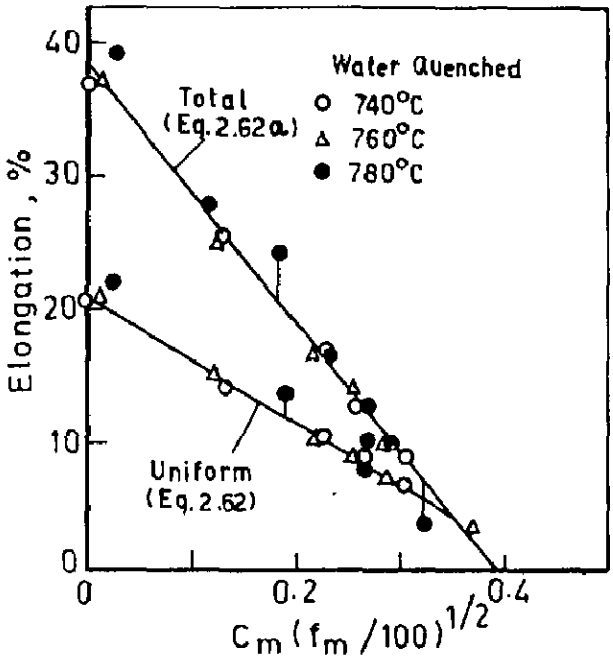

Fig.2.12_Effect of amount and carbon content of martensite phase on uniform and total elongation [50]

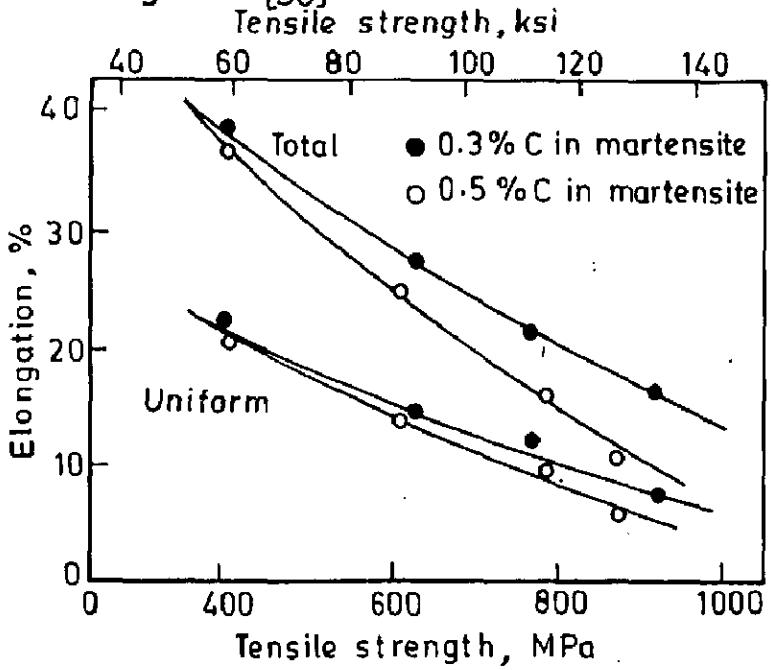

Fig.2.13_Relation between tensile strength and uniform and total elongation for water quenched 1.5 Mn ferrite martensite steels [50]

cracking of the martensite particle or decohesion of the martensite/ferrite interface then becomes more difficult. Rashid [63] has also argued on a basis similar to that of Speich and Miller [50], for explaining the improved ductility of dual-phase steels.

Distribution of the martensite phase in the ferrite matrix has also been found to influence ductility as observed by Becker and Hornbogen [66], and Kim and Thomos [67]. Obviously, for any given per cent martensite, a set of widely spaced, small martensite particles is desired. Chains of martensite particles that are linked up may be detrimental to ductility because this may offer an easy crack-propagation path through the matrix, although such effects are sensitive to the nature of the distribution and to the manner in which the sheet is stressed. Because the distribution of the martensite phase is determined by the nucleation of austenite particles at the cementite or pearlite phases present in the starting microstructure, it is important in intercritically annealed dual-phase steels that this microstructure be as uniform and fine as possible.

It has been observed by several investigators [63,68] that the carbon content of the ferrite phase plays an important role in influencing the ductility of dual-phase steels. Hayami et al [68] have argued that the ductility obtained after

water quenching is much inferior to that obtained with a mild cooling rate, because of the lower carbon content of the ferrite in the slower-cooled material. It has also been observed by Repas [7] that addition of silicon in dual-phase steels improves ductility. Although the exact explanation for the effect of silicon is uncertain yet it has been suggested by Thomas et al [23] that ductility improves from a lowering of the carbon content of the ferrite phase. However, Lagneborg [69] has challenged this conclusion, arguing that silicon addition increases the carbon content of the ferrte phase.

Huppi et al [70] and Lawson et al [36] have argued that the amount of epitaxial-or "new" ferrite formed upon cooling has an important effect on ductility. Ductility improves as the amount of epitaxial ferrite is increased and this improvement is considered to be caused by a lack of the precipitation of carbides and carbonitrides in the epitaxial ferrite, formerly present in old ferrite.

Furukawa et al [5] have observed that presence of retained austenite in dual-phase steels also enhances ductility. This is explained on the basis of transformation of retained austenite during plastic straining and the resultant increase in work-hardening rate an effect similar to the well-known transformation-induced-plasticity (TRIP) mechanism,

used to explain the high ductility of metastable austenitic stainless steels [71].

In contrast, Eldis [72] has observed no connection between retained-austenite content and ductility in a number of dual-phase steels. He has argued that because the retained austenite transforms during the early stages of plastic straining, it can not influence the onset of necking in the tension-test specimen, which occurs late in the plastic straining process. Speich and Miller [50] have also discounted the effect of retained austenite on ductility because of the small amounts of retained austenite (2 to 4%) present in their specimens.

The effect of retained austenite in dual-phase steels is therefore complex. When large amounts of retained austenite are present and stability of the austenite is sufficient, then transformation of retained austenite occurs late in the plastic-straining process, and in such cases large effects on uniform elongation can be expected.

2.5.4 Formability

Steels to be commercially used must have good formability i.e., should be able to easily form into the desired shapes. Because of the variety of shapes and stress distribution which are possible in the forming of metals, formability

can not be predicted on the basis of simple mechanical properties such as elongation or ultimate tensile strength (UTS). Moreover, there are no simple evaluation tests applicable equally to all forming operations. It can be stated in very general terms that a high uniform elongation, so as to decrease local plastic instability, and, a low yield stress and high UTS, so as to make flow easy but fracture difficult, are the combinations of mechanical properties most conducive to good formability. The greater the gap between yield stress and UTS, the greater will be strain-hardening capacity of material. It is generally considered that a high capacity for strain-hardening is conducive to good formability.

Plastic strain ratio or the R-value, defined as the ratio of the true width strain to the true thickness strain in a tensile test for sheet material. Generally, its value depends on the elongation at which it is measured.

The R-value is a measure of the ability of a material to resist thinning. In drawing operation, metal in the flange is stretched in one direction i.e., radially and compressed in the perpendicular direction i.e., circumferentially. A high R-value indicates a material with good drawing properties.

In practice, the R-value is calculated as the ratio of width true strain to thickness true strain in a tension test of specimen cut from sheet,

$$R = \frac{\ell n(W_i/W_f)}{\ell n(T_i/T_f)} \qquad \ldots (2.63)$$

where, W_i is the initial width

W_f is the final width

T_i is the initial thickness

T_f is the final thickness

Because measurement of the thickness of a thin sheet is subject to considerable error, it is commonly assumed that the volume of the specimen is constant, therefore,

$$R = \frac{\ell n(W_i/W_f)}{\ell n(L_f W_f/L_i W_i)} \qquad \ldots (2.64)$$

where, L_i and L_f are the initial and final lengths. The R-value can be measured at any point in the tension test between the end of the Luders strain and the maximum load.

Values of R are conventionally reported as an average, $\bar{R}$,

$$\bar{R} = \frac{R_o + 2R_{45°} + R_{90°}}{4} \qquad \ldots (2.65)$$

where, R_o is the value determined in the rolling direction (longitudinal),

$R_{45°}$ is the value determined at 45° to the rolling direction,

$R_{90°}$ is the value determined in the transverse direction.

$\bar{R}$-value is controlled by the texture of the sheet e.g., when a steel contains increasing number of grains, where <111> axis is normal to the plane of sheet, the $\bar{R}$-value increases. However when it contains increasing number of grains with <100> crystals normal to plane of sheet, it decreases. A relationship between the $\bar{R}$-value and the ratio in diffraction intensity of <111> to <100> plane has also been reported in literature [73,74].

Okamoto and Takahasi [75] have shown that the $\bar{R}$-value is not only controlled by the crystalline texture but also by the existence of martensite in box-annealed dual-phase steel. Similar effects of the hard phase on the $\bar{R}$-value are also reported for water-quenched dual-phase steel by Hosoya et al [76].

The formability of dual-phase steels has also been evaluated based on both the forming limit diagrams [77] and also the limiting dome height [78]. And it has been shown [3] that a dual-phase steel of tensile strength of 640 MPa has formability equivalent to a 440 MPa UTS steel.

Another consideration in making useful shapes from sheet materials, is the ability to predict and control the final shape i.e., to estimate 'Spring-back' occurring when the component is removed from the press. 'Spring-back' is usually thought to be proportional to the yield strength. Therefore the 'spring-back' of dual-phase steels is, in general, comparatively low. A more reliable measure of 'Spring-back' is the ratio of $E_e(E_e+E_p)$, where, Ee and Ep denote respectively the elastic and the plastic-strains. The structure-property correlations [41] for dual-phase steels show that microstructures containing appreciable amounts of retained austenite in addition to martensite, may have superior formability for certain forming operations becauese of their higher strain-hardening rate at low strains and greater uniform elongation. However, high martensite volume fractions in the dual-phase structures adversely affect formability.

2.5.5 *Impact resistance*

Davies [79] has observed that dual-phase steels are considerably tougher than the conventional HSLA steels and has concluded that the increased toughness is due to the following reasons:

a) the interface between martensite and ferrite is coherent while those between the carbides and ferrite

phase are, in general, incoherent. During straining, dislocations pile-up at the carbide-ferrite interface leading to the nucleation of voids and fracture. On the other hand, dislocations from ferrite phase are able to penetrate into the martensite, albeit with difficulty and thus there are no such large strain concentrations, fracture is found to occur at higher strains.

b) the ferrite phase in dual-phase structures, is more tough due to the presence of high dislocation as compared to that in the conventional HSLA steels. In the latter case strengthening occurs due to carbonitride precipitates which, in general, degrade impact properties.

2.5.6 Fatigue of dual-phase steels

Only few studies relating fatigue of dual-phase steels to microstructural and processing variables have been reported in literature [79,80]. More usually, these important properties have been tested on full-scale components under simulated, accelerated service conditions. It has been observed that at large strain amplitudes, microalloyed dual-phase steels have longer fatigue life than the same steel in hot-rolled condition. This is because the dual-phase steel is more ductile than the HSLA steel. At low strain amplitudes, the

fatigue life is controlled by the yield strength and under these conditions, dual-phase steels do not perform as well as hot-rolled HSLA steels. In tests simulating service conditions, the fatigue behaviour has generally been found to be satisfactory.

2.5.7 Tempering and strain ageing

Intentional tempering for improvement in ductility may be used in some continuous annealing operations especially when the dual-phase steels have been water-quenched from the intercritical annealing temperatures. Tempering also occurs during hot-dip galvanising operations. In addition, tempering of formed automobile components occurs during paint-baking cycles. Since the parts are already plastically strained and therefore tempering process for these is really a strain-ageing process.

Two types of tempering processes are used for components made of dual-phase steels viz. the low temperature tempering conducted at ~200°C and the high temperature tempering conducted at ~650°C.

Speich et al [81] have observed that on low temperature tempering, segregation of carbon atoms to dislocations by diffusion and elimination of residual stresses results in an increase in the yeild strength and a return of discontinous

yielding only if the volume fraction of martensite phase is below 30 per cent. This is shown schematically in Fig. 2.14. At higher volume fractions of martensite, the initial yielding behaviour appears to be less affected by tempering because of higher dislocation density and higher residual stresses. Speich et al [81] have further observed that tensile strength is lowered slightly after tempering at low temperature because of the decrease in hardness of the martensite phase, for steels with both low and high volume fractions of martensite.

Speich et al [81] have observed that on high temperature annealing, tempering results in a return of discontinuous yielding and a lowering of both the yield and tensile strengths, independent of the amount of martensite.

It has also been observed by Krupitzer [82] that as-annealed dual-phase steels are non-ageing at room-temperatures and exhibit sluggish ageing behaviour at elevated temperatures upto 260°C. However, deformation, either by cold rolling or by tensile straining, accelerates the ageing process.

Tanaka et al [8] have studied the return of the yield point in 0.06C-1.2Mn-0.5Cr dual-phase steel, after intercritical annealing after temper rolling 1 per cent, and, after straining in tension, for different ageing times at 100 and 170°C temperatures. They have observed that after intercritical annealing, the yield point does not return even

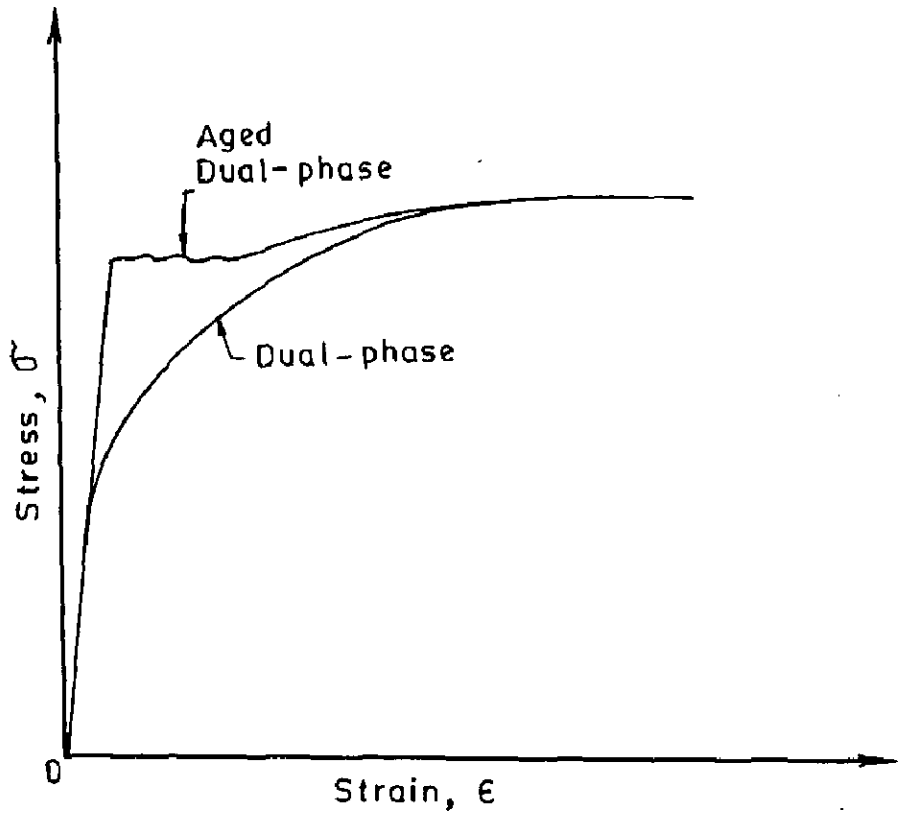

Fig.2.14 _ Diagram showing the effect of ageing on the stress-strain curve

after ageing for 125 hours at 100°C, but does return after ageing even for 40 minutes at 170°C. Similar behaviour is also observed after 1 per cent temper rolling. However, after straining 1 per cent in tension, a return of yield point is observed on ageing only after 2 hours at 100°C, and after 20 minutes at 170°C. Tanaka et al [8] have attributed the more rapid strain ageing behaviour after straining 1 per cent in tension to changes in dislocation distribution. In the as-quenched condition, the dislocation distribution in dual-phase steels is markedly non-uniform, and, in the region of high dislocation density, the excess carbon is drained locally before sufficient pinning of dislocations has been achieved to cause a return of the yield point. To get additional pinning, carbon must diffuse from the grain interior to the region of high dislocation density near the martensite/ferrite interface. However, this requires a long ageing time. If the specimen is slightly strained in tension, the dislocation density is made much more uniform than that already existing in the as-quenched or temper-rolled conditions. As a result, the carbon diffusion only needs to occur over short distances, and the yield-point returns quickly.

Rashid [83] has studied the change in strength and ductility of a number of different dual-phase steels after prestraining up to 25 per cent and ageing for 1 hour at 205°C. In all cases, the yield strength increases and the

ductility decreases. The change in tensile strength is more complex, increasing for all degrees of prestrain in micro alloyed steel containing Nb and V, but decreasing for low degrees of prestrain in steels without microalloying additions. Rashid [83] has explained this behaviour in terms of a reversal from a net softening, when the tempering of the martensite phase is important, to a net strengthening when ferrite strengthening resulting from the interaction between dislocations and NbCN or VCN precipitates is important. Davies [84] based on his studies has also proposed that the strain-ageing of microalloyed steels is influenced by the interaction of carbon atoms with clusters of vanadium atoms in the ferrite matrix.

2.5.8 Formulation of problem

From the above review of available published literature, it is obvious that most of the studies conducted in the past have been restricted to micro-alloyed and low-alloy high strength (HSLA) steels and little attempt has been made to study plain-carbon dual-phase steels, especially to elucidate the role of carbon in a wider range of composition. Further, most of the studies, have been conducted with fixed annealing times at which the austenite volume fraction reaches almost equilibrium value. Some kinetic studies reporting effect of time of intercritical annealing

have especially been made to elucidate the mechanism of austenite formation and little attempt has been made to study the effect of time on intercritical annealing on mechanical properties of dual-phase steels. During the isothermal annealing, the austenite phase after consuming pearlite grows into ferrite matrix and on quenching, the martensite volume fraction increases. This change in martensite volume fraction influences the mechanical properties of dual-phase steel. At long annealing times, the austenite volume fraction reaches its equilibrium value, but the carbon redistribution in ferrite and austenite continues to affect, after quenching the mechanical properties of constituent ferrite and martensite of dual-phase steel. A detailed understanding of different stages of austenite formation will provide additional control parameters of annealing time to obtain optimum properties.

There is, therefore, a need of correlation of mechanism of formation of dual-phase microstructure with mechanical properties of such dual-phase steels, and also to reveal the role of variation of carbon content from very low values to high values, to analyse its effect of different stages of formation of austenite and, therefore, on the over all mechanical properties of plain-carbon dual-phase steels. This necessitates studies of different annealing times from just few seconds to longer intervals to attain equilibrium volume fraction of austenite and elucidate role of redistri-

bution of carbon by diffusion in such dual-phase steels.

The intercritical annealing temperature is essentially dependent on carbon content of steel and will control the morphology and composition of constituent ferrite and martensite phase of quenched dual-phase steels and therefore its mechanical properties.

For prediction of strength of composite material, law of mixtures has been used by early workers. But no attempt has been made to incorporate the effect of shape of second phase particle embedded in the matrix in such composite materials. Expression developed by Prasad [56] for brittle matrix and ductile second phase particles for cast Al-Cu alloys, is also not applicable to dual-phase steels having a ductile matrix of ferrite and hard second phase martensite islands. In the present work, therefore, an attempt will be made to develop expression for calculating tensile strength of dual-phase steels based on law of mixture and model based on shear-lag analysis incorporating effect of shape of embedded brittle martensite islands in ductile ferrite matrix.

In order to achieve the above objectives, plain-carbon steel sheets containing 0.08 to 0.4 weight per cent carbon have been selected for the present investigation. The following aspects have been studied in the design of the detailed plan

of the present work,

(i) To study the isothermal kinetics of different stages of austenite formation during intercritical annealing of plain-carbon steels by quantitative metallographic technique and non-isothermal study of austenite formation by Differential Scanning Calorimetry. This study is expected to provide understanding of detailed steps involved towards the formation of equilibrium amount of austenite by intercritical annealing. The kinetic characteristics of different steps will also give an indication of the time scale involved and the possibility of arresting the structure away from equilibrium by quenching to produce dual-phase steel.

(ii) To study the impact of different stages of austenite formation on the over all mechanical properties of dual-phase steels. And this aspect has not been studied so far.

(iii) The contribution of different strengthening mechanism for example strain-hardening and superior load bearing capacity of martensite islands have been investigated within the frame work of shear-lag model of spherical and cylindrical particles. An effort will be made for the first time to take into account the varying range of shape i.e., r/ℓ (the ratio of radius to length

of the martensite island) varying from 0.4 to 0.6 within the frame work of single model.

(iv) To measure the mechanical properties of the dual-phase steels and compare the theoretical predictions with the experimentally observed values to gain further insight into the relative contribution of different strengthening mechanisms within the frame work of the proposed model.

(v) To study the dislocation substructure by Transmission Electron Microscope (TEM) to explain the continuous yielding behaviour and strain-hardening of dual-phase steels.

(vi) To study the fracture behaviour by Scanning Electron Microscope (SEM) and its change as the martensite volume fraction in a dual-phase steel increases.

CHAPTER - 3

MECHANICAL PROPERTIES : THEORETICAL ANALYSIS

3.1 Introduction

The microstructure of hypoeutectoid plain-carbon dual-phase steels consists of islands of martensite in the matrix of ferrite. Apart from martensite and ferrite as the main constituents, dual-phase steels also contain small amounts of pearlite and retained austenite. At the normal room temperature, the ferrite matrix in these dual-phase steels is ductile and continuous whereas martensite is hard, brittle and discontinuous. For theoretical analysis in the present work, dual-phase steels are, therefore, treated as composite materials containing brittle phase martensite embedded as islands in ductile ferrite phase. The strength of these dual-phase steels is governed by the microstructural modifications brought about by (i) changing carbon content, (ii) temperature of intercritical annealing, and, (iii) time of intercritical annealing. In the development of the theoretical analysis, the model developed by Prasad [56] assuming spherical embedded second phase particles and modifications made by incorporating work-hardening term are discussed in the next section in this chapter. Finally, to incorporate the effect of shape of embedded second phase particles, a model, considering

the martensite islands to be cylindrical in shape with hemispherical ends is developed in section 3.2.1 of this Chapter.

3.2 Development of Theoretical Model

Prasad [56] has developed a theoretical model for strength of composite materials based on assumptions already presented in section 2.5.2 and has arrived at the following expression,

$$\sigma_{u,c} = \sigma_{u,m} \left[V_m + \frac{4V_p}{\pi^2} (\bar{D}_i \; \bar{Z})^2 \right] \qquad \ldots (3.1)$$

where, $\sigma_{u,c}$ is the ultimate tensile strength of the composite,

$\sigma_{u,m}$ is the ultimate tensile strength of the matrix,

V_m and V_p are volume fractions of matrix and second phase respectively,

$\bar{D}_i$ is the average size of the particles on a planar section, and,

Z is the reciprocal of the planar section size D_i and the parameter, $\bar{Z}$ is defined as,

$$\bar{Z} = \frac{1}{N_o} \sum_{i=1}^{N_o} \frac{1}{D_i} \qquad \ldots (3.2)$$

N_o in this expression is the number of section sizes measured. However, calculated values of tensile strength of dual-phase

steels using Eq.(3.1), after Prasad, do not agree with the experimental values as shown in Figs.5.18-5.20. This discrepancy is attributed to following reasons:

(i) assumed spherical shape of the embedded second phase particles in development of Prasad's expression, which is not true in case of dual-phase steels.

(ii) ductile ferrite matrix and hard and brittle islands of second phase martensite of hypoeutectoid plain carbon dual-phase steels in contrast with the hard and brittle matrix and ductile second phase embedded particles in the Al-Cu casts composites studied by Prasad [56] in his work.

To overcome this difficulty, effect of strain-hardening after Ashby's work-hardening or strain-hardening [49] term is incorporated in Prasad's [56] expression for tensile strength of composites. On doing so, one arrives at the following expression,

$$\sigma_{u,c} = \sigma_{um}\left[V_m + \frac{4V_p}{\pi^2}\left(\frac{\bar{D}_i}{\bar{Z}}\right)^2\right] + KG\sqrt{\frac{\bar{b}V_p\varepsilon}{0.41\bar{D}_i}} \qquad \ldots (3.3)$$

where, K is a constant of the order of 1,

G is the shear modulus of the matrix,

$\bar{b}$ is the Burger's vector of the matrix dislocations,

ϵ is the true strain,

and other terms have been defined earlier.

In this equation, the first term of right hand side corresponds to expression of Prasad [56] i.e., Eq.(3.1), whereas the second term represents the Ashby's contribution of strain-hardening [49].

Calculated values of tensile strength using this expression in case of dual-phase steels show an increasing trend in tensile strength with an increase in martensite volume fraction as shown in Figs.5.18-5.20. However, calculated and experimental values are still far apart reflecting thereby that additional correction for shape of embedded particles is necessary.

In dual-phase steels, martensite islands neither conform to the spherical shape of embedded particles as assumed by Prasad [56] for Al-Cu cast composites nor resemble to the rod like shape depicted in certain eutectic systems such as tantalum carbide in a cobalt base matrix system [85]. Therefore, for the theoretical analysis in the present work, these martensite islands present in plain-carbon hypoeutectoid dual-phase steels are assumed to be of cylindrical shape with hemi-spherical ends and a suitable expression is derived for the tensile strength in the next sub-section.

3.2.1 Model for tensile strength of composite with embedded second phase particles of cylindrical shape with hemi-spherical ends

Fig. 3.1a shows a single cylindrical particle of diameter D_v, with hemi-spherical ends embedded in the elastic matrix subjected to a tensile stress, σ_m. The shape chosen in this model is more realistic as it takes up more load than spherical embedded particles. However, the stress distribution over different sections of this particle will be quite different in different segments as compared to spherical particles,

Following Eq.(2.50) and putting the values of $D_v = 2r$, and $D_i = 2[r^2-(r-\ell)^2]^{\frac{1}{2}}$ one can write the expression for stress, σ_{D_i}, in an element of the hemi-spherical ends, i.e., with $0 \leq \ell \leq r$,

$$\frac{\sigma_{D_i}}{\sigma_m} = \left[\frac{D_i}{D_v}\right]^2 = \left[\frac{r^2-(r-\ell)^2}{r^2}\right] \qquad \ldots (3.4)$$

where, ℓ is the length as shown in Fig.3.1a, of the embedded particle and r is its radius.

The forces acting on the element at the cylindrical part of the particle have been shown in Fig.3.1b. If τ be the shear stress at the particle-matrix interface, the expression for force balance on this section of radius, r, will be

$$2\pi r\, d\ell\, \tau = \pi r^2\, d\sigma \qquad \ldots (3.5)$$

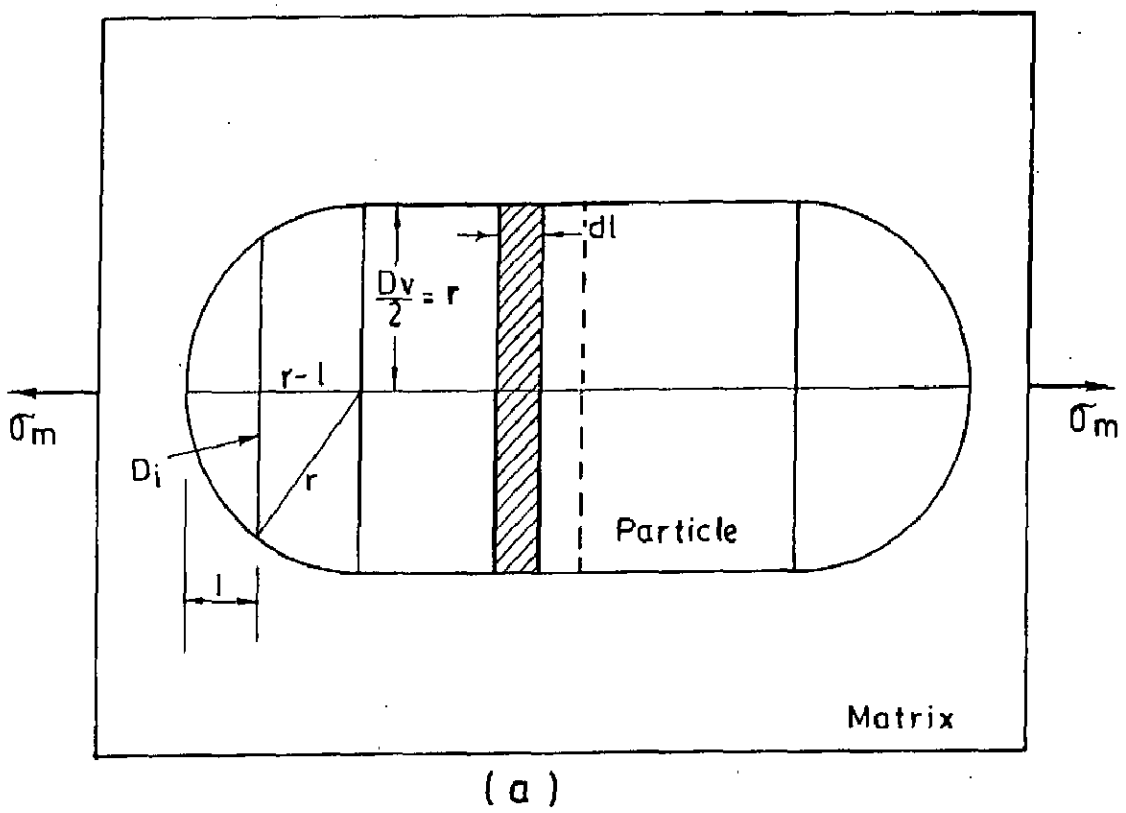

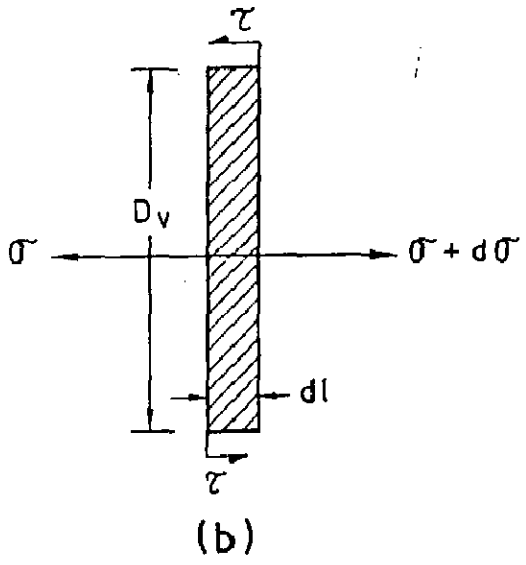

Fig. 3.1 – (a) Schematic representation of a single particle composite model (b) Elemental force balance at a section of the particle

Integrating Eq.(3.5),

$$\tau \int_{r}^{\ell_c} 2\pi r \, d\ell = \int_{\sigma_m}^{\sigma_f} \pi r^2 d\sigma \qquad \ldots (3.6)$$

where, ℓ_c is the minimium particle length loaded to fracture or the critical length.

Rearranging the terms in Eq.(3.6) and simplifying,

$$2\tau \int_{r}^{\ell_c} \frac{d\ell}{r} = \int_{\sigma_m}^{\sigma_f} d\sigma \qquad \ldots (3.7)$$

Or, $$\frac{2\tau}{r} (\ell_c - r) = (\sigma_f - \sigma_m)$$

which yields,

$$\ell_c = r\left[1 + \frac{(\sigma_f - \sigma_m)}{2}\right] \qquad \ldots (3.8)$$

Now, evaluating the value of average stress, $\bar{\sigma}$, upto a distance of r, in the spherical cap,

$$\bar{\sigma}_1 = \frac{1}{r} \int_{0}^{r} \sigma_m \left(\frac{D_i}{D_v}\right)^2 d\ell = I_1, \text{ say} \qquad \ldots (3.9)$$

Again, the average stress, $\bar{\sigma}_2$ in length from r to ℓ_c will be,

$$\bar{\sigma}_2 = \frac{1}{(\ell_c - r)} \int_{r}^{\ell_c} \sigma_\ell \, d\ell \qquad \ldots (3.10)$$

where, $$\sigma_\ell = \sigma_m + \frac{(\sigma_f - \sigma_m)}{(\ell_c - r)} (\ell - r) \qquad \ldots (3.11)$$

Since the stress rises linearly from σ_m at the end of the hemispherical end of the particle to σ_f i.e., the strength of the embedded particle or the fibre at critical length ℓ_c. Substituting the value of σ_ℓ from Eq.(3.11) in Eq.(3.10), one gets,

$$\bar{\sigma}_c = \frac{1}{(\ell_c - r)} \int_r^{\ell_c} [\sigma_m + \frac{(\sigma_f - \sigma_m)(\ell - r)}{(\ell_c - r)}] d\ell = I_2, \text{ say} \quad \ldots (3.12)$$

Similarly, the average stress, $\bar{\sigma}_3$, in length from ℓ_c to ℓ,

$$\bar{\sigma}_3 = \sigma_f = I_3, \text{ say} \quad \ldots (3.13)$$

Now, the average stress, $\bar{\sigma}_f$, in the entire embedded particle or the fibre, will be

$$\bar{\sigma}_f = \frac{r\, I_1 + (\ell_c - r) I_2 + (\ell - \ell_c) I_3}{\ell} \quad \ldots (3.14)$$

Substituting the value of $\left(\frac{D_i}{D_v}\right)$ from Eq.(3.4) in Eq.(3.9) and evaluating the integral I_1, one gets,

$$I_1 = \frac{1}{r} \int_0^r \sigma_m \left[\frac{r^2 - (r - \ell)^2}{r^2}\right] d\ell$$

$$= \sigma_m \int_0^r \left[\frac{r^2 - (r - \ell)^2}{r^3}\right] d\ell$$

which on simplification yields,

$$I_1 = \frac{2}{3} \sigma_m \quad \ldots (3.15)$$

Similarly evaluating I_2, one gets,

$$I_2 = \frac{1}{(\ell_c - r)} \int_r^{\ell_c} [\sigma_m + \frac{(\sigma_f - \sigma_m)(\ell - r)}{(\ell_c - r)}] d\ell$$

which on simplification yields,

$$I_2 = \frac{\sigma_m + \sigma_f}{2} \qquad \ldots (3.16)$$

Therefore, the average stress, $\bar{\sigma}_f$ in the entire embedded particle according to Eq.(3.14) will be,

$$\bar{\sigma}_f = \frac{1}{\ell} [r(\frac{2}{3}\sigma_m) + (\ell_c - r)\frac{\sigma_m}{2} + (\ell_c - r)\frac{\sigma_f}{2} + (\ell - \ell_c)\sigma_f] \qquad \ldots (3.17)$$

Which on rearrangement of terms yields,

$$\bar{\sigma}_f = [\sigma_f - \frac{1}{6}\frac{r}{\ell}(3\sigma_f - \sigma_m) - \frac{1}{2}\frac{\ell_c}{\ell}(\sigma_f - \sigma_m)] \qquad \ldots (3.18)$$

Now, applying law of mixture to the dual-phase steel under study,

$$\sigma_{u,c} = \bar{\sigma}_f V_f + \sigma_{u,m}(1 - V_f) \qquad \ldots (3.19)$$

Where, $\sigma_{u,c}$ is the ultimate tensile strength of dual-phase steel, $\bar{\sigma}_f$ is the average tensile strength of the embedded particle, $\sigma_{u,m}$ is the ultimate tensile strength of the ferrite matrix, and V_f is the volume fraction of the second phase martensite.

Now, substituting the value of $\bar{\sigma}_f$ from Eq.(3.18) in Eq.(3.19), and writing $\sigma_{u,f}$ and $\sigma_{u,m}$ in place of σ_f and σ_m respectively in Eq.(3.18), one gets the ultimate tensile strength, $\sigma_{u,c}$ of the dual-phase steel,

$$\sigma_{u,c} = \sigma_{u,f}\left[1 - \frac{1}{2}\left(\frac{\ell_c}{\ell} - \frac{1}{2}\frac{r}{\ell}\right) V_f + \sigma_{u,m}\left[1+\left\{\frac{1}{6}\frac{r}{\ell} + \frac{1}{2}\frac{\ell_c}{\ell} - 1\right\}V_f\right]\right] \quad \ldots (3.20)$$

As a simplification, assuming $\ell_c = r$, Eq.(3.20) reduces to the form,

$$\sigma_{u,c} = \sigma_{u,f}\left[1 - \frac{r}{\ell}\right]V_f + \sigma_{u,m}\left[1 + \left\{\frac{2}{3}\frac{r}{\ell} - 1\right\} V_f\right] \quad \ldots (3.21)$$

Adding Ashby's work-hardening term [49] to this expression, one gets expression for ultimate tensile strength of hypoeutectoid plain-carbon dual-phase steels as,

$$\sigma_{u,c} = \sigma_{u,f}\left[1 - \frac{r}{\ell}\right]V_f + \sigma_{u,m}\left[1 + \left\{\frac{2}{3}\frac{r}{\ell} - 1\right\} V_f\right] + KG\sqrt{\frac{\bar{b}V_{f,\varepsilon}}{0.41\bar{D}_i}} \quad \ldots (3.22)$$

Where, the symbols used in the additional term have already been explained in section (3.2) in relation to Eq.(3.3).

Use of this expression Eq.(3.21) is made for dual-phase steel with $\sigma_{u,f}$ = 2000 MPa [82], and $\sigma_{u,m}$ = 415 MPa [86], to depict the variation in the value of $\sigma_{u,c}$ with

(i) the value of $(\frac{r}{\ell})$ ratio as constant and varying V_f,

(ii) the value of V_f as constant and varying $(\frac{r}{l})$ ratio and are shown in Figs. 3.2 and 3.3 respectively.

It is to be noted that in Eq.(3.22) all the parameters are experimentally determinable and therefore an estimate of the tensile strength of dual-phase steels can readily be made.

Suitability of Eq.(3.22) for prediction of tensile strength of plain-carbon hypoeutectoid dual-phase steels will be discussed in Chapter 5 on results and discussion.

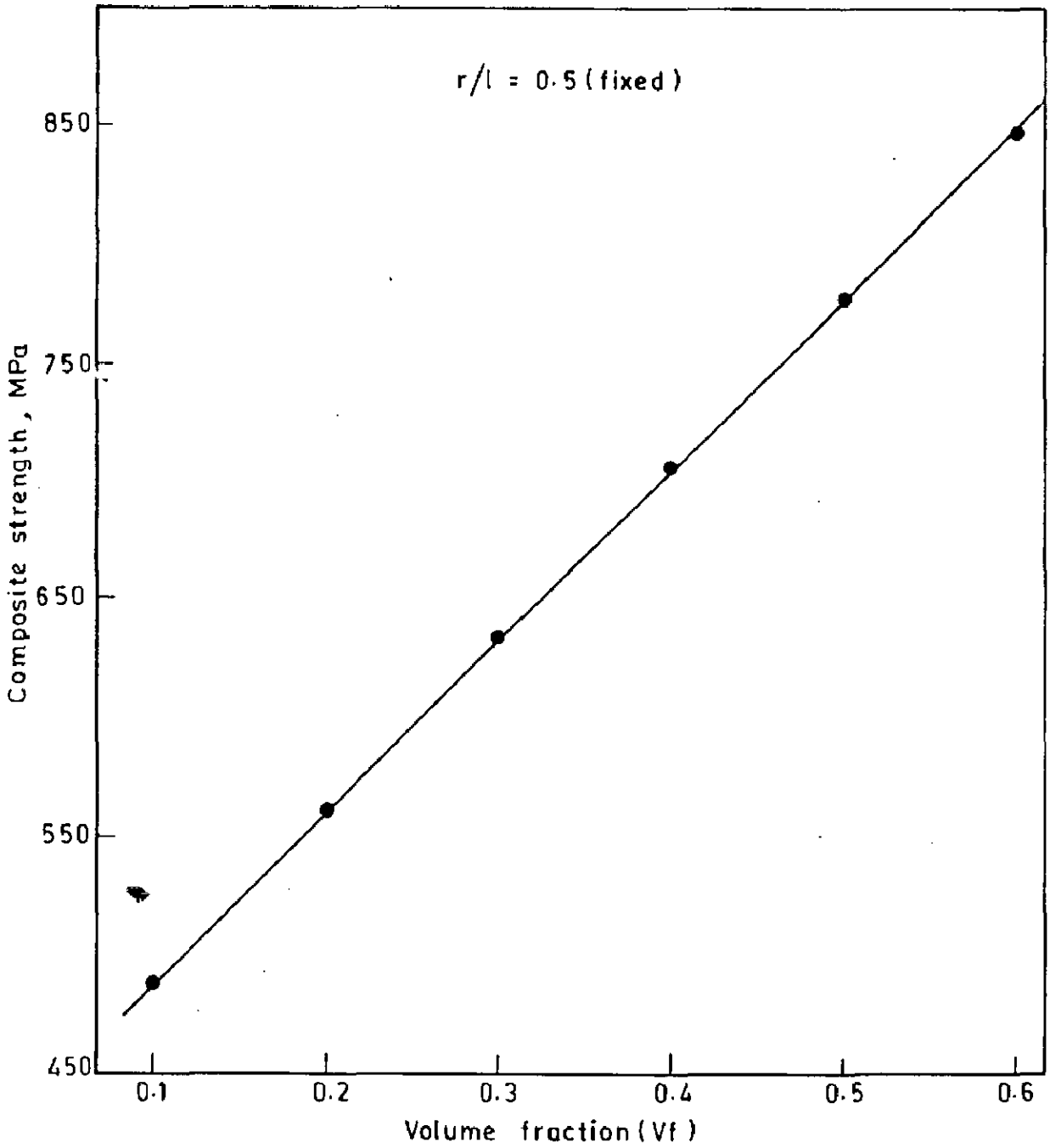

Fig. 3.2 – Variation of theoretical composite strength as a function of volume fraction of second phase according to Eq. (3.21)

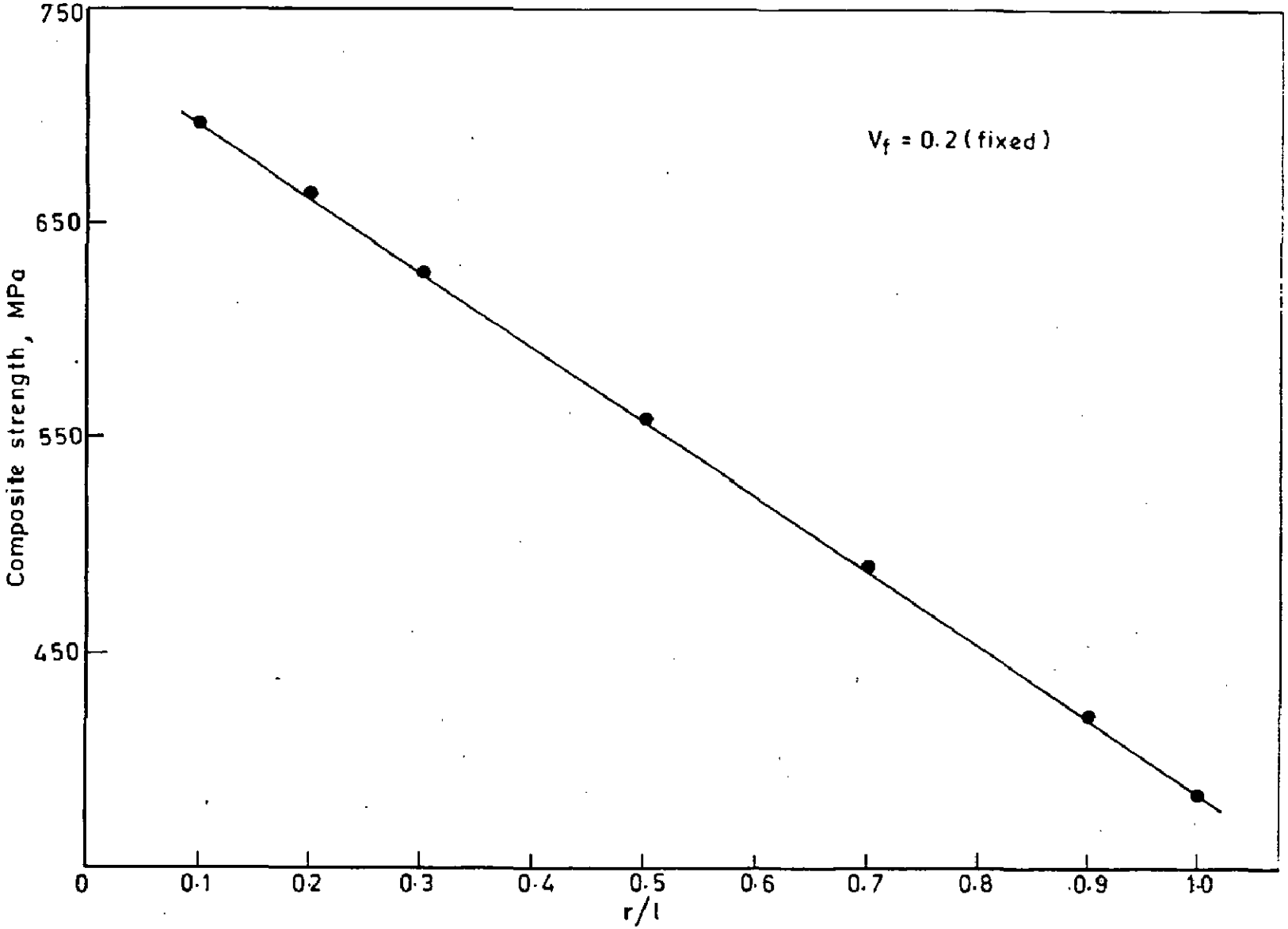

Fig. 3.3 – Variation of theoretical composite strength as a function of r/l according to Eq. (3.21)

CHAPTER - 4

EXPERIMENTAL

The dual-phase structure has been developed by inter-critical annealing at selected temperature and for selected intervals of time followed by water/oil quenching of the heated samples. The quenched samples are then tested for their mechanical properties viz., tensile strength, mean plastic strain ratio ($\bar{R}$-value) and microhardness; and quantitative metallography, SEM fractographic studies and TEM study. DSC technique has also been used on normalised original steel samples for study of non-isothermal kinetics of austenite formation. A brief account of the materials, experimental set-up and methods used is presented below.

4.1 Selection of Steel Samples

Plain carbon hypoeutectoid steel sheets of 1 mm thickness in the composition range of 0.08 to 0.4 wt.pct. carbon have been used for the present investigation, since this wide range allows variation of martensite volume fraction (MVF) in the resulting dual-phase steels with ductile ferrite matrix from a low (~7 pct.) to a sufficiently high (~82 pct.) value.

Three steels containing respectively 0.08, 0.115, and 0.4 wt.pct. carbon have been used and are designated as steel-A, steel-B, and steel-C respectively. Steel-A has been procured from local market but steel-B and steel-C have been respectively obtained from the RMI Steel Strips Ltd., Rishikesh and the TISCO, Jamshedpur. Chemical analyses of these steels is presented in Table 4.1.

4.2 Experimental Set-Up

For production of dual-phase structure by heat-treatment, an experimental set-up shown schematically in Fig.4.1, is locally fabricated. Essentially, it consists of a tubular electric resistance furnace, a device for suspending steel samples in the furnace tube for heat treatment and a quenching device. A vertical tubular electric resistance furnace is locally fabricated using a sintered alumina tube, with both ends open, of internal diameter 6.5 cm and length 67 cm by winding noninductively Kanthal wire of 18 SWG gauge and resistance of ~30 ohm as to yield in the centre of the furnace a uniform temperature zone (UTZ) of approximately 20 cm length. A circular sheet of asbestos, acted as a cover for the top end of alumina tube, and, had three openings-one for passing a chromel-alumel thermocouple, encased in protective refractory sheath , to measure temperature in the UTZ, the second for another chromel-alumel thermocouple also encased in protective refractory sheath, and, placed in

Table 4.1

Chemical Composition of Steels

Steel Designation	C	Mn	Si	S	P
A	0.08	0.45	0.03	0.04	0.04
B	0.115	0.47	0.02	0.035	0.035
C	0.40	0.50	0.031	0.02	0.02

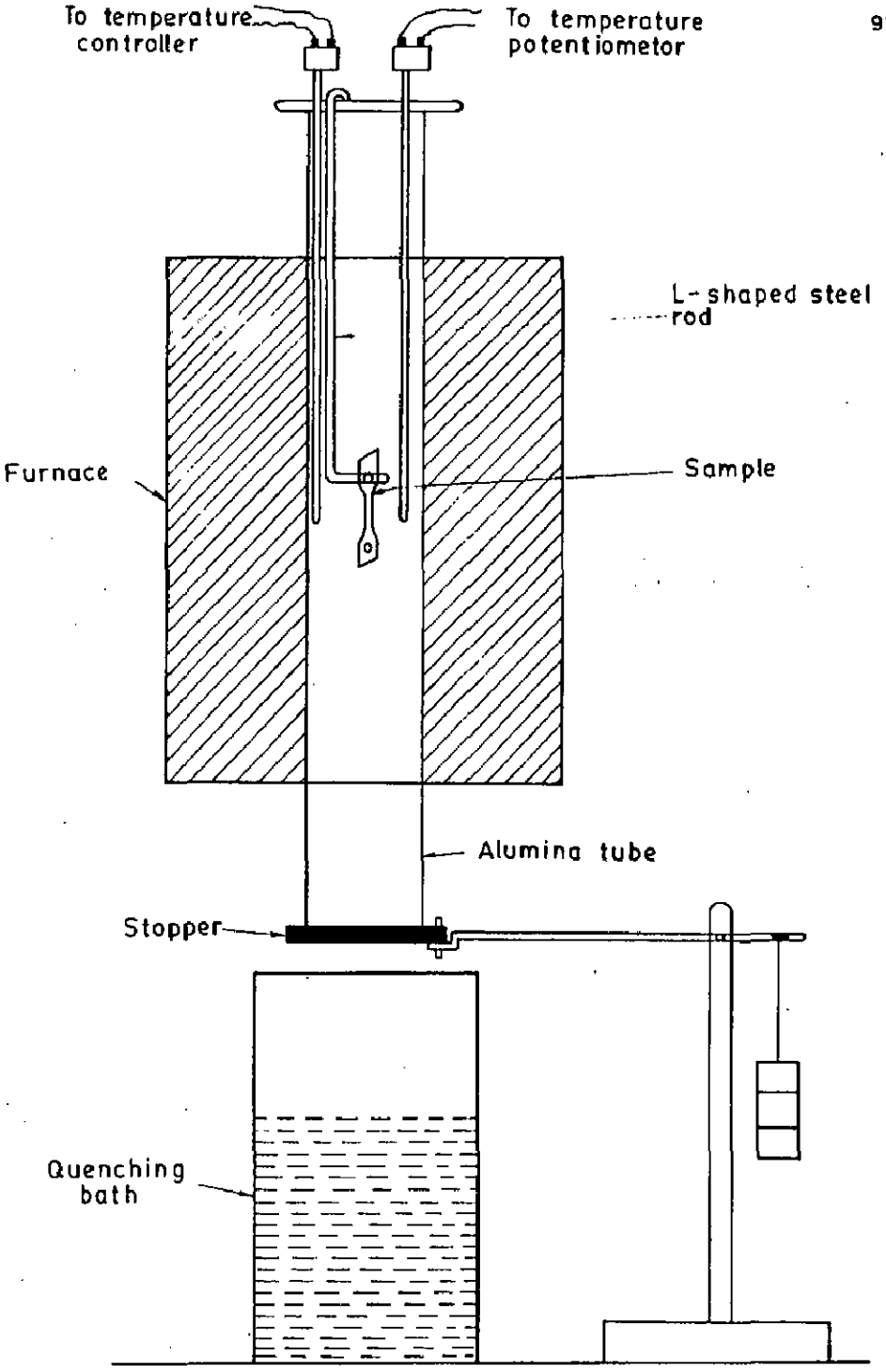

Fig. 4.1 _Schematic diagram of heat treatment set-up

the UTZ, and, connected to a on-off type temperature controller (range up to 1200°C), and, the third for passing a L-shaped steel sample hanger on which steel samples of suitable size and shape are suspended in the UTZ for heat-treatment. The lower end of the tube is covered with another asbestos sheet acting as an stopper and mounted on a counter-balance lever arm device, as shown in Fig.4.1. Immediately below the stopper, is placed a quenching bath-a cylindrical steel tank containing either water or oil as the quenching medium. Quenching is carried out by first removing the asbestos sheet stopper from the lower end of the alumina tube and then allowing the heated specimen to fall directly from L-shaped steel hanger into the quenching bath placed just below the furnace tube.

The furnace is supplied with single phase 220 volt a.c. power through an automatic solid state a.c. Servo-Voltage Stabiliser (NELCO make, 7.5 KVA, 175-266 V range, maximum current 30 amp.), a variable resistance (ESCORP make, Variac-240V, 28 amp. maximum load) and an automatic on-off type relay-operated temperature controller with indicator (APLAB make-Applied Electronics, Thana, India, range upto 1200°C), all mounted on a control panel with suitable indicator lights and electrical fuses and switches to enable precise temperature control upto ±2°C in the UTZ of the furnace. For temperature measurement, a Leeds-Northup type 8694 potentiometer, has been used.

For metallographic examination, steel samples are first prepared using cold mounting in plastic granules employing a CSICO, Agra, make mounting machine. These mounted samples are next manually polished in the usual manner and then finally sylvet-cloth polished on a MPE, Bombay, make polishing machine. A MeF_3 Model Reichert-Jung optical microscope is used for both qualitative and quantitative metallography - the latter using point counting technique, and also for the preparation of photomicrographs of typical structures.

For tensile testing and measurement of mean plastic strain ratio, the $\bar{R}$-value, Monsanto type W tensometer has been used.

For SEM fractographic studies, a Philips 501 Scanning Electron Microscope with a maximum rated resolution of 70A° has been used.

For TEM thin film study Philips EM400 Transmission Electron Microscope with a maximum rated resolution of 10A°, has been used.

For DSC studies, Stanton-Redcroft DSC 1500 model has been used.

4.3 Techniques Used for Study

4.3.1 Sample preparation

All the three types of steel sheets have been cut into sample of desired shape and size, as shown in Fig.4.2, using a standard die, also locally fabricated. As will be clear from the figure, the 'cut-sample' is typically a tensile specimen as per ASTM standard, with an extended end of 7 mm length beyond gripping length, which is cut from each heat-treated sample for metallographic testing , TEM-studies and also for the microhardness measurements.

4.3.2 Selection of heat-treatment variables

In the present investigation two parameters viz., intercritical annealing temperature and time have been varied for obtaining different MVF in the dual-phase steels. A close examination of the available published literature on preparation of dual-phase steels [52,53,67] reveals that, in general, the intercritical annealing time used has been either 10 minutes or 15 minutes at any one intercritical annealing temperature. However, this does not yield appreciable difference in MVF of dual-phase steels. Therefore, for the present investigation, three intercritical temperatures 740°C, 760°C, and 780°C; and intercritical annealing times right from 1 minute to 3 hours have been chosen. No attempt is

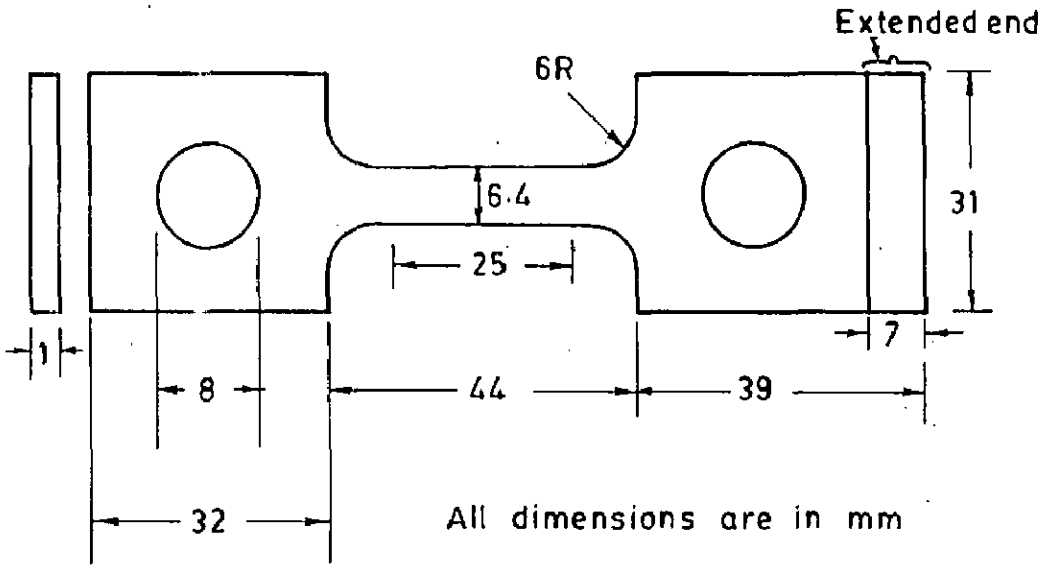

Fig. 4. 2 _ Tensile sample with extended end for metallographic sample

made here to optimise the process parameters as the objective of the study is to procure dual-phase steels with varying microstructure, so that sufficient data could be generated for determining their quantitative effects on the mechanical properties.

4.3.3 Heat-treatment procedure

For obtaining dual-phase structures, all the steel samples die-cut into the desired shape and size from the as received plain-carbon steel sheets are first normalised. For this purpose, samples cut from steel-A and steel-B sheets are normalised from 920°C whereas those cut from steel-C sheets are normalised from 860°C, with 5 minutes of soaking time in each case. For each intercritical annealing (ICA) heat-treatment, three samples normalised as above are suspended from L-shaped steel hanger in the UTZ of the furnace and the top end of alumina tube of the furnace is covered with the asbestos sheet as shown in Fig.4.1 in order to prevent heat loss. The temperature of the furnace drops during charging of the sample inside the furnace. Therefore, the start of intercritical annealing (ICA) time is considered from the moment the furnace temperature regains the original desired ICA temperature. After the lapse of specified soaking time for each heat-treatment, the asbestos stopper at the bottom end of the alumina tube of the furnace is removed

and the samples are made to fall directly from the L-shaped steel rod hanger into the quenching water/oil bath, placed just below the furnace tube. During the heat treatment, the temperature of the samples are continuously monitored with the chromel/alumel thermocouple.

Following the same procedure, all steel samples are heat-treated at the three specified intercritical temperatures viz. 740°C, 760°C and 780°C for specified annealing times viz., 1 min, 2 min, 5 min, 10 min, 15 min, 30 min, 1 hr, 2 hr . and 3 hr . In case of samples of steel-C containing 0.4 wt.pct. carbon, the quenching is done in oil instead of water-quenching to prevent cracking during quenching. Further an additional soaking time of 30 seconds is used for heat-treatment of this steel.

The dual-phase steel products obtained from samples of steel-A, steel-B and steel-C will henceforth be designated as dual-phase steel-A (DPS-A), dual-phase steel-B (DPS-B) and dual-phase steel-C (DPS-C) respectively for all future references.

4.3.4 Metallographic studies

Metallographic samples are cut from the heat-treated 'cut-samples' i.e., from the extended end beyond gripping length of the tensile samples as shown in Fig.4.2. These

samples are cold mounted using plastic granules. The mounted specimens are prepared for metallographic examination using standard metallographic procedure. The cloth polishing is carried out on a sylvet-cloth using 0.1 μm size alumina powder-suspension. After polishing, all the samples are etched with 2% Nital, washed, dried and finally examined under 'MeF_3 Reichert', optical microscope. Typical microstructural features of all the samples are photographed. These optical micrographs have been presented and discussed in Chapter-5. Optical micrographs of normalised samples of steel-A, steel-B and steel-C have also been prepared and presented in Chapter-5.

Quantitative measurements of the microstructural features are carried out to determine the volume fraction and size of martensite islands in the dual-phase steel samples. Volume fraction of martensite phase (MVF) is measured by point-counting technique. A grid containing 36 points is inserted into the eye-piece of the microscope. The magnification of the microscope is so adjusted that maximum resolution could be obtained and at the same time, the condition of having not more than one grid-point in one particle is satisfied. The number of grid point falling on martensite phase are counted at random locations. For each sample, 20 such observations have been taken. The volume fraction of martensite, V_p, is then calculated from the relationship,

$$V_P = \frac{\sum_{i=1}^{20} N_i}{20 \times 36} \qquad \ldots (4.1)$$

where, N_i is the number of grid-points falling in martensite islands in any particular observation.

The size of martensite particles is measured with a microscale inserted into the eye-piece of the microscope. The microscale is first calibrated with a given standard at the magnification of study. One division of the microscale measured is 5.4 μm of the object at a magnification of 200. One hundred martensite particles have been randomly measured on each sample and the average size ($\bar{D}_i$) and standard deviation are calculated using standard statistical procedure [87]. Results of the quantitative measurements are presented and discussed in Chapter-5.

4.3.5 Measurement of mechanical properties

Tensile-and mean plastic strain ratio ($\bar{R}$-value) tests and micro-hardness tests have been carried out for the determination of mechanical properties. After the intercritical heat-treatment, the different specimens are cleaned to remove any scale or oxide layer from the surface using an emery paper. Tensile tests are performed on a motorised monsanto type W tensometer using a cross-head speed of 1 mm/min. The dimensions of the test specimens have already been shown

in Fig. 4.2. Three specimens have been tested to find the average value which is then entered as one observation. Specimens of DPS-A and DPS-B are tested on a load-scale of 0-500 kg. with matching beam whereas specimens of DPS-C are tested on 0-1000 kg. load-scale with matching beam. Values of yield strength i.e., 0.2 per cent proof stress (YS), UTS, per cent uniform elongation and per cent total elongation are determined from these tests. Strength values are reported in MPa unit. During the tensile tests, the load-extension curves are also recorded on an automatic recording unit attached to the tensometer. The results of the tensile tests have been presented and discussed in Chapter-5.

Mean plastic stain ratio or $\bar{R}$-values have been determined on specimens of DPS-A and DPS-B. Specimens of DPS-C are not tested for $\bar{R}$-values, due to its low ductility. For determining $\bar{R}$-value, the specimens are stamped from the steel sheets in three directions-one along the direction of rolling, second perpendicular to the direction of rolling and the third in a direction 45° to the direction of rolling. Before the start of the tensile test, width of the test specimen within the region of gauge length is measured at five places and the average value of width constitutes one observation. Gauge-length of 25 mm have been chosen as per ASTM standard. During the tensile test as soon as the yield

point region, in the load-extension curve, is crossed to reach a total elongation of about 8 per cent, the test is interrupted and width of the gauge-langth region is measured at five places apart from measuring gauge-length of the elongated specimen. Using the expressions given in Section 2.5.4, R-values are calculated.

The tensile test is then carried further till the specimen fractures. The other specimens cut either perpendicular to the rolling direction or at 45° to the rolling direction are also tested similarly and mean plastic strain or $\bar{R}$-value is calculated using Eq.(2.65) given in Section 2.5.4. Similar tensile tests and $\bar{R}$-value measurements have also been made on normalised specimens of steel-A, steel-B and steel-C and the results obtained have been used for discussion in Chapter-5.

Micro-hardness measurements have also been made on selected DPS specimens using Tukon Micro-hardness tester under 10 gm. load. The results are presented and discussed in Chapter-5.

4.3.6 Scanning electron microscopy: fractographic studies

In order to gain an insight into the fracture behaviour, specimens fractured in the tensile tests are examined under

Philips 501 Scanning Electron Microscope (SEM), with a maximum rated resolution of 70A°. For this purpose, a small sample from the fractured specimen is carefully cut to avoid any damage to the fractured surface. The surface opposite to the fractured surface to be examined is made flat by wheel-grinding. The sample is then glued carefully in the specimen holder of the SEM by silver paste. The fractured surface is scanned thoroughly and the feature of interest is photographed. The results of the fractographic studies have been presented and discussed in Chapter-5.

4.3.7 Transmission electron microscopy : thin film studies

In order to examine dislocation substructure in the ferrite matrix resulting from the austenite to martensite transformation in the adjoining regions, thin films of dual-phase steels are prepared following Window technique [88]. A mixture of glacial acetic acid and perchloric acid is prepared by carefully mixing nine volumes of glacial acetic acid with one volume of perchloric acid. This solution is kept in a ice-bath. A small metallographic sample is polished on the emery-belt polisher till it becomes very thin. With the help of transparent tape, a window is made on the thin specimen by covering all the four edges. It is now dipped in the solution mixture as anode and a stainless steel cathode is used. Current density of approx. 0.1 amp/cm^2 is passed under a potential difference of $\sim$10 V. The specimen is conti-

nuously shaken in the solution. The moment a perforation appears in the specimen, current is switched-off and the thin film so-formed is removed from the anode holder and dipped in alcohol to prevent any oxidation and damage to it and then a small portion from the perforated region is cut and put over a copper-grid. The loaded-grid is then placed in TEM holder and examined under the Philips EM 400 Transmission Electron Microscope with a maximum rated resolution of 10A°. The thin film is scanned thoroughly and any features of interest are photographed. Results of the TEM studies have been presented and discussed in Chapter-5.

4.3.8 Non-isothermal austenitisation kinetic study by differential scanning calorimetric (DSC) technique

Non-isothermal kinetics of austenitisation in plain-carbon steel have been investigated by DSC. 15 mg of powder sample, obtained from the metallographic sample by filling with a clean Jeweller's file, has been put into the platinum crucible of DSC. The sample is heated in the static air for different heating rates and differential energy vs temperature curves have simultaneously been recorded by a x-y recorder. The heating is continued till the peak in differential energy plot appears indicating the maximum transformation rate. This experiment is conducted for three different heating rates to determine peak temperatures corresponding to each

DSC curve. Then using Eq.(2.27) presented in Section 2.2.4, value of activation energy, E, is calculated. In order to calculate the order of reaction, n, the same DSC response curves are used. Here, the area under the curve at different temperature is measured with the help of a planimeter. Then these areas are divided by total area under the curve to calculate the volume transformed at any temperature. Then using Eq.(2.30) given in Section 2.2.4, value of n is calculated. The results of this study are presented and discussed in Chapter-6.

Chapter - 5

RESULTS AND DISCUSSION : MICROSTRUCTURE AND MECHANICAL PROPERTIES

5.1 Introduction

In this chapter evolution of dual-phase (ferrite and martensite) structure during isothermal intercritical annealing followed by rapid cooling of three plain-carbon steels are presented. An attempt has been made to identify the micro-structures on the basis of various stages of austenite formation during isothermal intercritical annealing. Mechanical properties like YS (0.2 pct. off-set proof stress), UTS, ductility (pct. uniform - and total - elongations) and formability (mean plastic-strain ratio, $\bar{R}$-value) of dual - phase steels have been presented and discussed. Tensile strength of these steels have also been interpreted in the light of theoretical model developed in Chapter-3. Structure - property correlation of dual - phase steels is also presented. In order to gain an insight into the observed mechanical behaviour, the Scanning Electron Microscopy (SEM) of tensile fractured surfaces and Transmission Electron Microscopy (TEM) of thin film obtained from dual - phase steel , have been carried out and the results are presented and discussed.

5.2 Evolution of Microstructure

Variation of austenite volume fraction (AVF) i.e., martensite volume fraction (MVF) on quenching with intercritical annealing (ICA) time at intercritical annealing (ICA) temperatures viz. 740°C, 760°C and 780°C for steel - A, steel - B and steel - C, has been shown in Figs. 5.1 - 5.3 respectively. The microstructural evidence of increase of MVF with ICA time at ICA - temperature 740°C for steel - A is shown in the optical micrographs of Figs. 5.4 b to d. Fig. 5.4 a shows the initial normalised structure of steel - A. In all these micrographs ferrite phase appears bright and pearlite and martensite appear dark. However, pearlite can be distinguised from martensite as pearlite etches darker [20] than martensite. Fig. 5.4 b shows the presence of pearlite along with martensite in the matrix of ferrite. This indicates that the process of austenitisation starts by the dissolution of pearlite and simultaneous growth of austenite phase which on quenching transforms to martensite. This structure is obtained for one minute of ICA - time and contains about 7.4 pct. MVF, without any noticeable reduction in the proeutectoid ferrite phase. This is consistent with Speich's observations [16] that the first stage of the intercritical austenitisation is the dissolution of pearlite and simultaneous growth of austenite. The preferential formation of austenite nuclei at pearlite colony boundaries has been observed before by Speich etal. [16]. Austenite phase has also been found to

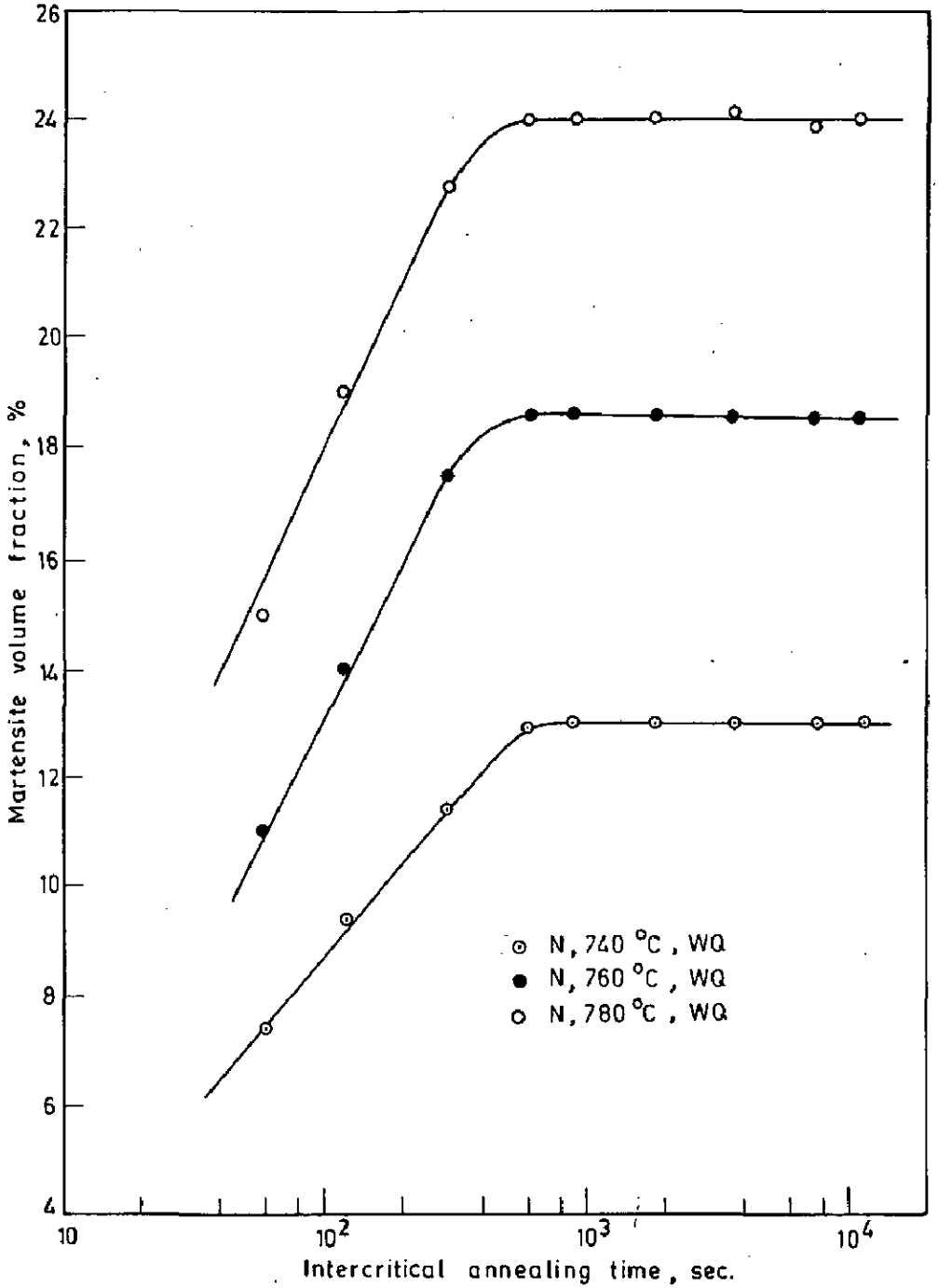

Fig. 5.1 – Variation of percent martensite volume fraction vs intercritical annealing time for 0.08 percent carbon dual-phase steel

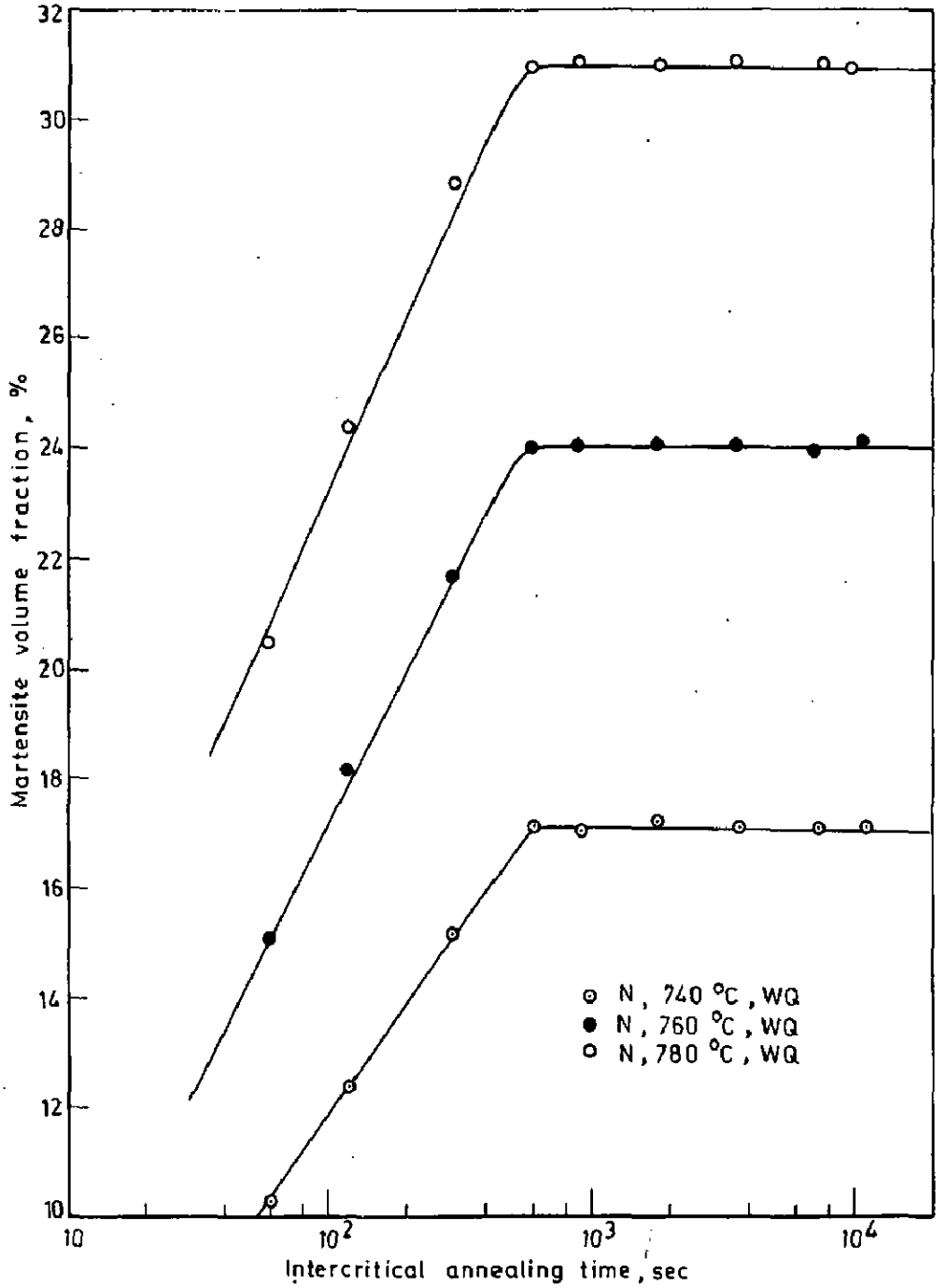

Fig. 5.2 – Variation of percent martensite volume fraction vs intercritical annealing time for 0.115 percent carbon dual-phase steel

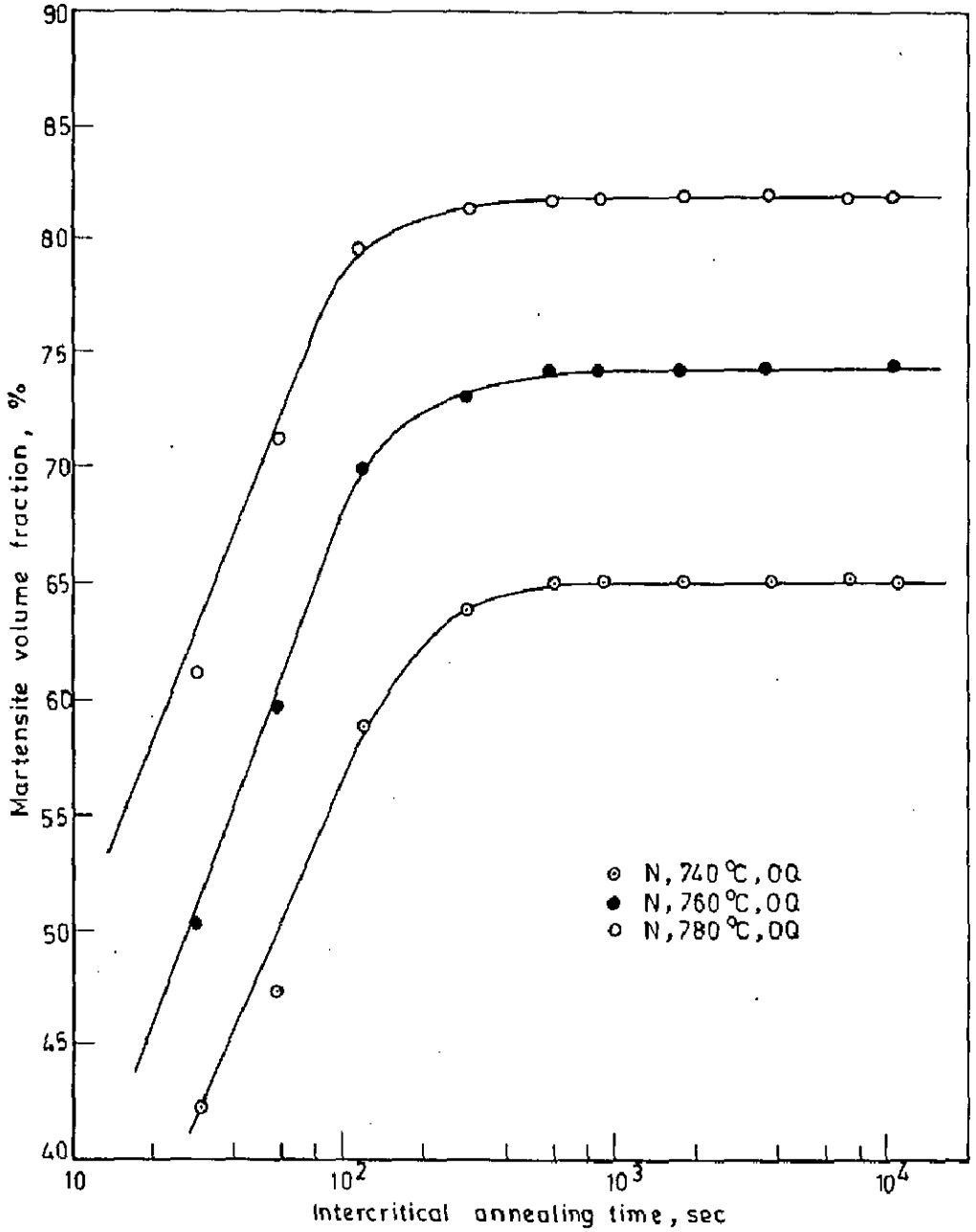

Fig. 5.3 – Variation of percent martensite volume fraction vs intercritical annealing time for 0·4 percent carbon dual-phase steel

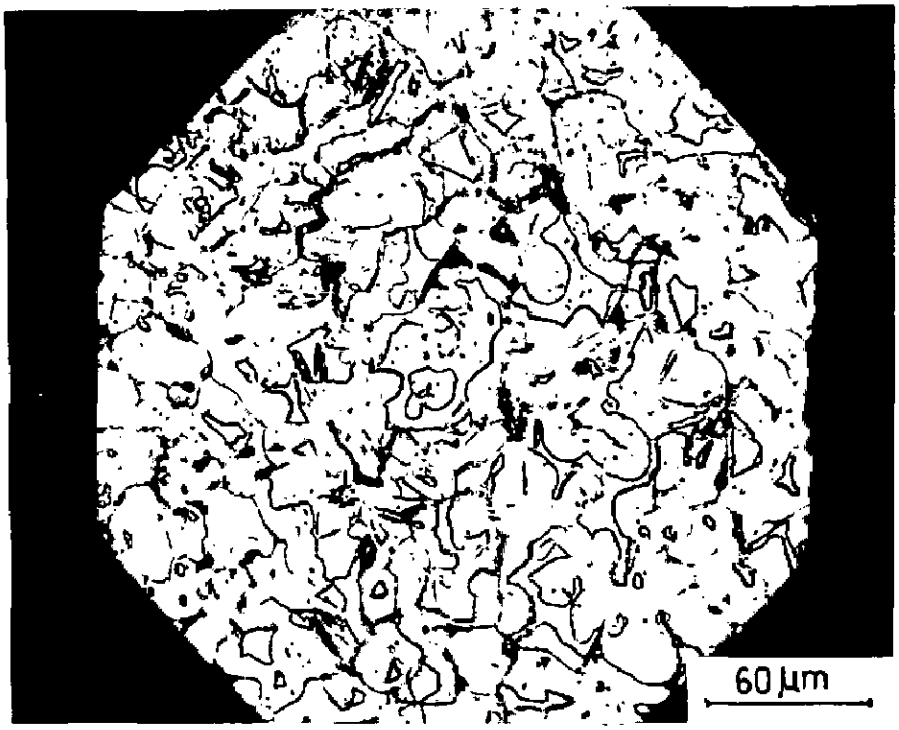

Fig. 5.4 a _Microstructure of normalised steel - A

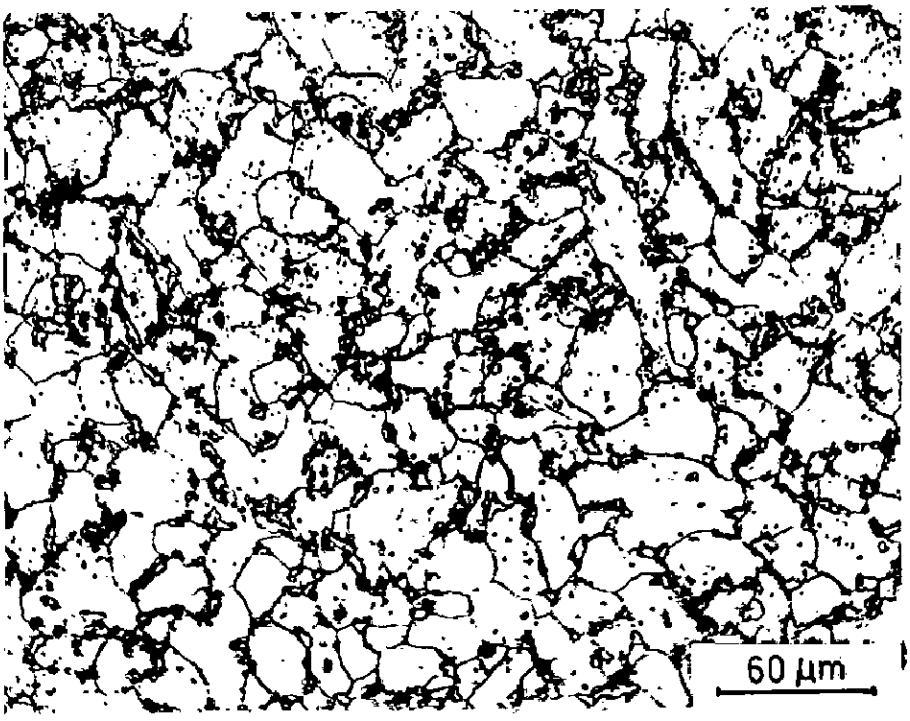

Fig. 5.4 b _Microstructure of dual-phase steel - A
(740 °C , 1 min , WQ)

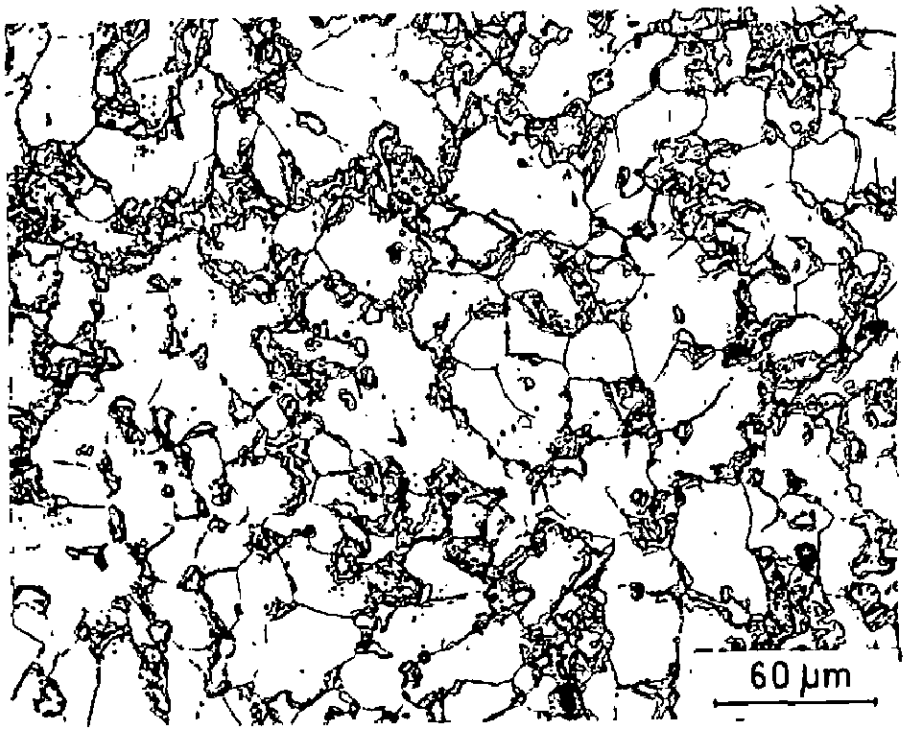

Fig. 5.4 c _ Microstructure of dual-phase steel - A
(740 °C , 5 min , WQ)

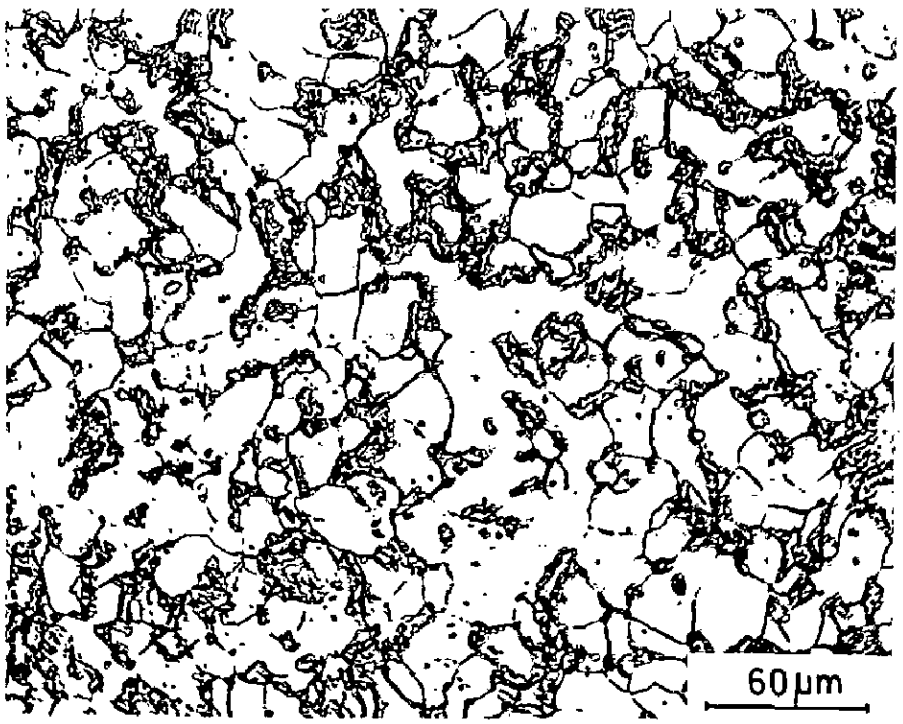

Fig. 5.4 d _ Microstructure of dual-phase steel - A
(740 °C , 10 min , WQ)

occur at the particles of cementite at the ferrite boundaries as shown in the microstructue of Fig. 5.4 b. The reason for this type of nucleation of austenite is the spheroidisation of pearlite [16,17,18]. The second stage of intercritical austenitisation has been noted after about 5 minutes of intercritical annealing when the austenite begins to grow into the proeutectoid ferrite phase as shown in Fig. 5.4 c . At this stage MVF has been found to be 11.4 pct. which is more than the volume fraction of pearlite (10 pct.) persent in the initial normalised structure of steel-A as shown in Fig. 5.4 a. At 10 minutes of intercritical annealing, MVF becomes 13 pct. as shown in Fig. 5.4 d and it remains so up to three hours, the longest annealing times used in the present work. It is the characteristic of third stage of intercritical austenitisation [16,17,20]. The microstructures of steel-A obtained at 760°C and 780° for the corresponding period of annealing time show similar trend except the higer MVF observed. The maximum MVF at 760° is 18.5 pct. and at 780°C, it is 24 pct. as shown in the optical micrographs of Figs. 5.5 a and b.

Similarly, microstructures of steel-B taken at 740°C, 760°C and 780°C for the period of annealing time corresponding to steel-A show resemblence in austenite nucleation sites and morphology as that of steel-A. However, higher maximum MVFs are obtained. For example, 17 pct., 24 pct. and 31 pct. maximum MVFs have been observed at 740°C, 760°C and 780°C ICA- temperatures respectively as shown in the microstructures of Figs. 5.6 b, c and d respectively. Fig. 5.6 a shows the normalised structure

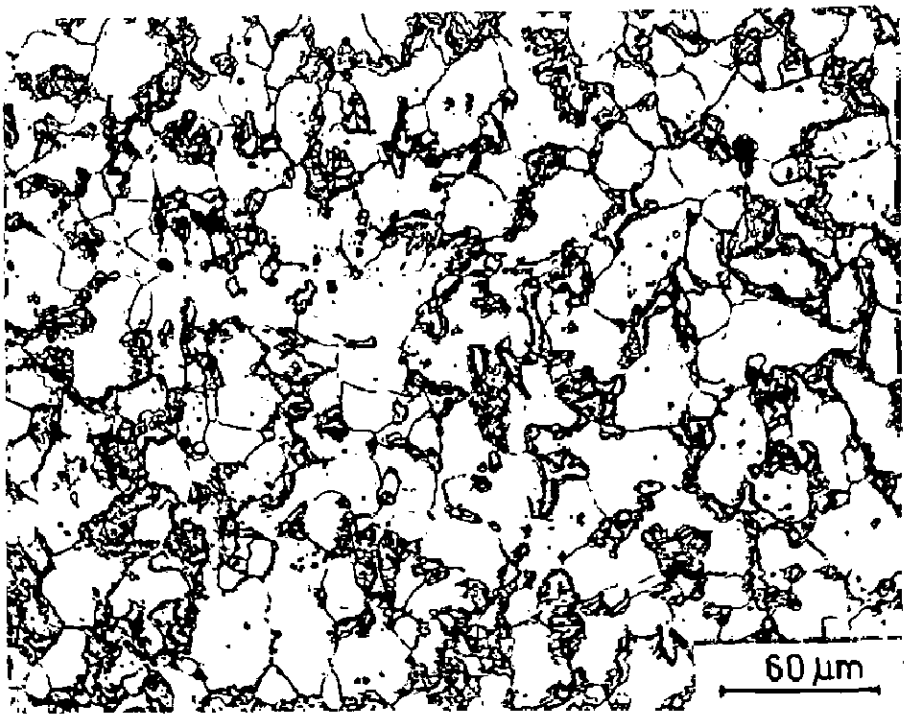

Fig. 5.5 a _ Microstructure of dual-phase steel – A
(760°C , 10 min , WQ)

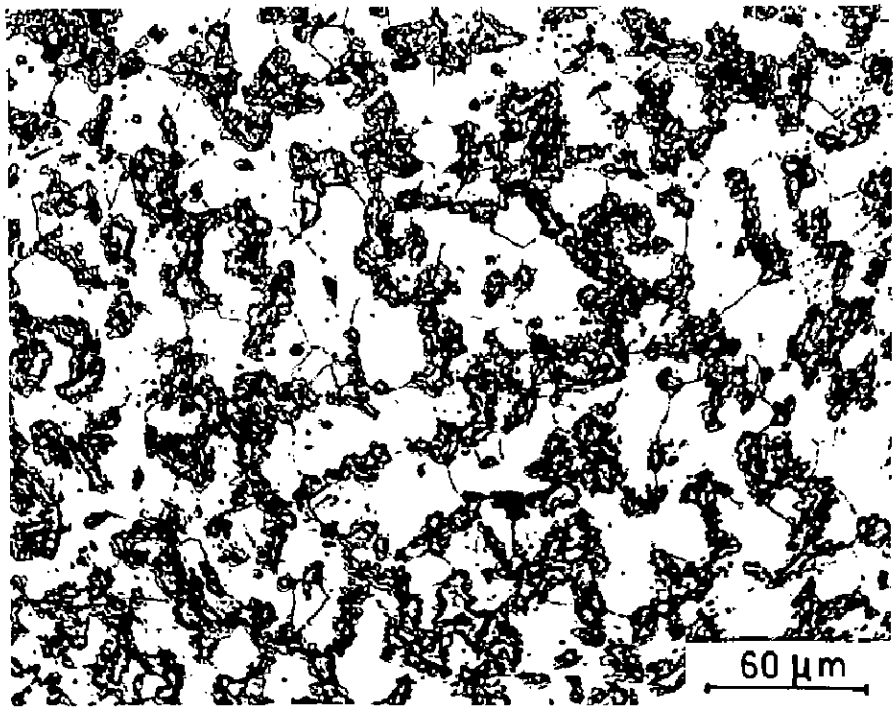

Fig. 5.5 b _ Microstructure of dual-phase steel - A
(780°C , 10 min , WQ)

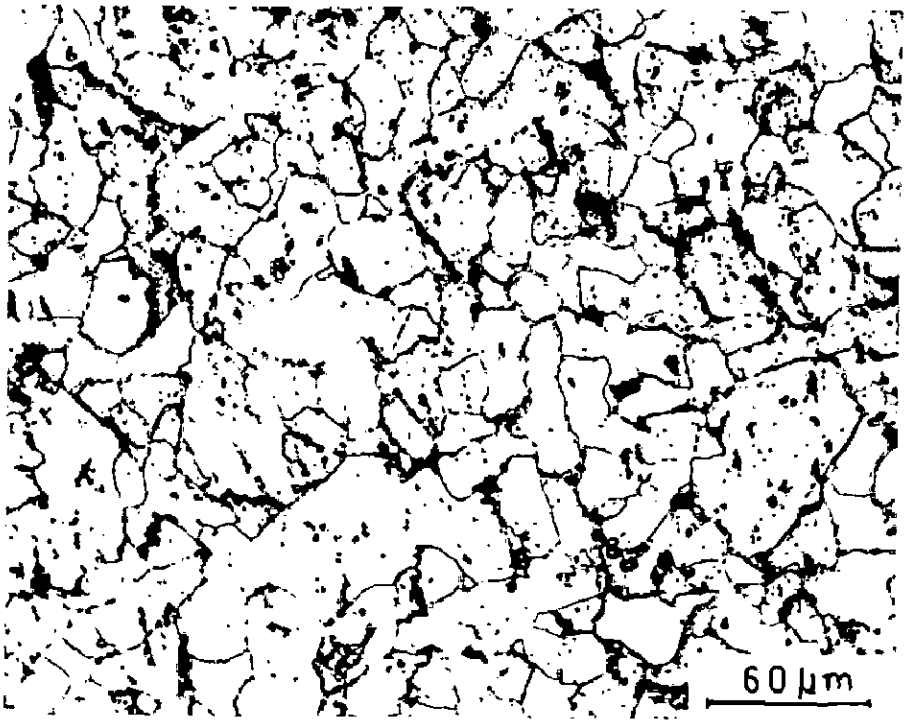

Fig. 5.6 a _ Microstructure of normalised steel - B

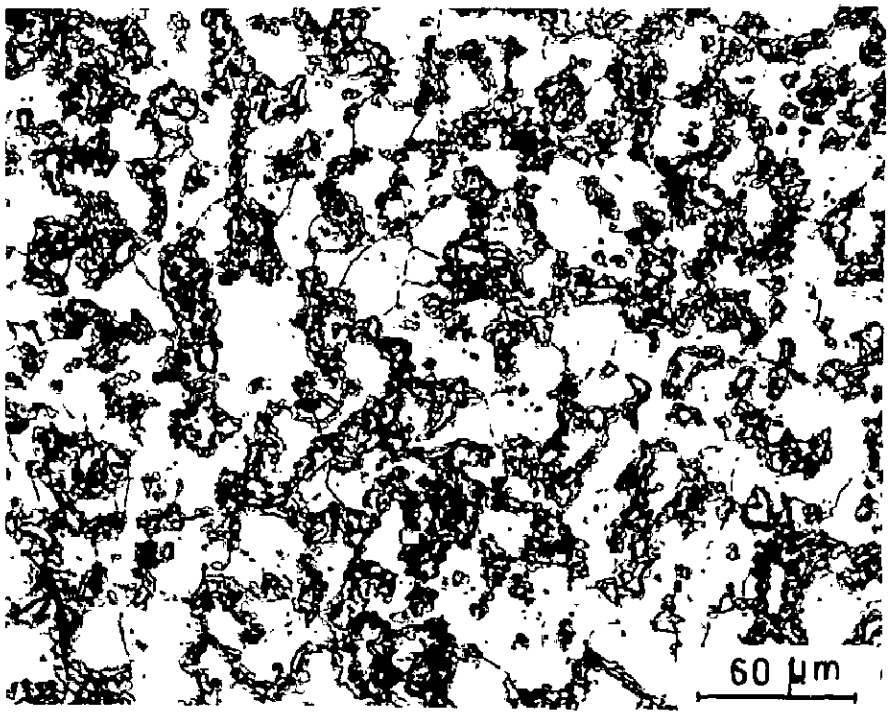

Fig. 5.6 b_ Microstructure of dual-phase steel - B
(740 °C , 10 min , WQ)

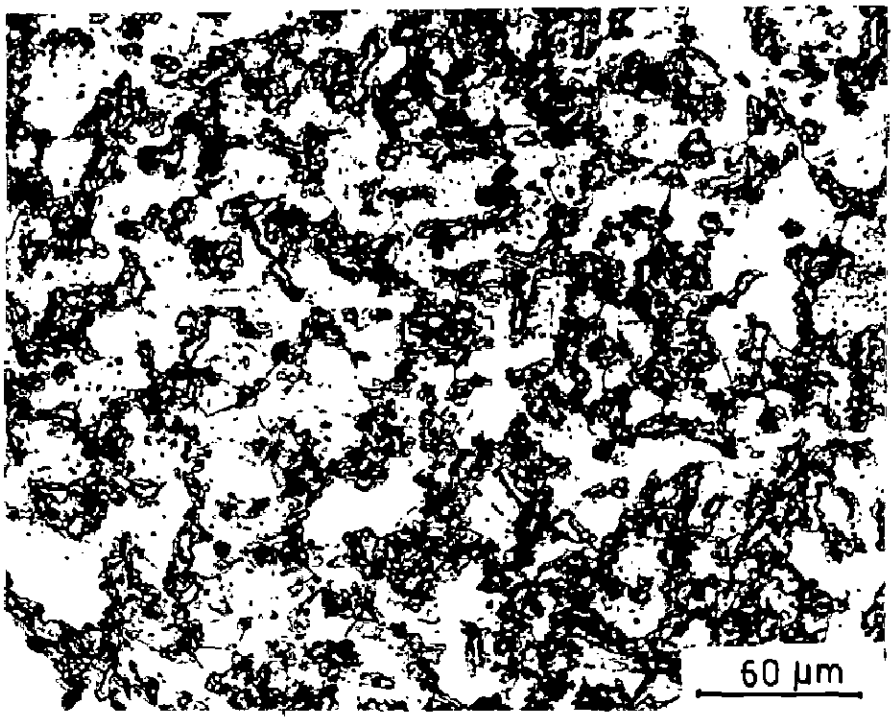

Fig. 5.6c _Microstructure of dual-phase steel - B
(760 °C, 10min, WQ)

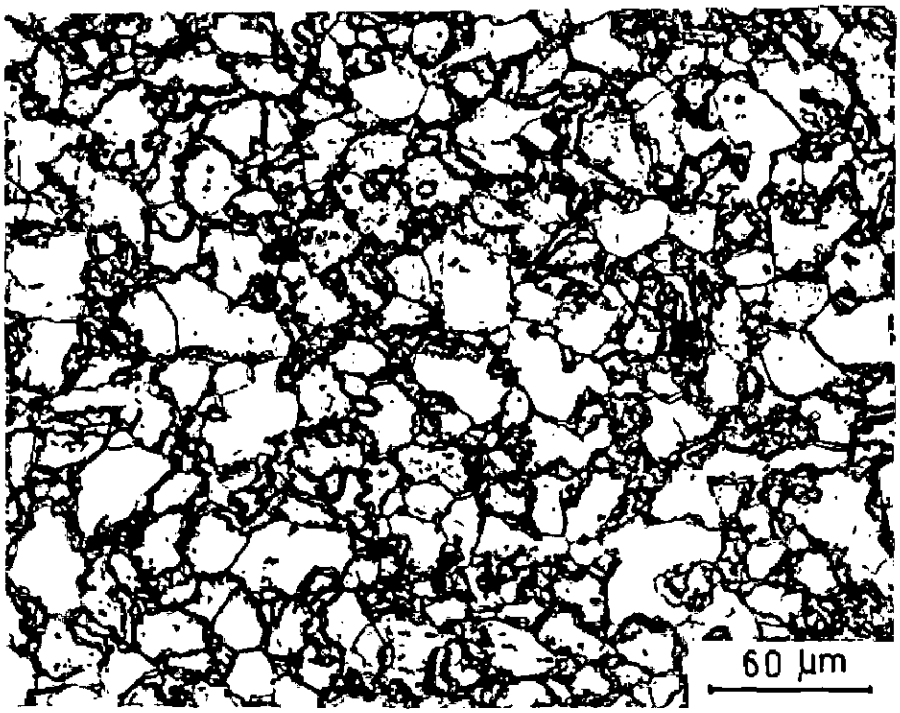

Fig. 5.6d _Microstructure of dual-phase steel - B
(780 °C, 10min, WQ)

of steel - B. Microstructures of steel - C taken at 740°C, 760°C and 780°C for the period of time corresponding to steel A and steel - B, show resemblence in the evolution of microstructure with the passage of intercritical annealing time. However, due to higher carbon content of steel - C (0.4%C) as compared to steel - A (0.08%C) and steel - B (0.115%C), much higher MVFs have been observed. Maximum MVFs observed at 740°C, 760°C and 780°C are 65 pct., 74.5 pct. and 82 pct respectively as shown in the microstructures of Figs. 5.7b, c and d. Fig. 5.7a shows the initial normalised structures of steel - C. Microstructures of DPS - C show finer morphology as compared to those of DPS - A and DPS - B. This is due to the starting finer grain structure of steel - C as compared to grain size of steel - A and steel - B. Martensite islands are much more inter-connected in DPS - C as compared to DPS - A and DPS - B. This is due to much higher MVF present in DPS - C as compared to those of steel - A and steel - B. For example DPS - C shows maximum MVF 65 pct at ICA - temperature of 740°C whereas DPS - A and DPS - B show 13 pct. and 17 pct. maximum MVF respectively for the corresponding temperature. The increase in MVF with increase in intercritical annealing temperatures i.e., 740°C to 760°C and to 780°C, is attributed to the formation of higher austenite volume fraction which can be shown applying lever rule in the intercritical region of Fe - C phase diagram.

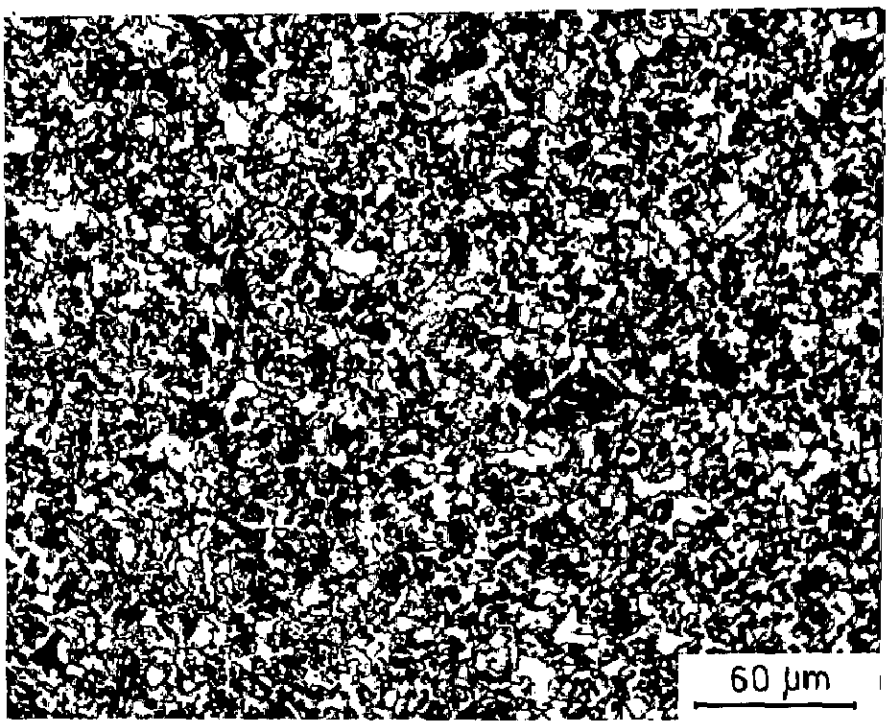

Fig. 5.7 a _ Microstructure of normalised steel - C

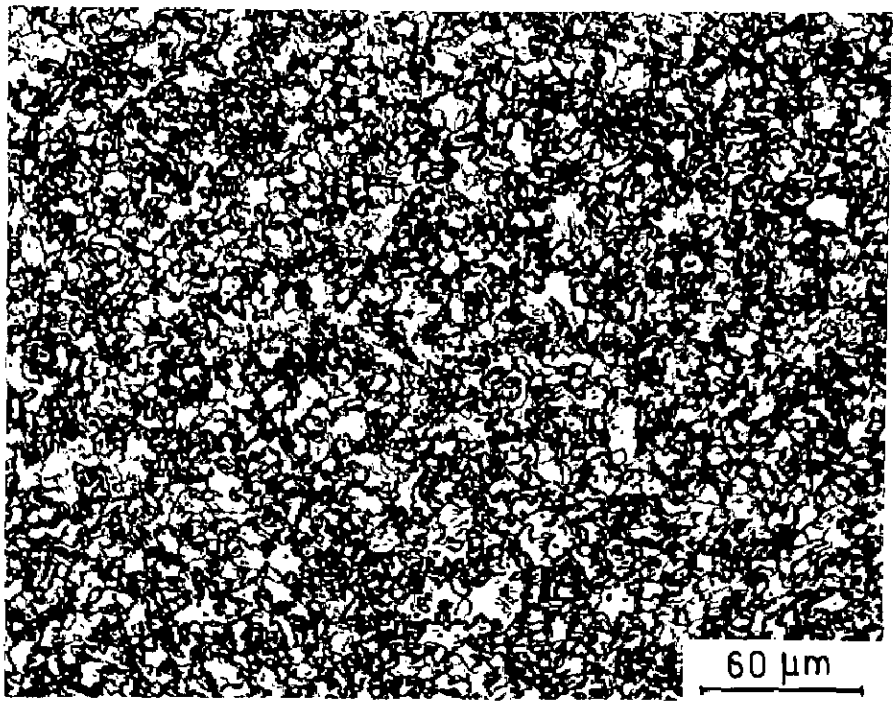

Fig. 5.7 b _ Microstructure of dual-phase steel - C
(740 °C , 10min, OQ)

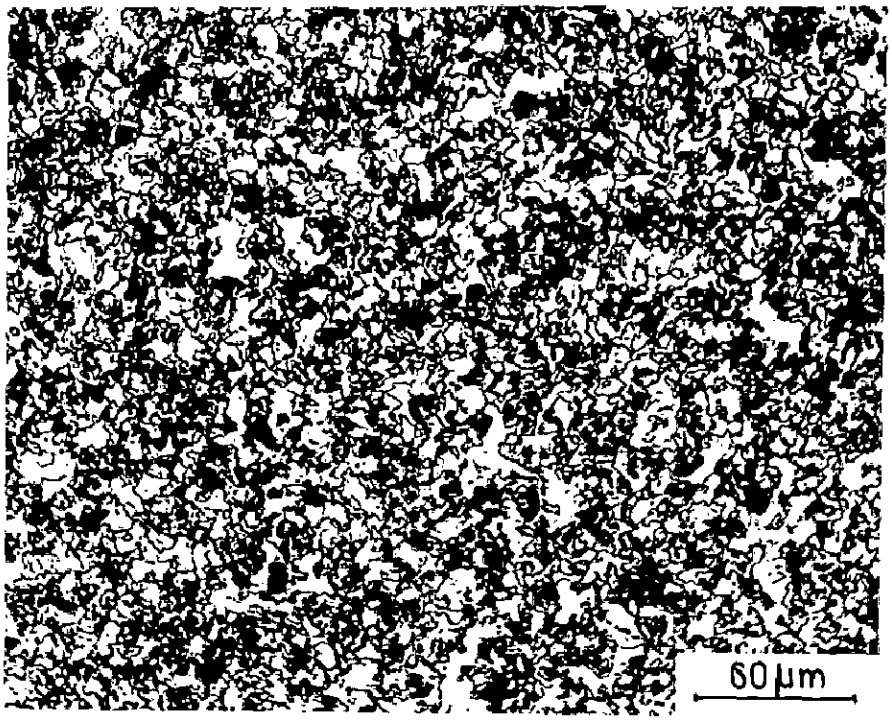

Fig. 5.7 c _ Microstructure of dual - phase steel - C
(760 °C , 10 min, OQ)

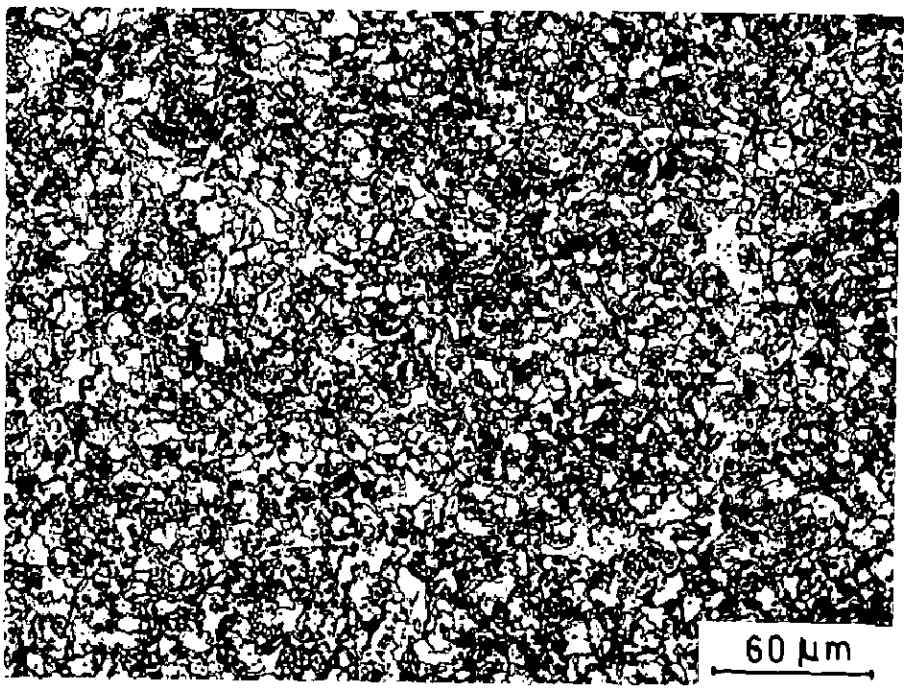

Fig. 5.7 d _ Microstructure of dual - phase steel - C
(780°C, 10 min, OQ)

It has been further noted that during third stage of intercritical austenitisation for longer holding time, although MVF remains constant but ferrite grain growth has been observed. This is shown in the microstructure of Fig.5.8a for DPS-A. Microstructure of DPS-A is also shown in dark-field mode to clearly show martensite islands (white areas) in the ferrite matrix in Fig.5.8b. TEM micrograph of DPS-A is shown in Fig.5.8c.

5.3 Results: Mechanical Properties

5.3.1 Strength of dual-phase steels

Experimental values of different parameters and calculated values of mechanical properties of different dual-phase steels studied and corresponding original steel sample in normalised condition are presented in Tables 5.1 - 5.3.

Typical tensile load - elongation curves of dual-phase steels - DPS-A, DPS-B and DPS-C specimens with different intercritical annealing (ICA) treatments have respectively been presented in Figs. 5.9 - 5.11.

Values of flow stress i.e., yield strength (YS), measured as 0.2 pct. off-set proof stress and ultimate tensile strength (UTS) have been obtained for the normalised original steel sample and the different DPS specimens prepared in the present work from such plots and are plotted against intercritical annealing time at three temperatures of ICA treatment, viz. 740°C, 760°C and 780°C respectively for all such specimens in Figs. 5.12 - 5.14.

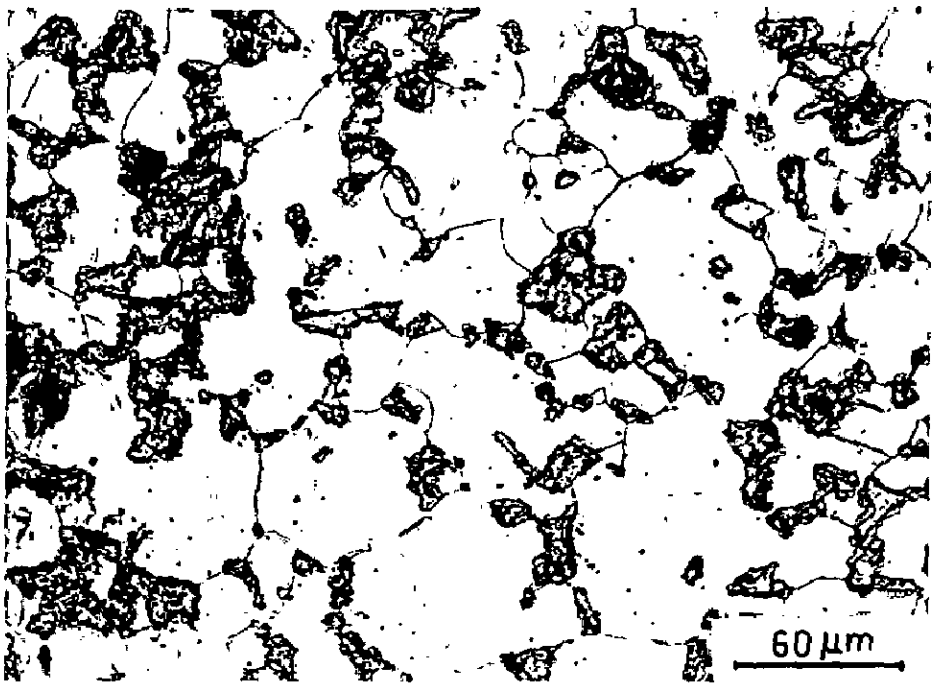

Fig. 5.8 a _ Microstructure of dual-phase steel-A showing grain growth in ferrite phase (740 °C, 1.5hr, WQ)

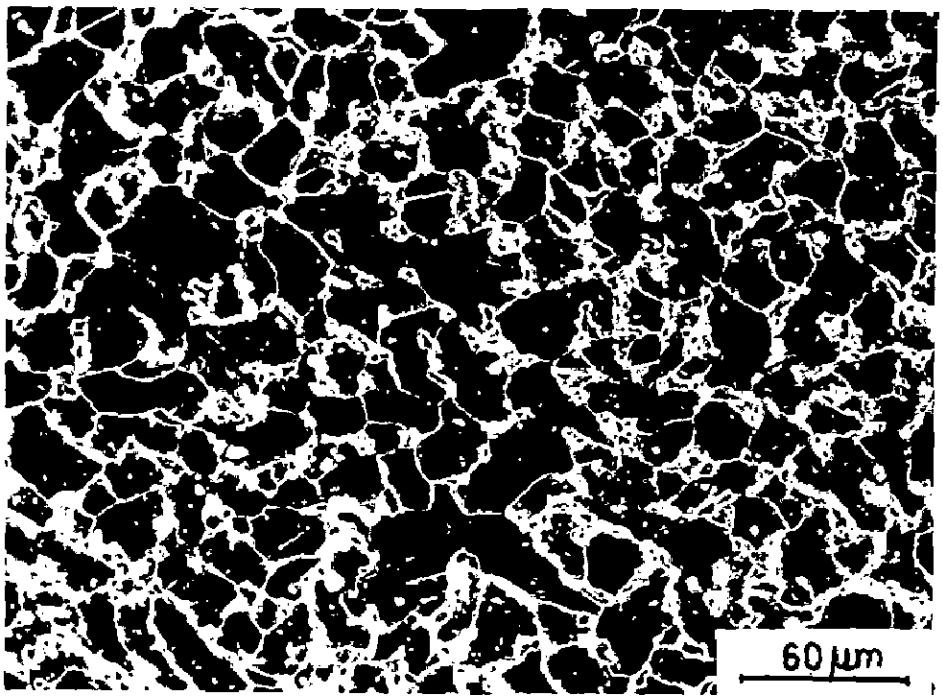

Fig. 5.8 b _ Dark-field optical micrograph of dual-phase steel-A (780 °C, 10min, WQ)

Fig. 5.8c – TEM micrograph showing dislocation substructure in the ferrite phase (bright region) of dual-phase steel-A (740°C, 10 min, WQ)

Table 5.1

Tensile Properties and Microstructural Parameters of Normalised Steel-A and Intercritically Annealed and Water Quenched DPS-A Specimens

Intercritical Annealing Temp. (°C)	Intercritical Annealing Time (Sec.)	YS (MPa)	UTS (MPa)	Total Elongation (%)	Uniform Elongation (%)	Mean Plastic strain Ratio, $\bar{R}$	MVF, (%)	Mean Martensite Island size (μm)
1	2	3	4	5	6	7	8	9
Normalised Steel-A	-	256	382	26.0	-	1.40	-	-
740	60	225	500	20.0	17.0	1.1	7.4	9.0
	120	235	510	19.8	16.7	1.08	9.4	11.3
	300	240	525	19.5	16.5	1.04	11.4	13.2
	600	245	540	18.0	15.0	1.00	13.0	13.4
	900	245	540	18.0	15.0	1.00	13.0	14.0
	1.8×10^3	225	480	14.0	11.0	1.00	13.0	-
	3.6×10^3	175	410	14.0	11.0	1.00	13.0	16.3
	7.2×10^3	140	340	14.0	11.0	1.00	13.0	-
	10.8×10^3	125	290	14.0	11.0	1.00	13.0	19.0
760	60	235	525	19.0	16.0	1.05	11.0	9.5
	120	240	540	18.5	15.5	1.02	14.0	12.3

Contd...

1	2	3	4	5	6	7	8	9
	300	250	550	18.0	15.0	1.0	17.5	13.6
	600	250	560	16.5	13.5	0.98	18.5	13.8
	900	250	560	16.5	13.5	0.98	18.5	14.5
	1.8×10^3	240	490	14.0	11.0	0.98	18.5	-
	3.6×10^3	180	440	14.0	11.0	0.98	18.4	17.5
	7.2×10^3	160	375	14.0	11.0	0.98	18.5	-
	10.8×10^3	150	325	14.0	11.0	0.98	18.5	20.0
780								
	60	250	550	18.5	15.4	1.0	15.0	10.0
	120	250.5	560	17.7	14.6	0.96	19.0	12.7
	300	260	575	16.0	13.5	0.94	22.8	14.2
	600	260	580	14.0	11.0	0.94	24.0	15.0
	900	260	580	12.0	9.0	0.94	24.0	-
	1.8×10^3	245	525	12.0	9.0	0.93	24.0	17.0
	3.6×10^3	200	450	12.0	9.0	0.94	24.2	17.5
	7.2×10^3	175	375	12.0	9.0	0.94	23.8	-
	10.8×10^3	150	350	12.0	9.0	0.94	24.2	20.5

Table 5.2

Tensile Properties and Microstructural Parameters of Normalised Steel-B and Intercritically Annealed and Water Quenched DPS-B Specimens

Intercritical Annealing Temp. (°C)	Intercritical Annealing Time (Sec)	YS (MPa)	UTS (MPa)	Total Elongation (%)	Uniform Elongation (%)	Mean Plastic strain Ratio, $\bar{R}$	MVF. (%)	Mean Martensite Island size (μm)
1	2	3	4	5	6	7	8	9
Normalised Steel-B	-	311	402	24.0	-	1.40	-	-
740	60	230	510	17.0	14.0	1.07	10.3	10.0
	120	235	525	16.5	13.5	1.04	12.3	11.8
	300	245	550	16.0	13.0	1.01	15.0	13.9
	600	250	575	16.0	13.0	0.98	17.0	14.5
	900	250	575	16.0	13.0	0.98	17.0	14.8
	$1x8x10^3$	220	495	15.5	12.0	0.97	17.1	16.3
	$3.6x10^3$	175	420	15.0	12.0	0.97	17.0	17.0
	$7.2x10^3$	140	340	15.0	12.0	0.97	17.0	-
	$10.8x10^3$	125	280	15.0	12.0	0.97	17.0	20.0
760								
	60	240	550	17.0	14.0	1.01	15.2	10.5
	120	250	560	16.5	13.5	0.98	18.2	12.8

Contd.

1	2	3	4	5	6	7	8	9
	300	260	580	15.0	12.2	0.97	21.8	14.0
	600	265	600	15.0	12.0	0.98	24.0	15.8
	900	265	600	15.0	12.0	0.97	24.1	16.0
	1.8×10^3	230	515	14.0	11.0	0.96	24.0	-
	3.6×10^3	180	425	14.0	11.0	0.96	24.0	18.2
	7.2×10^3	150	350	14.0	11.0	0.96	24.0	-
	10.8×10^3	130	300	14.0	11.0	0.96	24.0	20.5
780								
	60	255	575	16.0	13.0	0.97	20.6	11.0
	120	260	580	15.5	12.5	0.95	24.4	-
	300	275	625	15.0	12.0	0.94	28.9	-
	600	290	645	14.0	11.0	0.94	30.8	15.5
	900	290	645	14.0	11.0	0.94	31.0	15.7
	1.8×10^3	250	550	12.0	9.0	0.94	31.0	-
	3.6×10^3	200	450	12.0	9.0	0.94	31.0	18.9
	7.2×10^3	160	350	12.0	9.0	0.94	31.0	-
	10.8×10^3	140	300	12.0	9.0	0.94	31.0	21.0

Table 5.3

Tensile Properties and Microstructural Parameters of Normalised Steel-C and Intercritically Annealed and Oil Quenched DPS-C Specimens

Intercritical Temperature (°C)	Intercritical time, (sec.)	YS (MPa)	UTS (MPa)	Total Elongation (%)	Uniform Elongation (%)	Mean Plastic strain Ratio, R	MVF, (%)	Mean Martensite Island size (μm)
1	2	3	4	5	6	7	8	9
Normalised Steel-C	-	450	629	22.0	-	-	-	-
740	30	500	840	15.0	12.5	-	42.0	19.0
	60	550	900	14.0	11.5	-	47.5	19.2
	120	590	975	10.5	8.0	-	59.0	20.0
	300	650	1120	6.0	-	-	64.0	21.0
	600	700	1200	6.0	-	-	65.0	22.0
	900	700	1200	6.0	-	-	65.0	22.8
	1.8×10^3	640	1080	6.0	-	-	65.0	23.6
	3.6×10^3	575	1000	6.0	-	-	65.0	24.0
	7.2×10^3	525	900	6.0	-	-	65.0	24.5
	10.8×10^3	495	825	6.0	-	-	65.0	25.0
760								
	30	525	860	12.0	9.5	-	50.0	19.3
	60	600	1010	8.5	6.0	-	60.0	19.6

Contd...

1	2	3	4	5	6	7	8	9
	120	700	1160	6.0	-	-	70.0	-
	300	670	1280	4.0	-	-	73.0	-
	600	810	1360	4.0	-	-	74.5	22.8
	900	810	1360	4.0	-	-	74.5	-
	1.8×10^3	740	1220	4.0	-	-	74.4	-
	3.6×10^3	640	1080	4.0	-	-	74.5	24.7
	7.2×10^3	575	975	4.0	-	-	74.5	25.2
	10.8×10^3	520	880	4.0	-	-	-	26.0
780								
	30	605	1090	6.0	-	-	61.0	20.0
	60	685	1200	4.0	-	-	71.0	20.3
	120	760	1300	4.0	-	-	79.5	-
	300	800	1385	4.0	-	-	81.0	-
	600	860	1450	4.0	-	-	82.0	23.0
	900	860	1450	4.0	-	-	82.0	23.6
	1.8×10^3	795	1280	4.0	-	-	82.0	24.0
	3.6×10^3	720	1150	4.0	-	-	82.0	25.0
	7.2×10^3	640	1020	4.0	-	-	82.0	-
	10.8×10^3	600	950	4.0	-	-	82.0	27.0

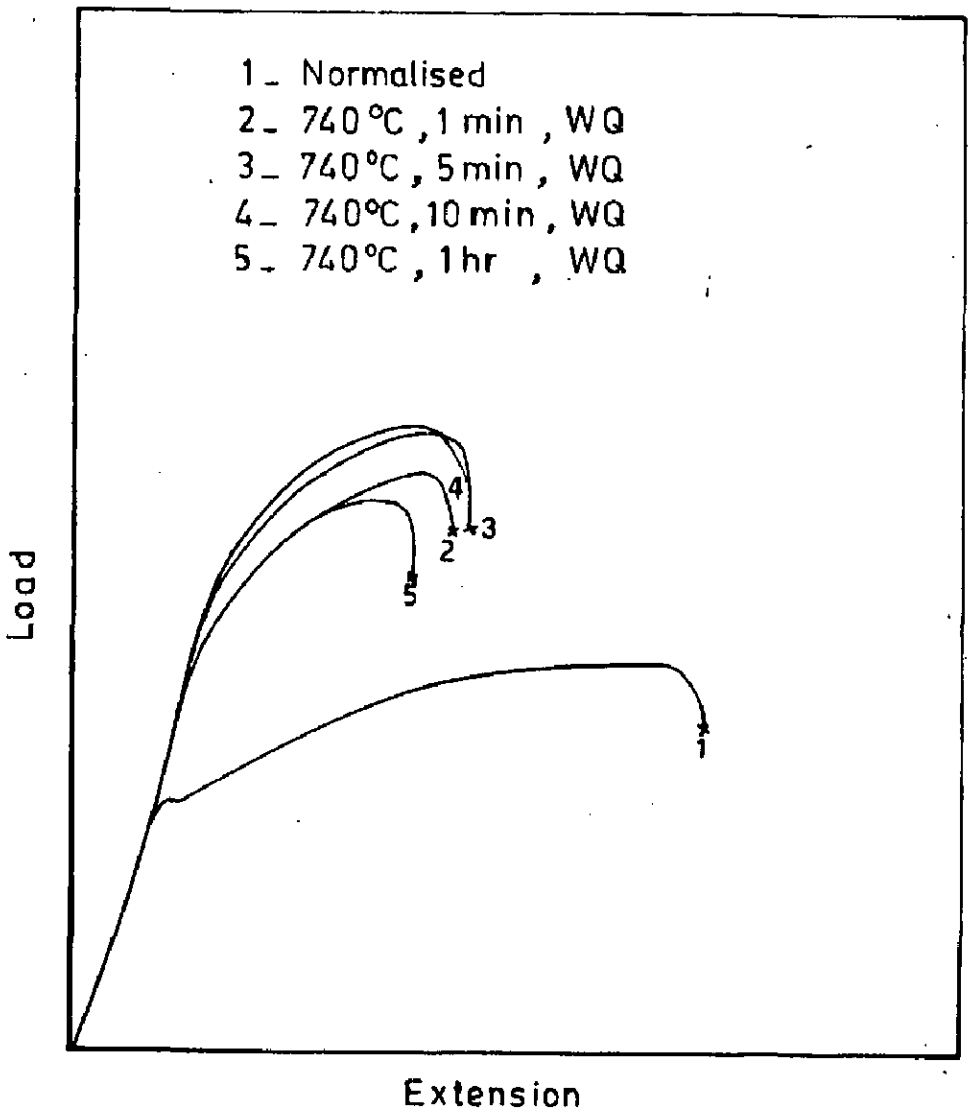

Fig. 5.9 _ Schematic representation of tensile load-extension curves for steel-A in normalised condition and with different intercritical heat-treatments

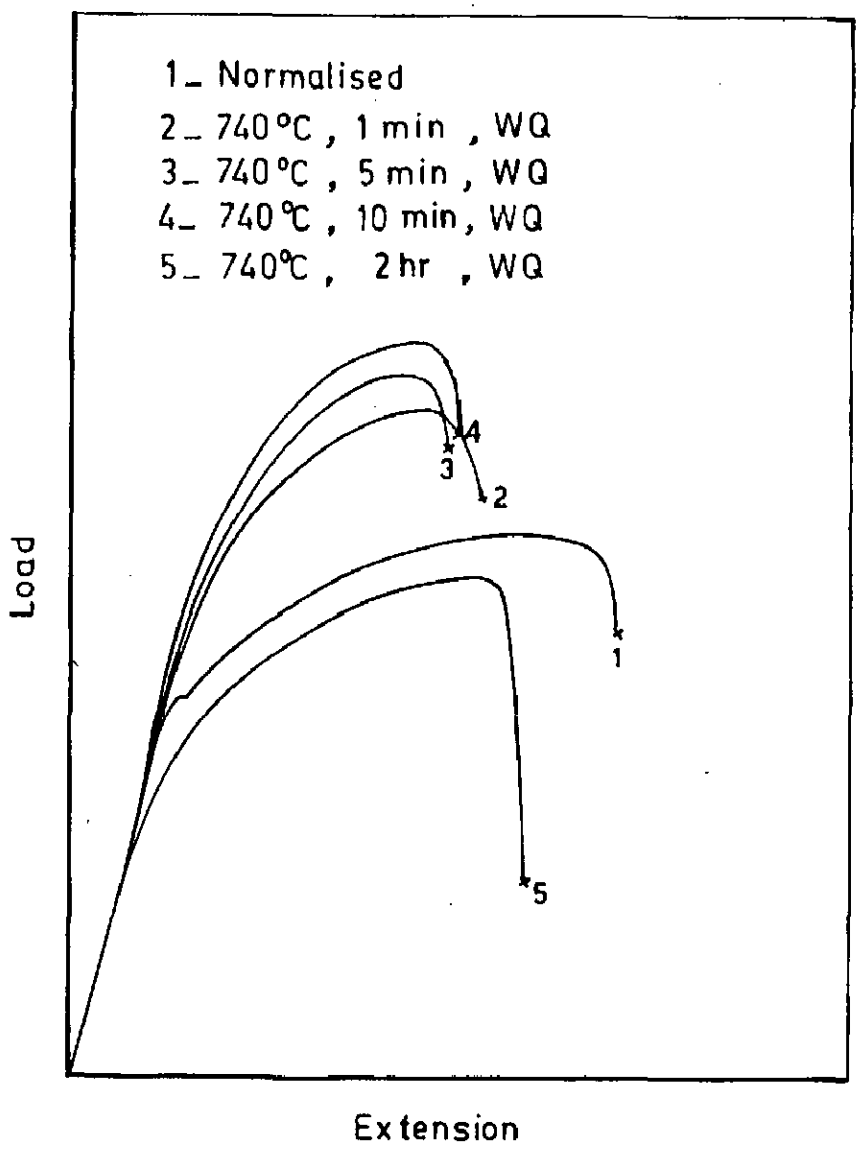

Fig. 5.10_ Schematic representation of tensile load-extension curves for steel-B in normalised condition and with different intercritical heat-treatments

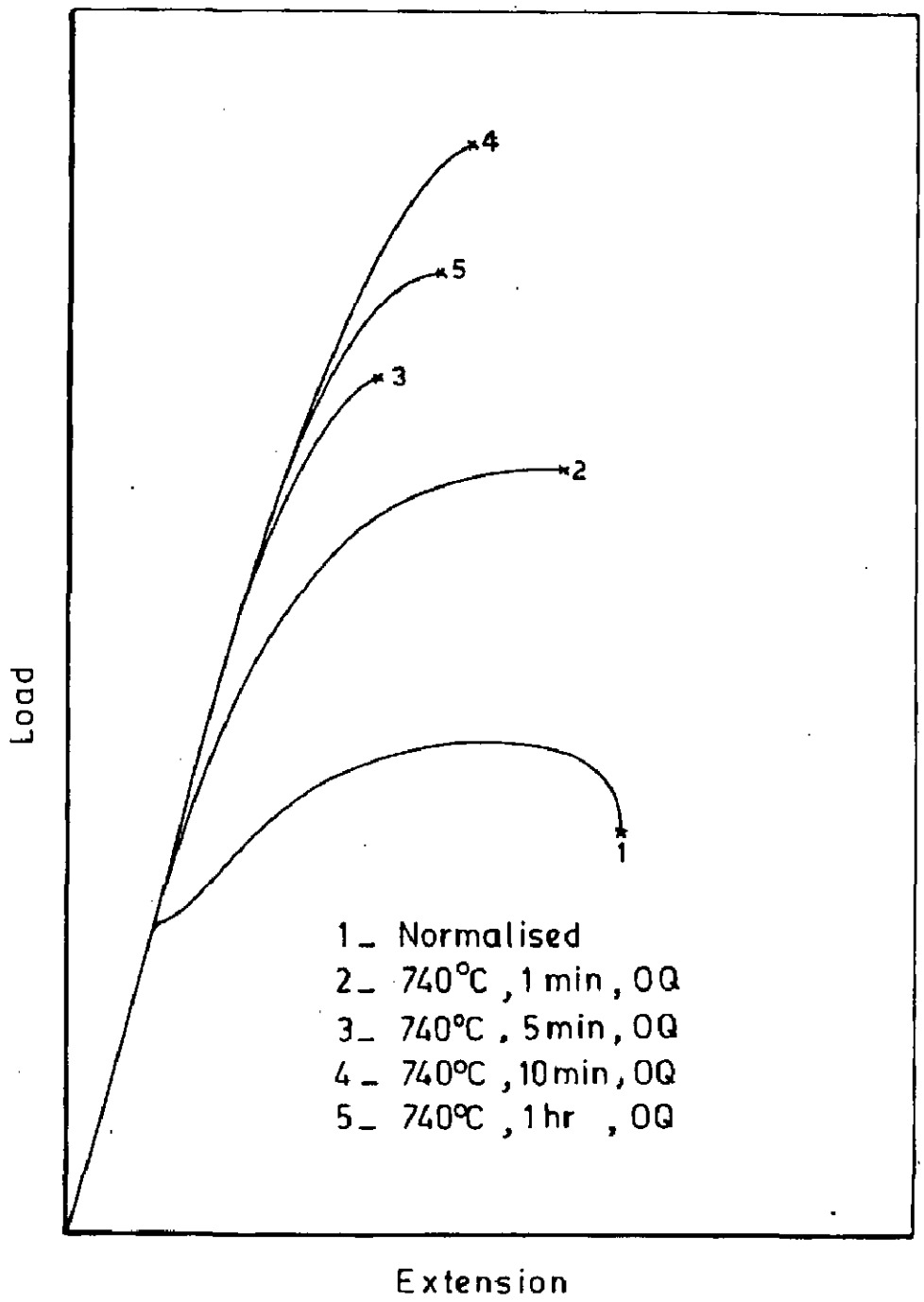

Fig.5.11 _ Schematic representation of tensile load-extension curves for steel-C in normalised condition and with different intercritical heat-treatments

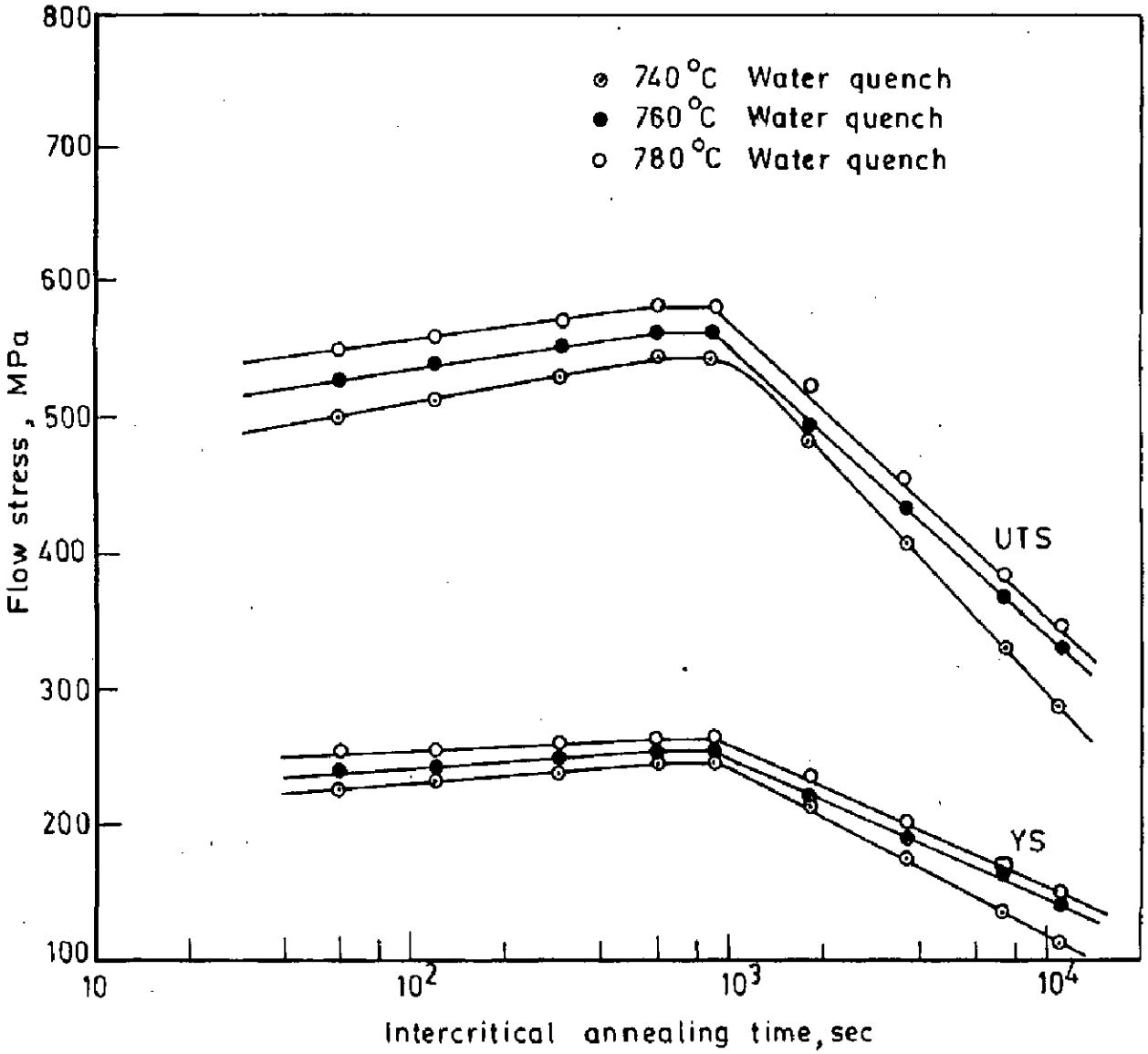

Fig. 5.12 _Variation of yield and tensile strengths as a function of intercritical annealing time in 0.08 percent carbon dual - phase steel

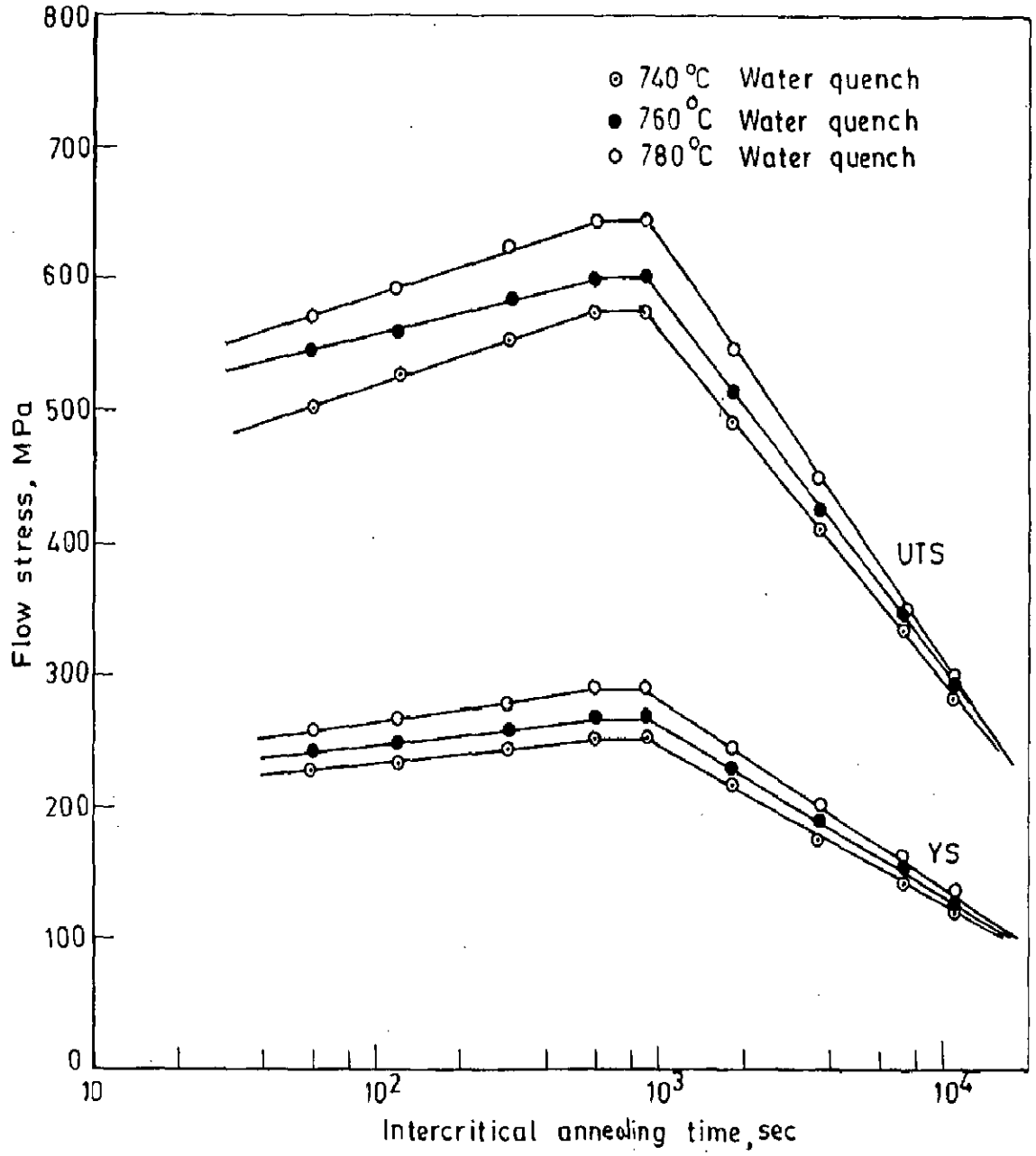

Fig. 5.13 _ Variation of yield and tensile strengths as a function of intercritical annealing time in 0.115 percent carbon dual-phase steel

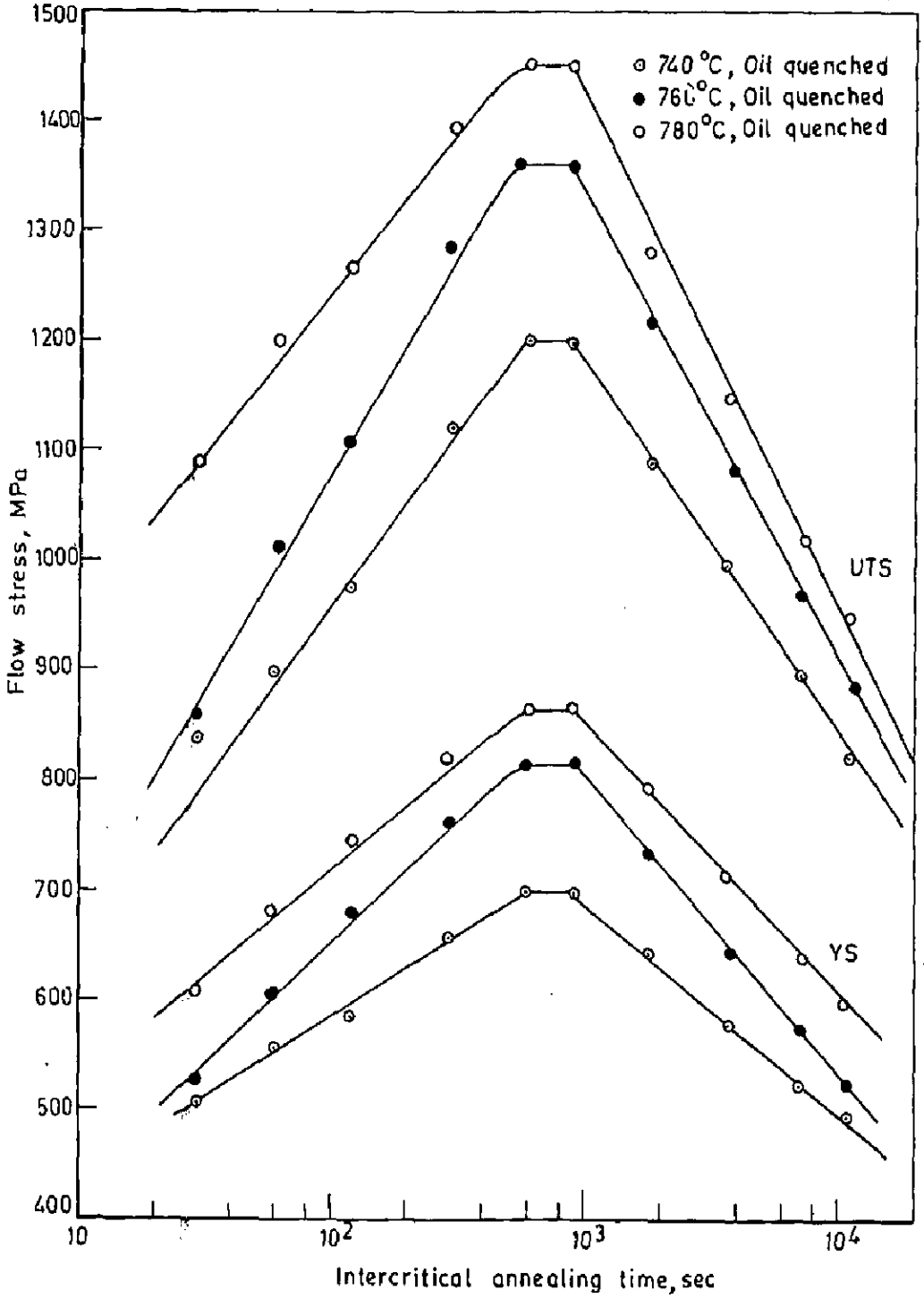

Fig. 5.14 Variation of yield and tensile strengths as a function of intercritical annealing time in 0.4 percent carbon dual-phase steel

The significant features reflected in Fig.5.9 are:

(i) The normalised steel shows discontinuous yielding whereas dual-phase steels produced from normalised steels by different ICA treatments, show continuous yielding i.e., absence of yield-point phenomenon,

(ii) at the same intercritical annealing temperature viz. at 740°C, UTS increases with the annealing time but ductility falls for all specimens of DPS-A.

The same trend is observed for all specimens of DPS-B and DPS-C also as shown in Figs.5.10 and 5.11 respectively.

Fig.5.12 reveals that YS and UTS of DPS-A annealed at 740°C, first increases with an increase in annealing time - the YS increases from a value of 225 MPa to 245 MPa as annealing time increases from 1 minute to 10 minutes whereas the UTS increases from 500 MPa to 540 MPa for the corresponding time of intercritical annealing (ICA-time). However, both the YS and UTS remain constant for annealing times ranging between 10 to 15 minutes but after the lapse of this ICA-time, start decreasing till 3 hours (maximum annealing time used in the present investigation). After 3 hours of ICA-time, the value of YS observed is 125 MPa and that of UTS is 290 MPa.

A similar trend in variation of these properties with ICA-time, has been observed for intercritical annealing of Steel-A at temperatures 760°C and 780°C. However, the maximum values of YS and UTS for DPS-A occurs at 250 MPa for YS and 560 MPa for UTS at ICA-temperature of 760°C, whereas the corresponding values are reported to be 260 MPa and 580 MPa respectively at ICA-temperature 780°C. Further DPS-B and DPS-C also show similar variations in the YS and UTS with ICA-time for the corresponding ICA-temperatures as shown in Figs.5.13 and 5.14 respectively. However, DPS-B shows higher values of maximum YS and UTS at all ICA-temperatures under investigation as compared to those in DPS-A. Similarly, for DPS-C, the maximum values of YS and UTS corresponding to the above ICA-temperatures, have been found respectively to be 700 and 1200 MPa, 810 and 1360 MPa and 860 and 1450 MPa, which obviously are more than those observed for DPS-A and DPS-B respectively.

It is interesting to note that the variation of YS and UTS with MVF for all dual-phase steels, is linear as reflected in Figs. 5.15 - 5.17 respectively for DPS - A DPS - B and DPS - C. It is also clear from Tables 5.1 - 5.3, that

(i) the MVF at any ICA - temperature increases with an increase in ICA - time it attains an equilibrium value (maximum value).

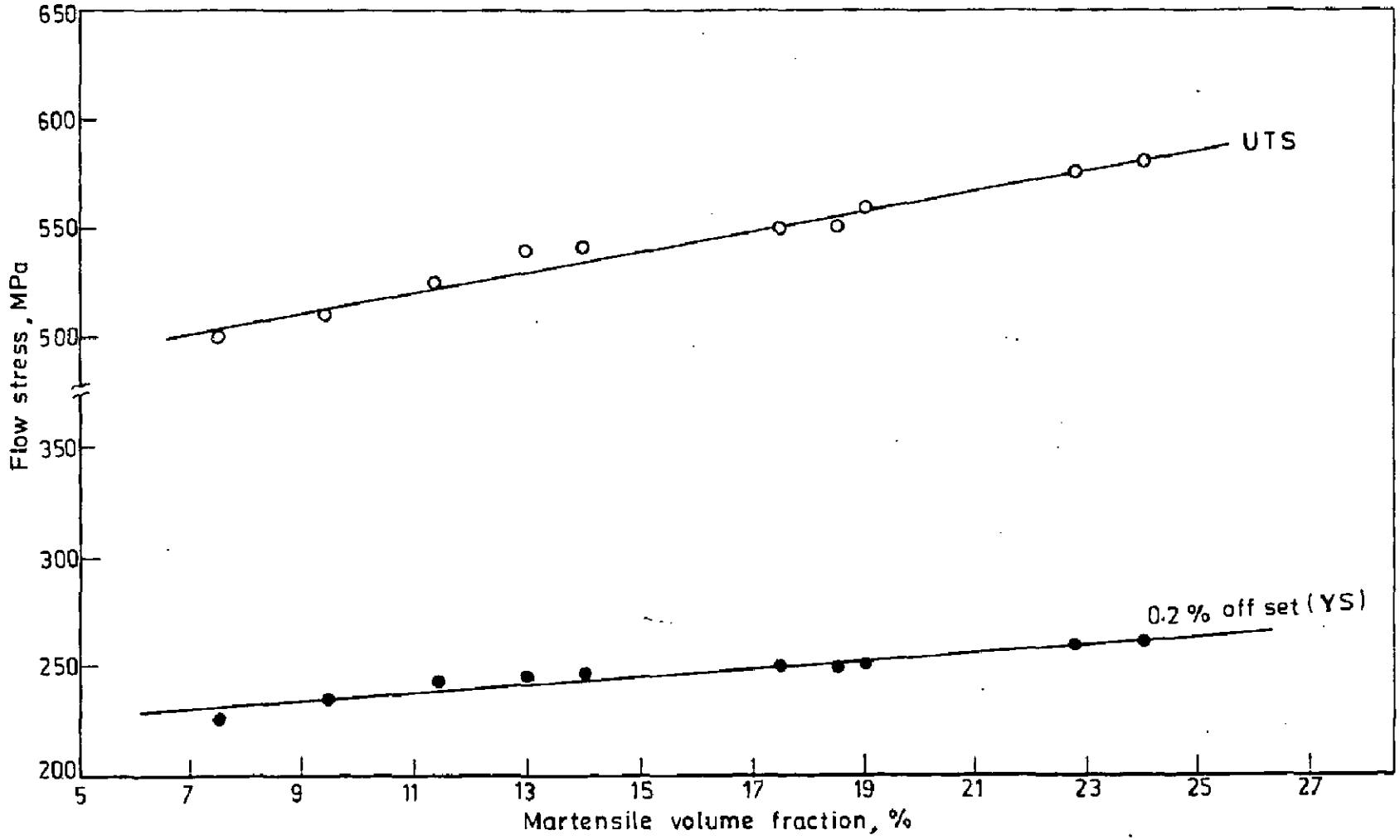

Fig.5.15 _ Variation of yield and tensile strengths as a function of percent martensite volume fraction in 0.08 percent carbon dual-phase steel

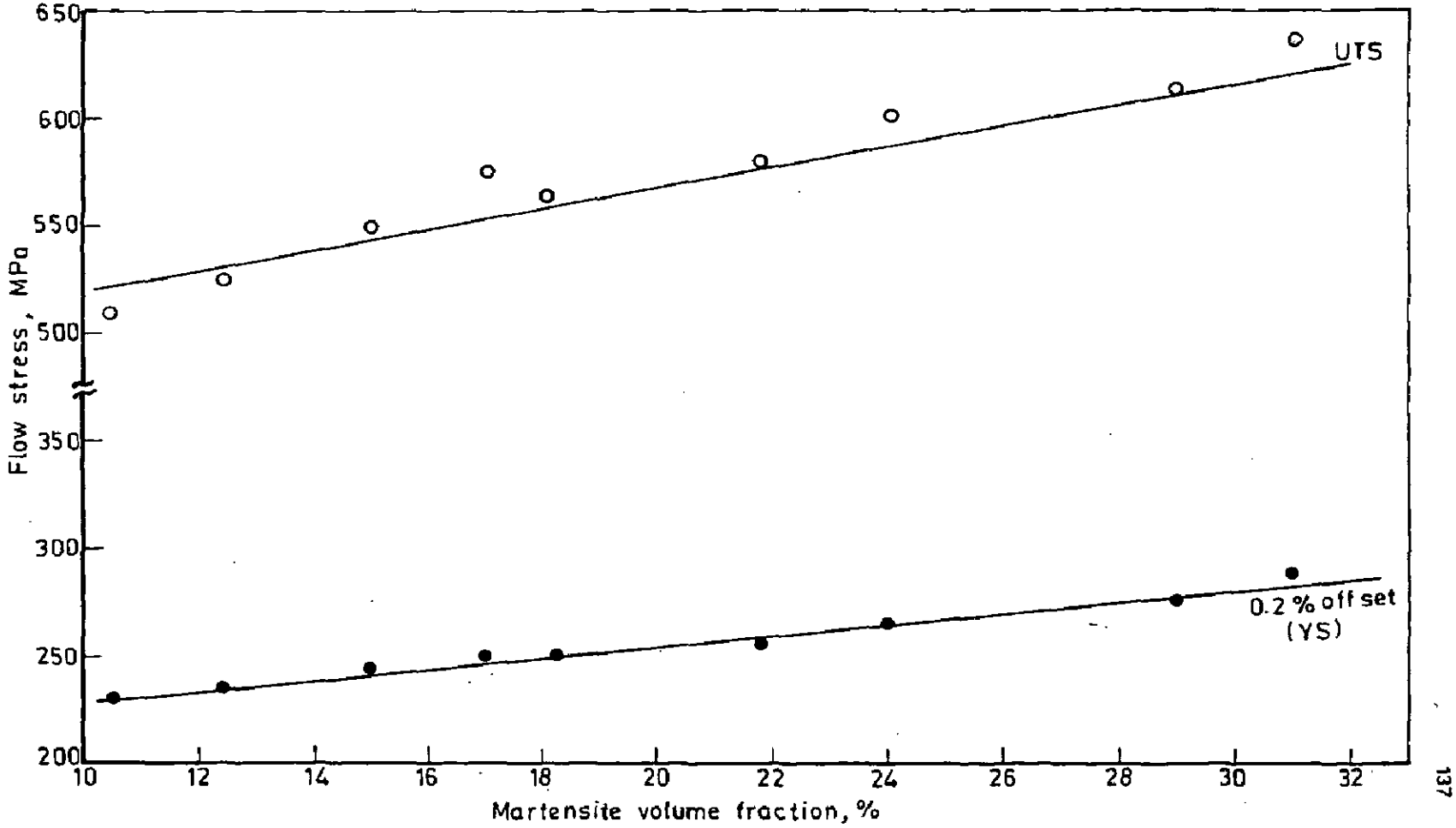

FIG. 5.16 _ Variation of yield and tensile strengths as a function of percent martensite volume fraction in 0.115 percent carbon dual-phase steel

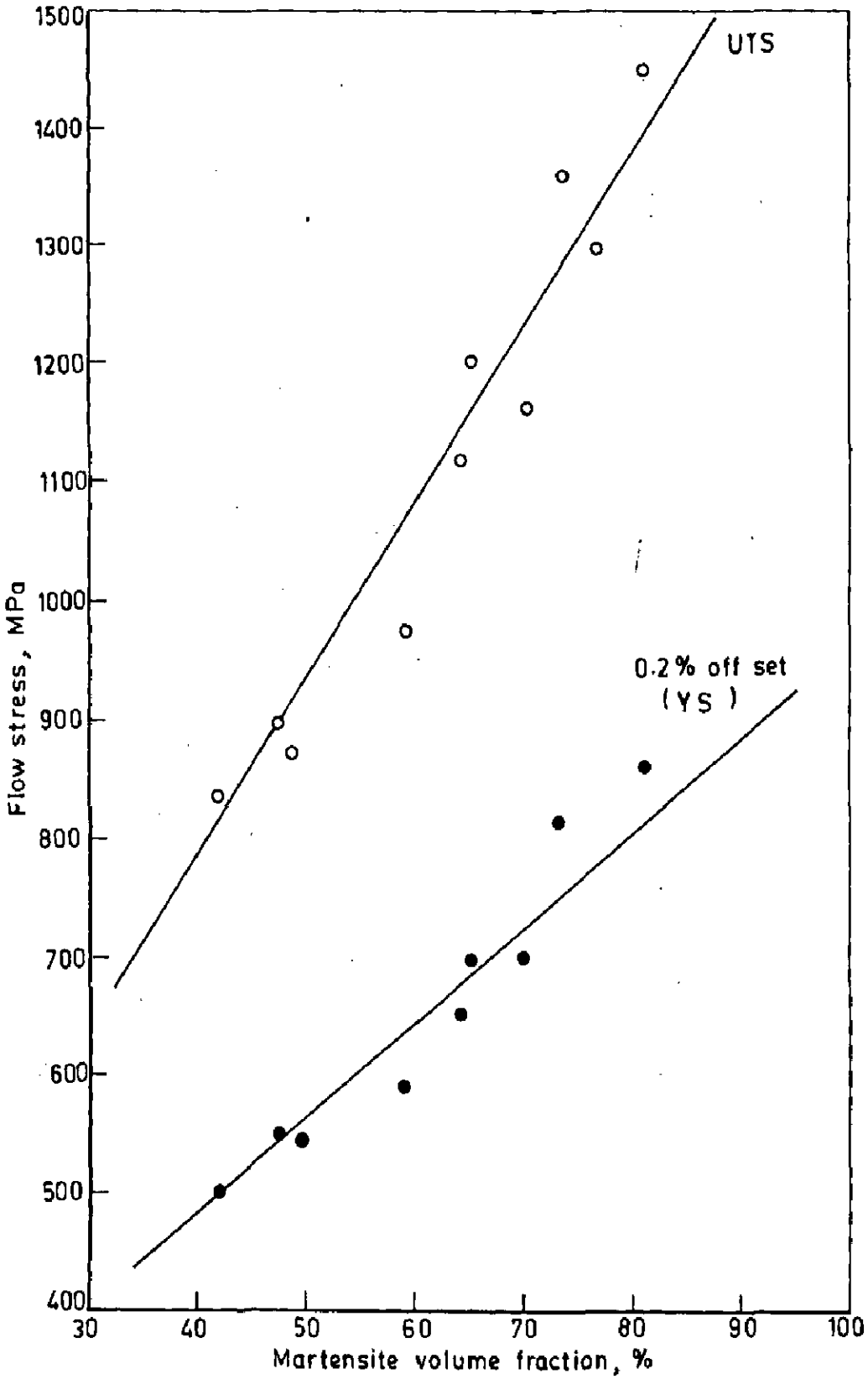

Fig. 5.17_ Variation of yield and tensile strengths as a function of percent martensite volume fraction in 0.4 percent carbon dual-phase steel

(ii) both the initial MVF and equilibrium MVF increases with an increase in ICA-temperature..

(iii) the strength (YS and UTS) increases with an increase in MVF.

5.3.2 Comparison of theoretical strength with observed strength of dual-phase steels - model approach.

The theoretical model developed in Chapter - 3 to calculate theoretically the UTS, $\sigma_{u,c}$, of dual-phase steels treated as composites, may be described in terms of the strengthening contribution of the matrix (ferrite) and the embedded second phase (martensite) using the rule of mixture plus the work-hardening effect of the ferrite matrix. Assuming the martensite islands to be spherical in shape, the final expression used for calculation of theoretical UTS of the dual-phase steel, $\sigma_{u,c}$ may be rewritten as,

$$\sigma_{u,c} = \sigma_{u,m} V_m + \frac{4Vp\ \sigma_{u,m}}{\pi^2} (\bar{D}_i \bar{Z})^2 + KG\sqrt{\frac{\bar{b}V_p\ \epsilon}{0.41\ \bar{D}_i}} \qquad \ldots (5.1)$$

where, the different symbols used in this expression have following meanings,

$\sigma_{u,m}$ - UTS of the ferrite matrix,

V_m - Volume fraction of ferrite matrix,

V_p - Volume fraction of martensite phase,

$\bar{D}_i$ - Average size of spherical martensite islands on a planar Section,

$\bar{Z}$ - Average of reciprocal of measured D_i values, already defined in the text in Section 2.5.2,

K - A constant of the order of 1,

G - Shear modulus of the matrix,

$\bar{b}$ - Burger's Vector of the matrix dislocation,

ϵ - True strain.

The first term on the right hand side of Eq. (5.1) represents the contribution of the matrix, the second term that of the spherical martensite islands whereas the third term represents the contribution of work - hardening of the ferrite matrix in the presence of embedded second phase martensite islands.

Typical values of some parameters, adopted from the available literature [86] for use in calculations in the present work are as under,

$\sigma_{u,m}$ = 415 MPa, K = 1, $\sigma_{f,u}$ = 2000MPa

G = 82,400 MPa, $[\bar{b}]$ = 0.247 nm

Substitution of these values in Eq. (5.1), yields,

$$\sigma_{u,c} = 415\ V_m + 168.19\ V_p\ (\bar{D}_i\ \bar{Z})^2 + 0.67\sqrt{\frac{V_p}{\bar{D}_i}} \qquad \ldots (5.2)$$

Using the measured values of V_m, V_p, $\bar{D}_i$ and $(\bar{D}_i\ \bar{Z})$ for various inter-critically annealed and quenched specimens of DPS-A, DPS-B and DPS-C, theoretical UTS for these may be calculated from

Eq.(5.2). These calculated values of theoretical UTS have been plotted for comparison with the experimentally observed values in Figs.5.18 - 5.20 for these dual-phase steels viz., DPS-A, DPS-B and DPS-C respectively. It is observed that the theoretical values are much lower than the experimentally observed values.

It is further clear from these figures that both theoretical and observed values of UTS vary linearly with MVF.

In order to evaluate the effect of shape of the embedded second phase particles i.e., the martensite islands, the expression arrived at in Section 3.2.1 during development of theoretical model for dual-phase steel composites having cylindrical particles with hemi-spherical ends, has been used for calculation of theoretical value of UTS of the dual-phase steels. Using similar symbols for the UTS, $\bar{\sigma}_{u,c}$, of the dual-phase steel and other parameters, this expression may be rewritten as,

$$\sigma_{u,c} = \sigma_{u,f}\left[1-\frac{r}{\ell}\right]V_p+\sigma_{u,m}\left[1+\left\{\frac{2}{3}\,\frac{r}{\ell}-1\right\}V_p\right]+KG\sqrt{\frac{\bar{b}V_p\varepsilon}{0.41\bar{D}_i}} \quad \ldots (5.3)$$

where, r and ℓ in this expression represents respectively the radius and half-length of the cylindrical particle with hemi-spherical ends and the ratio (r/ℓ) therefore represents a dimensionless parameter indicating deviation from the ideal spherical shape.

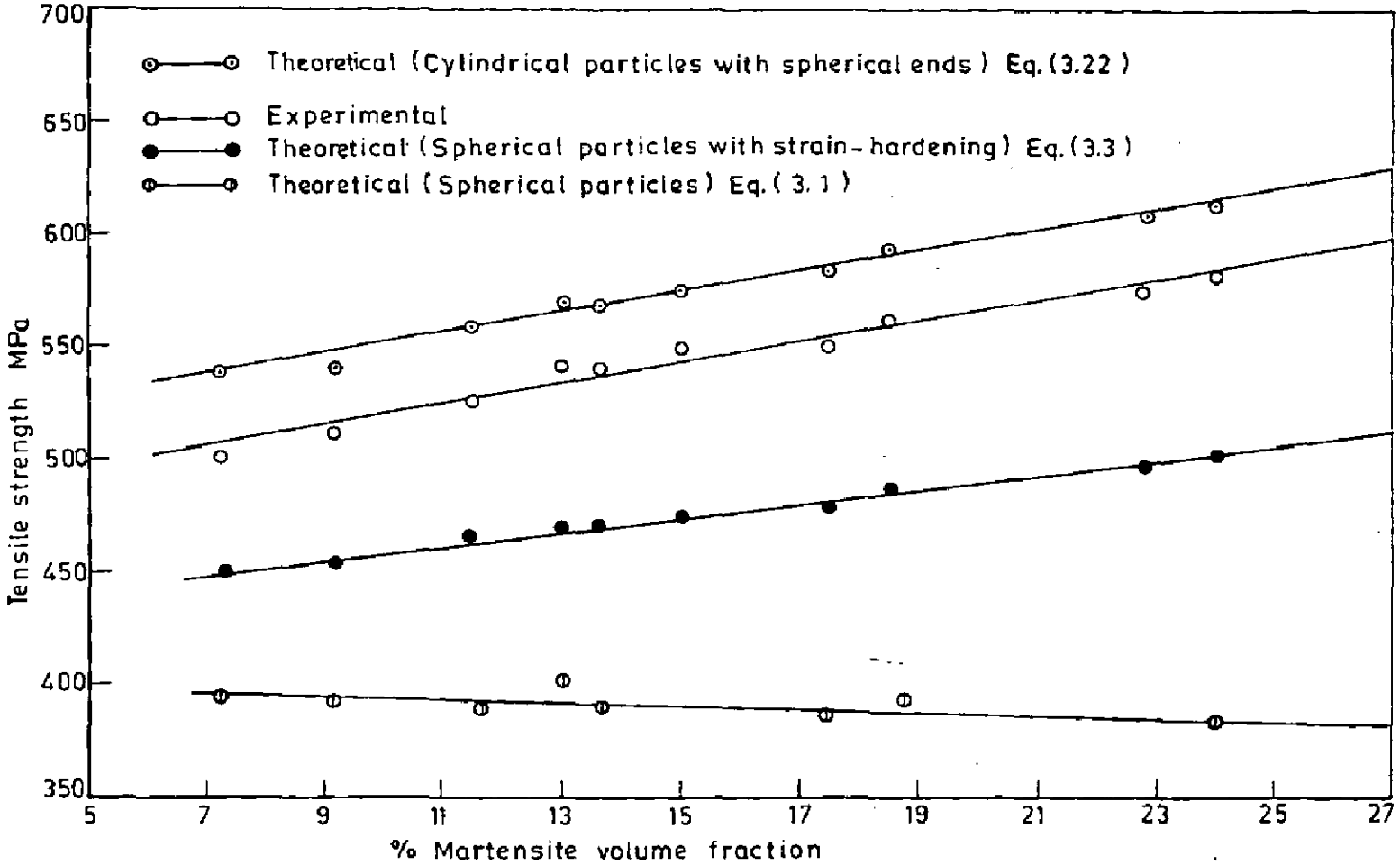

Fig. 5.18 _ Tensile strength of the experimental data are compared with those calculated from theoritical models in 0.08 percent carbon dual-phase steel

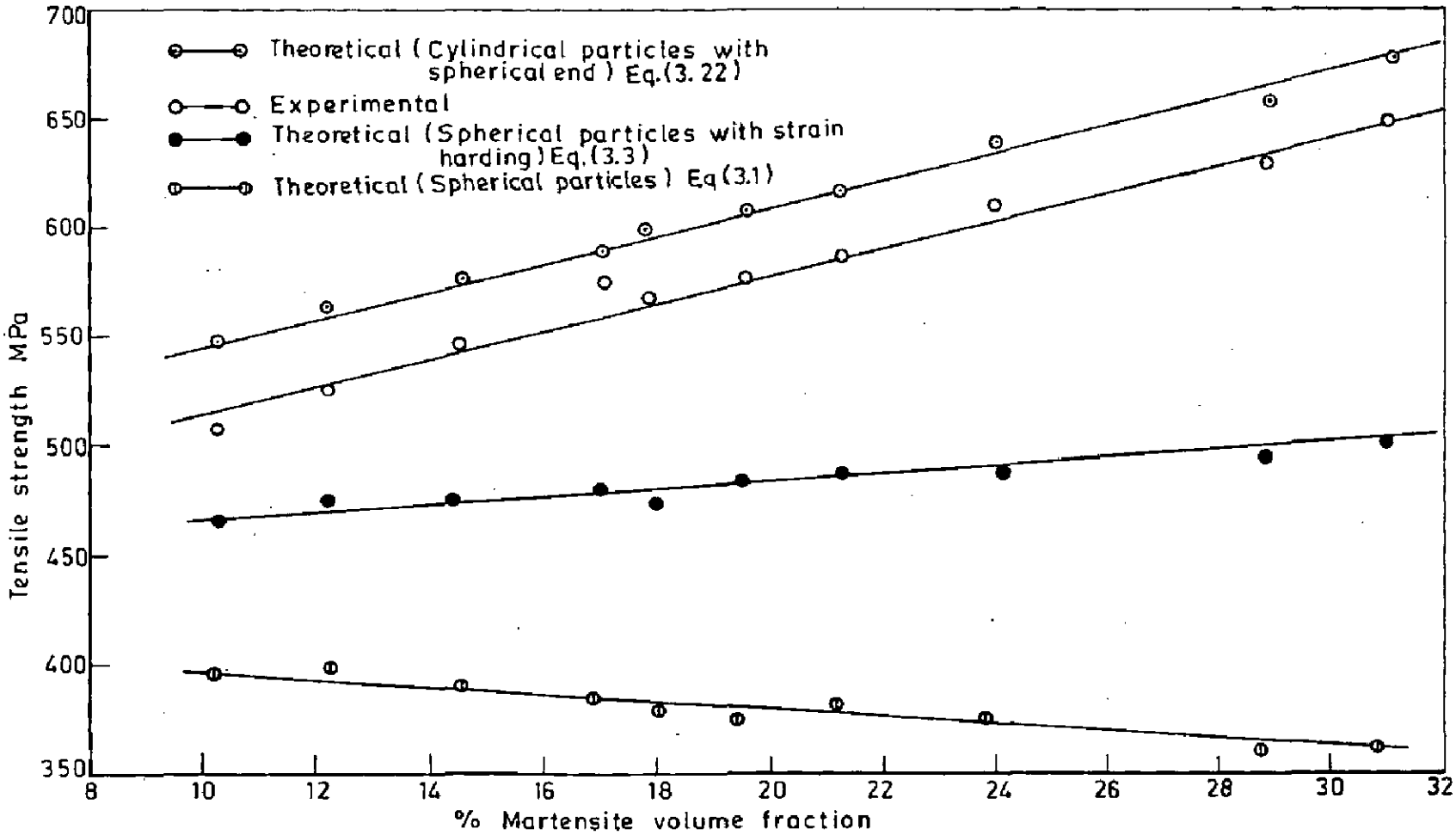

Fig.5.19 _ Tensile strength of the experimental data are compared with those calculated from theoretical models in 0.115 percent carbon dual-phase steel

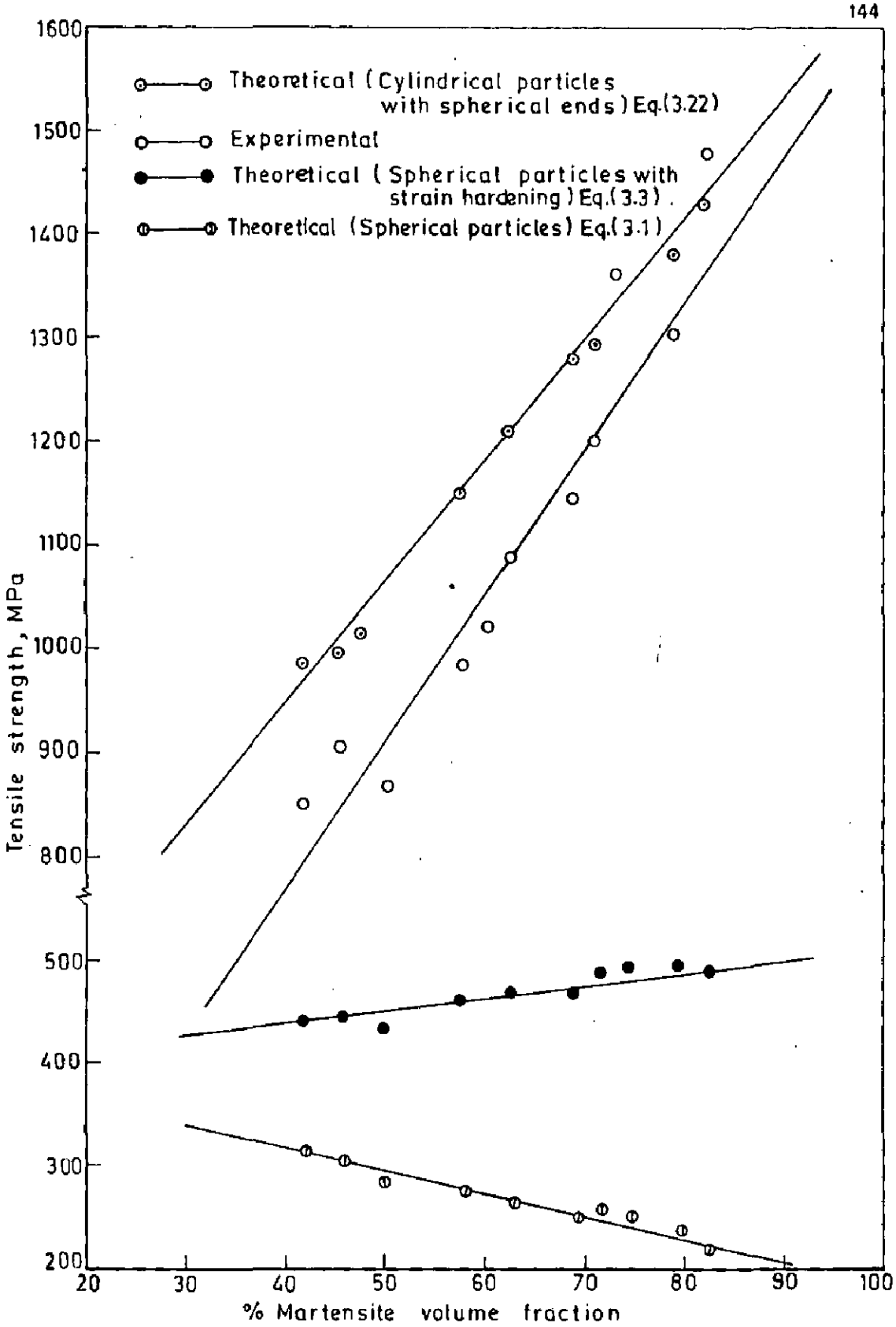

Fig. 5.20 _ Tensile strength of the experimental data are compared with those calculated from theoretical models in 0.4 percent carbon dual-phase steel

If the same numerical values for the above referred parameters viz., $\sigma_{u,m}$, $\sigma_{u,f}$, K, G and $\bar{b}$ be used, then Eq.(5.3) can be rewritten in the following alternate form,

$$\sigma_{u,c} = 2000\left[1-\frac{r}{\ell}\right]V_p+415\left[1+\left\{\frac{2}{3}\frac{r}{\ell}-1\right\}V_p\right]+0.67\sqrt{\frac{V_p}{\bar{D}_i}} \quad \ldots (5.4)$$

Using the measured values of V_p, $\bar{D}_i$ and (r/ℓ) ratio for various ICA-treated specimens of DPS-A, DPS-B and DPS-C, the UTS of dual-phase steels as composites, may be, theoretically calculated on the basis of Eq.(5.4). The theoretical values of UTS so calculated, have been plotted together with the corresponding experimentally observed values as a function of MVF in Figs.5.18-5.20 for three types of dual-phase steels viz., DPS-A, DPS-B and DPS-C respectively. As will be observed the theoretical values are slightly greater than the experimentally observed values. Figs.5.18 - 5.20 also reveal that both theoretical and observed values of UTS increase linearly with MVF.

Calculated values of theoretical UTS using only first two terms on the r.h.s. of Eq.(5.2) or Eq.(3.1) representing an expression equivalent to that arrived at by Prasad [56] in analysis of composite materials, have also been plotted in Figs.5.18 - 5.20 for the same group of dual-phase steels. It will be noted that these plots are linear in nature, each having a downward slope.

5.3.3 Ductility

The variation of total- and uniform-elongations with intercritical annealing (ICA) time at different ICA-temperatures of dual-phase steels viz., DPS-A, DPS-B and DPS-C is shown in Figs.5.21 - 5.23 respectively. It will be noted from Fig.5.21 that at 740°C ICA-temperature both the total-and uniform-elongations of DPS-A initially decrease with an increase in ICA-time and then attain a constant value. At 1 minute of ICA-time, the total elongation is 20 pct. and the uniform elongation is 17 pct. These val ues decrease to 14 pct. and 11 pct. respectively as ICA-time is increased to 30 minutes. It is further observed that both the total-and the uniform-elongations remain constant at 14 pct. and 11 pct. respectively with further increase in ICA-time beyond 30 minutes (to 3 hours which is the maximum ICA-time used in the present investigation). Fig.5.21 further shows that as ICA-temperature is increased to 760°C, both the total-and the uniform-elongations drop slightly to 19 pct. and 16 pct. respectively for 1 minute of ICA-time for this steel. But after 30 minutes of ICA-time, values of both the total-and the uniform-elongations reach the same low levels as those after 30 minutes of ICA-time at 740°C, beyond which these values remain constant. However, when the ICA-temperature is increased to 780°C, the minima in total-and uniform-elongation curves reach just in 15 minutes ICA-time instead of 30 minutes as observed at 740°C and 760°C ICA-temperatures. Fig.5.22 similarly reveals that at all ICA-

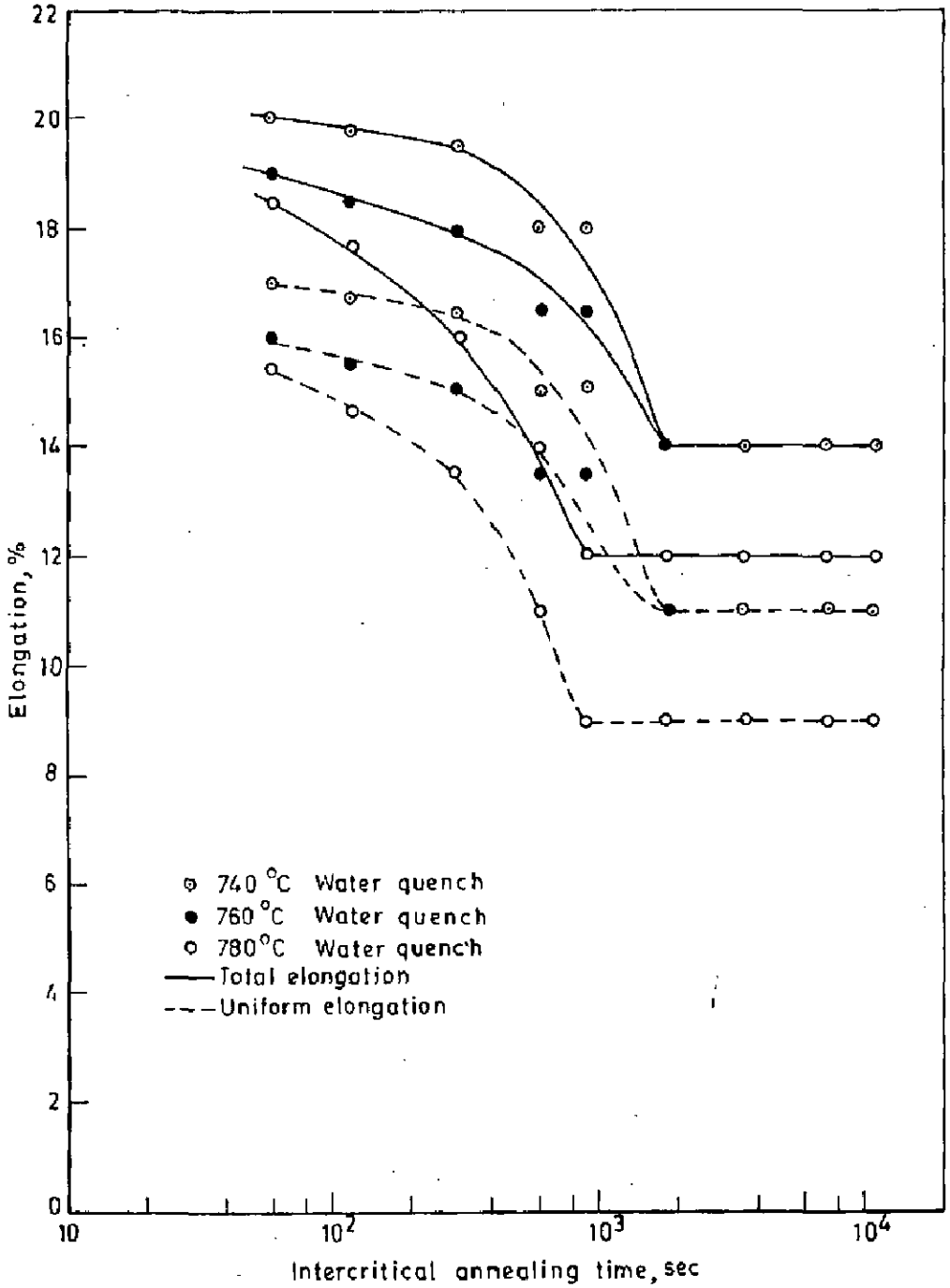

Fig. 5.21 _Variation of uniform and total elongations as a function of intercritical annealing time in 0.08 percent carbon dual-phase steel

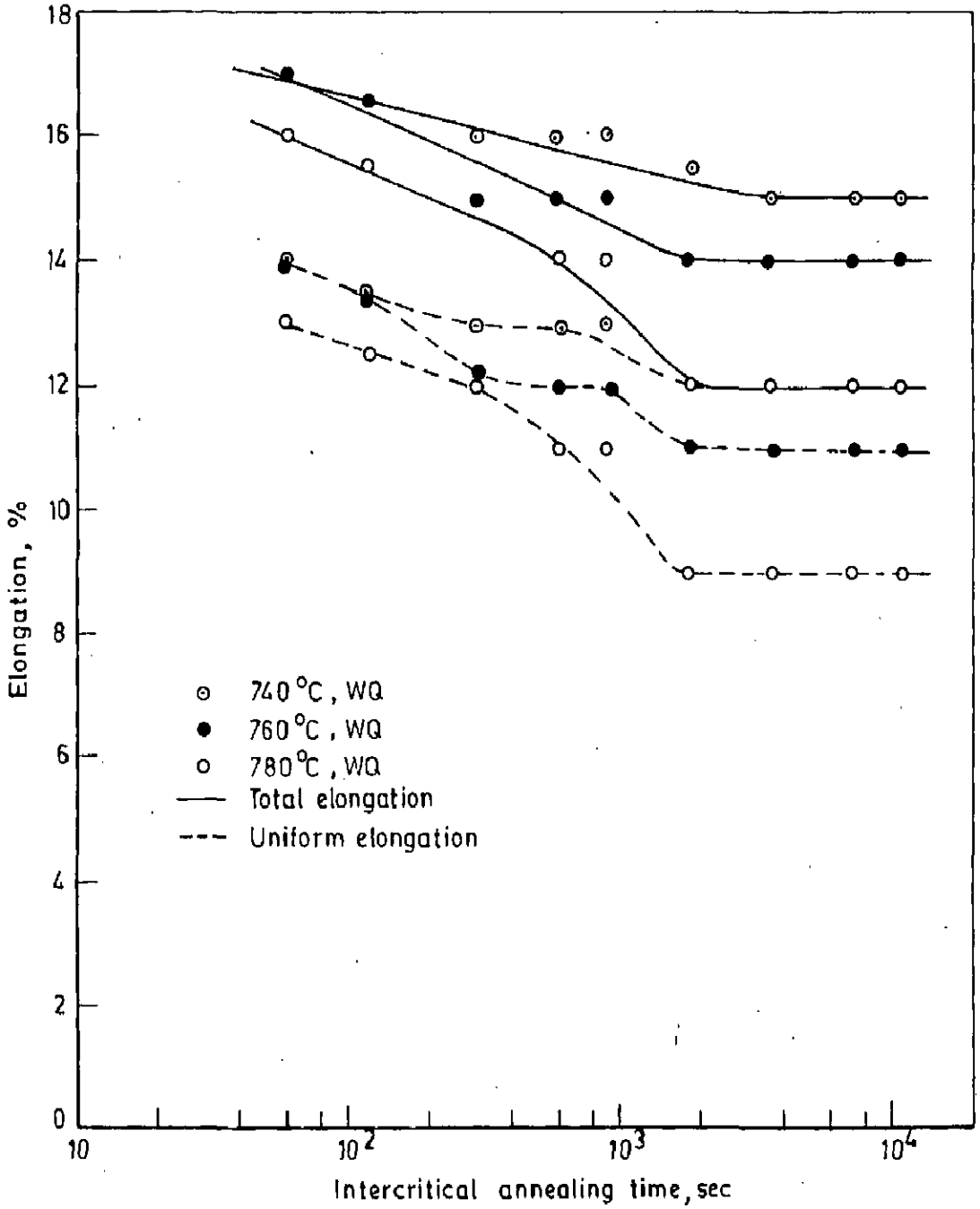

Fig.5.22_Variation of uniform and total elongations as a function of intercritical annealing time in 0·115 percent carbon dual-phase steel

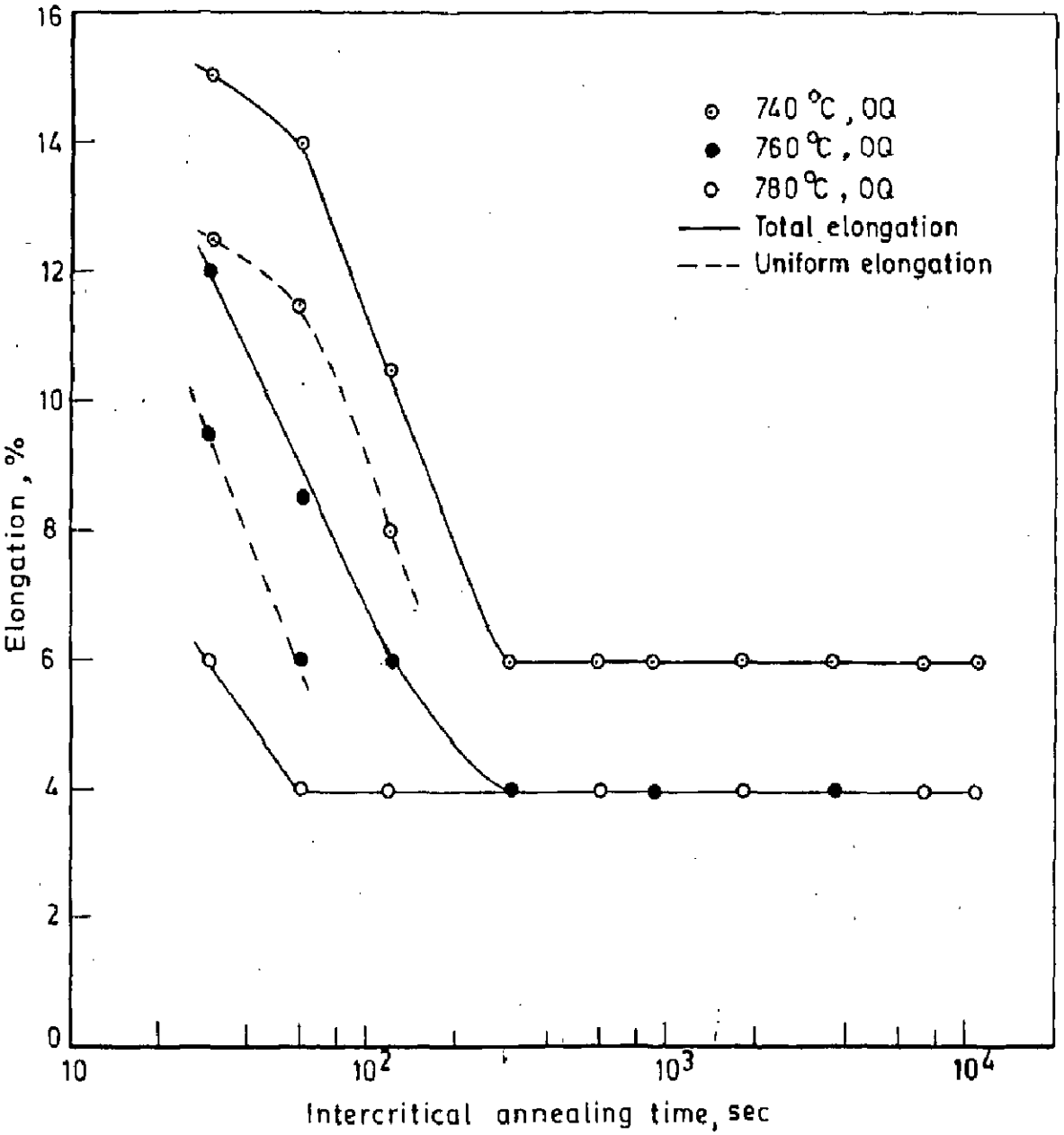

Fig.5.23 _ Variation of uniform and total elongations as a function of intercritical annealing time in 0.4 percent carbon dual-phase steel

temperatures for DPS-B, both the total-and the uniform-elongations decrease with an increase in ICA-time and then attain constant values as observed for DPS-A in Fig.5.21. However, lower total-and uniform-elongation values are observed for corresponding ICA-temperature and times as compared to those for the DPS-A.

The DPS-C also shows a similar decreasing trend with attainment of a constant minimum value of both the total- and the uniform-elongations with increasing ICA-time as depicted in Fig.5.23. However, much lower values of total-and uniform-elongation are attained for corresponding ICA-temperatures and times as compared to the corresponding values for DPS-A and DPS-B. For example, at 1 minute of ICA-time at 740°C, the total-and the uniform-elongation values are 14 and 11.5 pct respectively whereas at 760°C these are reduced to 8.5 pct. and 6 pct. respectively. At 780°C ICA-temperature, the total elongation in the sample is so low (~4 pct.) that the uniform elongation is not accurately measured. However, 30 seconds of ICA-time at three ICA-temperatures for DPS-C yields better ductility values, for example, the total-and the uniform-elongation values increase to 15 and 12.5 pct. at 740°C and 12 and 9.5 pct. at 760°C. Value of total elongation is 6 pct. at 30 second ICA-time at 780°C as compared to 4 pct. at 1 minute of ICA-time at the same temperature.

Variation of total-and uniform-elongations as a function of martensite volume fraction (MVF) of dual-phase steels,

DPS-A, DPS-B and DPS-C is shown in Figs.5.24-5.26 respectively.

Variation of MVF with ICA-time and temperature for all the three steels have been already discussed at the beginning of this Chapter as shown in Figs.5.1 - 5.3. It can be seen that MVF initially increases at any desired ICA-temperature, with an increase in ICA-time and then attains an equilibrium maximum value. This maximum value also increases with an increase in ICA-temperature and is attained almost at constant ICA-time of about 10 minutes. For example in DPS-A, values of MVF at 1 minute ICA-time vary from 7.4 to 11 pct. and then 15 pct. as the ICA-temperature is increased respectively from 740°C to 760°C and then to 780°C and attain constant maximum values of 13, 18.5 and 24 pct. respectively for the corresponding ICA-temperatures.

It will be noted therefore from Figs.5.24 to 5.26 that the ductility measured as total-and uniform-elongations decrease with an increase in MVF and this variation is almost linear in nature. For example, for DPS-A at ICA-time of 1 minute, the MVF varies from 7.4 to 11 to 15 pct. as the ICA-temperature varies from 740°C to 760°C and then to 780°C. The corresponding variation in total-and uniform-elongations at the same ICA-time are respectively 20 and 17 pct, 19 and 16 pct. and 18.5 and 15.4 pct. for these three ICA-temperatures.

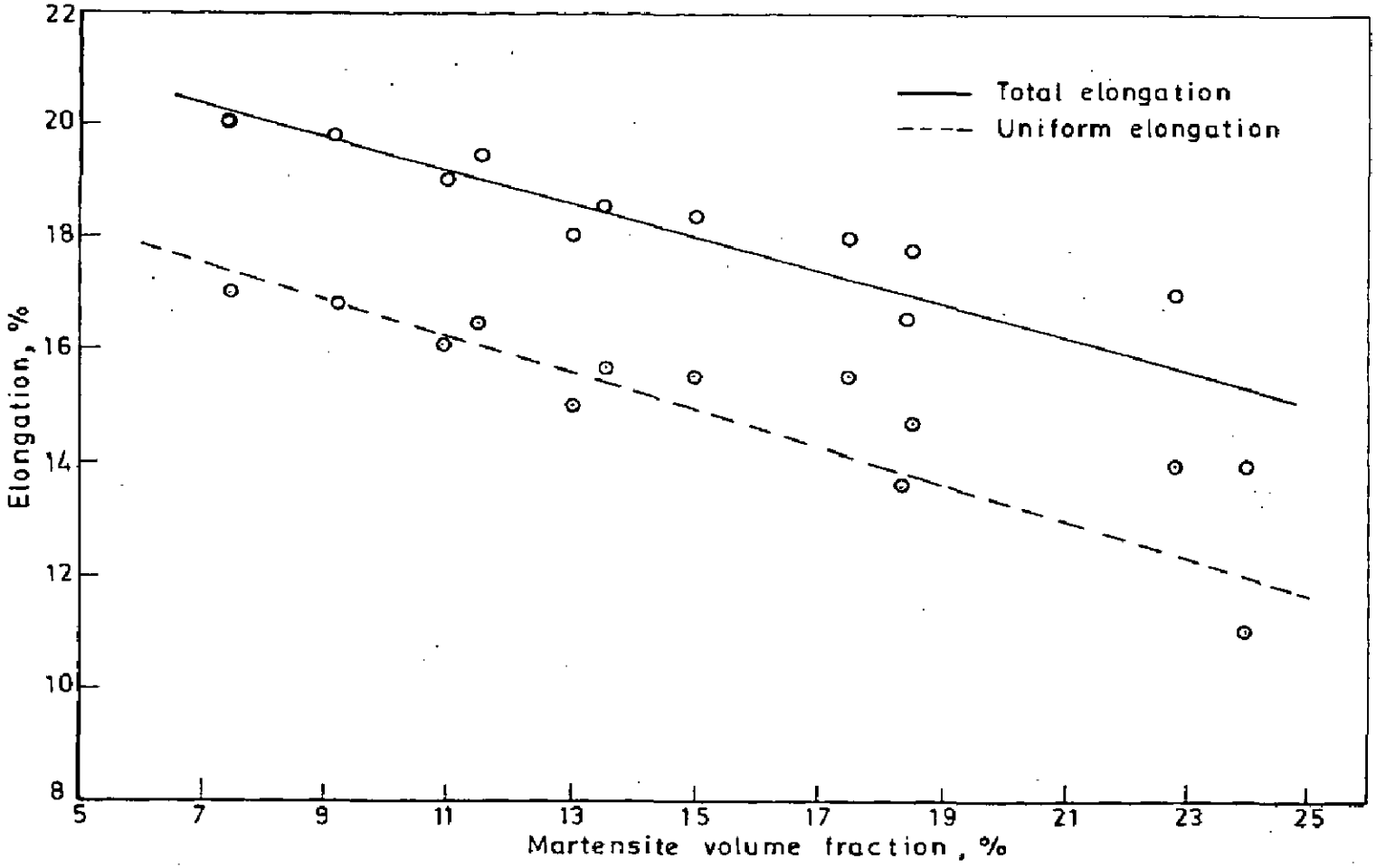

Fig. 5.24 _Variation of uniform and total elongations as a function of martensite volume fraction in 0.08 percent carbon dual-phase steel

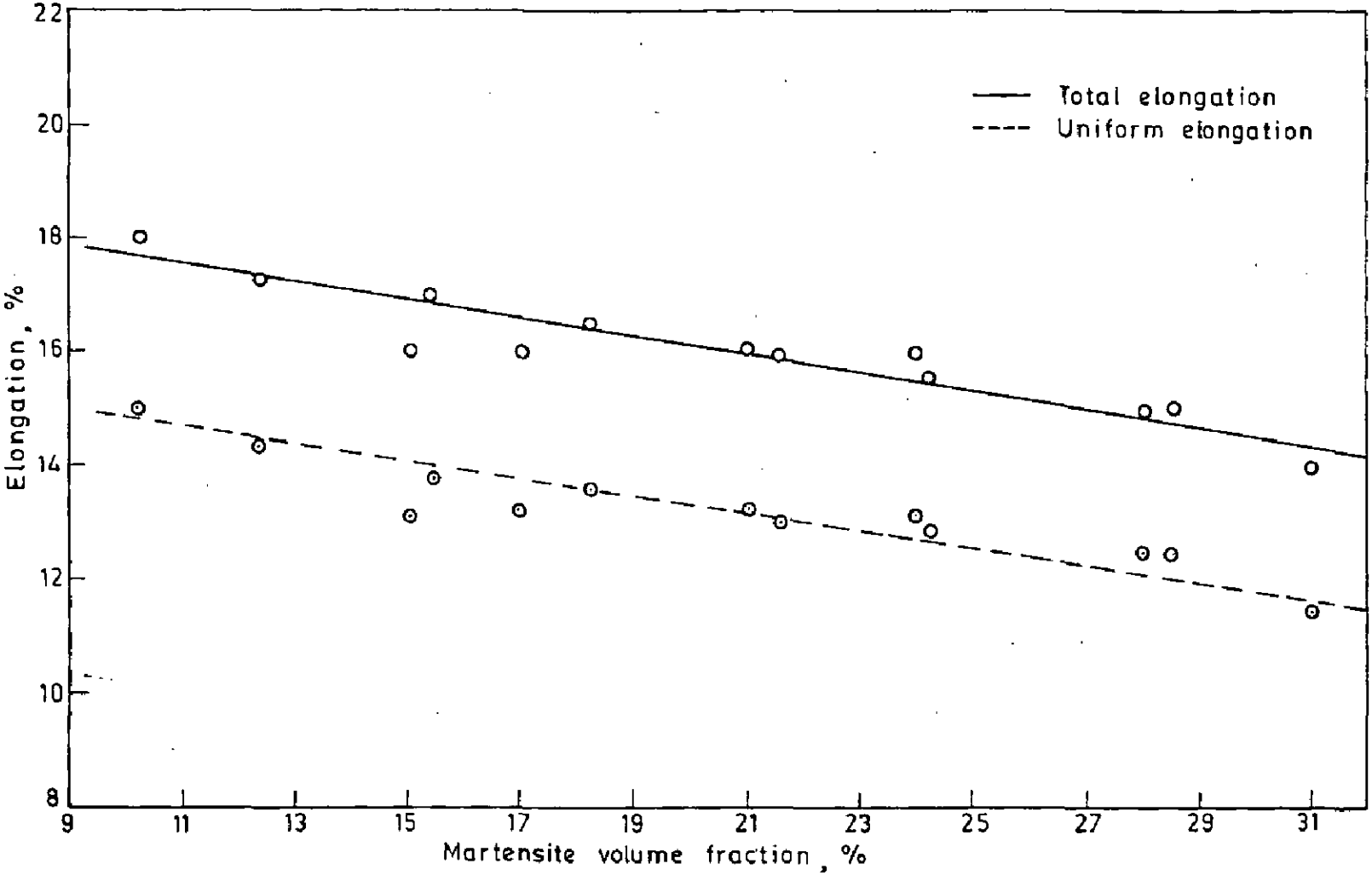

Fig. 5.25 _ Variation of uniform and total elongations as a function of martensite volume fraction in 0.115 percent carbon dual-phase steel

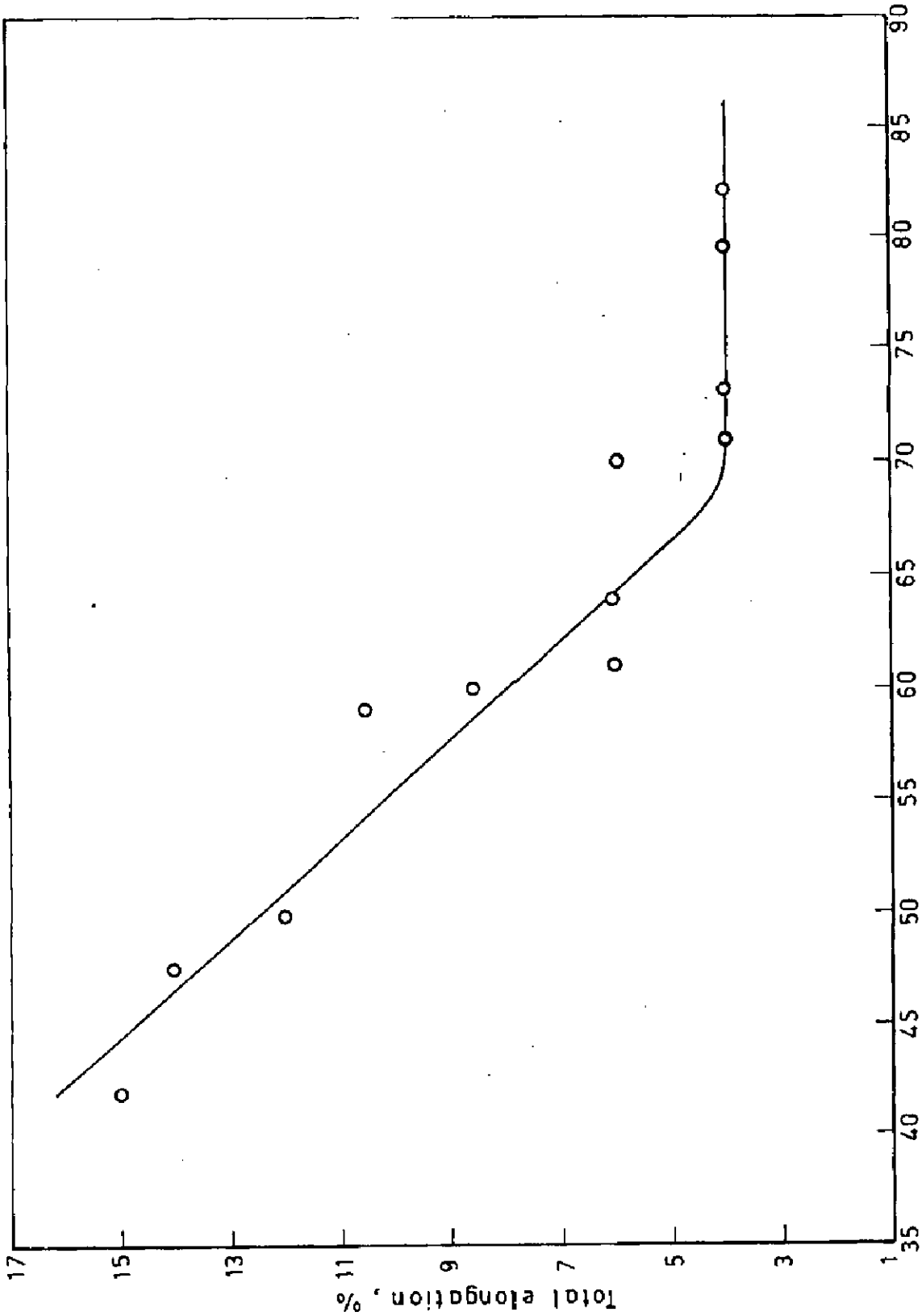

Fig.5.26_Variation of total elongation as a function of martensite volume fraction in 0.4 percent carbon dual-phase steel

The minimum value of ductility is, however, attained for DPS-A after 30 minutes of ICA-time at ICA-temperatures 740°C and 760°C but approximately after 15 minutes at 780°C. For DPS-B also a similar trend in variation of ductility with ICA-time at different ICA-temperatures is observed. However, for DPS-C, at 740°C ICA-temperature, the minimum ductility is attained at approximately 5 minute of ICA-time whereas at 760°C it reduces to 2 minute and at 780°C it is about 1 minute or even less.

5.3.4 Ductility Vs Strength

Variation of total elongation with yield strength (0.2 pct. off-set proof stress) of dual-phase steels DPS-A, DPS-B and DPS-C, is shown in Fig.5.27. It is clear from this figure that for DPS-A, the total elongation decreases linearly from 20 pct. at YS 225 MPa and ICA-temperature 740°C to 14 pct. as YS increases to 260 MPa at 780°C ICA-temperature. Similar trend of decrease in ductility measured as total elongation with an increase in the YS, is reflected for DPS-B also for which total elongation decreases from 17 pct. at 230 MPa YS at ICA-temperature 740°C to 14 pct. at 290 MPa YS and at 780°C ICA-temperature. It is also obvious from this figure that DPS-A and DPS-B show approximately a similar trend in fall in total elongation with respect to YS. However, in case of DPS-C, the total elongation first falls with an increase in YS and then remains constant with

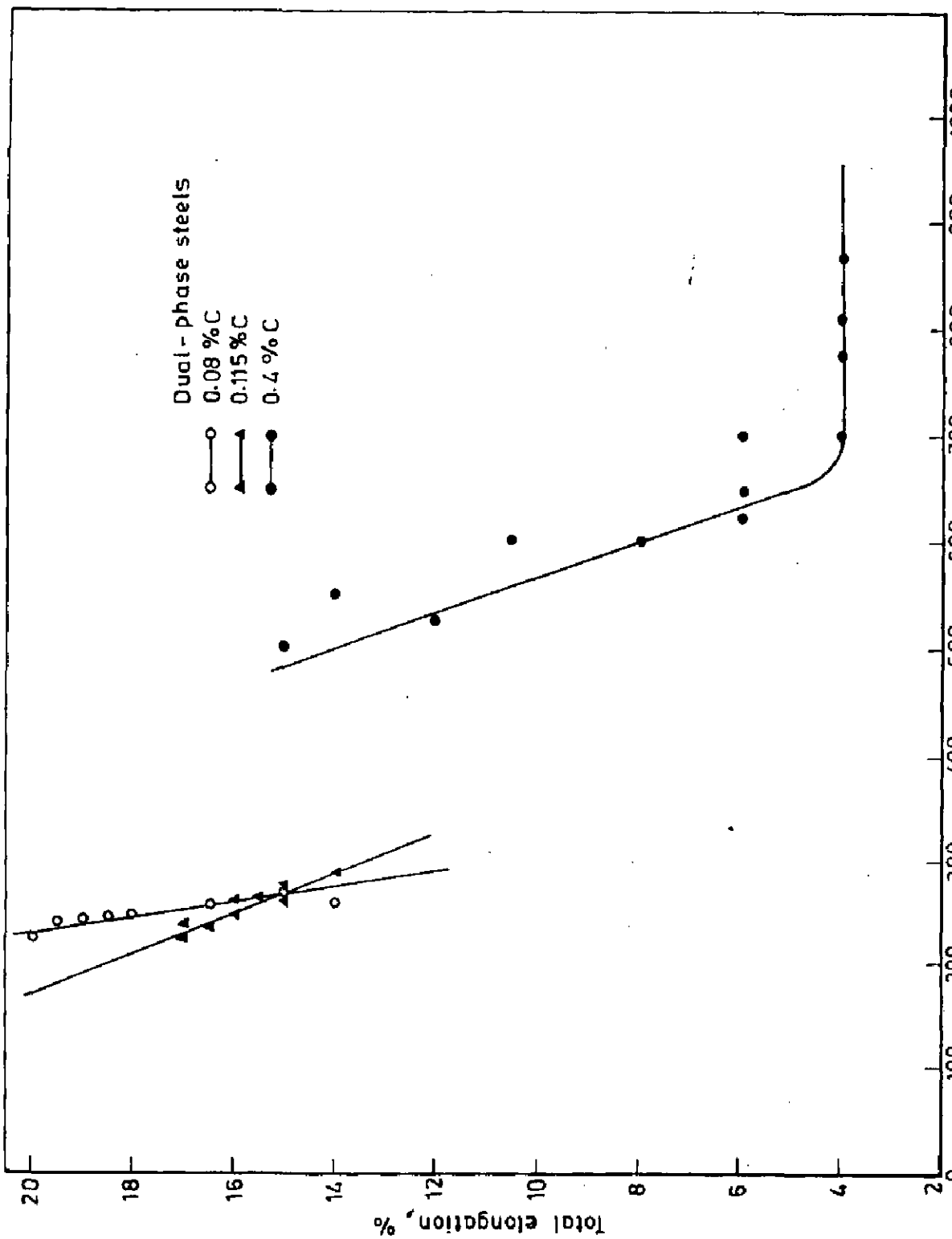

Fig.5.27_ Variation of total elongation vs yield strength for various dual-phase steels

further increase in the YS. For example the total elongation falls from 15 pct. at 500 MPa YS at ICA-temperature 740°C to 4 pct. at 685 MPa YS at 780°C ICA-temperature. It remains constant at this minimum value of 4 pct. total elongation as the YS is increased from 780 MPa to 860 MPa (maximum value obtained in the present investigation).

Variation of total elongation with UTS of dual-phase steels DPS-A, DPS-B and DPS-C, is shown in Fig.5.28 which also reflects to a similar trend of decrease and attainment of a constant minimum value as shown in Fig.5.27.

5.3.5 Formability

Variation of the mean plastic strain ratio, $\bar{R}$, an index of formability, as a function of the ICA-time of dual-phase steels DPS-A and DPS-B is shown in Figs.5.29 and 5.30 respectively. Fig.5.29 reveals that the $\bar{R}$-value for DPS-A initially decreases only slightly with an increase in ICA-time and then becomes constant. For example, for DPS-A, intercritically annealed at 740°C, the $\bar{R}$-value decreases from 1.1 to 1.0 as annealing time is increased from 1 minute to 10 minutes, but after this time, it remains constant at 1.0, even when the ICA-time is increased to 3 hours (Maximum time used in the present investigation).

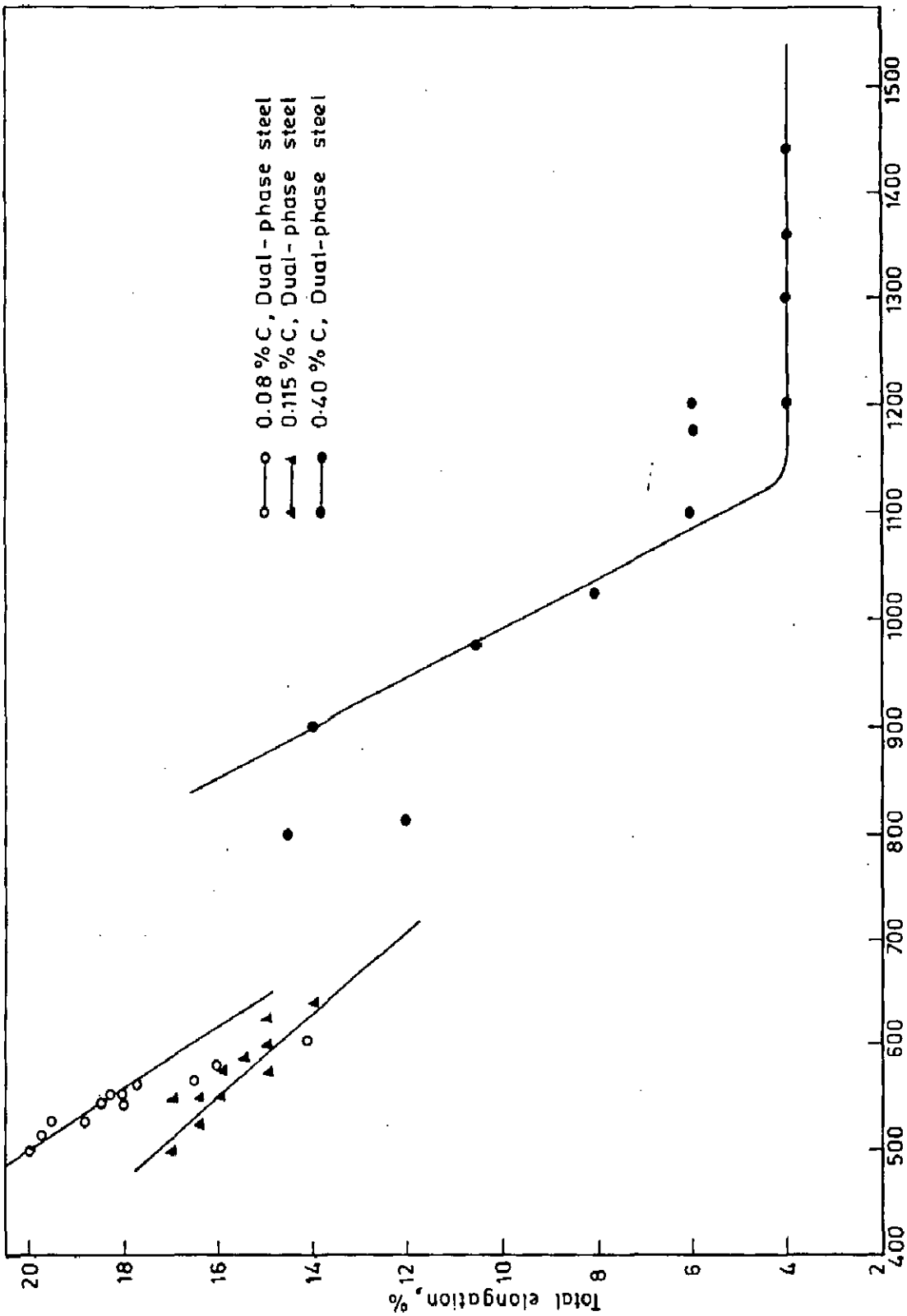

Fig. 5.28 – Variation of total elongation vs ultimate tensile strength of various dual-phase steels

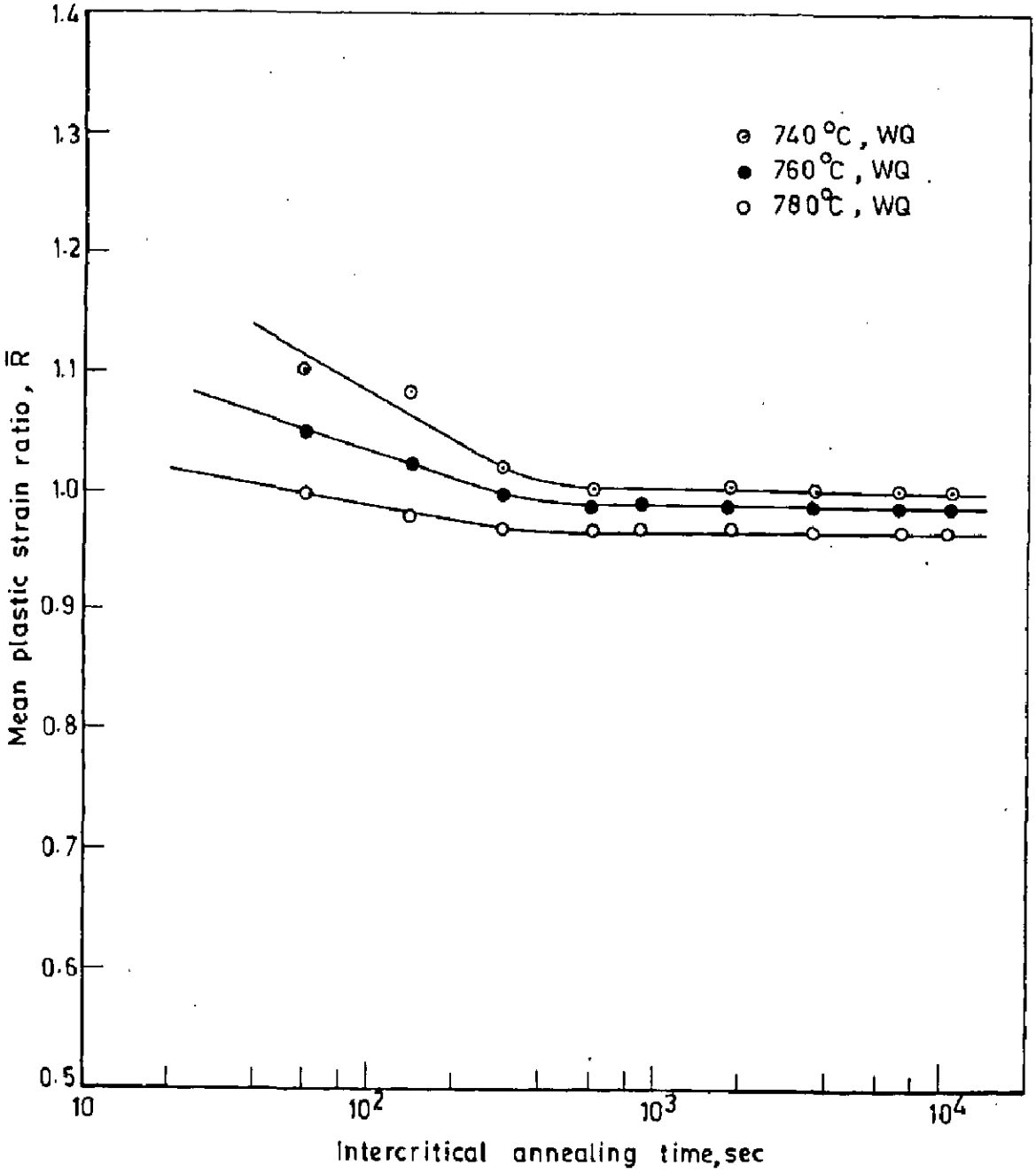

Fig.5.29 – Variation of mean plastic strain ratio $\bar{R}$ as a function of intercritical annealing time in 0.08 percent carbon dual-phase steels

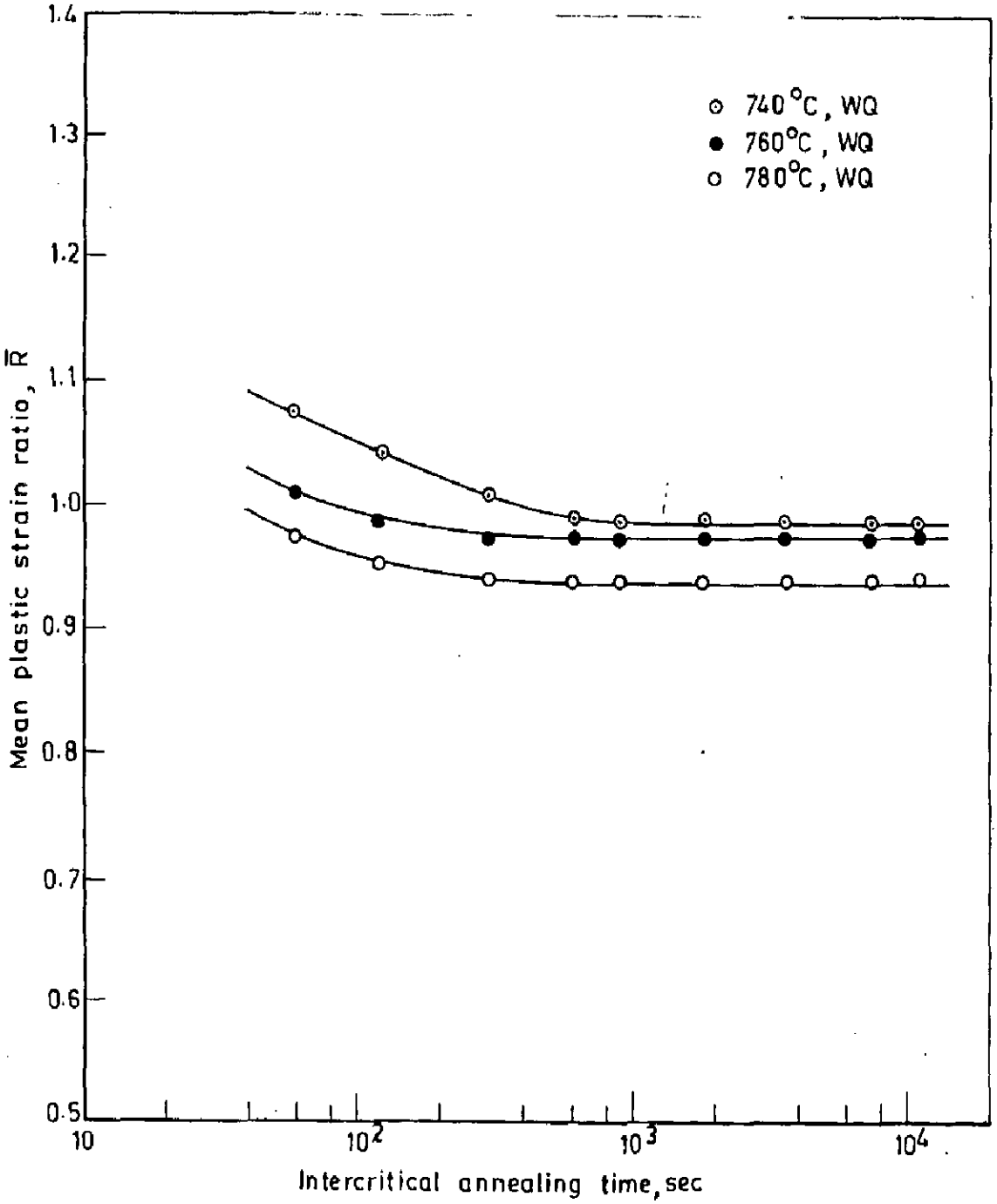

Fig.5.30 _ Variation of mean plastic strain ratio $\bar{R}$ as a function of intercritical annealing time in 0.115 percent carbon dual-phase steels

Similar trend is observed from Fig. 5.29 in the variation of $\bar{R}$ - values with ICA-time for this steel intercritically annealed at 760°C and 780°C. However, progressively lower $\bar{R}$ - values are observed when annealing temperature is increasesd. DPS-B also shows similar variation of $\bar{R}$ - values with anealing time as indicated in Fig. 5.30. However, lower $\bar{R}$ - values are observed for this steel for all ICA-temperatures and corresponding times as compared to those for DPS-A.

Variation of $\bar{R}$-values as a function of MVF of dual-phase steels DPS-A and DPS-B is shown in Fig. 5.31. Both these steels show similar trend in the variation of $\bar{R}$-values with respect to MVF.

The $\bar{R}$-value decreases initially rapidly with an increase in MVF and then slowly to become almost constant at high values of MVF. It is further to be noted that DPS-B shows lower $\bar{R}$ - values at all values of MVF as compared to those for DPS-A. $\bar{R}$ - values for DPS-C have not been measured due to much lower values of elongation obtained in this steel as compared to DPS-A and DPS-B.

5.3.6 Fractography

Fractured surfaces of several heat-treated samples of DPS-A, DPS-B and DPS-C, have been studied under Scanning Electron Microscope (SEM) and their transverse sections have been examined under optical microscope. It is observed that DPS-A shows ductile fracture at all ICA-temperatures viz.

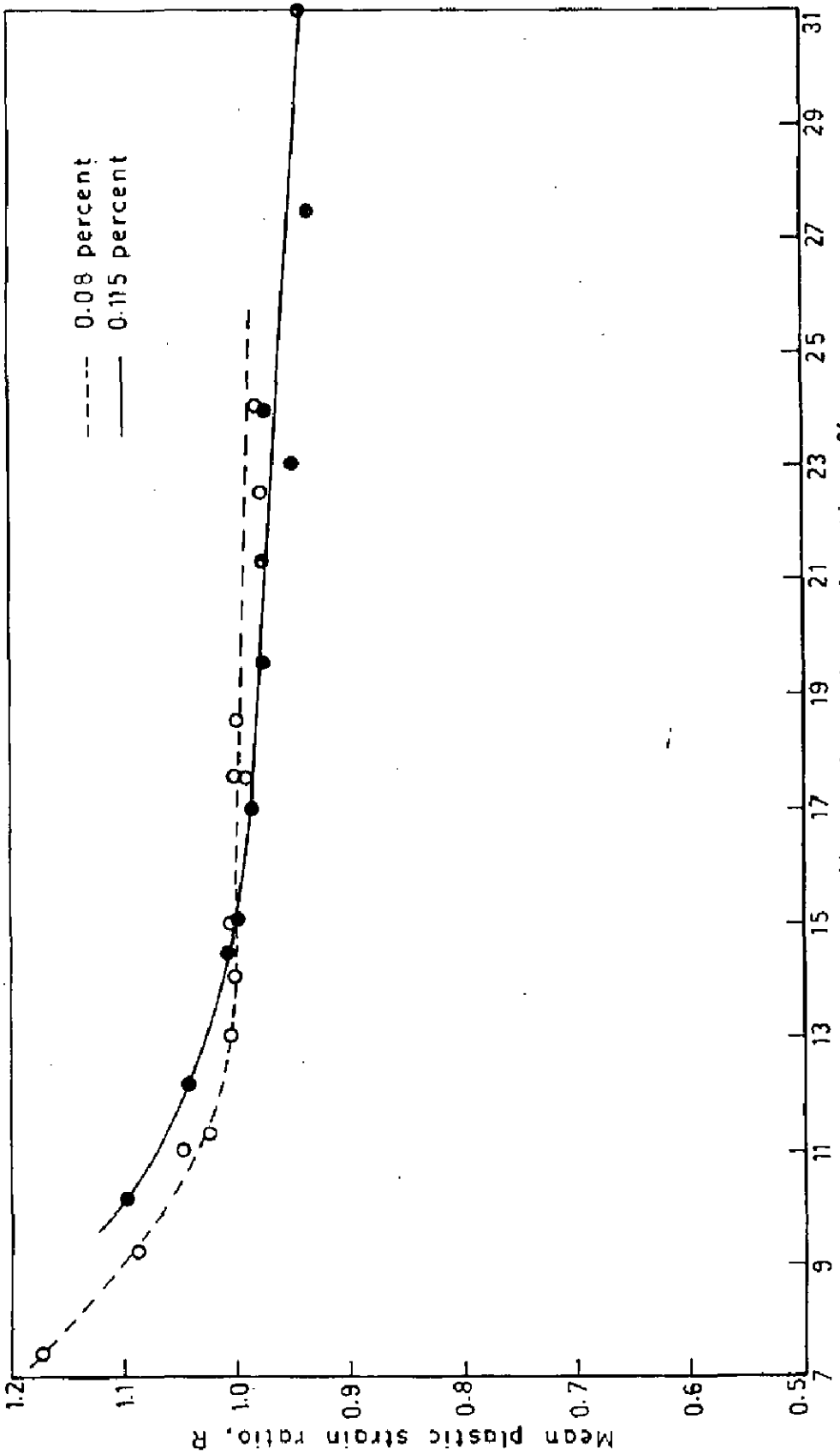

Fig.5.31_Variation of mean plastic strain ratio, $\bar{R}$ as a function of martensite volume fraction in 0.08 percent and 0.115 percent carbon dual-phase steels

740°C, 760°C and 780°C and for all ICA-times, right from 1 minute to 3 hours. To illustrate this point three fractographs of tensile fractured surface of DPS-A heat-treated respectively at 740°C for 1 minute, at 760°C for 10 minutes and at 780°C for 1 hour, are shown in Figs. 5.32 a-c.

DPS-B also shows similar ductile fracture at all ICA-temperatures and times. Three fractographs of tensile fractured surface of DPS-B with similar heat treatments as those used for DPS-A specimens are shown respectively in Figs. 5.33 a-c. The above fractographs for DPS-A and DPS-B specimens show dimples which are characteristic of ductile fracture. However, specimens of DPS-C show a different fracture behaviour. Specimens of this steel annealed for less than 5 minutes at ICA-temperatures of 740°C and 760°C, show ductile fracture as indicated in the fractographs presented in Figs. 5.34 a and b. However, fracture behaviour changes from ductile to a mixed mode of fracture after 5 minutes of annealing at 740°C and 760°C as shown in the fractographs in Figs. 5.35 a and b. The same behaviour is observed in DPS-C when intercritically annealed at 780°C for all annealing time i.e., right from 30 seconds to 3 hours. Figs. 5.36 a and b show two such fractographs of DPS-C intercritically annealed at 780° C for 30 seconds and 1 hour respectively. These fractographs show well defined cleavage fracture through martensite islands and dimpled fracture in the ferrite matrix. The extent of cleavage fracture increases with MVF.

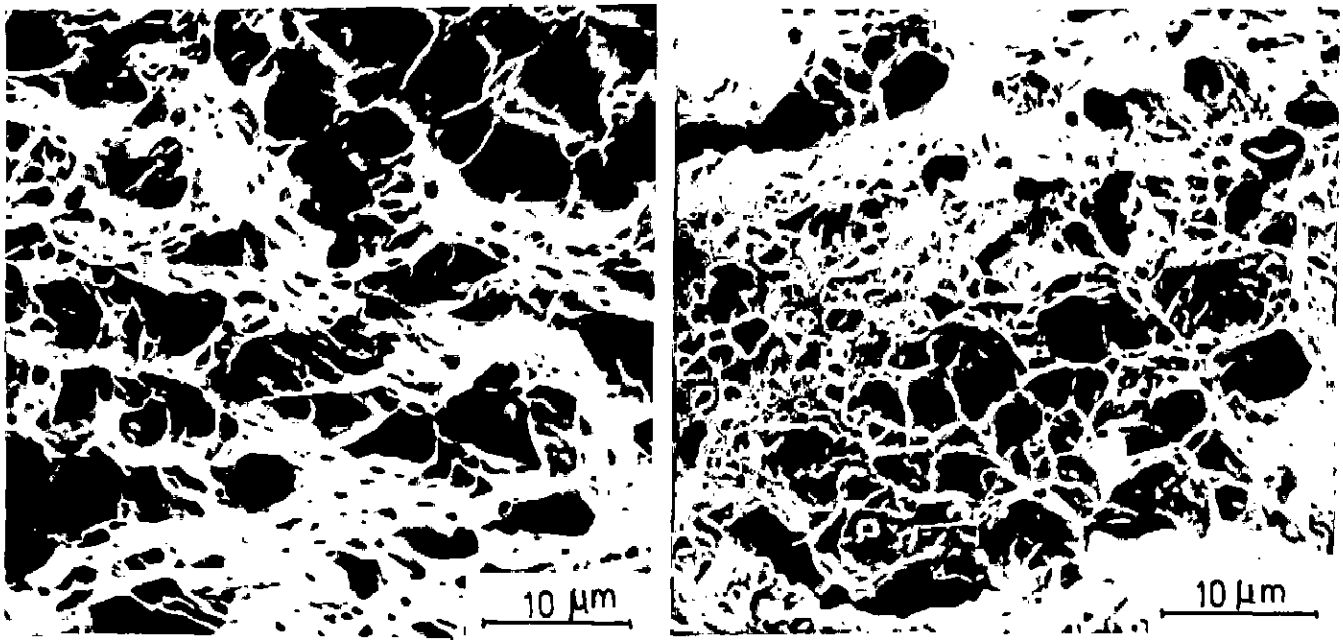

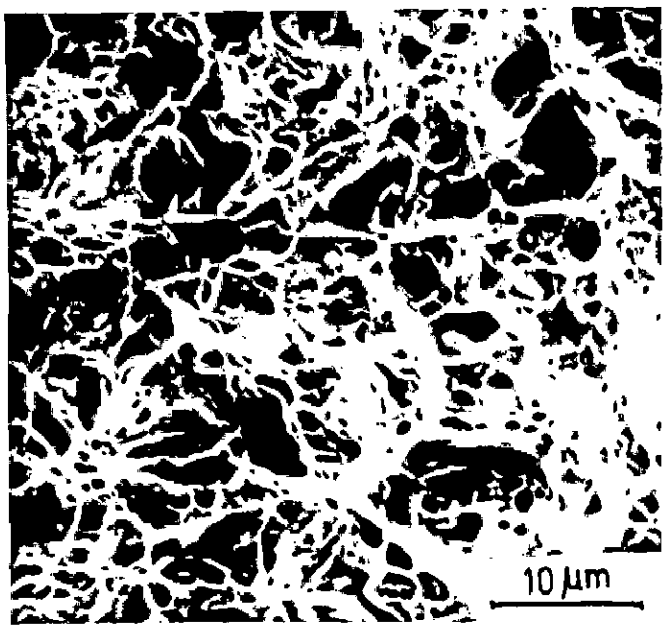

Fig. 5.32 _ SEM fractographs showing dimples in dual-phase steels - A
(a) 740 °C, 1min , WQ
(b) 760°C , 10min, WQ
(c) 780°C , 1 hr , WQ

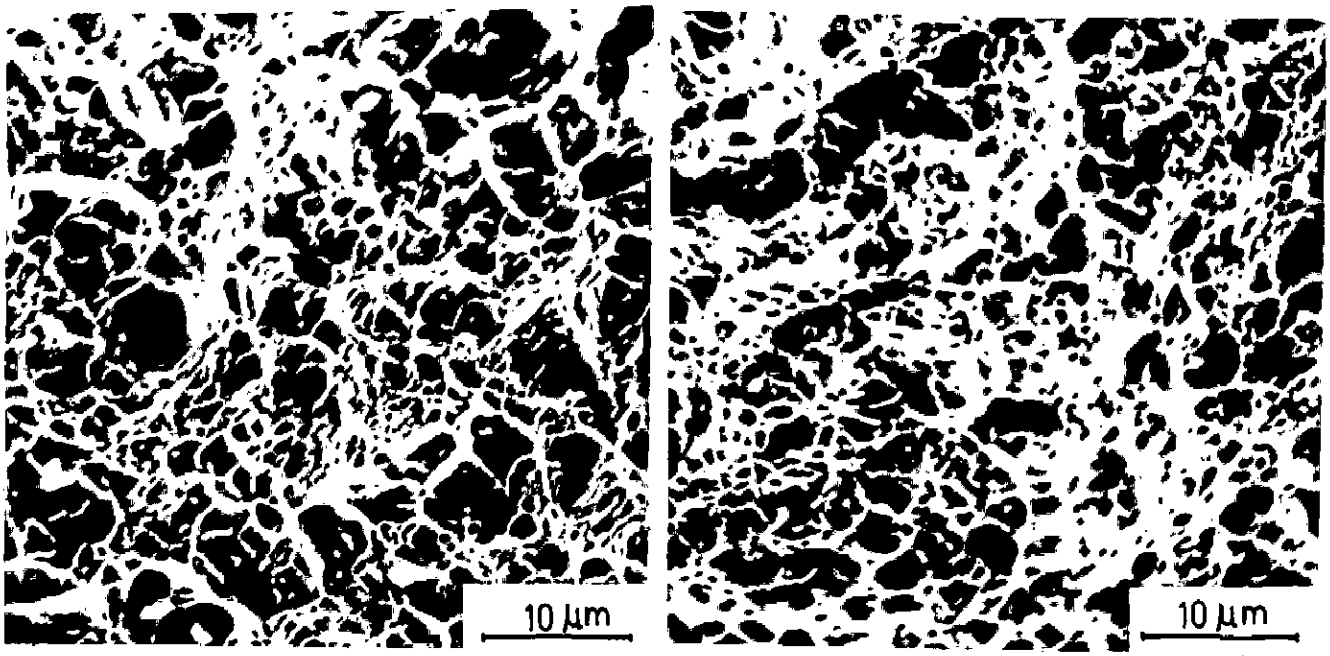

(a) (b)

(c)

Fig. 5.33 _ SEM fractographs showing dimples in dual-phase steels - B
(a) 740°C , 1 min , WQ
(b) 760°C , 10 min , WQ
(c) 780°C , 1 hr , WQ

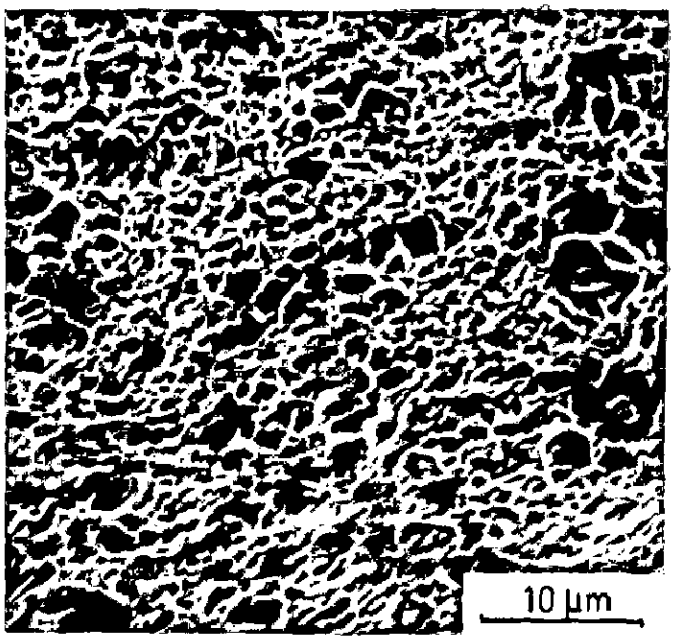

(a)

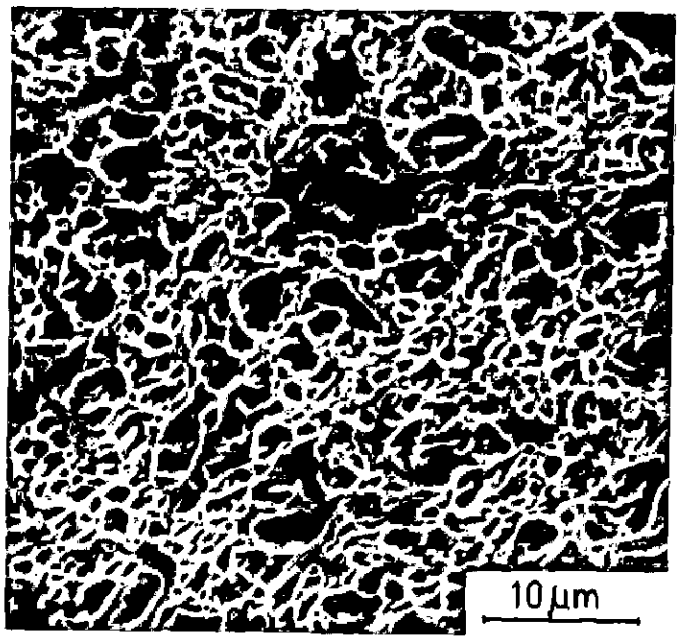

(b)

Fig. 5.34 _ SEM fractographs showing dimples in dual-phase steel - C
(a) 740°C , 1min , OQ
(b) 760°C , 1min , OQ

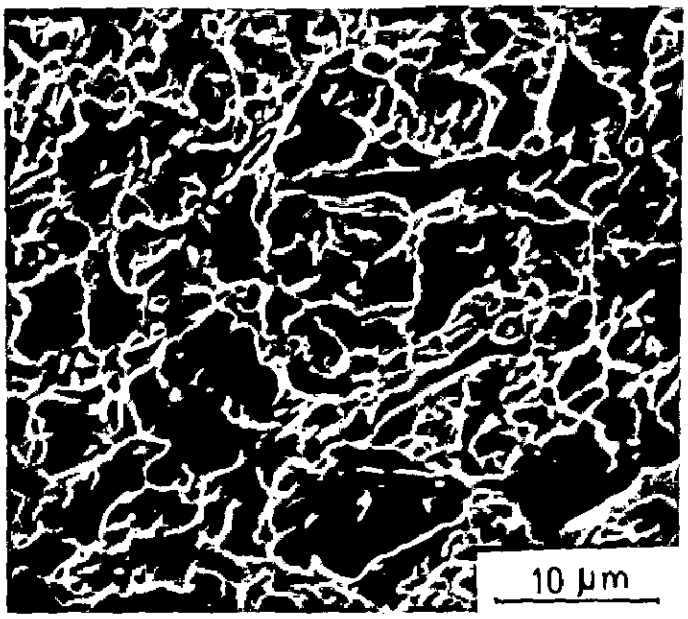

(a)

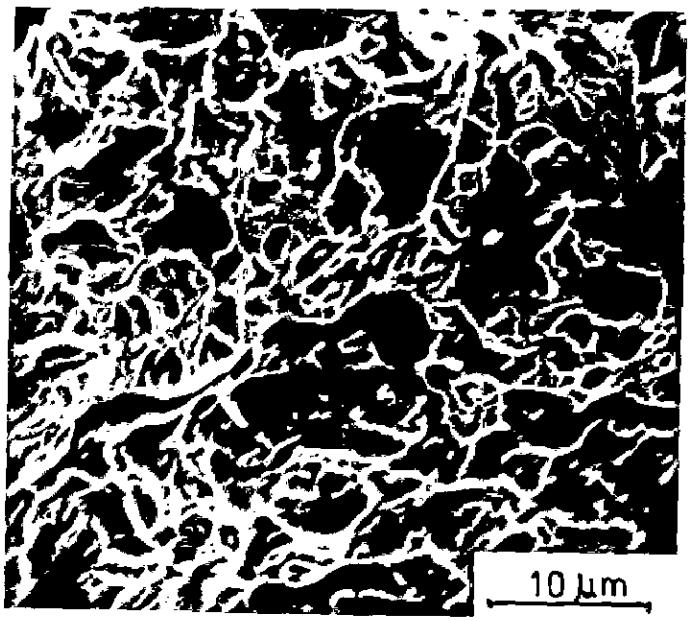

(b)

Fig. 5.35_SEM fractographs showing dimples and cleavages in dual-phase steel-C
(a) 740°C, 10 min, OQ
(b) 760°C, 10 min, OQ

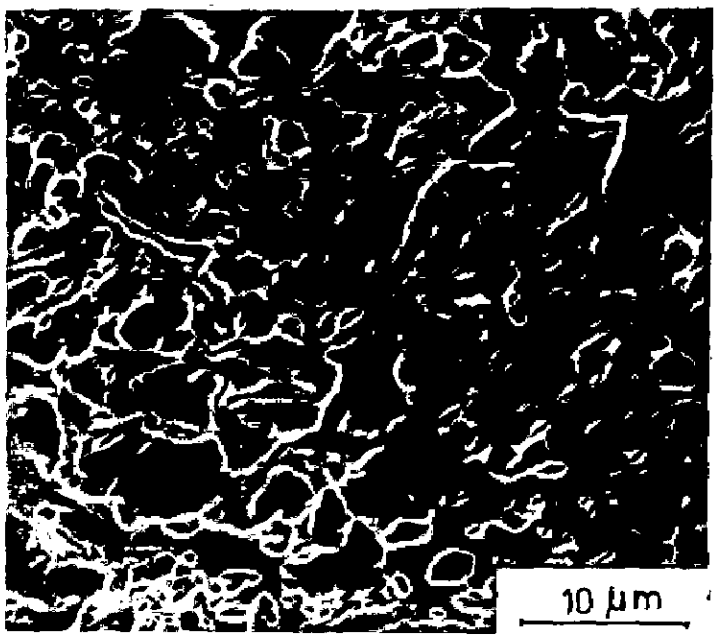

(a)

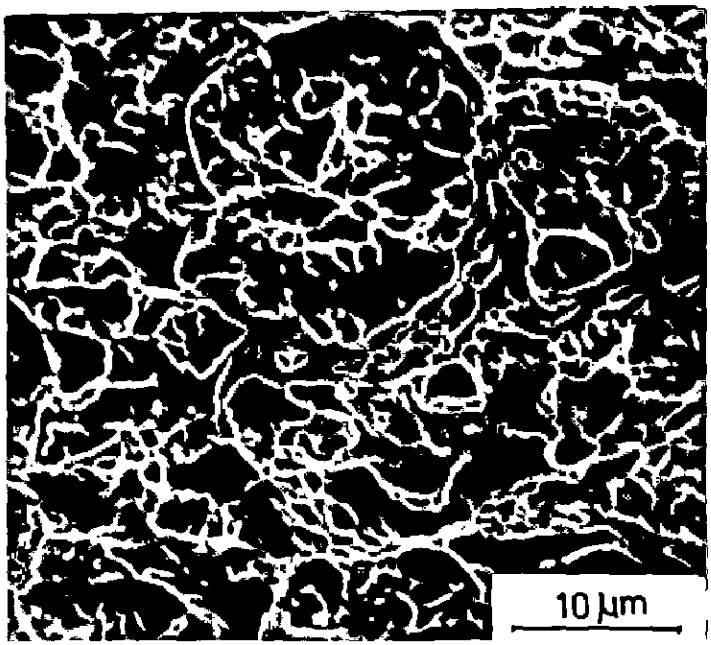

(b)

Fig. 5.36 _ SEM fractographs showing dimples and cleavages in dual-phase steel-C
(a) 780 °C, 30 sec, OQ
(b) 780 °C, 1 hr, OQ

The optical micrographs of cross-section of fracture surface of DPS-A and DPS-C are shown in Figs. 5.37 a and b respectively. Fig. 5.37a shows a zig-zag crack path passing predominantly through the interface of ferrite and martensite, whereas Fig. 5.37 b reveals that although the cracks in the specimen are also zig-zag but these are mostly along the martensite phase. Specimens of DPS-B show more or less similar crack-path as those shown by specimens of DPS-A and hence not presented.

5.4 Discussion on Results

5.4.1 Strengths of dual-phase steels.

The continuous yielding behaviour observed in tensile load-elongation curves of hypo-eutectoid plain-carbon dual-phase steels DPS-A, DPS-B and DPS-C studied in the present investigation as shown in Figs. 5.9 - 5.11 respectively, is in agreement with the observation of Rashid [3,63], Davies[44], Kim and Thomas [67] Tamura etal [65] and Luis etal [46]. The non-occurence of yield-point in these dual-phase steels with ferrite-matrix is attributed to the high dislocation density and residual stresses generated in the ferrite phase immediately surrounding the martensite islands. The transformation of islands of austenite in ferrite matrix into martensite on quenching is accompanied by approximately 4 pct. expansion in volume which is accomodated in the ferrite phase itself resulting in its plastic deformation. The presence of high dislocation density in ferrite matrix of dual-phase steel

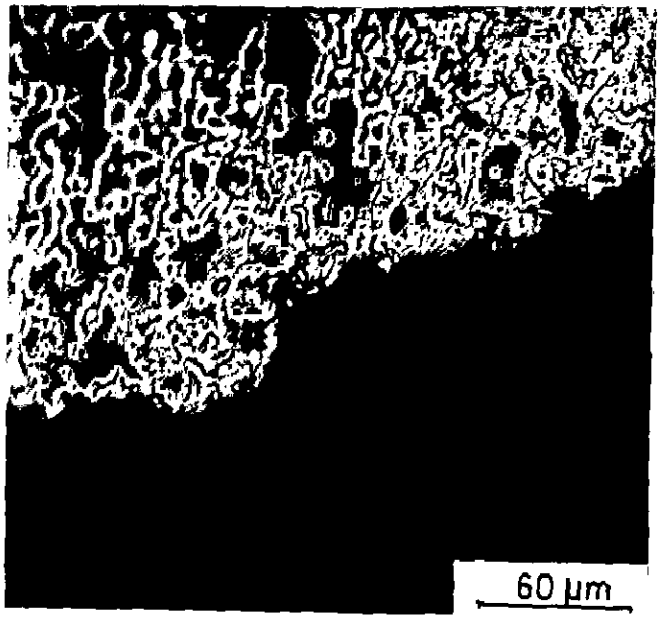

(a)

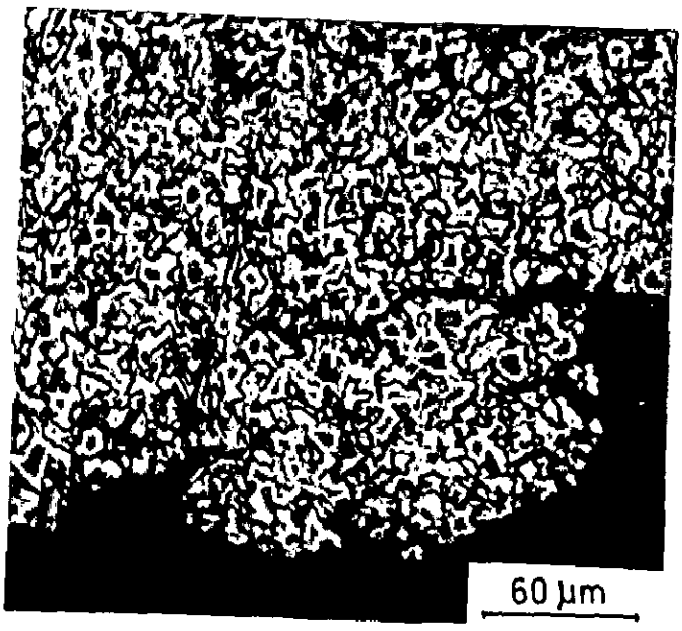

(b)

Fig. 5.37_Optical micrographs of transverse section of fractured surface showing zig-zag cracks
(a) Dual-phase steel - A
(b) Dual-phase steel - C

is testified by Fig. 5.8c, which represents a TEM micrograph of a typical DPS-A specimen intercritically annealed at 740°C for 10 minutes followed by water quenching. In this micrograph the high dislocation density is clearly visible in the bright ferrite matrix and the adjoining black regions represent the martensite phase.

The increase in yield strength (YS) and ultimate tensile strength (UTS) of dual-phase steels with an increase in intercritical annealing time (ICA-time) at any specific intercritical annealing temperature (ICA-temperature) is attributed to the formation of increased amount of austenite during austenitisation and martensite on subsequent quenching. As indicated in section 5.2 for DPS-A intercritically annealed at 740°C for 1 minute, 5 minutes and 10 minutes of annealing time, yields respectively 7.4, 11.4 and 13.0 pct. MVF. The MVF value then remains constant after 10 minutes till 3 hours of ICA-time. Reason for the increase in austenite/martensite volume fraction with ICA-time, has already been explained on the basis of three stages of austenite formation during intercritical annealing of hypo-eutectoid steel in section 2.2.1. Due to this increase in the volume fraction of martensite which is a strong and load-bearing phase in the dual-phase steel, the YS and the UTS increase as also shown in Fig. 5.12. After 10 minutes of ICA-time, maximum value of MVF is reached and increasing the ICA-time beyond this value, does not result in any further change in the value of MVF. However, as

will be noted from the data presented in Table 5.1, after 15 minutes of ICA-time, both the YS and the UTS start falling till 3 hours of ICA-time. One reason for this decrease in the YS and the UTS of DPS-A, is the start of grain growth of ferrite phase which is evident from the optical micrograph of this steel, shown in Fig. 5.8a intercritically annealed at 740°C for 1.5 hour. Another reason for the decrease in the YS and the UTS for longer ICA-times, is a decrease in the hardness of martensite phase and a slight increase in the hardness of ferrite phase due to the equilibration of carbon between austenite and ferrite [19]. The variation of microhardness of martensite and ferrite phase with ICA-time is shown in Fig. 5.38 for DPS-A.

The same reasoning is extended to explain the variation of YS and UTS with ICA-time of DPS-A, intercritically annealed at 760°C and 780°C temperatures. However, the reason for increased value of YS and UTS with increasing ICA-temperatures to 760°C and 780°C for a given ICA-time as compared to those in DPS-A, heat-treated at 740°C is attributed to the increased MVF in the dual-phase structure and the higher equilibrium amount of martensite as evident from the microstructures shown in Figs. 5.5 a and b.

Variation of the YS and the UTS with ICA-time of dual-phase steels DPS-B and DPS-C is also due to same reasoning. However, higher values of the YS and the UTS of these steels viz. DPS-B and DPS-C as compared to those for DPS-A for a

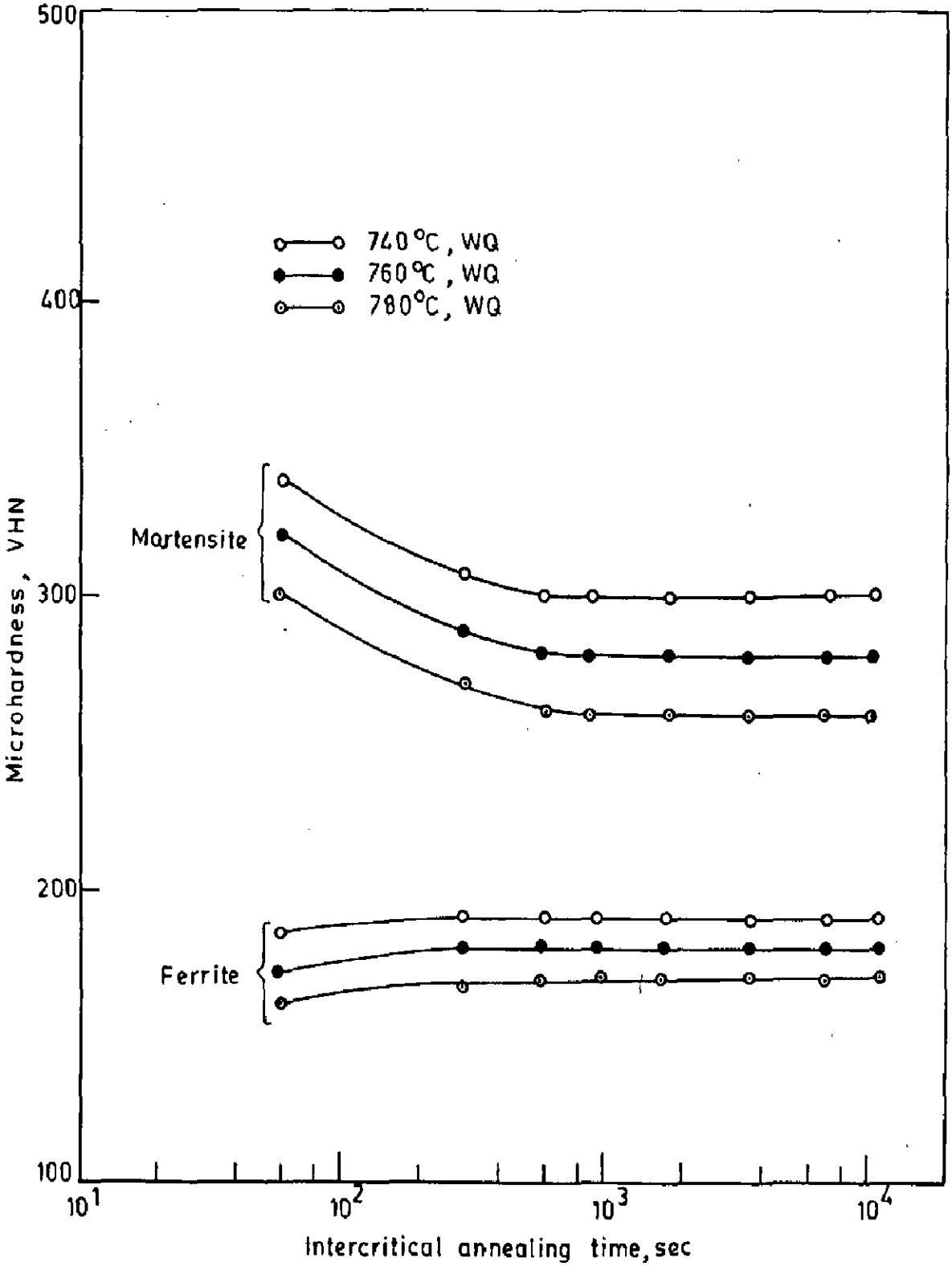

Fig. 5.38 – Variation of microhardness of ferrite and martensite phases of dual phase steel - A as a function of intercritical annealing time for different intercritical temperatures

given intercritical annealing time and temperature is attributed to their higher carbon content e.g., 0.115 pct. for DPS-B & 0.4 pct for DPS-C as compared to 0.08 pct. for DPS-A plus the finer grain size of DPS-C. The more the carbon content, the higherwillbe the MVF for given intercritical annealing time or temperature. The microstructural evidence of increased MVF with increasing carbon content is shown in Figs. 5.6 b and 5.7 b respectively. It has also been observed in chapter - 6 that the higher the carbon content of the steel, the faster is the kinetics of austenitisation.

The experimental values of UTS of dual-phase steel DPS-A, is plotted in Fig. 5.18 as function of MVF together with theoretically calculated values utilizing Prasad's expression Eq. (3.1) developed for a composite metal having spherical second phase ductile particles embedded in a brittle matrix. The calculated values show a negatives slope, reflecting to a decrease in UTS with increasing values of MVF. This is because Prasad's expression is not directly applicable to the case of dual-phase steels which have hard and brittle non-spherical martensite particles embedded in a matrix of ductile ferrite phase. Further, in the shear-lag analysis, the second phase spherical particles can not take up load exceeding that of the matrix. Hence, the spherical second phase embedded particles can not act as superior load-bearing

phase as compared to the matrix and hence can not result in an improvement in the overall load-bearing capacity of the dual-phase steels.

However, the second phase embedded particles act as obstacles to the movement of dislocations in the ferrite matrix according to Ashby's theory of work-hardening (49). When this work-hardening or strain-hardening factor after Ashby [49], is incorporated in Prasad's expression to yield Eq.(3.3) and values of UTS are calculated using this expression, an increasing trend is observed. It can be observed that from Fig. 5.18 that the experimental and calculated values using Eq. (3.3) are still far apart. This deviation in the two values is attributed to non-spherical shape of martensite particle assumed in the theoretical analysis of dual-phase steels. To verify this statement the modified Prasad's expression Eq. (3.3) is further corrected for the shape of embedded particles. For this purpose embedded martensite islands or particles are treated as cylindrical particles with hemi-spherical ends and an expression for UTS Eq. (3.22) is developed based on shear-lag analysis. Calculated values of UTS using this expression Eq.(3.22) are also plotted in Fig. 5.18 and show a good correspondence with the experimental results.

Similar theoretical calculations of UTS have been made for DPS-B and DPS-C and the calculated and experimental

values of UTS are plotted in Figs.5.19 and 5.20 respectively. These also show good correspondence, testifying to the applicability of the proposed model for theoretical calculation of UTSof dual-phase steels.

5.4.2 Ductility of dual-phase steels

The decrease of total-&uniform- elongations of dual-phase steels, DPS-A, DPS-B and DPS-C, observed in the present work with increasing ICA-time or ICA-temperature and also MVF, is in agreement with the results obtained by Davies [53], Kim and Thomas [67] and Luis et al [46]. With increase in ICA-time at any ICA-temperature, the MVF increases till its equilibrium amount is reached. As discussed earlier, an increase in the MVF causes increase in the yield and tensile strengths as the martensite phase is strong, hard and load-bearing and is dispersed in the ductile ferrite matrix. Due to this increase in strength of dual-phase steel, its ductility measured in terms of uniform-and total-elongations falls. However, for longer ICA-time, say beyond 15 minutes, for DPS-A at 740°C both the yield and tensile strengths start falling. It has also been observed that although the strength falls yet the ductility does not improve and attains almost a constant value i.e., 14 pct. total elongation and 11 pct. uniform elongation beyond 30 minutes ICA-time. This initial decrease in ductility followed by a constant value with a continuous decrease in strength

of DPS-A is attributed to loss of martensite strength (hardness) caused by redistribution of carbon in the 3rd stage of growth of austenite. At the same time, a slight increase in the hardness of ferrite is also noted as shown in Fig.5.38. Therefore, the overall ductility remains constant during longer annealing time. The DPS-A exihibits a decrease in ductility as the ICA-temperature is increased from 740°C to 760°C and then to 780°C. This decrease in ductility with an increasing ICA-temperature is attributed to an increase in the MVF in the dual-phase structure at corresponding ICA times as reflected from microstructures shown in Figs. 5.5a and b.

The DPS-B shows lower values of both the total and uniform-elongations at all ICA-temperatures and ICA-times as compared to the corresponding values of these parameters for DPS-A. This behaviour is attributed to the fact that DPS-B has a higher carbon content than DPS-A and hence results in higher MVF on similar treatments.

The DPS-C shows lowest values of total- and uniform-elongations at all values of ICA-temperatures and ICA-times as compared to the corresponding values for DPS-A and DPS-B. Since DPS-C contains highest amount of carbon viz., 0.4 pct. it possesses highest MVF. Therefore, the martensite islands in DPS-C are very much interconnected. This results in easier path for crack propagation and hence lower ductility.

Variation of ductility of dual-phase steels can also be explained quantitatively with the help of model developed by Mileiko [60] which has been first applied for Davies [53] for the interpretation of results on ductility of dual-phase steels. For this purpose the dual-phase steel is considered as a fibre-composite made of two ductile phase viz., ferrite and martensite which are tested in tension parallel to the fibre-axis. It is further assumed that there is good interface matching leading to load transfer between the phases. Knowing the mechanical properties of the two component phases viz., the martensite and ferrite, it is possible to calculate the change in uniform elongation measured as the strain-hardening exponent, n, with volume fraction, V, of the martensite phase from the expression.

$$V = \frac{1}{1 + \beta\left(\frac{\varepsilon_C - \varepsilon_m}{\varepsilon_F - \varepsilon_C}\right)\varepsilon_C^{(\varepsilon_m - \varepsilon_F)}} \qquad \ldots (5.5)$$

where,

$$\beta = \left(\frac{\sigma_m}{\sigma_F}\right) \frac{(\varepsilon_F)^{\varepsilon_F}}{(\varepsilon_m)^{\varepsilon_m}}, \left(\frac{\exp \varepsilon_m}{\exp \varepsilon_F}\right) \qquad \ldots (5.6)$$

In the above expressions, the symbols σ_m and σ_F represent the tensile strengths of the martensite and ferrite phases respectively, and symbols ε_C, ε_m and ε_F represent respectively the true uniform strains or the corresponding n-values for the dual-phase steel considered as composite, the martensite phase and the ferrite phase, Davies [53] has shown

$$\varepsilon_C = n_C \qquad \ldots (5.7)$$

$$\varepsilon_F = n_F \qquad \ldots (5.8)$$

$$\varepsilon_m = n_m \qquad \ldots (5.9)$$

For theoretical calculations of strain-hardening exponent, n_C, for the dual-phase steel considered as a composite, following empirical values of different parameters representing mechanical properties of ferrite and martensite phases, after Davies [53] have been used

$$\sigma_m = 2000 \text{ MPa}, \quad \varepsilon_m (\text{or } n_m) = 0.07$$

$$\sigma_F = 415 \text{ MPa}, \quad _F(\text{or } n_F) = 0.31$$

Substituting of these values and different values of V, in Eq.(5.5) and Eq.(5.6), the corresponding theoretical values of n_C are calculated and plotted as a function V in Fig.5.39, together with the values of n_C measured experimentally for two dual-phase steels DPS-A and DPS-B. It can be observed from Fig.5.39 that the experimental plot lies below the theoretical plot. However, the nature of variation for both n_C (theoretical) and n_C (experimental) with V, viz., MVF for DPS-A and DPS-B is similar. The lower values of n_C measured experimentally as compared to the theoretically calculated values, are attributed to the fact that both dual-phase steels viz., DPS-A and DPS-B are produced by water quenching which enhances the carbon content of ferrite [68] and reduces both the uniform-and total-elongations. The agreement of n(experimental) with n(theoretical) indicates

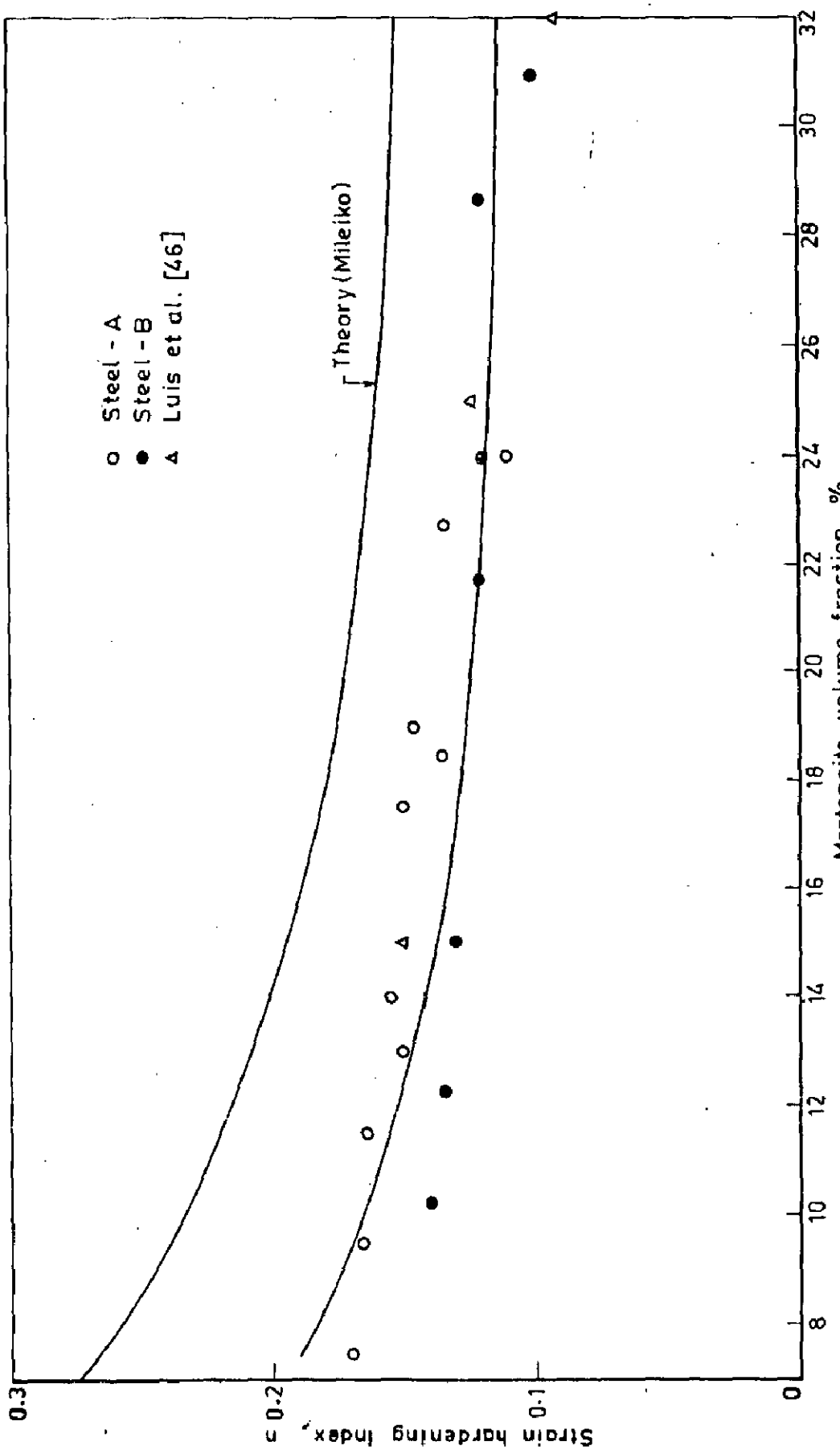

Fig.5.39 _ A comparison of the calculated and observed n values from theory of Mileiko [60]

that although the description of martensite in dual-phase steels is not in the form of fibres, the theory gives a reasonable description of the results. The condition of good interface matching assumed in the Mileiko's theory [60] will be better met in dual-phase steels with the second phase formed in situ than in any artificial composites.

5.4.3 Formability of dual-phase steels

It is obvious from Figs. 5.29-5.30 that the mean plastic strain ratio, $\bar{R}$, an index of formability, initially decreases with an increasing ICA-time and then becomes constant at any selected ICA-temperature. The initial decrease in the value of $\bar{R}$ with ICA-time for DPS-A, intercritically annealed at 740°C, is attributed to the increase in martensite volume fraction (MVF). Further, the value of $\bar{R}$ does not decrease beyond 10 minutes of ICA time for this steel because the MVF does not change after this ICA-time i.e., beyond the stage of attainment of maximum value of MVF. Although longer annealing time should improve the $\bar{R}$-values. Since this results in grain coarsing of ferrite grains. Blickwede [89] has observed an increase in values of $\bar{R}$ with increase in grain size of ferrite in case of rimming steels containing Ti. The attainment of a low constant value of $\bar{R}$ in the present work beyond 10 minutes of ICA-time is attributed to carbon content trapped in the ferrite phase on water quenching which is known to adversely affect the formability. It is

further to be noted that the DPS-A shows progressively lower values of $\bar{R}$ as the ICA-temperature is raised from 740°C to 760°C and then to 780°C for all values of ICA-times. This decrease is attributed to the increased value of MVF with an increase in the ICA-temperature. The initial decrease in $\bar{R}$ values with an increase in ICA-time and hence MVF at any selected ICA-temperature is also attributed to the activation of different slip system in the ferrite matrix adjacent to martensite islands than those which would have operated in the absence of martensite phase. It is because of the fact that the slip-systems of the ferrite phase get constrained due to the presence of harder martensite phase [76]. Hultgren [73] and Matsudo et al [74] have already established that the $\bar{R}$-value is controlled by the texture of the sheet. For samples of steel sheets containing many crystal with their <111> axis normal to the plane of the sheet, the $\bar{R}$-value increases, but for samples having many <100> crystals, in this direction, it decreases. Okamoto et al [75] have shown that the rate of heating during intercritical heat treatment also affect the $\bar{R}$-value of dual-phase steels. However, in the present investigation, the heating rate has been kept constant for all experimental runs and effect of this parameter has not been studied. The DPS-B also exhibits similar behaviour as that of DPS-A. However, it shows lower $\bar{R}$-values at all ICA-temperatures and ICA-times as compared to those for DPS-A. This difference in behaviour is attributed to the

higher carbon content of DPS-B as compared to the DPS-A. Hence higher MVF at all ICA-temperatures and - times.

Variation of $\bar{R}$-values with MVF for DPS-A and DPS-B also depicts similar behaviour. The $\bar{R}$-values decreses with increasing vlaue of MVF. It has also been observed that both DPS-A and DPS-B show lower $\bar{R}$-values as compared to those for these steels in the normalised state. This decrease is attributed to the higher strength and lower ductility of dual-phase steels DPS-A and DPS-B as compared to those of steel-A and steel-B respectively in the normalised state.

It is further to be noted that the trend of variation of $\bar{R}$-values with ICA-time at any desired ICA-temperature for DPS-A and DPS-B is in agreement with the results obtained by Okamato et al [75] on low alloy dual-phase steels. However, the $\bar{R}$-values obtained in their work are normally greater than the values obtained for DPS-A and DPS-B in the present work and this difference is attributed to higher uniform elongation of their steels studied as compared to those studied in the present investigation and also because water - quenching has been used in the present work which adversely affect the ductility measured in terms of the uniform-and total-elongations.

5.4.4 Fracture of dual-phase steels

Ductile fracture has been observed for all samples of dual-phase steels DPS-A and DPS-B studied in the present

investigation. This is attributed to lower values of martensite volume fraction (MVF) in the dual-phase steels. It must, however, be noted that the DPS-B contains higher carbon viz., 0.115 wt. pct. as compared to 0.08 wt. pct. of DPS-A. Inspite of this difference, the amount of martensite formed in DPS-B at all ICA-temperatures and - times, is not sufficient to cause brittle fracture.

It is further to be noted that the DPS-C depicts ductile fracture when intercritically annealed for less than 5 minutes at 740°C and at 760°C which is attributed to their lower martensite volume fraction. However, beyond this ICA-time, fracture mode changes from ductile fracture to mixed fracture or the ductile plus brittle fracture. This transition in fracture mode is also attributed to the increased MVF in the dual-phase structure, e.g., the MVF increases from 47.5 pct. to 64 pct. at 740°C as the ICA-time is increased from 1 minute to 5 minutes for this steel. It has also been observed by optical micrographs that martensite islands in the structure are highly interconnected as shown in Fig.5.7b. These interconnected martensite islands provide a easier path for crack-propagation and hence fracture. Similar arguments is extended to explain mixed-mode of fracture after 5 minutes of ICA-time at 760°C ICA-temperature.

It is further to be noted tht the DPS-C shows a mixed mode of fracture i.e., dimples as well as cleavages on the

fractured surfaces intercritically annealed right from 30 seconds to higher annealing time at 780°C. This is attributed to the fact that at 780°C even annealing at 30 seconds of ICA-time results in approx. 60 pct. of MVF in the dual-phase structure which is approximately equal to MVF obtained while annealing at 760°C for 5 minutes of ICA-time. Hence the fracture mode of sample intercritically annealed at 780°C for 30 seconds is equivalent to that of DPS-C intercritically annealed at 760°C for 5 minutes. It is also clear that the DPS-C intercritically annealed at 780°C for longer annealing time viz., 10 minutes, show higher extent of cleavage fracture than this steel intercritically annealed at 780°C for 30 seconds. This observation is obvious due to the higher value of MVF obtained viz., 82 pct. at 780°C and 10 minutes ICA-time and hence even greater amount of interconnected martensite islands and therefore easier crack propagation through the martensite phase.

The transverse section of the fractured surface of DPS-A reveals that the crack path is zig-zag and it passes through mostly the ferrite martensite interface. Reason for this preferred propagation of crack along the ferrite martensite interface is because of ductile and tough nature of ferrite phase as compared to brittle and strong nature of martensite phase. The resultant differential strain in ferrite and martensite phases creates a very high shear

stress at the interface resulting in debonding of ferrite and martensite phases and hence the fracture. Since DPS-A has relatively lower amount of martensite the interface does not provide continuous path for crack-propagation and crack has to pass through the ferrite grains mostly causing a ductile fracture. When the amount of martensite increases, the extent of crack-propagation through martensite - ferrite interface increases resulting in more brittleness as observed in DPS-C.

CHAPTER - 6

NON-ISOTHERMAL KINETICS OF AUSTENITISATION AND PREDICTION OF INTERCRITICAL TRANSFORMATION TIME

In this Chapter, results of study of non-isothermal Kinetics of austenitisation of three plain carbon steels, viz., Steel-A, Steel-B and Steel-C, using Differential Scanning Calorimetry (DSC) have been presented. Values of Kinetic parameters viz., activation energy, E, and order of reaction or the Avrami exponent, n, for this transformation have also been experimentally determined using Kissinger analysis. Using these Kinetic parameters and Johnson-Mehl-Avrami (JMA) equation, values of intercritical transformation time to obtain the equilibrium or maximum amount of austenite at different intercritical annealing temperatures for the three plain-carbon steels under study, have also been theoretically calculated and compared with experimentally determined values of this parameter.

6.1 Non-Isothermal Kinetics of Austenitisation by Differential Scanning Calorimetry (DSC)

DSC response curves of Steel-A, Steel-B and Steel-C in normalised condition, obtained at three different heating rates for each Steel, are shown in Figs.6.1-6.3 respectively.

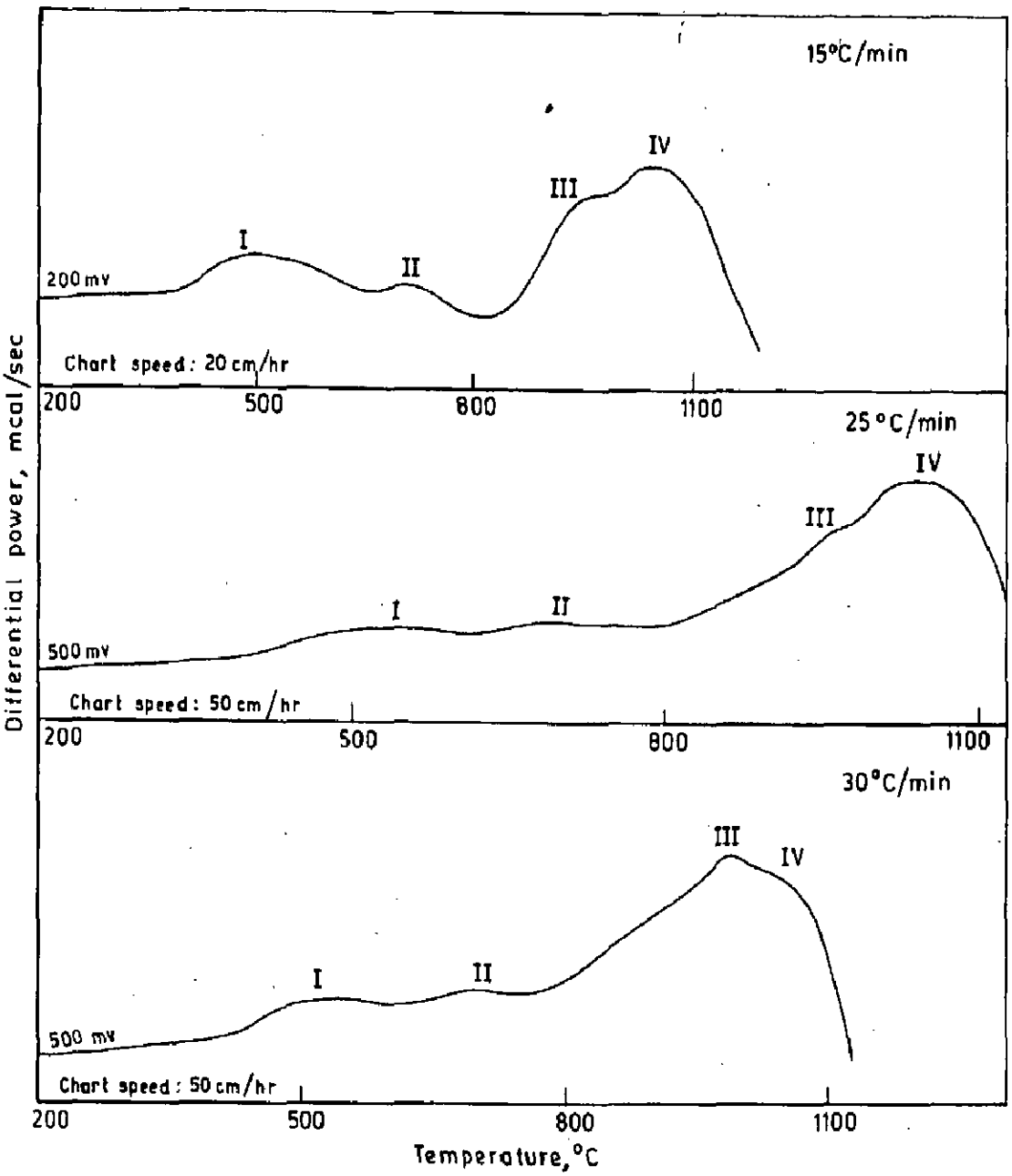

Fig. 6.1_ DSC response curves of 0.08 percent C-steel obtained at different heating rates

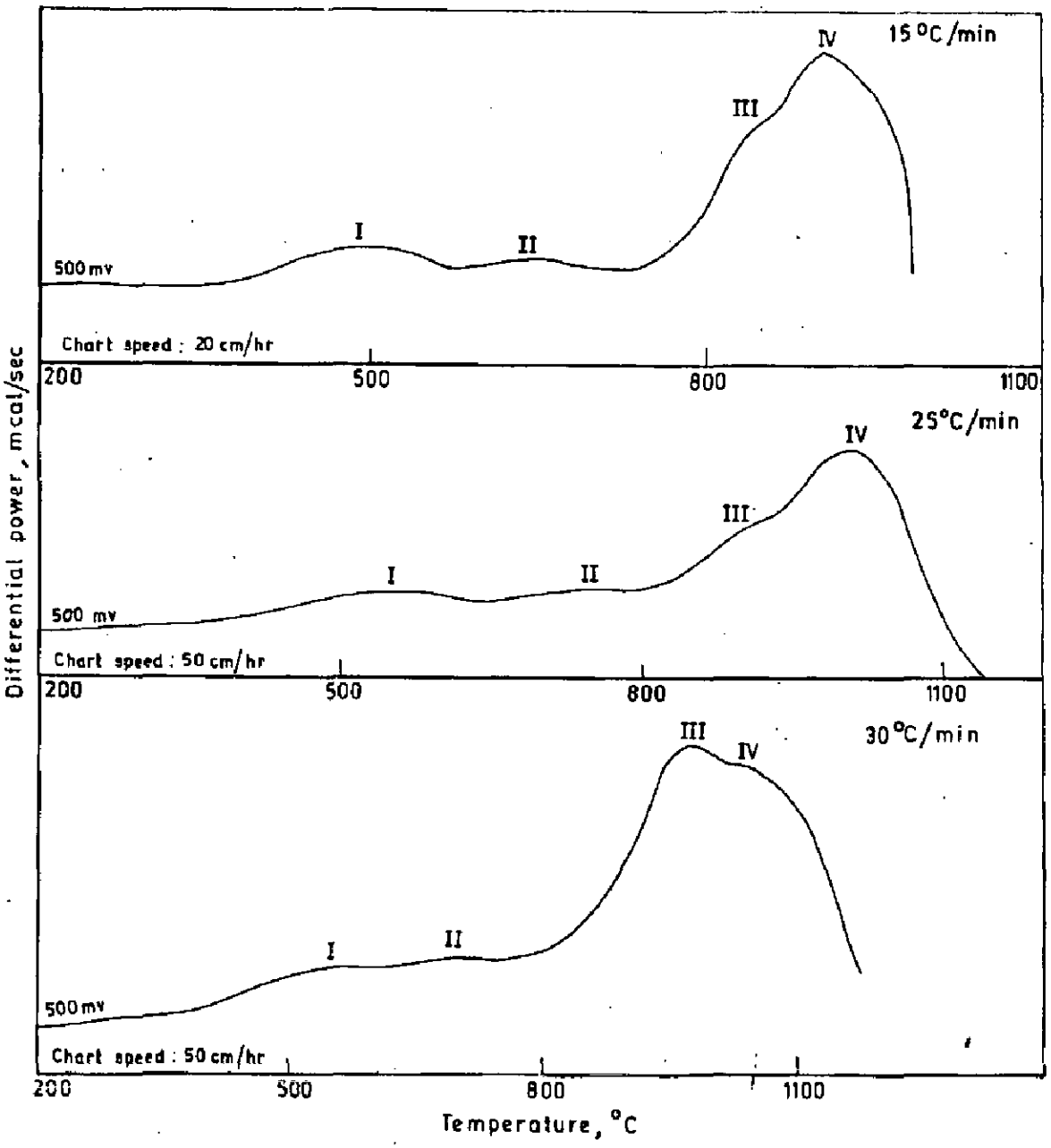

Fig. 6.2 – DSC response curves of 0.115 percent C-steel obtained at different heating rates

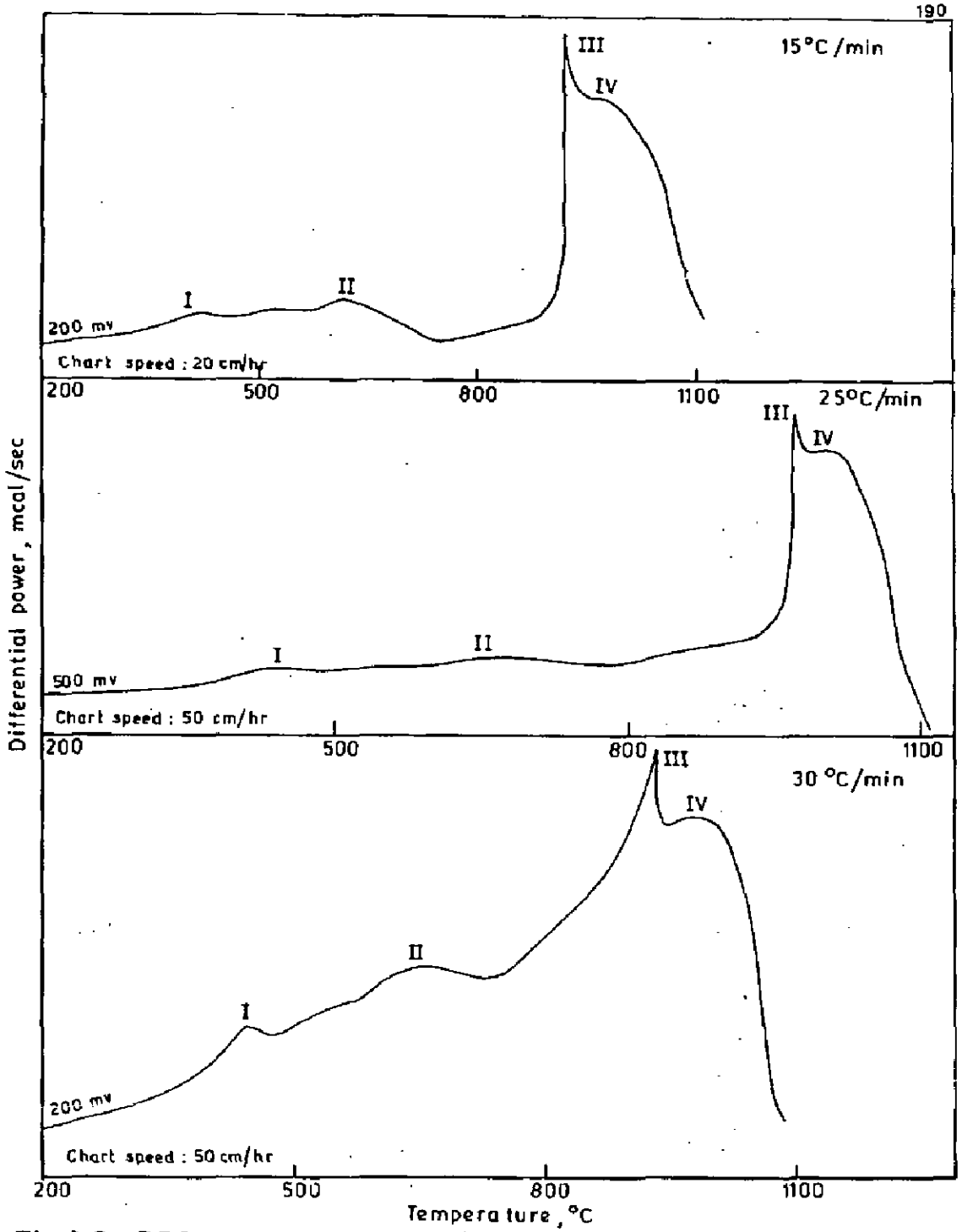

Fig.6.3 _ DSC response curves of 0.4 percent C - steel obtained at different heating rates

As will be noted from Fig.6.1, the DSC response curve of Steel-A obtained at a heating rate of 15°C/min., shows four peaks of varying magnitude. These are marked as peak-I, peak-II, peak-III and peak-IV. Of these, peaks-I and II are distinct whereas peaks-III and IV are overlapping. DSC response curves of this steel obtained at heating rates of 25°C/min. and 30°C/min. also show similar peaks. Steel-B and Steel-C also exhibit similar four peaks in each of these curves obtained at three different heating rates as depicted in Figs.6.2 and 6.3 respectively. It is, however, to be noted that peak-III for Steel-C is more distinct as compared to other steels.

These four peaks in the DSC response curve indicate a series of four processes occurring during heating of steel powder sample from room temperature to the elevated temperature corresponding to single phase austenite region of Fe-C phase diagram.

Peak-I of the DSC response curve occurring around 400°C is attributed to stress-relieving process of strain-hardened steel powder. This strain-hardening is introduced in the steel powder during its preparation as a result of filing operation of the sheet steel specimens. This is certified by the observation that the same powder sample of steel once tested by heating it to the single phase austenite region and cooled to room temperature in the DSC, does not show the first peak in the DSC response curve when heated second

time, due to absence of strain - hardening effect at this stage.

Occurrence of peak-II in the temperature range of 650-700°C in the DSC response curves for all steel sample tested is attributed to the spheroidisation of pearlite. Speich et al [16], Garcia et al [17], Yang et al [18], and Jeong et al [19] have reported that Spheroidisation of cementite within pearlite colonises is an important initial step of austenitisation. This fact is also reflected in the optical micrograph of DPS-A, intercritically annealed at 740°C for 1 minute shown in Fig.5.4b, depicting small particles of martensite dispersed mostly along the ferrite grain-boundaries and the untransformed pearlite. Austenite nucleates at the interface between ferrite and the spheroidised cementite.

Peak-III in the DSC response curve is attributed to dissolution of pearlite and nucleation and growth of austenite, whereas peak-IV is attributed to equilibration of carbon between austenite and ferrite phases, i.e., the final stage of austenitisation.

All processes of the present study indicated on the response curve by peaks, are endothermic in nature and hence the corresponding peaks appear above the base line on the DSC response curve [90]. However, exothermic processes would be indicated on the DSC response curve by peaks or humps below the base line. Further, size of these peaks are indicative

of the energies associated with such processes as the area under the peak is directly proportional to the enthalpy change associated with the corresponding process.

In the present investigation, values of Kinetic parameters such as activation energy, E, and order of reaction or Avrami exponent, n, are calculated using data obtained from DSC response curve and based on Kissinger analysis [28], presented in Section 2.2.4, Eq.(2.27) for the peak-III representing process of dissolution of pearlite and formation of austenite. These Kinetic parameters are used for calculation of intercritical (ICA) time for obtaining equilibrium or maximum amount of austenite at any selected intercritical annealing (ICA) temperature for any given steel. This is important for process optimisation in production of dual-phase steels as beyond this ICA-time, the mechanical property viz., strength, start decreasing.

For steel-A, values of temperature, T_m, expressed in degree Kelvin corresponding to peak-III are noted from the DSC response curves for each of the three heating rates, β, expressed in °C/Sec. units. Using these data, Kissinger plot between parameters $(n(\beta/T_m^2)$ and $\frac{1}{T_m}$ is drawn for steel-A as shown in Fig.6.4.

Similarly, Kissinger plots corresponding to peak-III are also drawn for Steel-B and Steel-C and are presented in the same Figure. As will be noted, these plots are linear

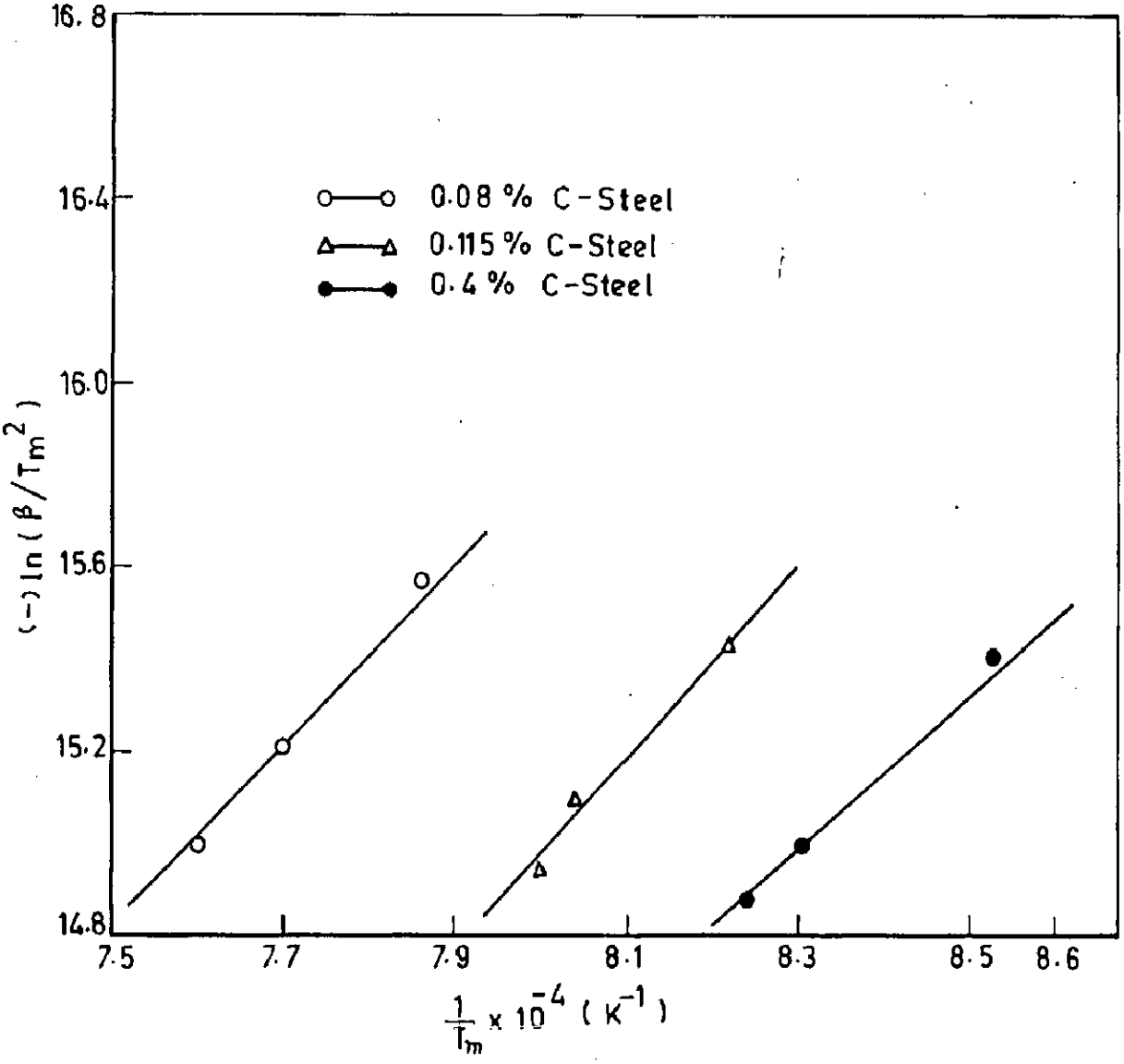

Fig. 6.4 – Kissinger plots of $\ln(\beta/T_m^2)$ against $1/T_m$ for the curves in Figs. 6.1-6.3

in nature and the slopes of which yield the values of apparent activation energy, E_a . Linear regression analysis of the data plotted is used to arrive at the values of slopes of straight line plots in Fig.6.4. Using this value of apparent activation energy, E_a , value of actual activation energy, E, can calculated using Eq.(2.28) on substitution of value of constant C_1 derived from data presented in Table 2.2, after Criado et al. [32].

For calculation of the value of order of reaction or Avrami exponent, n , making use of Eq.(2.30), plots of parameters $\ln\left(\ln\left(\frac{1}{1-\alpha}\right)\right)$ VS $\frac{1}{T}$ are drawn for each type of steel, Steel-A, Steel-B and Steel-C studied. These linear plots are presented in Fig.6.5. It is to be noted that values of the volume fraction of austenite, α, transformed at any temperature, T (expressed in degree Kelvin), are calculated from the areas under the peak-III of the DSC response curves. The value of α at any particular temperature, T, is equal to the ratio of area of the curve under the peak between the starting point of the peak and the vertical at that temperature to the total area under the peak. For this purpose, areas are measured using planimeter. Further, the slope of these straight line plots calculated using linear regression analysis, yields the value of parameter using Eq.(2.30), nE, where n is the Avrami exponent and E is the activation energy, value of which has already been calculated using Kissinger analysis. From these two values of parameters nE and

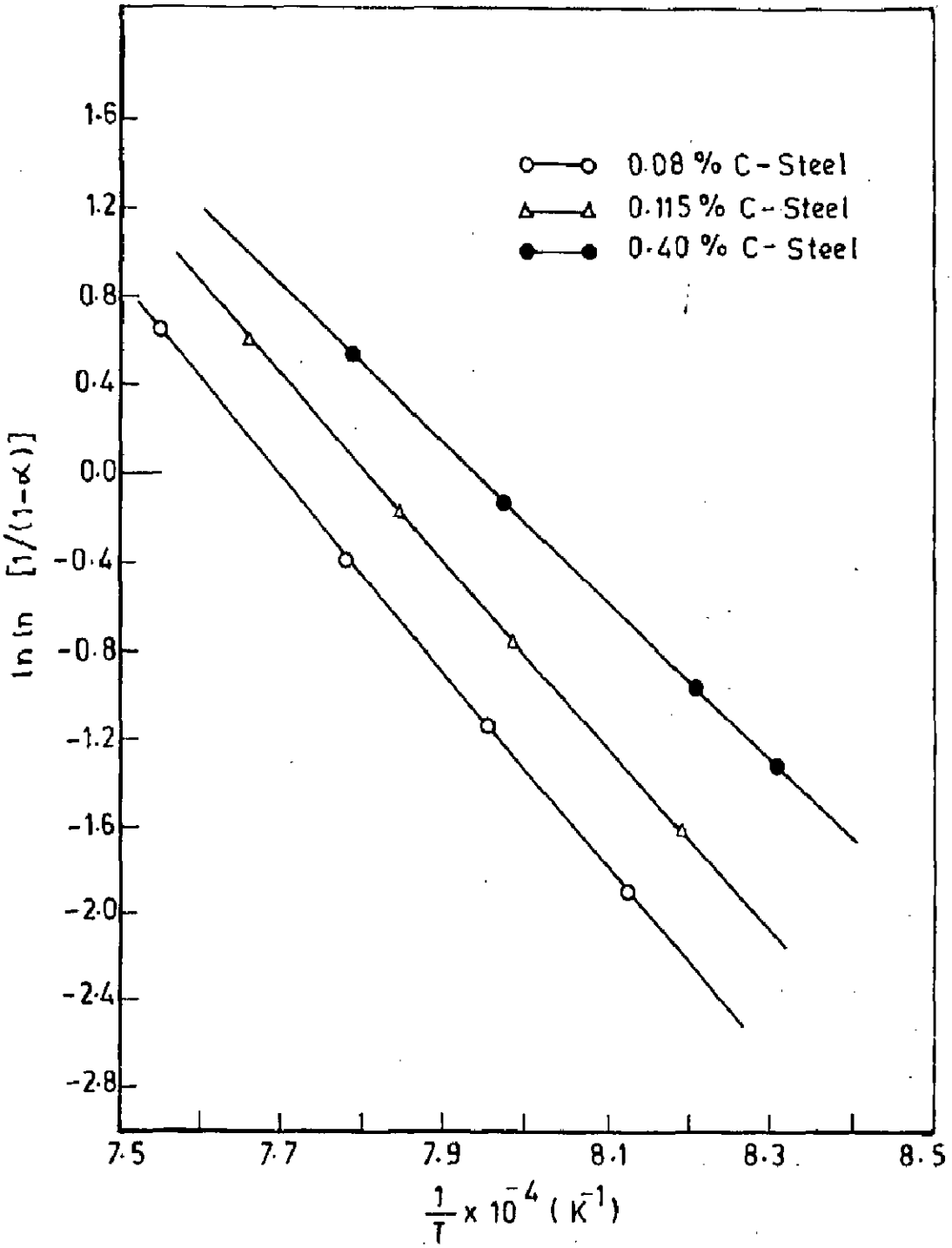

Fig. 6.5 _ Plots of ln ln [1/(1−α)] against 1/T for the data in curves obtained at β = 25°C/min of Figs. 6.1 – 6.3

E, the value of Avrami exponent or the order of reaction, n is calculated. Values of activation energy, E, and Avrami exponent, n, so obtained for Steel-A, Steel-B and Steel-C, are presented in Table 6.1.

In order to theoretically calculate the value of the intercritical annealing time for attaining equilibrium or maximum amount of austenite at any specific intercritical annealing temperature for a given steel, the following Johnson-Mehl-Avrami (JMA) Kinetic equation is used,

$$\alpha = 1 - \exp(-Kt)^n \qquad \ldots (6.1)$$

where, α is the austenite volume fraction transformed isothermally at any desired temperature in time 't'. K is rate constant and, n, is the order of reaction or Avrami exponent. Eq.(6.1) can be rewritten in the following alternative form,

$$\ln t = \frac{1}{n}\left[\ln\left(\ln\left(\frac{1}{1-\alpha}\right)\right)\right] - \ln K \qquad \ldots (6.2)$$

For use of Eq.(6.2), calculated values of Avrami exponent, n, for Steel-A, Steel-B and Steel-C using Kissinger analysis, have already been presented in Table 6.1. Value of α can be calculated theoretically for any plain carbon Steel for specific intercritical annealing temperature viz., 740°C, 760°C and 780°C using Fe-C, phase diagram Fig.2.3c.

For calculation of rate constant, of JMA Kinetic equation, the non-isothermal austenitisation equation after Criado et al. [32] i.e., Eq. (2.30), rewritten in the following

Table 6.1

Kinetic parameters of austenitisation of different steels

Plain Carbon Steel Designation	Activation Energy, E, KJ/mol.	Avrami Exponent n
Steel-A 0.08 wt.pct.Carbon	117.07	3.5
Steel-B 0.115 wt.pct.Carbon	113.43	3.6
Steel-C 0.4 wt.pct.Carbon	110.21	3.8

form, is used,

$$ln\ ln\left(\frac{1}{1-\alpha}\right) = ln\ \frac{AE}{\beta R} - 5.3 - \frac{1.05nE}{RT} \quad \ldots (6.3)$$

In this equation, symbol A (the ratio constant rewritten as Ko in Eq. (6.4) is the preexponential factor of Arrhenius equation and all other symbols have same meaning. Values of parameters α, n, E, β, R and T of Eq.(6.3) are known and hence that of preexponential factor, A can be calculated.

For Steel-A, using Eq.(6.3) with following substitutions,

α = 0.999 corresponding to the maximum reaction rate or the peak in the DSC response curve (β=25°C/min).

Temperature T, equals to T_m corresponding to the peak, i.e., 1025 °K of the DSC response curve,

n = 3.5,

β = 25°C/min or 0.416°C/Sec

E = 117.07 KJ/mol.

One gets,

$$A = Ko = 939.15 \quad \ldots (6.4)$$

Further, using Arrhenius equation,

$$K = Ko\ exp\ \left(-\frac{E}{RT}\right) \quad \ldots (6.5)$$

Where, K, is the temperature dependent rate constant, Ko, is the preexponential factor, E, is the activation energy

of phase transformation, T, is the absolute temperature of transformation and R, is the universal gas constant.

On substitution of values of Ko=939.15 from Eq.(6.4), E from Table 6.1 for Steel-A, R=8.314 J/mol. and the inter-critical temperature T=1013°K (740°C), in Eq.(6.5), one gets the value of rate constant at 740°C intercritical temperature as,

$$K = 8.62 \times 10^{-4}$$

Further, for Steel-A (C=0.08 wt. pct.) the value of α or the austenite volume fraction in equilibrium with ferrite at 740°C (1013°K) measured from Fe-C phase diagram, equal to 11 pct.

$K = 8.62 \times 10^{-4}$ as calculated above and , n = 3.5 from Table 6.1, substituting these values in Eq.(6.2), one gets

$$t = 627.03 \text{ Sec}$$
$$= 10.45 \text{ min.},$$

The theoretical intercritical annealing times for Steel-A can similarly be calculated at other intercritical temperature viz., 760°C and 780°C used in the present work and are presented in Table 6.2.

Values of theoretical intercritical annealing time for Steel-B and Steel-C are similarly calculated by using values of their activation energies and Avrami exponent

Table 6.2

Theoretically calculated and experimental values of austenite volume fraction and intercritical annealing time at three temperatures for different steels

Plain Steel Designation	Austenite Volume Fraction* , %						Intercritical Annealing Time, minute					
	Theoretically Calculated			Experimental			Theoretically Calculated			Experimental		
	740°C	760°C	780°C	740°C	760°C	780°C	740°C	760°C	780°C	740°C	760°C	780°C
Steel-A 0.08 wt.pct. Carbon	11.0	15.5	22.0	13.0	18.5	24.0	10.45	8.87	7.66	10.0	10.0	10.0
Steel-B 0.115 wt.pct Carbon	15.0	20.0	26.5	17.0	24.0	31.0	9.33	7.85	6.72	10.0	10.0	10.0
Steel-C 0.4 wt.pct. Carbon	60.0	70.0	82.0	65.0	74.5	82.0	11.9	9.93	8.54	10.0	10.0	10.0

*Martensite Volume Fraction (MVF) after quenching.

CHAPTER - 7

CONCLUSIONS

Following conclusions are drawn from the present investigations:

(i) The intercritical annealing heat treatment of plain-carbon steels for development of dual-phase microstructture at any specific intercritical annealing temperature should not be carried out beyond the time required for transformation to maximum volume fraction of austenite (and hence martensite on quenching) since the strength starts falling inspite of the ductility and formability saturating at their minimum.

(ii) The strength of dual-phase steels after attaining a maximum falls due to grain-growth in ferrite phase and equilibrium of carbon between ferrite and austenite phases during the final stage of intercritical austenitisation of steel.

(iii) The decrease in ductility and formability is initially due to increased value of martensite volume fraction in dual-phase structure followed subsequently by equilibration of carbon between ferrite and austenite phase during the final stage of intercritical austenitisation.

respectively taken from Table 6.1 and utilising Eq.(6.2) and Eq.(6.3). The calculated values are also presented in Table 6.2.

It will be noted from the data presented in Table 6.2, that fairly good correspondence is observed between the theoretically calculated and experimentally determined values of intercritical annealing time for attaining maximum austenite or martensite volume fraction at the specific intercritical annealing temperatures viz., 740°C, 760°C and 780°C, used in the present work for all the three plain carbon steels viz., Steel-A with 0.08 wt. pct. carbon, Steel-B with 0.115 wt. pct. carbon and Steel-C with 0.4 wt. pct. carbon respectively.

This reflects to an excellent applicability of the Kinetic data obtained from non-isothermal austenitisation Kinetics based on DSC studies and the Johnson-Mehl Avrami Kinetic equation to the system under present investigation. This also bears testimony to the fact that extensive experimentation is not essential for optimisation of intercritical annealing operation of plain carbon Steels to attain the desired mechanical properties of dual phase steels.

(iv) Value of strength of dual-phase steels can be theoretically calculated using a modified expression arrived at by (a) treating dual-phase steels as composites, (b) based on the shear-lag analysis and (c) taking into account the shape of embedded martensite island or particle.

(v) Similarly, the value of intercritical annealing time to attain equilibrium or maximum austenite (and hence martensite on quenching) volume fraction at any specific intercritical annealing temperature for plain-carbon steels can also be theoretically calculated using Johnson-Mehl-Avrami (JMA) Kinetic equation with substituted experimental values of relevant Kinetic parameters obtained from non-isothermal austenitisation.

SUGGESTIONS FOR FUTURE WORK:

Based on the results obtained in the present investigations, the following suggestions are made for further work in this area:-

(i) Shorter intercritical annealing times as low as 10 seconds should be used to investigate specially the effect on ductility and formability of plain-carbon dual-phase steels.

(ii) Fatigue properties of the plain-carbon dual-phase steels should be investigated to explore new applications for these steels.

(iii) Transmission Electron Microscopy (TEM) should be used along with optical microscopy to reveal in greater detail the various stages of isothermal intercritical austenitisation of steels.

(iv) For possible applications of dual-phase steels under corrosive environments and also the cryogenic conditions, their behaviour should be investigated under such conditions.

(v) Work on similar lines can be extended on role of different alloying elements in the production of dual-phase steels.

REFERENCES

1. R.A.Grange, Proc. Second Int. Conf. on the Strength of Metals and Alloys, Vol. 3, ASM, pp. 861-876, (1970).

2. S.Hayami and T.Furukawa, Proc. Micro-Alloying 75, Union Carbide Corporation, New York, pp. 311-320, (1977).

3. M.S.Rashid, SAE Preprint 760206, paper presented at the Automotive Engg. Congress and Exposition, Detroit, Feb., (1976).

4. J.H.Bucher and E.G.Hamburg, High-Strength Formable Sheet Steel, SAE Reprint 770164, (1977).

5. T.Furukawa, H.Morikawa, H.Takechi and K.Koyama, Proc. Conf. on Structure and Properties of Dual-Phase Steels, R.A.Kot and J.W.Morris, ed., AIME, New York, pp. 281-303, (1979).

6. K.Nakaoka, Y.Hosoya, M.Ohmura and A.Nishimoto, pp. 330-345, ibid.

7. P.E.Repas, Proc. Conf. on Dual-phase and Cold-Forming Vanadium Steels in the Automobile Industry, Vanitec, Berlin, pp. 13-22, (1978).

8. T.Tanaka, M.Nishida, K.Hashiguchi and T.Kato, Proc. Conf. on Structure and Properties of Dual-Phase Steels, R.A.Kot and J.W.Morris, ed., AIME, New York, (1979).

9. T.Matsuoka and K.Yamomori, Met. Trans., 6A, pp. 1613-1622, (1975).

10. P.R.Mould and C.C.Skena, Proc. Conf. on Formable HSLA and Dual-Phase Steels, R.A.Kot and J.W.Morris, ed., AIME, New York, pp. 183-205, (1979).

11. A.P.Coldren, G.T.Eldis, R.M.Buck, G.Tither, P.Boussel and T.Chihara, J. of Molybdenum Technology, Vol. 14, No.3, pp. 3-12, (1980).

12. A.P.Coldren and G.Tither, J. Metals, Vol. 30, No.4, pp.6-19, (1978).

13. A.P.Coldren, G.Tither, A.Cornford and J.R.Hiam, Proc. Conf. on Formable HSLA and Dual-Phase Steels, R.A.Kot and J.W.Morris, ed., AIME, New York, pp. 207-228, (1979).

14. G.T.Eldis and A.P.Coldren, J. Metals, Vol. 32, No.4, pp.41-48, (1980).

15. P.E.Repas, Proc. XVII Conf. on Mech. Working and Steel Processing, AIME, New York, pp. 277-305, (1979).

16. G.R.Speich, V.A.Demarest and R.L.Miller, Met. Trans. A., Vol. 12A, pp. 1419-1428, (1981).

17. C.I.Garcia and A.J.Deardo, Met. Trans. A., Vol. 12A, pp.521-530, (1981).

18. D.Z.Yang, E.L.Brown, D.K.Matlock, and G.Krauss, Met. Trans. A. Vol. 16A, pp. 1523-1526, (1985).

19. Woo Chang Jeong and Chong Hee Kim, J. Material Science, Vol. 20, pp. 4392-4398, (1985).

20. M.M.Souza, J.R.C. Guimaraes and K.K. Chawla, Met. Trans. A, Vol. 13A, p. 575, (1982).

21. J.B.Gilmour, G.R.Purdy and J.S.Kirkaldy, Met. Trans., Vol. 3, p. 3213, (1972).

22. M.D.Geib, D.K.Matlock and G.Krauss, Met. Trans. A, Vol. 11A, pp. 1683-1689, (1980).

23. G.Thomas and J.Y.Koo, Proc. Conf. on Structure and Properties of Dual-Phase Steels, R.A.Kot and J.W.Morris, ed., AIME, New York, pp. 183-201, (1979).

24. M.Avrami, J.Chem. Phys., Vol. 8, p. 212, (1940).

25. A.Roosz, Z.Gacsi and E.G.Fuchs, Acta Metall., Vol. 31, No. 4, pp. 509-517, (1983).

26. J.W.Christian, The Theory of Transformations in Metals and Alloys, Pergamon Press, Oxford, (1965).

27. A.M.Gokhale, C.V.Iswaran and R.T. Dehoff, Met. Trans. A, Vol. 11A, p. 1377, (1980).

28. H.E.Kissinger, Analyt. Chem. Vol. 29, p. 1702, (1957).

29. D.W.Henderson, J. Non-Cryst, Solids, Vol.30, p. 301, (1979)

30. M.Matsuura and K.Suzuki, J.Material Science, Vol. 14, p. 395, (1979).

31. L.V.Meisel and P.J.Cote, Acta Metall., Vol. 31, p. 1053, (1983).

32. J.M.Criado and A.Ortega, Acta Metall., Vol. 35, No. 7, pp. 1715-1721, (1987).

33. C.D.Doyle, J. Appl. Polym. Sci., Vol. 6, p. 639, (1962).

34. H.Horowitz and G.Metzger, Analyt. Chem. Vol. 35, p. 1464, (1963).

35. D.K.Matlock, G.Krauss, L.F.Ramos, and G.S.Huppi, Proc. Conf. on Structure and Properties of Dual-Phase Steels, R.A.Kot and J.W.Morris, ed., AIME, New York, Pp. 62-90, (1979).

36. R.D.Lawson, D.K.Matlock, and G.Krauss, Metallography, Vol. 13, pp. 71-87, (1980).

37. G.Krauss and A.R.Marder, Met. Trans. Vol.2, p. 2343, (1971).

38. J.M.Moyer and G.S.Ansell, Met. Trans. A, 6A, pp. 178-179, (1975).

39. D.S.Dabkowski and G.R.Speich, Proc. XV Conf. on Mechanical Working and Steel Processing, AIME, New York, pp. 284-312, (1977).

40. H.Hillert, Jerkontorets Annaler, Vol. 141, pp. 67-89, (1989).

41. J.M.Rigsbee and P.J.Vander Arend,, Proc. Conf. on Formable HSLA and Dual-Phase Steels, R.A.Kot and J.W.Morris, ed., AIME, New York, pp. 56-86, (1979).

42. B.V.Narashima Rao and G.Thomas, Proc. Conf. on Martensite Transformations, Cambridge, Mass., pp. 12-21, (1979).

43. Z.Nishiyama, Martensitic Transformation, Academic Press, New York, NY, (1978).

44. R.G.Davies, Met. Trans., 10A, pp. 113-118, (1979).

45. K.Nakoaka, K.Araki and K.Kurihara, Conf. Proc. on Formable HSLA and Dual-Phase Steels, R.A.Kot and J.W.Morris, ed., AIME, New York, pp. 126-141, (1979).

46. Luis F. Ramos, David K. Matlock, and George Krauss, Met. Trans. A., Vol. 10A, pp. 257-261, (1979).

47. T.Gladman, Metals Technology, Vol. 10, pp. 274-281, (1983).

48. N.K.Balliger and T.Gladman, Metal Science, pp. 95-108, (1981).

49. M.F.Ashby, Philosophical Magazine Vol. 14, p. 1157, (1966).

50. G.R.Speich and R.L.Miller, Conf. Proc. on Structure and Properties of Dual-Phase Steels, R.A.Kot and J.W.Morris, ed., AIME, New York, pp. 145-182, (1979).

51. W.C.Lesile and R.J.Sober, Trans. ASM, Vol. 60, pp. 459-484, (1967).

52. J.Y.Koo, M.J.Young, and G.Thomas, Met. Trans. A., Vol. 11A, pp. 852-854, (1980).

53. R.G.Davies, Met. Trans. A, Vol. 9A, pp. 671-679, (1978).

54. G.T.Eldis, Proc. Conf. on Structure and Properties of Dual-Phase Steels, R.A.Kot and J.W.Morris, ed., AIME, New York, pp. 202-220, (1979).

55. A.R.Marder and B.L.Bramfitt, Proc. Conf. on Structure and Properties of Dual-Phase Steels, R.A.Kot and J.W.Morris, ed., AIME, New York, pp. 242-259, (1979).

56. P.R.Prasad, Ph.D. Thesis on Microstructure and Mechanical Properties of Rheocast Aluminium-Copper Alloys, University of Roorkee, Roorkee, India, (1983).

57. P.S.Theocaris and S.A.Paipetis, Stresses in Three Dimensional Composites with Limiting Shear Properties in Developments in Composite Materials-1 G.S. Holister ed., Applied Science Publishers, London, p. 197, (1977).

58. K.Sezawa and B.Miyazaki, Proc. Japan Soc. Mech. Engrs., Vol. 31, p. 625, (1928).

59. R.T.Dehoff and F.N.Rhines, Quantitative Microscopy, McGraw-Hill Book Company, p. 140, (1968).

60. S.T.Mileiko, J. Materials Science, Vol. 4, pp. 974-977, (1969).

61. A.Considere, Ann. Ponts de Chauss, Vol. 9, pp. 574-575, (1985).

62. G.Dieter, Mechanical Metallurgy, McGraw Hill Inc., New York, (1961).

63. M.S.Rashid, Proc. Conf. on Formable HSLA and Dual-Phase Steels, R.A.Kot and J.W.Morris, ed., AIME, New York, pp. 1-24, (1979).

64. K.Araki, Y.Takada and K.Nakoaka, Trans. Iron and Steel Inst. Japan, Vol. 17, 710-717, (1977).

65. I.Tamura, Y.Tomata, A.Akao, Y.Yamaoha, M.Ozawa, and S.Kanotoni, Trans. Iron and Steel Inst. Japan, Vol. 13, pp. 283-292, (1973).

66. J.Becker and E.Hornbogen, Proc. Conf. on Structure and Properties of Dual-Phase Steels, R.A.Kot and J.W.Morris, ed., AIME, New York, pp. 20-39, (1979).

67. N.J.Kim and G.Thomas, Met. Trans. A., Vol. 12A, pp. 483-489, (1981).

68. S.Hayami, T.Furukawa, H.Gondoh and H.Takechi, Proc. Conf. on Formable HSLA and Dual-Phase Steels, R.A.Kot and J.W. Morris, ed., AIME, New York, pp. 169-182, (1979).

69. R.Lagneborg, Proc. Conf. on Dual-Phase and Cold-Pressing Vanadium Steels in the Automobile Industry Vanitec, Berlin, pp. 43-50, (1978).

70. G.S.Huppi, D.K.Matlock and G.Krauss, Scripts Met., Vol.14, pp. 1239-1243, (1980).

71. V.F.Zac Kay, E.R.Parker and D.Fahr and R.Burch, Trans. ASM, Vol. 60, pp. 252-259, (1967).

72. G.T.Eldis, Proc. Conf. on Structure and Properties of Dual-Phase Steels, R.A.Kot and J.W.Morris, ed., AIME, New York, pp. 202-220, (1979).

73. F.A.Hultgren, Blast Furnace and Steel Plant, pp. 149-156, (1968).

74. K.Matsudo and T.Shimomura, Trans. Iron and Steel Inst. Japan, Vol. 10, pp. 448-458, (1970).

75. A.Okamoto and M.Takahasi, Proc. Conf. on Fundamentals of Dual-Phase Steels, R.A.Kot and B.L.Bramfitt, ed., The Metallurgical Society of AIME, Chicago, Illinois, pp. 427-445, (1981).

76. Y.Hosoya, K.Kurihara and K.Nakaoka, paper presented at Fall Meeting of the Iron and Steel Inst. Japan, Toyama, Japan, (1978).

77. M.S.Rashid, SAE Preprint 770221, (1977).

78. W.G.Brazier and R.Stevenson, SAE Preprint 780137, (1978), (LDH).

79. R.G.Davies, Met. Trans. A., Vol. 9A, pp. 41-52, (1978).

80. A.M.Sherman and R.G.Davies, Met. Trans. A., Vol. 10A, pp. 929-933, (1979).

81. G.R.Speich and R.L.Miller, Proc. Conf. on Fundamentals of Dual-Phase Steels, R.A.Kot and B.L.Bramfitt, ed., The Metallurgical Society of AIME, Chicago, Illinois, pp. 279-304, (1981).

82. R.P.Krupitzer, ibid, pp. 315-330.

83. M.S.Rashid, ibid, pp. 37-39.

84. R.G.Davies, Met. Trans. A, Vol. 10A, pp. 1549-1555, (1979).

85. M.C.Flemings, Solidification Processing, McGraw-Hill, Inc., p. 94, (1974).

86. W.B.Morrison, Trans. ASM, Vol. 59, pp. 824-846, (1966).

87. J.Topping, Error of Observations and their Treatment, Chapman and Hall, London, (1972).

88. G.Thomas, Transmission Electron Microscopy of Metals, John Wiley and Sons, Inc. 1962, p. 154.

89. D.J.Blickwede, Trans. ASM., Vol.61, p.653, (1968).

90. R.C.Mackenzie, Differential Thermal Analysis, Vol.1, Academic Press, London and New York, p. 32, (1970).